2012

pH MODULATION OF FIBRIL DISSOCIATION AND COPPER BINDING PROPERTIES OF THE PRION PROTEIN

Xu Qi
The University of Montana

pH MODULATION OF FIBRIL DISSOCIATION AND COPPER BINDING PROPERTIES OF THE PRION PROTEIN

By

Xu Qi

B. Med., Zhejiang College of Traditional Chinese Medicine, Hangzhou, China, 1994
M. Med., Xi'an Jiaotong University School of Medicine, Xi'an, China, 2001

Dissertation

presented in partial fulfillment of the requirements
for the degree of

Ph.D.
in Integrative Microbiology and Biochemistry

The University of Montana
Missoula, MT

Official Graduation Date (July 27, 2012)

Approved by:

Dr. JB Alexander Ross, Dean of the Graduate School
Graduate School

Dr. Michele McGuirl, Research Advisor
Division of Biological Sciences

Dr. J. Stephen Lodmell, Examination Chair
Division of Biological Sciences

Dr. Scott Samuels
Division of Biological Sciences

Dr. J. B. Alexander Ross
Department of Chemistry and Biochemistry

Dr. William Laws
Department of Chemistry and Biochemistry

TABLE OF CONTENTS

TABLE OF CONTENTS ii
LIST OF FIGURES iv
LIST OF TABLES vi
ABSTRACT vii
ACKNOWLEDGEMENTS viii
CHAPTER I: GENERAL INTRODUCTION 1
I. Prion diseases and amyloid diseases 2
A. Protein-only hypothesis 5
B. Prion-like mechanisms in other amyloid diseases 8
II. The cellular prion protein (PrP^{C}): structure, biology and function 9
A. Structural features of PrP^{C} 10
B. Cell biology of PrP^{C} 13
C. Putative physiological functions of PrP^{C} 16
III. The scrapie prion protein (PrP^{Sc}): structure, conversion and strains 21
A. Proposed structures of PrP^{Sc} 21
B. PrP^{Sc} neurotoxicity 26
C. Prion strains and the species barrier 29
IV. Prions beyond disease 32
V. Concluding remarks 33
CHAPTER II: DISSOCIATION OF RECOMBINANT PRION PROTEIN FIBRILS INTO SHORT PROTOFILAMENTS: POSSIBLE ROLES FOR THE N-TERMINAL DOMAIN AND VESICLES OF THE LATE ENDOCYTIC PATHWAY 35
I. Introduction 36
A. Mechanism of conversion of PrP^{C} to PrP^{Sc} 36
B. Rationale and aims 41
II. Experimental procedures 44
A. Protein expression and purification 44
B. Preparation of recombinant PrP23-232 conformers 46
C. Dissociation of rPrP fibrils and preparative ultracentrifugation 47
D. Asymmetric flow field-flow fractionation (AF4) and light scattering analysis of prion conformers 47
E. Circular dichroism (CD) and thermal denaturation 48
F. Fourier transform infrared (FT-IR) spectroscopy 49
G. Proteinase K (PK) digestion 49
H. In-gel tryptic digestion and mass spectrometry 49
I. Transmission electron microscopy 51
J. Kinetic analysis 52
III. Results 53
A. Mildly acidic conditions induce protofilament formation 53
B. Composition of the protofilaments amyloid core 56
C. Purification and size determination of soluble protofilaments 61

D. The effect of pH and salt on protofilament formation 64
E. Characterization of soluble protofilaments 66
F. Ability of protofilaments to accelerate PrP conversion 69
IV. Discussion 72
A. Mechanism of fibril dissociation 73
B. Protofilament structure and seeding capability 74
C. Pathological relevance of pH-induced protofilament formation 75
CHAPTER III: EFFECT OF pH AND FIBRILLATION ON COPPER BINDING TO PRION PROTEIN 78
I. Introduction 79
A. Copper binding in the octarepeat region 79
B. Copper binding at the fifth binding site 83
C. The affinity of PrP for Cu(II) 85
D. Physiological significance and pathological implications of PrP-Cu(II) interaction 87
E. Techniques to elucidate PrP-Cu(II) interactions 89
F. Rationale and Aims 94
II. Experimental procedures 96
A. Protein expression and purification 96
B. Mutagenesis 96
C. Preparation of recombinant PrP conformers 97
D. Asymmetric flow field-flow fractionation (AF4) 97
E. Circular dichroism (CD) 98
F. Isothermal titration calorimeter (ITC) 98
G. Electron paramagnetic resonance (EPR) 99
III. Results 101
A. Copper binding to the fifth binding site at neutral pH 101
B. Copper binding to the fifth binding site at pH 5.5 109
C. Copper binding to the octarepeat region at neutral pH 111
D. Copper binding to octarepeat region at pH 5.5 120
IV. Discussion 124
E. The role of copper binding in PrP aggregation 125
F. Location of the fifth copper binding site 127
G. pH dependence of copper binding in PrP 128
H. Effect of fibrillation on copper binding 132
CHAPTER IV: GENERAL DISCUSSION 134
I. Low-pH induced fibril dissociation 135
II. Copper binding to prion conformers 141
CHAPTER V: APPENDIX 148
CHAPTER VI: REFERENCES 164

LIST OF FIGURES

Figure 1-1. Structural features of the Syrian hamster PrP^{C}. 11
Figure 1-2. Overview of PrP^{C} biosynthesis and its conversion to PrP^{Sc}..... 16
Figure 1-3. Proposed structures of PrP^{Sc} and other amyloid fibrils. 24
Figure 1-4. Schematic model for PrP^{L} production. 27
Figure 2-1. Structural features of the Syrian hamster PrP^{C}. 38
Figure 2-2. Models for mechanisms of PrP^{C} to PrP^{Sc} conversion. 40
Figure 2-3. TEM images of rPrP23-232 and rPrP90-232 fibrils showing pH-triggered dissociation of rPrP23-232 fibrils. 55
Figure 2-4. SDS-PAGE analysis of the PK-resistant regions of rPrP fibrils and protofilaments. 57
Figure 2-5. MALDI-TOF/TOF spectrum of the 1306.94 peak detected in the 12 kDa fragment. 60
Figure 2-6. Purification and size determination of soluble protofilaments. 63
Figure 2-7. Effect of salt on the dissociation of rPrP23-232 fibrils into protofilaments. 65
Figure 2-8. Biophysical characterization of rPrP23-232 protofilaments. 67
Figure 2-9. Protofilament-seeded conversion of rPrP23-232 α-monomer under mildly acidic, non-denaturing conditions. 70
Figure 3-1. Structure of Cu(II) bound pentapeptide, HGGGW. 80
Figure 3-2. Models of the coordination modes of Cu(II) binding to the octarepeats region. 82
Figure 3-3. Models of the coordination modes of Cu(II) binding to the fifth binding site. 84
Figure 3-4. Schematic diagram of an ITC instrument. 90
Figure 3-5. Schematic diagram of EPR theory. 93
Figure 3-6. Original Peisach-Blumberg Plot of type II Cu(II) complexes [374]. 94
Figure 3-7. ITC isotherms for copper binding to rPrP90-232 conformers and mutants. 101
Figure 3-8. Titration of rPrP90-232 conformers with Cu(II) at pH 7.0. 108
Figure 3-9. Titration of rPrP90-232 conformers with Cu(II) at pH 5.5. 110
Figure 3-10. ITC isotherms for copper binding to rPrP23-232 conformers. 112
Figure 3-11. Characterization of post-ITC products of rPrP23-232 and rPrP90-232 α-monomer. 114
Figure 3-12. Titration of rPrP23-232 conformers with Cu(II) at pH 7.0. 117
Figure 3-13. Titration of rPrP23-232 conformers with Cu(II) at pH 5.5. 122
Figure 4-1. Dissociation of rPrP23-232 fibrils into protofilaments in lysosome-like buffer. 140
Figure 4-2. Schematic diagram of the proposed thio-histidine and EXAFS experiments. 146
Figure 5-1. MALDI-TOF spectra of tryptic digest peptides of rPrP23-232 α-monomer. 150
Figure 5-2. MALDI-TOF spectra of in-gel tryptic digest peptides of rPrP23-232 fibril.

.....153
Figure 5-3. MALDI-TOF spectra of in-gel tryptic digest peptides of the 12 KDa PK-resistant fragment of rPrP23-232 fibrils. 156
Figure 5-4. MALDI-TOF spectra of in-gel tryptic digest peptides of the 9 KDa PK-resistant fragment of rPrP23-232 fibrils. 158
Figure 5-5. MALDI-TOF spectra of in-gel tryptic digest peptides of the 7 KDa PK-resistant fragment of rPrP23-232 fibrils. 160
Figure 5-6. MALDI-TOF spectra of in-gel tryptic digest peptides of the 5.5 KDa PK-resistant fragment of rPrP23-232 fibrils. 162

LIST OF TABLES

Table 2-1. MALDI/TOF Analysis of peptides generated from the tryptic digestion of PK-resistant fragments 58
Table 2-2. Secondary-structure composition of rPrP23-232 conformers as estimated from CD Spectra 67
Table 3-1. ITC parameters of Cu(II) binding to truncated rPrP90-232 conformers .. 103
Table 3-2. Measured EPR parameters of Cu(II) complexes formed with rPrP90-232 and rPrP23-232 conformers. 123
Table 3-3. Alignment of prion sequence 91-120 of hamster, mouse human and chicken. 128
Table 5-1. Parameters for copper complexes (expansion of the original Peisach-Blumberg plot)..... 163

ABSTRACT

Xu, Qi, Ph.D., July 2012 Integrative Microbiology and Biochemistry

Abstract Title: pH modulation of fibril dissociation and copper binding properties of the prion protein

Chairperson: Dr. Michele McGuirl

The cellular form of prion protein (PrP^{C}) is a cell-surface glycoprotein attached to lipid rafts via its glycosylphosphatidylinositol anchor. Conversion of PrP^{C} to its "scrapie" conformer (PrP^{Sc}, the fibrillar form) constitutes the key event of the etiology of prion diseases. Fibril dissociation is necessary for efficient conversion and continued propagation of the disease state. Recent studies have revealed that conversion occurs along the endocytic pathway. To better understand the dissociation process, we have investigated the effect of low pH on the stability of recombinant prion fibrils. We show that under conditions that mimic the endocytic environment, amyloid fibrils made from full-length recombinant prion protein dissociate both laterally and axially to form protofilaments. About 5% of the protofilaments are short enough to be considered soluble and contain ~100-300 monomers per structure; these also retain the biophysical characteristics of the filaments. We propose that protonation of His residues and charge repulsion in the N-terminal domain trigger fibril dissociation. Our data suggest that lysosomes and late endosomes are competent milieus for propagating the misfolded state not only by destabilizing the normal prion protein, but by accelerating fibril dissociation into smaller structures that may act as seeds for further fibril formation.

PrP^{C} binds four Cu(II) in its octarepeat region and another at the fifth binding site. Previous work has demonstrated detailed structural information on copper binding to these sites at neutral pH. Both types of binding sites contain ionizable groups, thus the effect of pH on copper binding needs to be clarified. Moreover, much less attention has been devoted to understanding copper binding in PrP^{Sc}, which is more pathologically relevant. These two aspects are investigated here using isothermal titration calorimetry and X-band electron paramagnetic spectroscopy. Our results confirm that copper binding to both the octarepeats and the fifth binding site is pH-dependent. We show that both sites bind copper in the fibrillar form with coordination modes similar to their monomeric counterparts. However, the ratios of the different coordination modes have changed in the fibril, which might suggest changes in their affinities after conversion and have potential effects on the redox properties of fibrils.

ACKNOWLEDGEMENTS

I would like to express my gratitude and sincere thanks to my adviser, Dr. Michele McGuirl, for her guidance, knowledge, understanding, and patience during my graduate study at University of Montana. Her enthusiasm for science not only established a role model for me, but also encouraged me to take up the challenge of future career. I found myself benefit a lot from her great mentorship, both academically and personally.

I also wish to extend my full appreciation to my all committee members, Dr. Stephen Lodmell, Dr. Scott Samuels, Dr. J. B. Alexander Ross, and Dr. Bill Laws, for their academic expertise and constructive critiques, which make this dissertation possible.

I am indebted to Dr. Jim Driver for his exceeding patience since the day one and great help in finishing electron microscopy work. I am also thankful to Dr. Jesse Hay, Dr. Mark Grimes for assistance in ultracentrifugation; Beverly E. Parker for helping with mass spectrometry, and Doreen Brown for electronic paramagnetic resonance spectroscopy. I must also convey my thanks to Roger Moore for providing methods and valuable discussion.

Many thanks to past and present members of the McGuirl lab, Dr. Hui-Chun Yeh, Dr. Michael Machczynski, Dr. Scott Hennelly, Chris Lennon, Marty Rice, Jessica Gilbert, Dr. Valerie Mosser, Michalee Moen and Dr. Lara Taubner for help in the lab and sharing their knowledge. I am also grateful to all the colleagues, graduate student fellows, faculty and staff of the Division of Biological Sciences for their continuous support and hard work.

Finally and foremost, my deepest thanks and love go to my wife Yongxian Jin and sons Hao and Yue. Their understanding, patience and encouragement were the bedrock upon which my PhD studies have been built. Their cheering smile always soothes my stress in an otherwise monotoned world. I would also thank my parents, Zhirong and Hanfang, for their unending spiritual support. It is their faith in me that makes my scientific career possible.

CHAPTER I:

GENERAL INTRODUCTION

The infectious pathogen of scrapie, one form of transmissible spongiform encephalopathies (TSEs) that occurs in sheep, was recognized in the 1960's as a protein due to its unusual resistance to UV inactivation and ionizing radiation [1, 2]. This agent was named "prion", which stands for proteinaceous infectious particle, by Prusiner in 1982 [3]. The major protein component of scrapie prion isolated from hamster brain was then purified and identified as prion protein (PrP) [4]. Since then, tremendous efforts have been devoted to understanding the biochemical and biophysical features of the prion protein and unraveling the enigmatic relationship between prion protein and formation of the prion particle, which is believed to be the cause of TSEs. Recent advances in protein research also reveal that prion may represent a more common phenomenon than was previously thought, from both physiological [5] and pathological [6] perspectives. The term prion has been used in yeast to describe the templated conformational change of yeast proteins into differently folded states, which can propagate in a way similar to that of infectious mammalian prion [7, 8], despite the fact that there is no sequence similarity between them. This chapter provides an overview of the main characteristics and biological and pathological relevance associated with normal mammalian cellular PrP (PrP^{C}) and its related misfolded scrapie conformers (PrP^{Sc}). The structures and functions of yeast prions are briefly addressed as well.

I. Prion diseases and amyloid diseases

Amyloid diseases are disorders caused by the accumulation of misfolded

proteins, which lead to the formation of extracellular ordered aggregates, i.e. amyloid [9] or intracellular aggregates, such as Lewy bodies [10]. Among these are TSEs, also called prion diseases, where the misfolded protein is the prion protein. Prion diseases are notorious for their unique ability to transmit disease from one individual to another and often across species [11]. However, there is increasing evidence that other amyloid diseases may adopt a similar prion-like transmission mechanism under specific circumstances, which are known as prionoids [12].

Prion diseases are a group of neurodegenerative diseases that are associated with the accumulation of a misfolded conformer of PrP (PrP^{Sc}) in the central nervous system (CNS) of animals and humans. Examples include Creutzfeldt-Jakob disease (CJD), Gerstmann-Sträussler-Scheinker syndrome (GSS), kuru, fatal familial insomnia (FFI) and sporadic fatal insomnia in humans, scrapie in sheep, chronic wasting disease in elk and deer (CWD), and bovine spongiform encephalopathy in cattle (BSE) [13-15]. These fatal diseases are pathologically characterized by neuronal vacuolation and loss, synaptic dysfunction, and reactive gliosis of the CNS [13, 16, 17]. In addition, peripheral nerves, spleen, muscle tissue and lymphoid tissue such as tonsils, also harbor PrP^{Sc} [18]. Although the deposition of amyloid plaques in the brain is the hallmark of amyloid diseases [19], in prion diseases they are restricted to certain subtypes, including kuru, MV2 subtype of sporadic CJD (sCJD) [20, 21] and variant CJD (vCJD). The amyloid plaques of vCJD have a unique florid appearance, which distinguish it from the other human prion diseases [22]. Despite their heterogeneity, disease-associated PrP^{Sc} form large and insoluble

aggregates and are thus partially resistant to digestion by the protease proteinase K (PK), whereas PrP^{C} is PK-sensitive [3, 23]. However, a novel human prion disease characterized by the presence of PK-sensitive PrP^{Sc} has been described, which shows a distinct phenotype from the known prion diseases [24].

In humans, prion infection is associated with a long incubation time, which can exceed 50 years in some cases [25]. One unique feature of prion diseases is the existence of three distinct manifestations. Sporadic CJD with no known cause accounts for approximately 90% of human prion diseases, whereas 10% are inherited (autosomal dominant) disorders associated with more than 30 mutations in the regulatory and coding regions of the prion gene, *PRNP* (familial CJD, GSS, FFI) [15, 26]. In addition, a very small number of cases are acquired forms of this disease. These include kuru, iatrogenic CJD and vCJD, which are caused by exogenous infection [26, 27]. The vCJD has gained special interest due to an outbreak in the mid 1990's in the United Kingdom, which is thought to have resulted from the consumption of BSE-contaminated beef. Although the number of confirmed human vCJD cases is relatively modest (183 cases worldwide to date) [28, 29], it still raises significant public-health concerns due to the lack of early diagnosis and effective treatment, and the deficit in our knowledge about its transmission routes [29]. Horizontal transmission, mainly through the oral route [30], plays a major role in the spread of prion disease. Prion infectivity, however, has also been detected in urine, blood, saliva, milk and other body fluids in infected animals and humans, which suggests the need for caution [31, 32]. Although vertical transmission has been

demonstrated in a transgenic mouse model [33], to date there is no evidence for vertical transmission in humans [34]. However, the latter may require a longer incubation time before a firm conclusion can be reached.

Interestingly, the susceptibility to sporadic or acquired CJD in humans is profoundly influenced by the *PRNP* gene polymorphism. Heterozygosity at residue 129 (methionine/valine) and 219 (glutamate/lysine) is highly protective against sporadic and acquired prion diseases in Europeans [35, 36] and the population in the Asia-Pacific region [37] respectively. On the other hand, homozygosity at residue 129 increases the risk of sCJD development and the acquisition of iatrogenic CJD [35, 36]. Furthermore all the vCJD cases diagnosed to date are homozygous for M129 [38]. In a mechanism that is poorly understood, the M/V129 polymorphisms can influence the phenotypes of sporadic and acquired prion disease [39]. In addition, phenotypes of familial prion diseases are also influenced by the M/V129 polymorphism. For example, the D178N mutation causes FFI in combination with V129, but results in CJD with M129 [40]. Accumulating evidence suggests that the polymorphism may change intermolecular β-sheet formation that results in different prion protein variants [41].

A. Protein-only hypothesis

According to the generally accepted protein-only hypothesis, conversion of the normal cellular prion protein, PrP^{C}, proceeds through the direct interaction of this protein with PrP^{Sc} [3, 42]. PrP^{Sc} acts as a conformational template and uses PrP^{C} as a substrate, causing PrP^{C} to misfold and become part of the continuously growing

aggregate, thus propagating the misfolded state [3].

Though definitive evidence that the infectious agent of prion diseases is strictly proteinaceous is still missing, a large body of evidence has provided compelling support for this model in the past few decades. Some of the strongest supporting evidence comes from PrP^{C} knockout mice, which do not contract prion disease even after inoculation with brain homogenate from scrapie infected mice [43]. Although the existence of other infectious agents cannot be ruled out by this study, it shows that PrP^{C} is necessary for PrP^{Sc} propagation and infectivity. Another important line of evidence is the successful conversion of purified brain PrP^{C} into a protease-resistant form similar to PrP^{Sc} in a cell free system. However, the yield of the PrP^{Sc}-like conformers is very low and no obvious infectivity has been detected [44]. One technological breakthrough is the protein misfolding cyclic amplification (PMCA) assay, in which a mixture of PrP^{Sc} seed and healthy brain homogenate is subject to a cyclical process involving incubation and sonication [45]. Unlike experiments using purified PrP^{C}, both PrP^{Sc}-like conformers and infectivity can be recapitulated in the PMCA assay, which provides direct evidence that PrP^{Sc} infectivity can be achieved in a cell-free system [46]. In a more recent attempt, de novo PrP^{Sc} was generated from brain homogenate using a modified PMCA protocol [47]. These reports lend direct support to the prion hypothesis. However, since PMCA uses brain homogenate as substrate, there is no way to exclude the contribution of other constituents present in the brain homogenate to the propagation and subsequent infectivity. This point is confirmed by the failure to reproduce prion

infectivity in PMCA using recombinant PrP^{C} (rPrP) as substrate [48]. Supplementing the system with poly(A) RNA rescues the infectivity, which highlights the crucial role played by cofactors in PrP^{Sc} infectivity [48].

Another line of studies in favor of the protein-only hypothesis comes from the finding that fibrils made from truncated recombinant PrP (residues 89-231) are able to induce the transmissible form of prion disease in transgenic mice that overexpress PrP (Tg9949). Fibrils isolated from these mice can transmit disease to both Tg9949 and wild type animals in a second passage [49]. Again, this experiment is not conclusive in identifying PrP^{Sc} as the only infectious agent because it requires mice expressing extremely high levels of PrP and much longer incubation than typical PrP^{Sc} strains [25]. Alternatively, the low infectivity might be due to the extremely high stability of the recombinant prion fibrils, which are quite resistant to denaturation; the concentration of guanidine hydrochloride (GdnHCl) required to reach 50% denaturation ($GdnHCl_{1/2}$) is about ~4.5 M [50]. In an attempt to reconcile the discrepancy between the behavior of rPrP fibrils and authentic PrP^{Sc}, Baskakov proposes that the rPrP fibrils have to undergo maturation before they are fully infectious [51]. This may involve interaction with unknown cellular cofactors and/or conformational adaptation, which implies that the infectivity is generated *in vivo*. This hypothesis is partially supported by the observation that infectivity of full-length recombinant prion fibrils can be reconstituted after annealing in the presence of normal brain homogenate [52]. Although the nature of these cofactors remains unclear, they could either be a constituent of PrP^{Sc} that stabilizes its

structure or a component that facilitates the conversion from PrP^{C} to PrP^{Sc} [51]. A recently developed PMCA protocol that includes well-defined components to recapitulate the PrP^{Sc} infectivity *in vitro* suggests a promising way to identify these cofactors [53].

Despite these and other important advances, there is still evidence against the protein-only hypothesis. One of the strongest criticisms comes from the existence of multiple strains of TSEs (see below) that are characterized by diverse phenotypes in prion diseases [13]. This raises the question of how the prion protein can encode information required for strain-specific properties, which is always specified by a nucleic acid genome in conventional infectious diseases [54, 55]. However, no nucleic acid consistently associated with PrP^{Sc} has been identified. Instead, a growing number of observations now strongly indicates that the PrP^{Sc} strains can be rationalized in the frame of the protein-only hypothesis, with strain diversity representing the conformational diversity of the PrP^{Sc} aggregates [56-59].

B. Prion-like mechanisms in other amyloid diseases

To date, about 40 amyloid diseases have been identified; each is associated with a specific misfolded protein [9]. A growing body of evidence implicates that a prion-like template-directed misfolding and auto-seeding mechanism might be employed by the culprit proteins in these diseases [6, 60]. Examples include Aβ in Alzheimer's disease, α-synuclein in Parkinson's diseases, huntingtin in Huntington's disease and tau in tauopathies [6, 10, 61-64]. Understanding the mechanism of prion formation and replication and its role in prion diseases could therefore potentially

extend our understanding of other amyloid diseases, in addition to the direct benefit to understanding prion diseases. Interestingly, interactions between PrP^{Sc} and Aβ have been reported recently, which leads to the acceleration and exacerbation of both pathologies [65]. A cross-talk mechanism between different amyloidogenic proteins, or cross-seeding, has been suggested. The authors also propose that patients having one amyloid disease may have a higher risk of developing a second one [65].

Although prion disease is the first contagious amyloid disease that can transmit between individuals, recent data indicate that AA amyloidosis, a disease caused by the accumulation of serum amyloid A protein in a variety of organs, may also be contagious [66, 67]. In a mouse model, this disorder can easily be transmitted between animals by both intravenous and oral routes [68]. Transmission in the wild within the same species (cheetah) and also across species (from duck or goose to mice) has also been suggested [69, 70].

II. The cellular prion protein (PrP^{C}): structure, biology and function

PrP^{C} is a highly conserved cell-surface glycoprotein attached to lipid rafts via its glycosylphosphatidylinositol (GPI) anchor [71]. It is ubiquitously expressed in all mammals and avian species with high expression in central nervous system, especially on the presynaptic membrane [72, 73]. The structure and biosynthesis of PrP^{C} have been elucidated; however, its physiological function is still puzzling despite worldwide research.

A. Structural features of PrP^C

Most mammalian prion proteins have ~210 amino acid residues after the cleavage of the N-terminal signal peptide and processing of the C-terminal GPI anchor sequence. Because it is difficult to obtain enough protein in a highly purified state [48], structural studies of PrP^C are mostly done on recombinant proteins. To date, the structures of recombinant PrP^C from more than 20 different species [74] have been solved by NMR [75] or X-ray crystallography [76]. These proteins lack both glycosylation and the GPI anchor, but reveal a consensus structure composed of a large disordered N-terminal domain (~ 100 residues), a highly conserved globular domain (residues 125-228) and a short flexible C-terminal tail (residues 229–230/232) [75, 77] (**Figure 1-1**, **A** and **B**).

Depending on the species, the N-terminal domain contains at least four glycine-rich octarepeats (OR), which are highly conserved among species [77]. The ORs, which encompass residues 60-91 in hamster that contain four identical copies of PHGGGWGQ, have a high affinity for divalent cations, especially for Cu(II) ions (see chapter III). Another conserved region in the N-terminal domain is the hydrophobic domain (HD) downstream to the ORs, which contains a high percentage of alanine residues [29]. This domain has received special interest because the corresponding peptide exhibits neurotoxicity [78-80] and has a high propensity to form β-sheets [81] and amyloid fibrils [82, 83] *in vitro*. Deletion or mutation of the HD domain produces lethal cation flux in host cells [84-86]. This aberrant current may be caused by the formation of new ion channels or by the

disturbance of the functions of existing ion channels [84, 85].

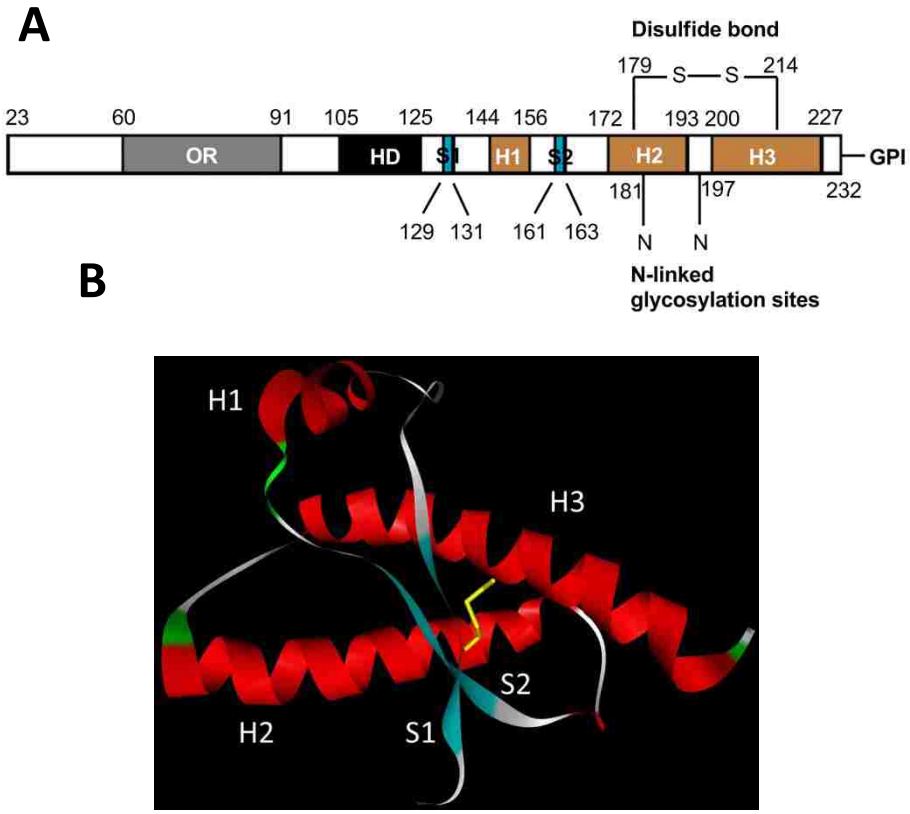

Figure 1-1. Structural features of the Syrian hamster PrP^C.

(A) Schematic depiction of the structural elements of processed hamster PrP^C (residues 23-232). The N-terminal signal peptide (residues 1-22) and the C-terminal GPI anchor signal sequence (residues 233 – 253 have been removed by cellular processing enzymes. The numbering of amino acid residues is from PDB 1B10 [87]. OR (grey), octarepeat; HD (black), hydrophobic domain; S1 and S2 (blue), β-strands; H1, H2 and H3 (brown), α-helices. Adapted from reference [88]. (B) Tertiary structure of PrP^C (residues 125-228) as deduced from solution NMR spectroscopy (PDB 1B10 #3) [87]. The figure was generated using ViewerLab. The N-terminal domain (residues 23 – 124) is disordered.

Although intrinsically disordered, the conformation of the OR regions is heavily influenced by the environment. As revealed by NMR spectroscopy, the unfolded state is in equilibrium with a β-turn conformation under physiologically relevant conditions. This folded state is more favored at neutral pH [89]. In a membrane environment, the ORs may attach to the membrane through tryptophan

anchors and form well-defined loops that are linked by the flexible glycine triplets [90]. In addition, the ORs gain ordered structure in the presence of certain ligands. Copper binding results in a β-turn conformation ordered around the Cu(II) ions, and might be involved in prion pathogenesis [91]. Binding of ORs to sulfonated glycans also triggers the formation of a repeating loop-turn motif, similar to that found in the copper-bound state [92].

The structured globular domain consists of 3 α-helices (H1, H2 and H3) and 2 short anti-parallel β-strands (S1 and S2) preceding H1 and H2 respectively [87]. This region contains a conserved hydrophobic core, which endows the global domain with stability. The hydrophobic core is mainly found between H2 and H3 and between H1 and the loop located around H3 [93, 94]. Many germline mutations associated with inherited human prion diseases cluster in the globular domain. Even though none of these cause dramatic changes in global structure [95, 96], an increased population of partially structured intermediates has been reported in a vast majority of cases [97]. Some mutations may modify the contact surface between H2 and H3, resulting in the disturbance of normal PrP folding pathway [96, 98].

The conformation of H1 is significantly influenced by environmental pH. The last three residues of H1 adopt a 3_{10} helix at neutral pH and a more flexible structure at pH 4.5 [99]. During PrP^{C} to PrP^{Sc} conversion, dissociation of the S1-H1-S2 region from the H2-H3 region promotes the misfolding of PrP^{C} [100]. The second and third α-helices are bridged by a disulfide bond formed between Cys179 and Cys214, which remains intact in PrP^{Sc} [101]. A threonine stretch in H2 destabilizes this helix,

but this is partially compensated by contacts between H2 and the unstructured N-terminal domain [102]. The loop between S2 and H2 (residues 166-175 in hamster) is highly flexible in most species, whereas it is well-ordered in cervids due to the presence of Asn and Thr at position 170 and 174 [103, 104]. In cervids the rigidity of this loop is also modulated by long-range interactions between residues 166 and 225 [105]. Introduction of these two substitutions into mouse PrP renders mice with high susceptibility (100%) to spontaneous prion disease [104, 106]. It is still unclear whether this is caused by the rigid structure or is simply a result of manipulating the mouse genome [104].

The global domain also contains two N-linked glycosylation sites [77]. In many studies recombinant PrP, which lacks the glycosylation and GPI-anchor, has been utilized to characterize the structure of PrP^C. Glycosylation only enhances the thermodynamic stability of the protein by ~1 kcal/mol, which may not be significant [74]. Furthermore, molecular dynamics simulation on di-glycosylated and GPI-anchored PrP implies that post-translational modifications do not significantly alter the structure or dynamics of PrP^C as compared with rPrP [107], suggesting that rPrP is an appropriate substitute for prion protein structural research.

B. Cell biology of PrP^C

Translocation of the nascent PrP into the endoplasmic reticulum (ER) is initiated when the emerging N-terminal signal sequence is recognized by the signal recognition particle (SRP). This results in the arrest of translation and targeting of the ribosome-PrP complex to the Sec61 translocon. Binding of SRP to its receptor on

the ER membrane resumes the translation and transfers the polypeptide into the ER lumen cotranslationally [108-110].

PrP^C glycosylation is achieved in the ER by transferring the core oligosaccharide unit to the nascent chain while it is still associated with the translocon. PrP^C contains two N-linked glycosylation sites [109]. Under physiological conditions, PrP^C can be di-, mono-, and un-glycosylated [111]. Shortly after PrP^C is fully translocated into the ER lumen, the C-terminal signal peptide is cleaved and a GPI anchor is attached to the terminal serine residue [108, 109]. The N-terminal signal peptide is also cleaved in the ER lumen [108]. The properly folded PrP^C is then transported into the Golgi apparatus, where the N-linked glycosylation and GPI-anchor are trimmed and structural diversity in the carbohydrates is introduced in a cell type-specific manner [108, 109] (**Figure 1-2**). The glycosylation pattern is also influenced by the differentiation state of neuronal cells [112].

Recent studies show that PrP^C can be targeted to lipid rafts by the GPI-anchored heparan sulfate proteoglycan glypican-1, which binds to its N-terminal region [113]. Some of the PrP^C molecules on the surface will be internalized and constitutively recycled between the plasma membrane and the endocytic compartments, involving a transit time of ~60 min. Two internalization pathways, the clathrin-dependent pathway [114] and the caveolae-dependent pathway [115], have been described for PrP^C. Both of them participate in the Cu^{2+}-stimulated internalization of PrP^C [115].

The PrP signal sequence is less efficiently translocated than the signal sequences of other proteins [108], which results in the formation of a minor

proportion of aberrant PrP molecules when they interact with the Sec61 translocon. These include cytosolic PrP (cyPrP) and two topological conformers; ^{Ntm}PrP in which the N-terminus resides in the ER, and ^{Ctm}PrP in which the C-terminus resides in the ER [108, 116]. Although increased levels of cyPrP have been shown to be detrimental in cultured cells [117], other studies show that cyPrP has a protective effect [118]. ^{Ctm}PrP has been shown to confer neurotoxicity at elevated level as well [108, 119]. Under physiological conditions, cyPrP and ^{Ctm}PrP are subject to lysosomal and proteasomal degradation, which keeps their concentrations at low levels (~ 1% of total) [108]. However, in TSE, the accumulation of PrP^{Sc} in cells may cause lysosomal dysfunction and proteasome inhibition, leading to higher levels of cyPrP and ^{Ctm}PrP. This may contribute to the neurodegeneration noted in TSEs [116, 118]. Both cyPrP and ^{Ctm}PrP are not transmissible and do not convert to PrP^{Sc}.

Other aberrant forms include the GPI-free form, which may take part in signal transduction. At least four mechanisms have been associated with the formation of soluble PrP: these include the removal of its GPI-anchor by escape of glycolipidation [120]; cleavage of the GPI anchor by phospholipase C [121]; secretion by exosomes [122]; and alpha cleavage mediated by ADAMs (A Disintegrin And Metalloproteases) [123].

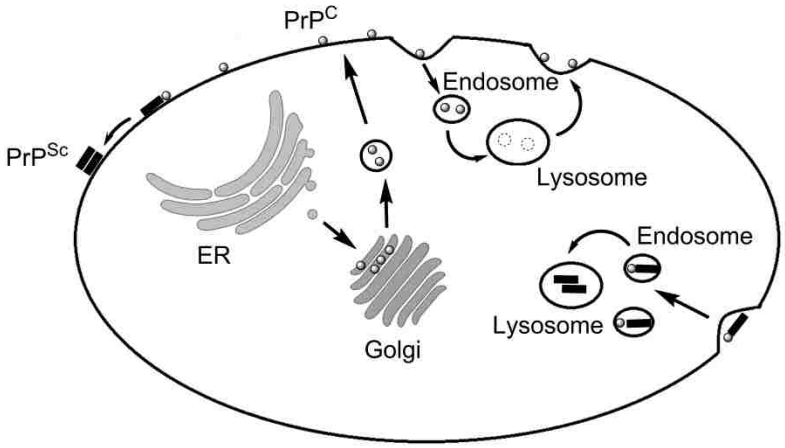

Figure 1-2. Overview of PrP^C biosynthesis and its conversion to PrP^{Sc}.

After being synthesized in the ER and trimmed in the Golgi apparatus, PrP^C is targeted to the cell surface. PrP^C constitutively recycles between the plasma membrane and the endocytic compartments, eventually being degraded in lysosomes. Conversion of PrP^C to PrP^{Sc} occurs on the cell surface after PrP^C reaches the plasma membrane and in the endocytic pathway when PrP^C recycles back from the membrane. The presence of preformed PrP^{Sc} substantially enhances the conversion efficiency although spontaneous conversion is also possible. Once it is formed, PrP^{Sc} can accumulate on the cell surface or in the endosome-lysosome system. Adapted from references [67, 108].

C. Putative physiological functions of PrP^C

The widespread expression of PrP^C in vertebrates in almost all tissues and its remarkably conserved sequence and structure among species suggest that PrP^C may participate in fundamental biological processes [124]. Therefore, it was surprising that PrP knockout mice did not show any overt abnormality as compared with wild-type animals [125]. The results suggest that either the functions of PrP^C are non-essential or that redundant proteins exist. Nowadays, PrP^C or PrP^C-mediated events are thought to be required for or associated with a variety of physiological processes, although its exact function(s) is still poorly understood.

A number of PrP^C interaction partners have been identified. Unfortunately, the

physiological relevance of most of these interactions is still controversial [119, 126-129]. Furthermore, some physiological functions proposed for PrP^C are based on disturbances in cellular activities while PrP^C expression is manipulated, rather than the direct observation of protein activity. The following paragraphs therefore describe only a few partners and functions for which strong evidence exists.

As a GPI-anchored protein localized in lipid rafts, one popular hypothesis is that PrP^C may serve as a scaffold protein to interact with a wide variety of molecules at the plasma membrane and in different subcellular compartments [127]. This would facilitate the assembly of various sets of functional protein complexes, integrating distinct intracellular pathways and providing signals for not only the survival but also the differentiation and functional integrity of the cells [130]. Some of the proposed functions are summarized below.

Knowledge of the role of PrP^C in signal transduction has been advanced by recent studies. Research on non-receptor tyrosine kinase Fyn shows that antibody-mediated cross-linking of PrP^C is able to induce the activation of Fyn in a caveolin-1-dependent manner, which results in the downstream activation of extracellular signal-regulated protein kinases of the ERK1/2 pathway [131]. Interaction between endocytosed PrP^C and growth factor receptor binding protein (Grb2) has been reported to provide signals for neuronal survival by activating ERK 1/2 and mitogen activated protein (MAP) kinases [132]. Other signaling pathways or signaling proteins, such as PI3-kinase/Akt [133], cyclic AMP/protein kinase A (PKA) [134] and PKCδ [135], have also been proposed to involve PrP^C-mediated signal

transduction.

The expression of PrP^C throughout the entire CNS and its purported involvement in many signaling pathways strongly support a functional role of PrP^C in the nervous system. Several processes in the nervous system have been shown to be influenced by PrP^C. Evidence from PrP^C-deficient mice implies that the absence of PrP^C may result in changes in neurotransmission and synaptic plasticity [136], altered circadian rhythms and sleep [137, 138], damaged hippocampal spatial memory [139], impaired olfactory behavior and physiology [140], and depression-like behavior [141]. It is now believed that PrP^C may regulate neurotrophic activities by modulating neuronal survival and differentiation, neurite outgrowth, and synaptic functions through selective interaction with a wide array of ligands and transmembrane signal pathways [128]. This aspect of PrP^C function is tightly related to its cytoprotective activity (see below). Support for this hypothesis comes from studies on stress inducible protein 1(STI1) [134, 142]. Binding of STI1 to PrP^C triggers both protection against anisomycin-induced apoptosis by the PKA pathway and neuritogenesis by the ERK 1/2 pathway [134, 143]. The list of ligands involved in PrP^C-mediated neurotrophic activities has been reviewed in depth elsewhere [127, 128]. Loss of the neurotrophic functions of PrP^C during conversion to PrP^{Sc} has been proposed as a mechanism of neuropathological changes observed in prion diseases [128]. Researchers studying PrP mutants postulate that PrP^C interacts with a hypothetical signal transduction protein (Tr) in two sites (the C-terminal and the HD domains) and generates non-essential signals for neuronal

survival. When only the C-terminal binding site is occupied, Tr undergoes a conformational change and elicits neurotoxic signals [144].

Several lines of evidence have emerged suggesting that PrP^C may exert cytoprotective activity, particularly against stress-induced apoptosis. One of the clearest examples comes from the experiment in which PrP potently protects human fetal neurons from Bax-induced apoptosis [145]. The OR region is essential since deletion or mutation in this region completely or partially abolishes the anti-apoptotic effect [146]. While glycosylation confers PrP^C with apoptosis-resistance properties [111, 147], the GPI-anchor is not required for this activity [145]. This conclusion was confirmed by subsequent research conducted by the same lab, which showed that the cytosolic PrP (cyPrP) is the predominant anti-Bax PrP form [118]. The anti-apoptotic effect of PrP^C is influenced by the basal level of PrP^C expression. While expression of PrP^C in PrP^C-deficient cells exhibits anti-apoptotic effects, PrP^C overexpression in different cell lines displays pro-apoptotic properties [148]. Current evidence suggests that instead of directly inhibiting Bax apoptotic activity, PrP^C probably prevents the initial Bax conformational change that converts cytosolic Bax into a pro-apoptotic protein. Along with Bcl-2, both proteins maintain Bax in an inactive state and prevent apoptosis [149].

Some of the PrP^C ligands identified to date play a role in cell adhesion, including laminin [150], the laminin receptor (LRP/LR) [151], STI1 [134, 142] and neural cell adhesion molecules (NCAM) [152]. Engagement of PrP^C with these

ligands contributes to cell adhesion on a matrix enriched with laminin and triggers different downstream events in a cell type-specific manner. The role of PrP^C in embryonic cell adhesion and cell-cell communication has also been demonstrated in zebrafish in which the PrP knock-down animals are characterized by impairment of embryonic cell adhesion and arrested gastrulation [153]. Both Ca^{2+}-independent and Ca^{2+}-dependent cell adhesion are modulated by PrP [153]. The participation of PrP^C in early embryonic stem cells differentiation has also been suggested [154, 155]. In mammals, the functions of PrP^C in embryonic development are able to be compensated by other molecules since no birth defect has been reported in PrP^C knock-out animals [114, 156].

Other functions proposed for PrP^C are its involvement in copper metabolism (see chapter III), and development and maintenance of the functions of the immune system [157]. One recent research reports an interesting link between Alzheimer's disease (AD) and prion disease, revealing that PrP^C inhibits the cleavage of amyloid precursor protein, which makes PrP^C a potential target for AD treatment [158]. More recently, an involvement of PrP^C in mediating the cytotoxicity of other beta-sheet-rich conformers of completely different origins has been observed [159], which does not require prion propagation. This implies a toxic signaling role of PrP^C beyond its assumed cytoprotective functions.

III. The scrapie prion protein (PrP^{Sc}): structure, conversion and strains

Although chemically identical to PrP^{C}, PrP^{Sc} is insoluble and aggregates in nature, showing partial resistance to PK digestion [160, 161]. The conversion of PrP^{C} into PrP^{Sc} involves both the global rearrangement of the peptide backbone and protein polymerization. Recent studies indicate that PrP^{Sc} may be generated either at the plasma membrane or, more likely, in compartments along the endocytic pathway, which have acidic pH [162] (**Figure 1-2**). The latter observation led to the proposal that conversion is favored under low pH conditions [163, 164] (See Chapter II). However, the location for conversion might be cell type-specific since the distribution of PrP^{C} and PrP^{Sc} depends on cell types [162]. Several critical aspects of PrP^{Sc} remain elusive, including its high-resolution structure(s), its role(s) in prion neurotoxicity, and the molecular basis of prion strains and the transmission barrier.

A. Proposed structures of PrP^{Sc}

Attempts to resolve the structure of PrP^{Sc} using conventional techniques, such as X-ray crystallography and NMR, have been hampered due to its insoluble and fibrillar nature. Therefore, lower resolution techniques have been widely used for structure determination. For example, electron microscopy demonstrates that PrP^{Sc} displays a wide variety of morphologies and aggregation characteristics, which are believed to be strain-specific [165]. X-ray fiber diffraction reveals that PrP amyloid fibrils share a common cross-β strand core with other types of amyloid fibrils, in

which the individual strands of each β-sheet run perpendicular to the fibril axis (4.7 Å spacing) and the β-sheets (~ 10 Å spacing) are parallel to the fibril axis [166]. Fourier transform infrared (FT-IR) analysis has revealed a marked increase in β-sheet content (~ 20% in the full-length protein) at the cost of α-helix (~ 14% in the full-length protein) and random coil [167, 168]. Interpretation of the secondary structure of PrP^{Sc} from these low resolution techniques remains controversial, as different techniques yield conflicting results [169]. The truncated form of prion protein (PrP90-232 in hamster) has been widely used in structural studies because it encompasses the entire sequence of protease-resistant core of PrP^{Sc} [4] and it is sufficient to propagate prion disease. In addition, most known point mutations associated with human prion diseases are located in this region [96]. However, our recent findings (Chapters II and III) suggest that truncated PrP90-232 may not be an ideal mimic of PrP^{Sc}.

A number of *in silico* mammalian PrP^{Sc} models have been proposed over the past 15 years [170-175]. Among them, the β-helical model (**Figure 1-3A**) was constructed by threading residues 89–175 of PrP through a known β-helical fold [171]. This model proposes that the core region of PrP^{Sc} is composed of left-handed β-helices which associate into trimers. The trimers are stackable along the fibril axis. The two C-terminal α-helices are largely unaffected in this structure. The β-spiral model (**Figure 1-3B**) is derived from molecular dynamics simulations using the D147N mutant of hamster PrP (109–219) under moderately acidic conditions [170]. The heart of the β-spiral model contains a three-strand sheet (E1-E3) and an isolated

strand E4 from another monomer. Similar to the β-helical model, most of the α-helices found in PrP^C retain their native conformations. Docking of an incoming PrP substrate to the growing end through the E1-E4 interface propagates the amyloid fibrils. A detailed comparison between these two models has been published, and comparison with experimental data favors the β-spiral model [175]. One deficiency of the β-helical model is that it is not consistent with the cross-β diffraction pattern, since no β-sheet is aligned parallel to the fibril axis [169].

In addition to these theoretical models, another model has recently emerged (**Figure 1-3C**), based upon experimental data obtained from hydrogen/deuterium exchange mass spectrometry (HXMS) [176] and site-directed spin labeling electron paramagnetic resonance (SDSL-EPR) spectroscopy [177]. These studies examined amyloid fibrils formed by recombinant human PrP corresponding to residues 90-231. The β-sheet core of this structural model encompasses residues ~160-220, which form single β-strand layers that stack on top of each other with parallel, in-register alignment, with dimensions of 10 × 3.5 nm [176-178]. In sharp contrast to above-mentioned *in silico* models shown in Figure 1-2A and 1-2B, in this model all three original α-helices in PrP^C undergo major refolding upon conversion, and no native α-helices are present in PrP^{Sc} [176-178]. The starting point of the β-sheet core has also been confirmed by atomic force microscopy, which maps the amyloid core to residue ~164-169 [179]. However, this model is not in agreement with maps of antibody-binding that indicate many epitopes are retained upon conversion [96].

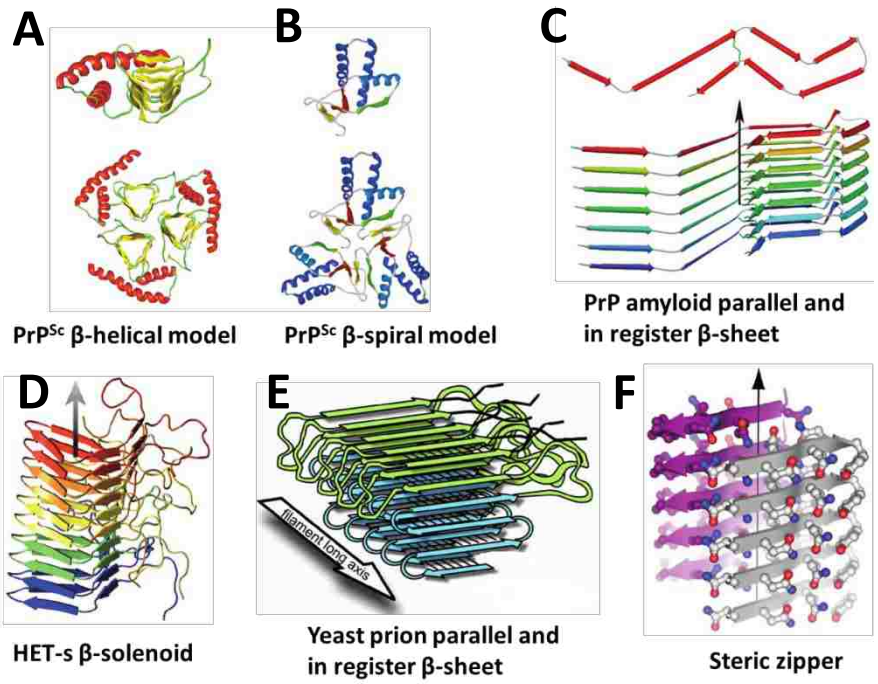

Figure 1-3. Proposed structures of PrP^{Sc} and other amyloid fibrils.

The figures are adapted from reference [66], reprinted with permission from American Chemical Society, Copyright 2009. (A) PrP^{Sc} left-handed β-helical model based on a threading analysis (reproduced from reference [171], reprinted with permission from the National Academy of Sciences, Copyright 2004). (B) PrP^{Sc} β-spiral model, derived from molecular dynamic simulations (reproduced from reference [170], reprinted with permission from the National Academy of Sciences, Copyright 2004). (C) Parallel and in-register β-sheet model determined on recombinant human PrP(90-231) amyloid fibrils, deduced from spin labeling EPR and H/D exchange (reproduced from reference [66], reprinted with permission from American Chemical Society, Copyright 2009). (D) Left-handed β-solenoid structure of amyloid fibrils formed by yeast prion HET-s, determined by solid-state NMR (reproduced from reference [180], reprinted with permission from AAAS, Copyright 2008). (E) Parallel and in-register β-sheet model of yeast prion Sup35NM as suggested by solid-state NMR (adapted from reference [181], reprinted with permission from the National Academy of Sciences, Copyright 2006). Amyloids of yeast prion, Ure2p, and Rnq1, may adopt similar structures [182-184]. (F) Steric zipper motif determined using X-ray crystallography of microcrystals formed by a heptapeptide of yeast Sup35 (reproduced from reference [185], reprinted with permission from Macmillan Publishers Ltd., Copyright 2005).

The highly protected region in the parallel, in-register structure varies slightly depending on the source of the species. Recombinant prion fibrils generated by

PMCA and seeded with PrP^{Sc} contain a much longer protected region, spanning from residues ~117-133 to the C-terminus [186]. In brain-derived GPI-anchor-free PrP^{Sc}, the protected core extends up through residues ~80-90 [187]. These differences in the β-sheet core region may explain the low infectivity of rPrP fibrils [187]. Research on full-length rPrP fibrils from mice, cow, and elk show that in addition to the C-terminal region (residues ~182-212), the region encompassing residues ~24-98 is also highly protected. The residues in between these regions are less solvent exposed than those in PrP^{C} but more exposed than the protected region [188]. The involvement of the N-terminal region in forming a PK-resistant core has also been recently reported by Baskakov and coworkers [189]. The identification of multiple structures for the β-sheet core suggests that it might be different in distinct prion strains.

Despite the lack of high-resolution structural data for mammalian prions, the past decade has seen advances in resolving the structures of yeast prions and of amyloid-like fibrils formed by short peptides. With the exception of the amyloid fibrils formed by the HET-s (218-289) peptide, which has a left-handed β-solenoid structure [180] (**Figure 1-3D**), most amyloid fibrils formed by yeast prions characterized adopt a common parallel, in-register β-sheet structure [182, 190] (**Figure 1-3E**). Using microcrystals formed by a variety of short peptides, including the heptapeptide of the yeast Sup35 and fragments of disease-related amyloidogenic proteins, X-ray crystallography has revealed that the basic unit of a cross-β structure is composed of a pair of beta strands with the facing side chains interdigitated in an

anhydrous (dry) interface called the “steric zipper” (**Figure 1-3F**) [185, 191, 192].

B. PrP^{Sc} neurotoxicity

The precise nature of the neurotoxic species and the mechanism of neurotoxicity in prion disorders remain elusive. A simple relationship between the loss of PrP^{C} function upon conversion and neurotoxicity can be excluded, as PrP^{C}-deficient mice are essentially normal [125] and neuron-targeted deletion of PrP^{C} in adult mice does not result in neurodegeneration [193].

Although the presence of PrP^{Sc} is generally considered essential for definitive diagnosis of prion disease, the direct association between PrP^{Sc} and prion-induced neurotoxicity has been increasingly challenged due to the discrepancies between amyloid plaque deposition in the brain and clinical symptoms or neuronal loss [20, 194-197]. To the contrary, a number of results suggest that PrP^{Sc} accumulation and neurotoxicity can be uncoupled. This is supported by the study on subclinical prion infection in which the first passage mice infected with mouse-adapted hamster scrapie are free of any clinical disease, even though the PrP^{Sc} load and scrapie infectivity reach high levels in the mice (asymptomatic carriers) [198]. In addition, a recent study with transgenic mice expressing $GPI^{-/-}$ PrP^{C} (anchorless) has shown that after inoculation with mouse scrapie, only minimal neurotoxicity is observed in these mice, despite extensive build-up of $GPI^{-/-}$ PrP^{Sc} adjacent to blood vessels [199]. Moreover, after knockout of PrP^{C} expression in neurons, early cognitive deficits and neurophysiologic dysfunction established in young adult mice could be reversed, although PrP^{Sc} propagation continues in glia [195, 196].

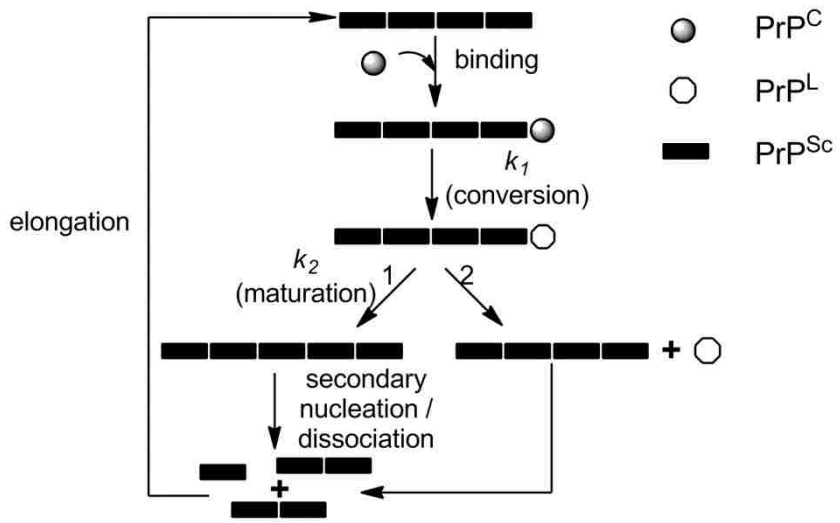

Figure 1-4. Schematic model for PrP^L production.

In this model, PrP^L can be generated either as an intermediate (pathway 1) or an off-pathway product (pathway 2) during PrP^C to PrP^{Sc} conversion. PrP^L matures into PrP^{Sc} if it is generated as an intermediate. Otherwise, it will not be incorporated into the growing PrP^{Sc}. Adapted from ref [200].

Infectivity and neurotoxicity of prion are generally accepted to be two related but distinct events [200, 201]. The neurotoxic species, which has been termed PrP^L (for 'lethal'), may correspond to soluble prefibrillar intermediates or off-pathway products generated during the conversion of PrP^C to PrP^{Sc} [200, 201]. Nonetheless, our knowledge of this species is currently limited due to the lack of a precise physical definition for these soluble intermediates or off-pathway products. According to the toxic templated intermediate model, PrP^C to PrP^{Sc} conversion is composed of four steps, i.e., binding of PrP^C to a PrP^{Sc} surface, conversion to PrP^L, maturation of PrP^L into PrP^{Sc} and finally dissociation (**Figure 1-4** pathway 1). The levels of PrP^L and PrP^{Sc} are controlled by the interplay between two independent rate constants, the rate of conversion (k_1) and the rate of maturation (k_2). The clearance rate of PrP^L also affects the level of PrP^L. An increased k_2/k_1 ratio (**Figure 1-4**) leads

to accumulation of PrP^{Sc}, or infectivity, but with little or no neurotoxicity because most PrP^{L} will be consumed to form PrP^{Sc}. In this regard, mature amyloid fibrils can be considered to act as a "graveyard" for removing the toxic species from circulation [196].

As an alternative, the off-pathway product model proposes that the on-pathway intermediates are benign and that PrP^{L} is generated as an off-pathway product using PrP^{Sc} particles as a catalytic surface (**Figure 1-4** pathway 2). The latter mechanism is favored by a recent experiment that demonstrates that prion propagation in mice can be divided into two distinct phases [201]. The infectious but non-toxic PrP^{Sc} accumulates in the first phase and reaches maximal titer after a short time, regardless of the original PrP^{C} concentration. The second plateau phase is accompanied by the production of toxic PrP^{L}, which will eventually trigger the onset of prion disease when it reaches a critical concentration. The duration of the plateau phase is inversely proportional to the PrP^{C} expression level. The relationship between PrP^{Sc} and PrP^{L} is largely in agreement with recent research on Alzheimer's disease in which intermediates between Aβ peptides and Aβ amyloid are believed to be the neurotoxic species [202]. One caveat of the second PrP^{L} production pathway is that PrP^{L} has to be generated intra-neuronally [194]. A possible explanation for the lack of neurotoxicity in $GPI^{-/-}$ PrP^{C} transgenic mice is that $GPI^{-/-}$ PrP^{C} does not attach to the plasma membrane and is not recycled back into the cells to generate PrP^{L} [199]. This concept is supported by the fact that PrP^{Sc} replication in astrocytes is not sufficient for prion neurotoxicity while neuron-specific propagation is required

[203].

Mechanisms proposed for the neurotoxicity of prion diseases include impairment of lysosomal functions [108] and ER stress [204-207] caused by accumulation of PrP^{Sc}, proteasome inhibition [116, 207, 208], neurotoxic signal transduction [86], calcium homeostasis dysregulation [209], metal imbalance [210], and formation of aberrant ion [86] channels. Since PrP^{C} is required to manifest neurotoxicity, one cannot rule out the potential toxic roles assumed by cellular partners of PrP^{C} in prion diseases. Neurodegeneration in TSEs may not be caused by a single mechanism and several parallel mechanisms may contribute to the disease to varying extents.

C. Prion strains and the species barrier

An important aspect of prion diseases is the existence of multiple strains. Strains differ in the physicochemical properties of PrP^{Sc} and are associated with distinct phenotypes: including stability to denaturation by guanidine, conformational templating activities, morphology (shape, diameter, length and twist/periodicity), proteinase K (PK) digestion profiles, glycosylation patterns, incubation time before the onset of symptoms, and patterns of neuropathological targets (histopathological lesion profiles and specific neuronal target areas) [66, 67, 165, 189, 211-213]. Kinetic modeling further indicates that different strains may display distinct rates of fibril dissociation and aggregation [214]. Strain features are not altered even after repeated passaging in experimental animals [66].

Research on yeast and mammalian prions suggest that PrP^{Sc} strain diversity

might be encoded in their physical structures, resulting in strain-specific conformations [56-58, 189, 215]. Strain diversity also reflects variation in the steric zipper. Two distinct steric zipper polymorphisms have been identified in microcrystals formed by short peptides. In the packing polymorphism, the steric zipper is built from the same peptide, which assembles in an alternative packing arrangement. In the segmental polymorphism, the steric zipper is formed by different segments of the same protein [59]. Additional polymorphisms, including the combinatorial polymorphism and the single-chain registration polymorphism, have been proposed. Neither of them has been observed in microcrystals yet [59]. Yet another factor contributing to strain diversity is the glycosylation patterns of PrP [212]. Different glycosylation patterns may modulate the surface accessibility of PrP^{C} and its conversion efficiency into PrP^{Sc} [107]. The presence of glycans may also constrain protein molecules in PrP^{Sc} to adopt different conformations or alter its packing by introducing specific steric constraints [66].

Prion strains are quasi-species - a group of conformationally related sub-strains or types that only bear subtle differences between each other [216]. Unlike RNA viruses in which the heterogeneity of quasi-species is caused by point mutations, in the case of prion strains, the heterogeneity originates in structure. Interconversion between different sub-strains is relatively easy because they are separated by a low energy barrier. On the other hand, interconversion between different strains is more difficult due to the presence of a relatively higher energy barrier [216]. Like other quasi-species, the prion strains are subject to constant selective pressure arising from

the environment, which may result in the development of new phenotypes during transmission [216-218] or the emergence of a so-called “new strain” within different tissues [219]. Co-infection of the host with two prion strains may also cause the appearance of novel phenotype due to interference between strains, although there is no new strain generated in this case [220]. Whether a specific prion disease phenotype is always associated with a distinct PrP^{Sc} strain/sub-strain is still not clear, as host genetic variability and other factors may significantly modify the phenotype [213]. All the phenotypes identified in human prion disease patients are thought to be caused by a limited number of PrP^{Sc} strains [213].

As mentioned earlier, PrP^{Sc} strains are mainly determined by their structural diversity, despite there being no high resolution PrP^{Sc} structure. If true, the search for a unified PrP^{Sc} structure might be unattainable [74].

Another feature tightly associated with PrP^{Sc} strains is the so-called “species-barrier,” which is invoked to explain the observation that initial passage of prion diseases between different species, when possible, is always inefficient, and is characterized by a much longer and more variable incubation period in the new host as compared with transmission within the same species. Subsequent passage of PrP^{Sc} in a homologous host leads to shortened incubation times, which resembles intra-species transmission [13, 26, 221]. Studies done with transgenic mice have shown that species barriers are determined not only by the PrP sequence differences between the donor and the recipient [222, 223], but also by prion strains. The sequence-dependent effect of the species barrier appears to be governed by a few key

residues [223]. One model proposes that the effects of these two factors on the species-barrier can be ascribed to the conformational selection mechanism. This describes the ability of donor PrP^{Sc} to adopt conformations that are thermodynamically accessible to the host PrP^{Sc} [213]. The PrP sequence affects the transmission barrier by altering the spectrum of possible PrP^{Sc} conformations in a given species. If the conformation of donor PrP^{Sc} is not accessible to host PrP^{Sc}, a transmission barrier will be observed [26, 66, 200, 224]. During cross-species transmission, characteristics of the donor strain might switch due to the selection of an optimal sub-strain for more efficient propagation in the new host, or the conformational conversion of the donor strain to accommodate the available host PrP^{Sc} conformations [66, 200].

IV. Prions beyond disease

In addition to its well established role in prion diseases, prion-like behavior may also have physiological functions. In yeast, recent studies indicate that a prion mechanism might function as an epigenetic regulatory strategy by influencing important cellular pathways. The yeast translation termination factor Sup35p is deactivated in its prion state, [PSI^{+}], which leads to increased levels of nonsense suppression and programmed frameshifting. This can confer selective advantages to the host under diverse conditions [225, 226]. Other yeast prions, as demonstrated by [*URE3*] and [*GAR*], are connected with the regulation of nitrogen metabolism and energy sources [227, 228]. However, other results imply that prion status is

detrimental to yeast based on the finding that it is not widespread in wild strains [229]. The acquired phenotype offered by prions is transmissible to daughter cells by non-Mendelian cytoplasmic inheritance [230].

In mammalian cells, the melanocyte-specific glycoprotein, Pmel17, is able to form self-propagating aggregates and play a role in mammalian skin pigmentation [231]. Furthermore, recent studies show that amyloid may serve as a reservoir for several peptide and protein hormones in pituitary secretory granules [5]. It remains unclear that whether these amyloid-like aggregates are transmissible. However, these findings suggest a new approach in investigating prion biology and the role of protein structure in determining function.

V.Concluding remarks

Despite extensive research, there are still many aspects regarding the physiological functions of PrP^{C} and prion disease pathogenesis that are poorly understood. Key questions exist regarding the role of PrP^{C} in the nervous system, the effect of conversion on the physiological functions of PrP^{C}, the molecular mechanism underlying the PrP^{C} to PrP^{Sc} conversion, and the toxic species that is responsible for neurodegeneration, and these need to be elucidated.

Data from this dissertation research aim to address two different topics related to prion disease pathogenesis: the behavior of rPrP fibrils (as a model for PrP^{Sc}) under conditions that resemble those of lysosomal vesicles, and the characteristics of copper binding to different rPrP conformers. These are discussed in detail in Chapter

II and Chapter III, respectively. The overall conclusions drawn from this research and work to be done in the future are discussed in the last chapter. The results provide deeper insight into the pathway of conversion of PrP^{C} to PrP^{Sc} and the interaction between copper and PrP, offering new avenues for prion research.

CHAPTER II:

DISSOCIATION OF RECOMBINANT PRION PROTEIN FIBRILS INTO SHORT PROTOFILAMENTS: POSSIBLE ROLES FOR THE N-TERMINAL DOMAIN AND VESICLES OF THE LATE ENDOCYTIC PATHWAY

This chapter is a modified version of the manuscript published in *Biochemistry* in May 2012; http://pubs.acs.org/doi/suppl/10.1021/bi300201e

I. Introduction

A. Mechanism of conversion of PrP^{C} to PrP^{Sc}

It is believed that PrP^{Sc} is more thermodynamically stable than PrP^{C} and may represent the global minimum of the energy landscape [232]. However, the folding of PrP into its monomeric PrP^{C} form is extremely fast, with a rate constant at 20 °C under physiological conditions reaching 20,000 s^{-1} [98]. In contrast, folding to the PrP^{Sc} form is slower by several orders of magnitude. As a result, PrP is kinetically trapped in the PrP^{C} state under physiological conditions [232].

Conversion of PrP^{C} to PrP^{Sc} requires crossing a high energy barrier, including the formation of "amyloid-competent" intermediates and the oligomerization of these intermediates [232]. Initial steps of conversion are favored under acidic conditions [163, 164]. Experimental data show that the second half of helix 2 (H2) and segments of helix 3 (H3) bear intrinsic conformational flexibility [102, 233] (**Figure 2-1**). Extensive molecular dynamics studies suggest that these regions undergo a loss of helical structure with the gain of β-sheet characteristics at low pH [234-239]. Dissociation of the S1-H1-S2 region from the H2-H3 region also takes place at acidic pH, which is associated with the protonation of His187 that connects S1-H1-S2 and H2-H3 at neutral pH [100, 240]. H1 is believed to be the least stable helix at low pH whereas H3 is the most stable one [240]. The conformational rearrangement is accompanied by an increased exposure of hydrophobic patches on the surface of the protein as well as a more solvent exposed peptide backbone [99, 241-243]. These

changes in turn facilitate conversion and result in a high propensity for intermolecular aggregation. The effect of acidic conditions on conversion and aggregation is evidenced by *in vitro* formation of recombinant human PrP fibrils at pH 4.5 without any denaturants [178].

The unstructured N-terminal region may also play a role in the conversion process. It has been shown that the N-terminal region in PrP^{Sc} is not accessible to antibodies targeted to the same region in PrP^{C}, and *vice versa* [244, 245]. These data indicate that the N-terminal region undergoes a conformational change during the conversion. Molecular dynamic simulation reveals that the N-terminal region forms an extended structure in the form of β-sheet at low pH, which further extends to helix 1 [246]. However, these data are inconsistent with more recent experimental results, which show that the N-terminus is left unattached in PrP^{Sc} [176, 177, 187]. Interestingly, transgenic mice carrying N-terminal deleted PrP^{C} stay healthy for longer than 400 days whereas deletion of the C-terminal α-helices causes spontaneous disease [247]. There are also mutations in the N-terminal region that are associated with inherited forms of prion diseases. Together, the data suggest that the N-terminal region is heavily involved in the pathogenesis of prion diseases.

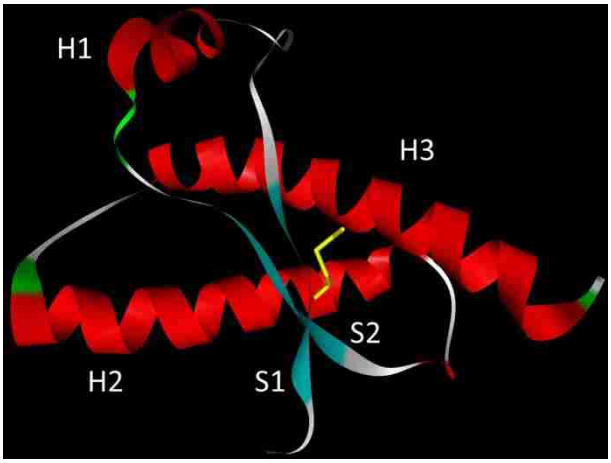

Figure 2-1. Structural features of the Syrian hamster PrP^C.

Tertiary structure of the PrP^C (residues 125-228) as deduced from solution NMR spectroscopy [87]. The figure was generated from PDB 1B10 # 3 using ViewerLab. Three α-helices (H1-3), 2 β-strands (S1-2) and a single disulfide bond can be seen.

The nature of "amyloid-competent" intermediates is still elusive. Kinetic studies on PrP folding using continuous-flow measurements identify a monomeric intermediate that forms on the microsecond time scale (~50 μs) [241, 248]. It populates and becomes stabilized under mildly acidic conditions [241, 248]. A series of locally unfolded intermediates, which are in equilibrium with the α-monomers and unfolded PrP, have been suggested by NMR spectroscopy studies [249]. Oligomeric and multimeric on-pathway, β-sheet-rich intermediates have also been reported [250-252]. All atom computation simulations suggest that the likely pathway is from monomers to an initial nucleus of octamers, with tetramers as the transition state. Once nuclei are formed, there will be no major energy barriers to forming higher order aggregates [253]. Recent studies show that conversion can also be initiated from

a yet uncharacterized soluble β-sheet-rich oligomer [254, 255]. However, a slow, concentration-dependent equilibrium between β-oligomer and α-monomer has been observed in these studies, which makes the identity of the true on-pathway intermediate questionable. The resultant fibrils from this intermediate distinguish themselves from the fibril formed from α-monomer by its worm-like morphology [254, 255]. This pathway does not require a nucleation process.

Incorporation of PrP^{C} into the end of a growing fibril can be described by a dock-and-lock mechanism, in which the initial binding of a PrP^{C} -monomer to the PrP^{Sc} occurs in the first stage (dock), followed by the conformational change of bound monomer to adopt the structure of PrP^{Sc} (lock). The lock stage is the rate-limiting step of the reaction [256-258]. Further conformational changes may be required to obtain the structural features of mature amyloid. *In vitro* studies indicate the presence of a series of high molecular mass, on-pathway multimeric species [232, 251]. Among them are multimer I and II. Both of these are enriched in β-sheet. Multimer I is considered to be the conformer that commits the protein to amyloidogenesis, a process that has been generally believed to be irreversible [251]. It is noteworthy that multimer I lacks the ability to bind the amyloid-specific dye Thioflavin T (ThT). It has to convert to higher order multimers, such as multimer II, to acquire the ThT binding activity [251].

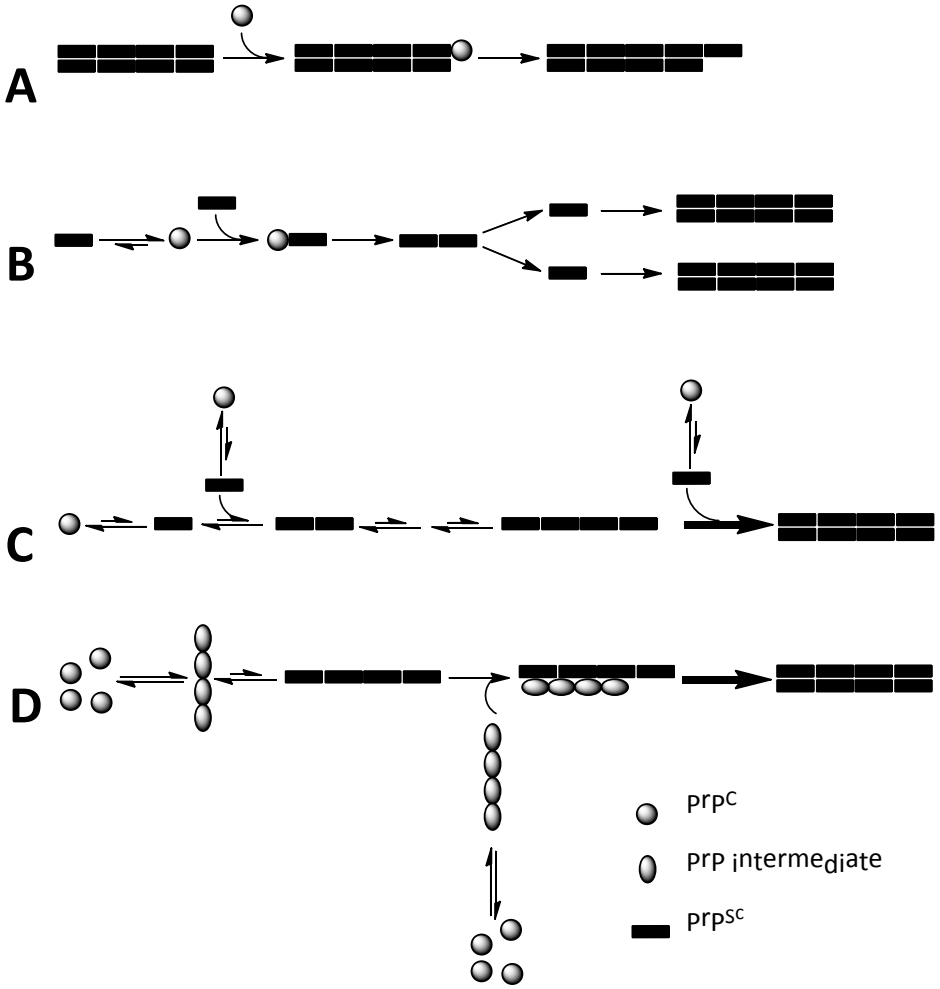

Figure 2-2. Models for mechanisms of PrP^{C} to PrP^{Sc} conversion.

(A) Templated assembly (TA), (B) Monomer-directed conversion (MDC), (C) Nucleated polymerization (NP) and (D) Nucleated conformational conversion (NCC) models. Adapted from reference [259, 260]. See text for details.

Although conversion is still not fully understood, several models have been proposed to address the mechanism of conversion, including the templated assembly (TA), monomer-directed conversion (MDC), the nucleated polymerization (NP) and the nucleated conformational conversion (NCC) models [259, 260]. In the TA model, conversion of PrP^{C} to PrP^{Sc} occurs coincidently with the assembly of PrP^{C} monomer into PrP^{Sc} amyloid. Assembly is the cause of PrP^{C} to PrP^{Sc} conversion, during which the PrP^{Sc} amyloid acts as a template (**Figure 2-2A**). The MDC model considers that

the spontaneous conversion of PrP^{C} to PrP^{Sc} is unfavorable because of the aforementioned kinetic trap. Conversion requires the formation of a PrP^{C}-PrP^{Sc} heterodimer, which lowers the energy barrier between PrP^{C} and PrP^{Sc} and templates the conversion [261, 262]. The product is then assembled into PrP^{Sc} amyloid. In this mechanism, assembly is the result of conversion (**Figure 2-2B**). For the NP model, PrP^{C} and PrP^{Sc} are proposed to be in an equilibrium that strongly favors the formation of PrP^{C}. Once the slowly-formed PrP^{Sc} aggregates exceed the critical nucleus size (nucleation), further addition of PrP^{Sc} monomer, generated from the equilibrium, into the PrP^{Sc} amyloid becomes thermodynamically favorable (**Figure 2-2C**) [263]. The NCC model is a combination of MDC and NP models with additional features. Here the formation of PrP^{C} oligomer and nuclei by conformational arrangement is followed by slow conversion to nuclei of PrP^{Sc}. Once PrP^{Sc} nuclei are present, further conversion of PrP^{C} nuclei into PrP^{Sc} and assembly will be greatly accelerated through the templating mechanism (**Figure 2-2D**) [260, 264].

B. Rationale and aims

In addition to the primary nucleation events discussed above, fibril dissociation is necessary for efficient conversion of α-monomeric PrP to its misfolded state and continued propagation into amyloid [66]. Fibrils must dissociate into smaller nuclei that can seed additional conversions in a process known as secondary nucleation [66, 265, 266]. If not, the conversion process is too inefficient to accumulate much product. Thus, the rate of fibril dissociation contributes significantly to the overall rate of propagation [214, 267].

Studies on mammalian PrP suggest that the conversion of PrP^{C} to PrP^{Sc} takes place both on the plasma membrane and along the endocytic pathway [42, 67, 162, 268, 269]. The majority of PrP^{Sc} has been shown to accumulate in the lysosomes of infected cells [270]. Interestingly, $Atg5^{-/-}$ fibroblasts, which lack the ability to execute autophagy and thus transport PrP^{Sc} aggregates into lysosomes, show significantly increased resistance to prion infection [271]. Together these results indicate that there must be a mechanism within the endocytic pathway to dissociate the mature PrP^{Sc} into seeds and thus continue efficient propagation [200]. One potential environmental contributor to dissociation is the acidic pH of lysosomes [272].

We have observed that the solution circular dichroism (CD) spectrum for amyloid fibrils generated from full-length recombinant hamster PrP (rPrP23-232) can be measured only at acidic pH. As large fibrils merely scatter the CD light, we postulated that dissociation of some fibrils was occurring under acidic conditions. We therefore investigated the behavior of recombinant PrP fibrils under mildly acidic conditions that mimic the endocytic environment. The first aim of this thesis is to evaluate the stability of recombinant fibrils under different conditions. This aim is achieved by using asymmetric flow field fractionation, which is theoretically able to separate particles in the size range of 1 nm to 1 μm under normal operation mode. The second aim of these experiments is to characterize any smaller species that are detected in the first aim. This goal is achieved by various biophysical and biochemical techniques, including circular dichroism spectroscopy, Fourier-transform infrared spectroscopy, transmission electron microscopy, mass spectrometry, and proteinase K

digestion. Additionally, the radius of gyration (R_g) of isolated species, which describes the distribution of mass elements in an object around its center of mass, is determined by static multi-angle light scattering. The truncated recombinant hamster PrP (rPrP90-232) fibrils are also included for comparison. The third aim is to evaluate the competency of these smaller species to catalyze the fibrillation of α-monomer *in vitro*, under physiologically relevant conditions. This aim is achieved using the ThT assay and fluorescence spectroscopy. These aims provide a possible explanation for how PrP^{Sc} is able to propagate efficiently in vivo. Successful completion of these aims will aid in further understanding of the mechanism of prion disease pathogenesis.

Overall, we demonstrate that full-length fibrils dissociate both laterally and axially to form shorter oligomeric structures we term protofilaments; ~5% of these are soluble and contain ~100-300 monomers. Regardless of their length, the protofilaments retain the characteristic intermolecular β-sheet structure of the mature fibrils. Compared with intact fibrils, they are more efficient at accelerating fibril formation on a per monomer basis since they are shorter and provide more ends to facilitate conversion. We propose that protonation of histidine residues in the N-terminal region of PrP is involved in fibril dissociation; suggesting that this region, which is intrinsically disordered in the α-monomeric form of PrP, might take on structure when amyloid fibrils are formed. Our results provide new insight into the mechanism for dissociation of mammalian PrP fibrils, and help to extend our knowledge on the molecular events of prion propagation in vivo.

II. Experimental procedures

A. Protein expression and purification

The genes encoding residues 23-232 or 90-232 of golden Syrian hamster PrP were amplified by PCR from plasmid pHaPrP [273] by Dr. Hui-Chun Yeh. Hamster PrP is 86% identical to human PrP but contains an additional amino acid at position 228. The amplified genes were inserted into the expression vector pET24a^{+} and transformed into BL21(DE3)-Rosetta cells (Novagen). Proper gene insertion was confirmed by DNA sequencing at the Murdock Sequencing Facility (University of Montana, Missoula, MT).

Recombinant hamster PrP (rPrP23-232 or rPrP90-232) was expressed and purified using modifications of published protocols [273, 274]. Typically, 1% of a starter culture was inoculated into 2xYT media containing 50 μg/mL kanamycin and 34 μg/mL chloramphenicol; this was grown at 37 °C until the OD_{600nm} reached 1-2. Expression was induced by the addition of 0.5 mM isopropyl-β-d-thiogalactoside and cells were harvested 6 h after induction. Cell pellets were resuspended in lysis buffer (50 mM Tris-Cl, 2 mM EDTA, pH 7.5 containing 100 μg/ml lysozyme and 10 μg/ml DNase), and lysed by several freeze/thaw cycles. The lysate was centrifuged at 4 °C at 12,000 rpm for 20 min and the resulting pellet was then washed twice with 50 mM Tris-Cl, pH 7.5 containing 1% Triton X-100, followed by an extra wash with 20 mM Tris-Cl, pH 7.4 containing 150 mM NaCl and 2 M urea. After solubilization of the inclusion bodies in buffer A (8 M urea, 0.1 M KPO_4, pH 8.0), the sample was

centrifuged at 19,000 rpm for 30 min and the supernatant was passed through a 0.45 µm mixed cellulose ester syringe filter (Fisherbrand) prior to loading the Ni(II)-charged Chelating Sepharose Fast Flow resin (GE Healthcare). For every 3 liters of initial culture, 100 mL of pre-equilibrated resin was added, and the slurry was incubated at 37 °C for 2 h with continuous shaking. The suspension was then poured into a 5 x 20 cm Bio-Rad Econocolumn and washed with 5 column volumes of buffer A. Next, the protein was refolded on the column by applying a linear gradient (20 column volumes) from buffer A to buffer B (0.1 M KPO_4 , pH 8.0) at a flow rate of 10 mL/min, followed by washing with 5 column volumes of buffer B. The protein was then eluted using 60 mM imidazole in buffer B, followed by a second elution with 200 mM imidazole in buffer B.

For rPrP90-232, eluent from immobilized metal affinity chromatography was further purified using hydrophobic interaction chromatography. About 20 mg of protein was equilibrated in buffer containing 4.5 M guanidine hydrochloride (GdnHCl), 1 M $(NH_4)_2SO_4$, 0.1 M KPO_4 at pH 8, and then passed through a 0.22 µm regenerated cellulose membrane syringe filter (Corning). Protein was purified on an AKTA-FPLC using a HiPrep Phenyl Sepharose 16/10 column (GE Healthcare) pre-equilibrated with buffer C (4 M urea, 1 M $(NH_4)_2SO_4$, 0.1 M KPO_4, pH 8.0). Recombinant PrP90-232 was eluted using a linear gradient from buffer C to buffer D (4 M urea, 0.1 M KPO_4, pH 8.0) between 30-50% buffer D.

The purity of rPrP was confirmed by SDS-PAGE (8-25% gradient gels) on a PhastSystem (GE Healthcare, Inc). Stocks of purified protein were stored in 6 M

GdnHCl, 0.1 M KPO_4, pH 8.0 and used within two weeks. The concentration of the stock GdnHCl was determined on a refractometer [275]. Protein concentration was determined spectrophotometrically in 6 M GdnHCl using ε_{280} = 61,025 M^{-1} cm^{-1} for rPrP23-232 and 24,345 M^{-1} cm^{-1} for rPrP90-232, as calculated using the ProtParam program on the ExPASy web server [276].

B. Preparation of recombinant PrP23-232 conformers

The α-helical, PK-sensitive monomeric form of rPrP (α-monomer), which is structurally similar to PrP^C but lacks the GPI anchor and glycosylation [107], was used in all experiments. The α-monomer was formed by extensively dialyzing the stock solution against 20 mM sodium acetate (NaOAc), pH 4.5. We also prepared a previously characterized octameric conformer that is highly enriched in β-sheet structure, which is termed the β-oligomer [232, 274], as follows: 120 μM recombinant PrP23-232 in 6 M guanidine-HCl, 10 mM KPO_4, pH 8 was diluted 6-fold with conversion buffer (3.6 M urea, 160 mM NaCl, 60 mM NaOAc, pH 3.7) and incubated overnight at 37°C, followed by dialysis into 20 mM NaOAc, pH 4.5 [232, 274]. The secondary structures of the α-monomer and the β-oligomer were confirmed using circular dichroism (CD).

To generate the initial PK-resistant amyloid-like fibrils, stock solutions of rPrP were first refolded into the α-monomer by dialyzing the protein from the GndHCl storage buffer into 15 mM KPO_4, pH 6.5. This protein was then diluted 3-fold into denaturant fibrillation buffer, to give a final concentration of 1 mg/mL protein in 15 mM KPO_4, 0.5 M GdnHCl, 1.2 M urea, pH 6.5 [277-279]. Samples (0.6 - 1 mL) were

incubated at 37 °C under continuous orbital shaking at 600 rpm in 1.5 ml siliconized Eppendorf tubes (Fisher). Fibrils were collected by centrifugation at 15,000 g for 10 min for use in other experiments. The amyloid nature and morphological characteristics of the fibrils were confirmed by ThT fluorescence assay [251] and transmission electron microscopy (TEM), respectively.

C. Dissociation of rPrP fibrils and preparative ultracentrifugation

Approximately 300 μM rPrP fibrils were incubated in 20 mM sodium acetate (NaOAc), pH 4.5 at 37 °C for 3 days, with continuous rotation at 8 rpm (Labquake Shaker Rotisserie). Samples were then ultracentrifuged using a TLA-55 rotor at 120,000 g for 2 h and the supernatant, which contained very short protofilaments, was used for further studies.

D. Asymmetric flow field-flow fractionation (AF4) and light scattering analysis of prion conformers

As previously reported, the α-monomer does not behave ideally on a size exclusion chromatography column, perhaps due to electrostatic and/or hydrophobic interactions between the protein and the column matrix [280]. Consequently, prion conformers were isolated, analyzed, and sized by AF4 using an AF2000 instrument (PostNova, Inc), equipped with in-line UV-Vis and 7-angle light scattering (MALS) detectors [274, 281]. Samples were loaded in one 20-30 μl injection and then focused for 4 min with a crossflow of 3.5 ml/min on a regenerated cellulose membrane (5-kDa

MWCO). Samples were first eluted with 20 mM NaOAc, pH 4.5, at a channel flow of 1.5 ml/min and a crossflow of 2.5 ml/min for 30 min. The crossflow was then decreased to 0.1 ml/min linearly over 10 min, followed by a constant crossflow of 0.1 ml/min for another 30 min [282, 283]. The molar mass and radius of gyration (R_g) of the protofilament peak were determined using the software provided by the manufacturer [284] and the resulting plots were evaluated using the Berry method [285, 286], as it is well suited for the analysis of non-spherical polymers.

E. Circular dichroism (CD) and thermal denaturation

Far-UV circular dichroism spectra between 180 and 300 nm were recorded on a Jasco 810 spectrophotometer equipped with a Peltier temperature controller using the following parameters: protein concentration, 1 mg/mL; cuvette path, 0.01 cm; scan speed, 20 nm/min; response time, 4 s [287]. Typically, five spectra were averaged and smoothed after subtracting out the rather small contribution of the buffer, which improved the signal to noise ratio. Protein secondary structure analysis from CD spectra was performed using the DICHROWEB server and the CDSSTR program [288, 289] with Dataset #3.

Thermal denaturation of PrP conformers was monitored in a 0.1 cm cuvette at 12 μM protein concentration, using a scan speed of 200 nm/min. The samples were equilibrated at 25 °C and the temperature was incrementally increased at a rate of 2°C/min, where the temperature in a cuvette was monitored using an external microprobe. Each spectrum represents the average of three scans.

F. Fourier transform infrared (FT-IR) spectroscopy

FT-IR spectroscopy was performed using a Thermo Nicolet NEXUS 670 FT-IR spectrometer with continuous nitrogen purge. Samples for FT-IR were exchanged into D_2O buffer and analyzed in a demountable liquid cell fitted with two CaF_2 windows separated by a 50 μm Teflon spacer. Spectra were obtained from 128 cumulative scans at 1400–2000 cm^{-1} with 2 cm^{-1} resolution. Spectra were corrected by scaled subtraction of a water vapor spectrum until the region from 1900 to 1750 cm^{-1} no longer showed a negative lobe [290, 291]. Peak assignment was performed with OMNIC 5.2 software provided by the manufacturer.

G. Proteinase K (PK) digestion

Samples for PK digestion were adjusted to a final concentration of 2 mg/mL in 15 mM KPO_4, pH 6.5 or 20 mM NaOAc, pH 4.5. PK digestion was performed for 2 h at 37 °C at PK:rPrP ratio of 1:10; higher concentrations of PK resulted in significant PK auto-cleavage. Digestion products were separated and analyzed by SDS-PAGE on a PhastSystem using high density gels (GE Healthcare Life Sciences). Molecular weights of the individual PK-resistant bands were estimated from their relative mobility compared with peptide standards (MW-SDS-17S, Sigma).

H. In-gel tryptic digestion and mass spectrometry

To determine which residues comprise the PK-resistant core, the PK-resistant protein bands were subjected to trypsinolysis and mass spectrometry analysis. Trypsin (sequencing grade, modified, Promega) digestion was performed using the in-gel

protocol of Shevchenko et al with slight modifications [292]. Briefly, after staining the SDS-PAGE gels with Bio-Safe Coomassie stain (BioRad), the protein bands were excised, washed with 50 mM NH_4HCO_3, dehydrated with acetonitrile for 10 min, and then further dried in a Speed Vac (Savant). The protein was reduced by incubation in a minimal volume of 10 mM DTT, 25 mM NH_4HCO_3 for 30 min at 56 °C. After washing with 25 mM NH_4HCO_3, all protein thiols were alkylated by reaction with 100 mM iodoacetamide in 25 mM NH_4HCO_3 in the dark at room temperature for 15 min. The gel was then washed with 25 mM NH_4HCO_3, dehydrated, vacuum-dried and resuspended in a minimal volume of trypsin digestion buffer provided by the manufacturer and trypsin was added at approximately 10% of the PrP concentration. After overnight incubation at 37 °C, the supernatant was collected. Gel pieces were further extracted twice with 60% acetonitrile, 0.1% trifluoroacetic acid (TFA). The supernatant and the extracts were pooled and dried. Tryptic peptides were re-dissolved in 10 μL of 50% acetonitrile + 0.1% TFA for MALDI-ToF (Matrix Assisted Laser Desorption Ionization-Time of Flight) mass spectrometry (MS) analysis.

For MALDI-ToF, 1 μL of the tryptic digest was mixed 1:1 with a saturated solution of α-Cyano-4-hydroxycinnamic acid (α-CHCA) matrix. MS spectra were acquired on an ABI Voyager DE Pro workstation (Applied Biosystems) in reflectron mode at the University of Montana Mass Spectrometry and Proteomics Core Facility. MALDI-ToF MS/MS was carried out with a Bruker Daltonics AutoFlex ToF/ToF in reflectron mode at the Montana State University Proteomics & Mass Spectrometry Facility. Both instruments were calibrated using peptide calibration standard I (Bruker

Daltonics). Data were processed using mMass software [293].

I. Transmission electron microscopy

TEM was done at the Electron Microscopy Facility of the University of Montana. A 5 μL aliquot of sample (20 – 50 μM) was cast on a Formvar coated copper grid and allowed to adsorb for 3 – 30 min in a constant humidity chamber. The grid was then rinsed with distilled water and stained with 2% (w/v) uranyl acetate for 30 sec before briefly washing again with water. Varying the staining time did not change the results. After air drying, the sample was viewed using a Hitachi H-7100 instrument at 75 kV at standard magnifications of 20,000× and 100,000× [251]. Fibril dimensions were determined using Image J software (NIH, Bethesda, MD); between 30 and 450 individual structures were measured per image. Widths and lengths are reported as mean ± SD; average lengths are reported as the geometric mean.

R_g of the soluble protofilaments was also estimated from TEM images using the following formula based on the total moment of inertia of a rigid, solid cylinder [294].

For a rigid solid cylinder of radius *r*, height *h* and mass *m*, its moment of inertia along the *z* axis can be described as

$$I_Z = \frac{mr^2}{2}.$$

Its moment of inertia along the *x* and *y* axis can be described as

$$I_X = I_Y = \frac{m}{12}(3r^2 + h^2).$$

So the total moment of inertia of a rigid solid cylinder is

$$I_{Total} = m\left(R_g\right)^2 = I_X + I_Y + I_Z = m\left(\frac{r^2}{2} + \frac{1}{6}(3r^2 + h^2)\right)$$

,

R_g of a rigid solid cylinder can then be calculated as

$$R_g = \left(\frac{r^2}{2} + \frac{1}{6}(3r^2 + h^2)\right)^{\frac{1}{2}}$$

,

where *r* is treated as the arithmetic mean of the radius of protofilaments; and *h* is the geometric mean of their length.

J. Kinetic analysis

The kinetics of fibril formation from the α-monomer of rPrP23-232 was monitored under de novo (unseeded), and protofilament-seeded conditions, using buffer that did not contain denaturants. Conversion was carried out in a 96-well non-binding microplate (Corning #3651) with a total reaction volume of 0.2 mL/well containing 50 μM of α-monomer in 20 mM NaOAc, 0.1 M NaCl, pH 4.5 and 10 μM ThT; at this concentration ThT has a negligible effect on the kinetics of fibril formation [295]. For seeded reactions, soluble protofilaments were added into the reaction mixture to a final concentration of 0.5%, 1% or 2% (w/w). Plates were covered with Crystal Clear sealing film (Hampton Research) and incubated at 37 °C in the SpectraMax M2^e Microplate Reader (Molecular Devices). The fluorescence emission intensity at 488 nm was recorded hourly (excitation at 445 nm, plate was shaken briefly just prior to each measurement) using the bottom-read function in conjunction with a 475 nm emission cutoff filter.

III. Results

A. Mildly acidic conditions induce protofilament formation

Negative stain TEM images revealed that fibrils formed under partially denaturing conditions from either N-terminally truncated rPrP90-232 or full-length rPrP23-232 consisted of long unbranched structures. They were typically well over 1000 nm in length, with widths of 27 ± 2 nm and 27 ± 3 nm (mean ± SD) respectively (**Figure 2-3**). Both fibrils displayed twists, with a periodicity of about 180 nm for rPrP90-232 and 250-360 nm for rPrP23-232. This suggests that the fibrils are composed of at least two thinner strands, as has previously been described [165, 277], and which we will refer to as protofilaments. The amyloid nature of fibrils was further confirmed by high ThT fluorescence.

To determine whether the acidic environment of endosomes might encourage fibril dissociation, rPrP23-232 and rPrP90-232 fibrils were resuspended in pH 4.5 buffer for 3 days with continuous rotation at 8 rpm. The slow rotation prevented fibrils from settling to the bottom of the reaction tubes. TEM showed that the morphology of the rPrP90-232 fibrils was unaffected by the decrease in pH; no changes in twist, width, or length were noted (**Figure 2-3A→D**). In contrast, the rPrP23-232 sample was dramatically different. TEM revealed that at low pH the fibrils were changed into a population of structures of various lengths that were devoid of twist (**Figure 2-3E→H**). We then used ultracentrifugation (120,000 g for 2 h) to isolate the smallest of these structures, which were recovered from the

supernatant and deemed soluble according to the standards of Hjelmeland and Chrambach. These researchers state that particles remaining in the supernatant after centrifugation at 100,000 g for 1 h are regarded as soluble [296]. About 5% of the original rPrP23-232 fibrils were present in the supernatant (**Figure 2-3I**). The lengths of these soluble structures ranged from 20 to 150 nm (mean = 65 nm). We also noted a consistent 50% decrease in width (15 ± 2 nm for supernatant and 14 ± 2 nm for pellet) and a lack of twist for both the soluble and insoluble samples (**Figure 2-3I & J**). The TEM images indicate that at pH 4.5 the rPrP23-232 fibrils dissociate both laterally and axially to form protofilaments that are heterogeneous in length.

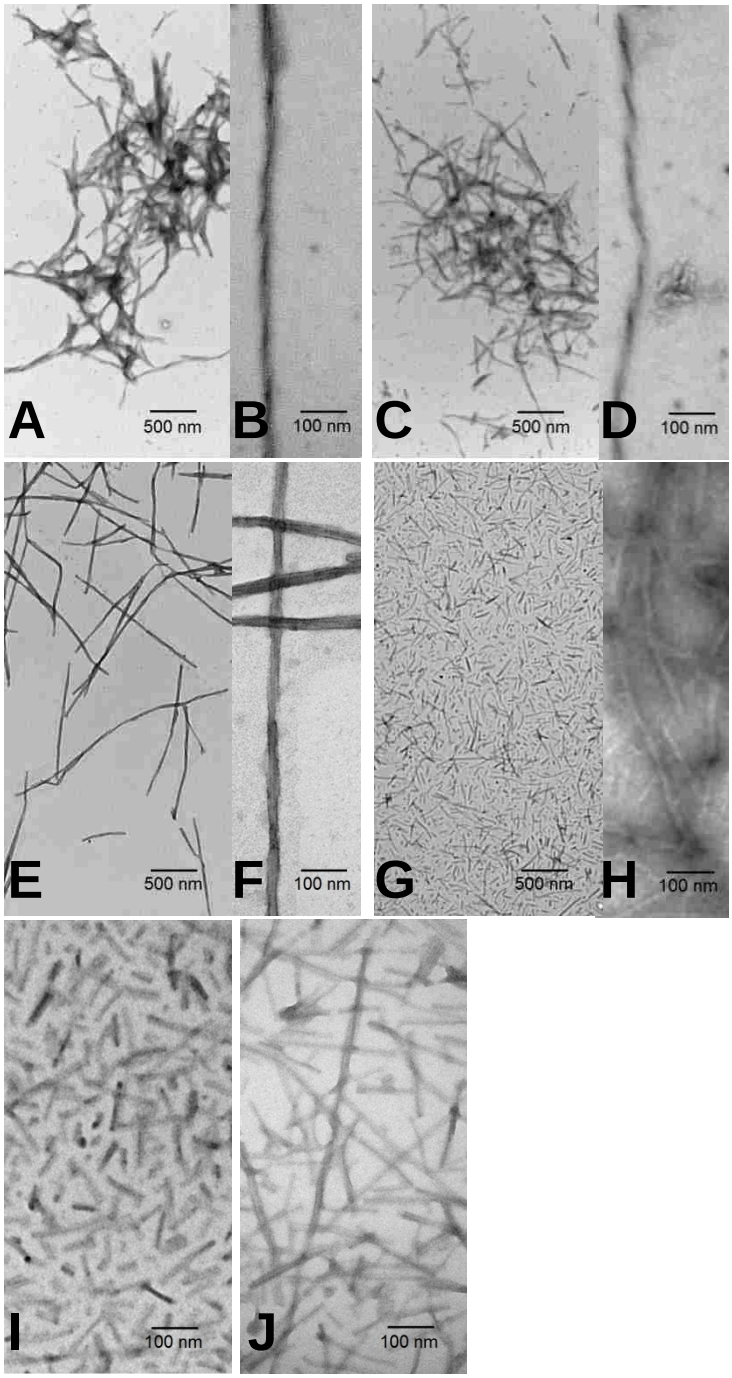

Figure 2-3. TEM images of rPrP23-232 and rPrP90-232 fibrils showing pH-triggered dissociation of rPrP23-232 fibrils.

Top panel: truncated rPrP90-232 fibrils at pH 6.5 (A, B) and after three days incubation at pH 4.5 (C, D). Middle Panel: full-length rPrP23-232 fibrils at pH 6.5 (E, F) and after three days incubation at pH 4.5 (G, H). Bottom Panel: The sample in (G, H) was ultracentrifuged at 120,000 g for 2 h to separate the soluble portion (I) from the insoluble portion (J). Images were taken at 20,000× (scale bar 500 nm) or 100,000× magnification (scale bar 100 nm).

B. Composition of the protofilaments amyloid core

To compare the composition of the amyloid cores of the protofilaments with those of their parent fibrils, we performed proteinase K (PK) digestion. Full-length PrP fibrils were digested at pH 6.5 and also after the fibrils had been resuspended in pH 4.5 buffer. In the pH 4.5 experiments, PK digestion was performed immediately after the change in pH and again 72 hours later. TEM imaging indicated that at 72 hours, the sample has mostly dissociated into protofilaments of varying lengths. This pre-incubated sample was further processed by centrifugation to remove the majority of the insoluble protofilaments prior to PK digestion.

The results were then analyzed by SDS-PAGE (**Figure 2-4** top). At pH 6.5 (lane 1), the most intense PK-resistant band is ~5.5 kDa, although bands at 5 and 7 kDa are also visible. Lane 2 shows the results of the sample digested immediately after the pH was lowered to 4.5. A triplet of bands at 7, 9, and 12 kDa are detected. This shift of the PK-resistant PrP bands with pH is attributed to the pH dependence of PK specificity [297]. The same triplet was also present in the pre-incubated sample (lane 3), although the band intensities were slightly different.

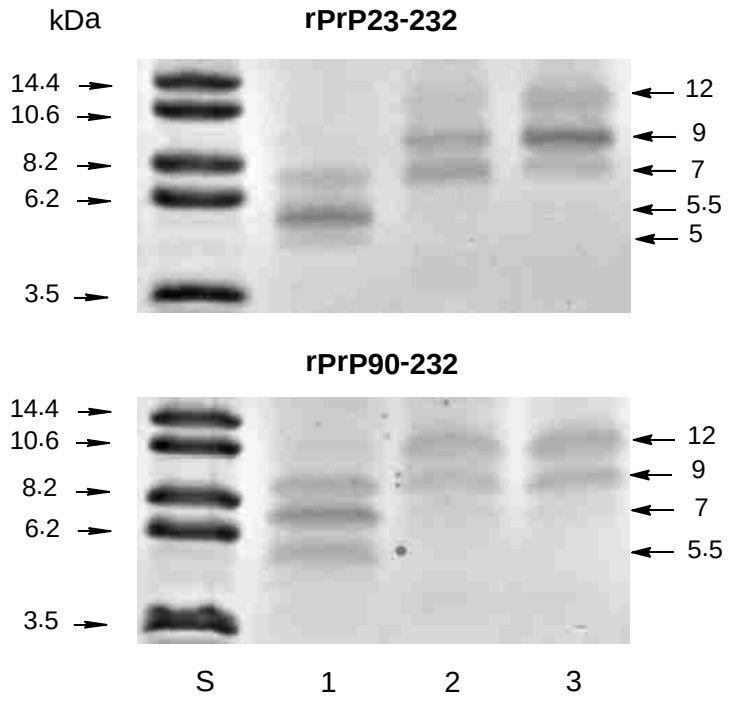

Figure 2-4. SDS-PAGE analysis of the PK-resistant regions of rPrP fibrils and protofilaments.

Samples (2 mg/ml) were treated with PK at a PK:protein ratio of 1:10 for 2 h at 37 °C and analyzed by SDS-PAGE. Top: full-length rPrP23-232; Bottom: truncated rPrP90-232. Lane S, MW standard; lane 1, pH 6.5; lane 2, pH 4.5; lane 3, samples pre-incubated at pH 4.5 for 72 hours prior to PK digestion. For lane 3 samples, the full-length sample was centrifuged prior to digestion but the truncated sample was not.

For control purposes, PK digestion of truncated rPrP90-232 fibrils was also performed (**Figure 2-4** bottom). Conditions were identical to those in full-length PrP except that the centrifugation step was omitted from the sample that was pre-incubated, since no protein could be found in the supernatant. As expected, the 72-hour pre-incubation had no effect on the PK-resistance, as the truncated fibrils do not dissociate at low pH. There were slight variations in the band intensities, but overall the PK-resistance of truncated fibrils was similar to that of full-length PrP.

Table 2-1. MALDI/TOF Analysis of peptides generated from the tryptic digestion of PK-resistant fragments

Position	Expected mass	Observed Mass						Modification
		rPrP23-232 α-monomer	rPrP23-232 fibril	12 kDa in gel	9 kDa in gel	7 kDa in gel	5.5 kDa in gel	
23-27	713.51	/	/	/	/	/	/	
28-37	988.46	988.74	988.62	/	/	/	/	
38-48	1089.51	1089.81	1089.68	/	/	/	/	
49-101	5332.35	/	/	/	/	/	/	
102-104	331.20	/	/	/	/	/	/	
105-106	244.17	/	/	/	/	/	/	
107-110	493.24	/	/	/	/	/	/	
111-136	2363.14	2363.27	2363.44	/	/	/	/	
	2379.14		2379.41	/	/	/	/	Met Oxidation
	2395.13		2395.38	/	/	/	/	Met Oxidation
	2411.13		2411.46	/	/	/	/	Met Oxidation
137-148	1534.62	1534.84	1534.79	/	/	/	/	
	1550.62		1550.79	1551.08	/	/	/	Met Oxidation
	1566.61		1566.79	1567.08	/	/	/	Met Oxidation
139-148	1306.53		/	1306.94	/	/	/	
	1322.52		/	1322.94	/	/	/	Met Oxidation
149-151	501.25	501.65	501.35	501.81	501.42	/	/	
152-156	663.29	663.49	663.53	663.87	663.57	/	/	
	679.28		679.53	679.87	679.59	/	/	Met Oxidation
157-164	1102.53	1102.85	1102.71	1102.91	1102.76	1103.08	/	
165-185	2475.17	2475.28	/	/	/	/	/	
	2532.19		/	/	/	/	/	Cys Alkylation
186-194	1016.54		1016.88	/	/	/	/	
195-204	1153.54	1153.86	1153.68	1153.91	1154.24	1154.09	1154.38	
205-208	548.29	548.46	548.49	548.86	548.47	548.81	548.98	
	564.28		564.48	564.85	564.46	564.80	564.98	Met Oxidation
209-220	1457.68	1458.07	/	/	/	/	/	
	1514.70		1514.89	1515.16	1515.41	1515.21	1515.61	Cys Alkylation
	1530.69		1530.89	1531.16	1531.41	1531.23	1531.61	Cys Alkylation+ Met Oxidation
221-229	1088.46	1088.78	1088.64	1088.83	1088.70	/	/	

For each gel lane in Figure 2-4, the peptides bands were excised, digested with trypsin and analyzed by mass spectrometry to map the composition of each fragment. The results were summarized in Table 2-1 (refer to Chapter V Figure 5-3, 5-4, 5-5, and 5-6 for representative MALDI spectra). No peptides from residues 23-137 were detected in any PK-resistant fragment. This confirmed that protofilament formation

did not involve refolding of all or part of the N-terminal domain into a PK-resistant β-sheet structure. The 1306.94 peak was abundant in the spectra of 12 KDa fragment, whereas its signal dropped significantly in the spectra of 9 KDa fragment and was not detectable in the 7 KDa fragment. This indicated that this section has been PK-digested in both 9 KDa and 7 KDa fragments. The identity of the peak was verified by MALDI-ToF/ToF as peptide 139-148 (Figure 2-5). Altogether, the data in Table 2-1 show that the 12, 9, and 7 kDa peptide fragments begin at residues 137-139, 149 and 157, respectively. There was little difference in the MS data collected for identical masses derived from different gel lanes. The start site for the 5.5 KDa fragment was ambiguous due to the gap encompassing residues 165-194. Based on its mass and the identity of the C-terminal tryptic peptide, we estimate that this PK-resistant peptide begins near residue 175. This region showed a relatively high mobility by SDSL-EPR compared with other portions of the amyloid core and may correspond to a loop or turn in the core [177].

y ion #	Sequence	Expected mass	b ion #	Sequence	Expected mass
1	R	175.12	1	M	
2	DR	290.15	2	MH	269.11
3	EDR	419.19	3	MHF	416.18
4	WEDR	605.27	4	MHFG	473.20
5	DWEDR	720.29	5	MHFGN	587.24
6	NDWEDR	834.34	6	MHFGND	702.27
7	GNDWEDR	891.36	7	MHFGNDW	888.35
8	FGNDWEDR	1038.43	8	MHFGNDWE	1017.39
9	HFGNDWEDR	1175.49	9	MHFGNDWED	1132.42
10	MHFGNDWEDR	1306.53	10	MHFGNDWEDR	

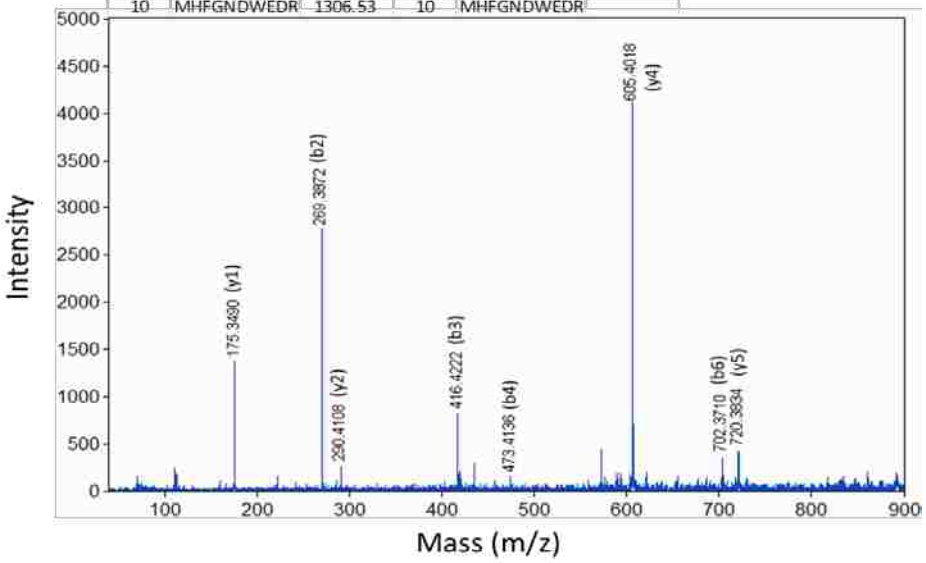

Figure 2-5. MALDI-TOF/TOF spectrum of the 1306.94 peak detected in the 12 kDa fragment. The y and b ions identify this peptide as residues 139-148.

The identity of the 7 kDa peptide (~residues 157-220) is consistent with the amyloid core detected by hydrogen/deuterium exchange mass spectrometry [176] and site-directed spin labeling electron paramagnetic resonance spectroscopy [177] for human rPrP90-232. We attribute the presence of larger peptide fragments in these samples to the inability of PK to fully access non-amyloid regions of PrP [176]. PK-resistant, non-specific aggregates have been shown to form after the N-terminal domain of amyloid PrP is cleaved and/or partially digested [277]. It is believed that the exposure of hydrophobic residues causes non-specific aggregation that impedes PK digestion. Therefore, the presence of larger PK-resistant peptides noted in Table 2-1 does not mean that the amyloid core of the protofilaments has extended beyond

the 7 kDa β-sheet core identified for recombinant PrP fibrils by other techniques [177].

Overall, it appears that fibrils and protofilaments possess similar global architectures in their amyloid core regions; there is no evidence that protofilament formation involves reorganization of the N-terminal domain into an amyloid state.

C. Purification and size determination of soluble protofilaments

We then used AF4 and MALS to further purify and analyze the soluble protofilaments of rPrP23-232 that were isolated by ultracentrifugation (**Figure 2-6A**). The majority of the sample eluted under low crossflow at 42.6 min along with 2 minor components that elute at 6.8 and 20.9 min under high crossflow. The molar mass elugram (**Figure 2-6B**) revealed this major peak had significant polydispersity with the centroid at 5.8 MDa, which is equivalent to ~250 monomeric subunits. The radius of gyration (R_g) for the species eluted at the centroid is 29.5 nm, which is close to the R_g value of 27 nm that we estimated from the TEM images. This value was calculated using the average radius of 7 nm and a mean particle length of 65 nm (**Figure 2-3I**) and treating the protofilaments as rigid cylinders. This result confirms that the soluble protofilaments observed by TEM are the main constituent purified by AF4 from the supernatant. The elution profiles of 2 minor components at 6.8 and 20.9 min are similar to those of α-monomer and β-oligomer prepared independently by refolding.

As expected, no peaks were observed in the supernatant of low pH treated rPrP90-232 fibrils (**Figure 2-6A**). We also note that the starting material (the long,

twisted amyloid fibrils) is undetectable under the AF4 crossflow conditions used here. Re-injection of the 42.6 min peak after storage for an additional 3 days showed no significant changes (**Figure 2-6A**). SDS-PAGE analysis confirmed that the purified protofilaments contain full-length rPrP; no degradation products were observed (**Figure 2-6C**). These results demonstrate that the soluble protofilaments are quite stable under acidic conditions. Axial dissociation of the long, insoluble protofilaments to form short, soluble structures reached a steady state maximum after ~ 2 days incubation at pH 4.5 (**Figure 2-6D**).

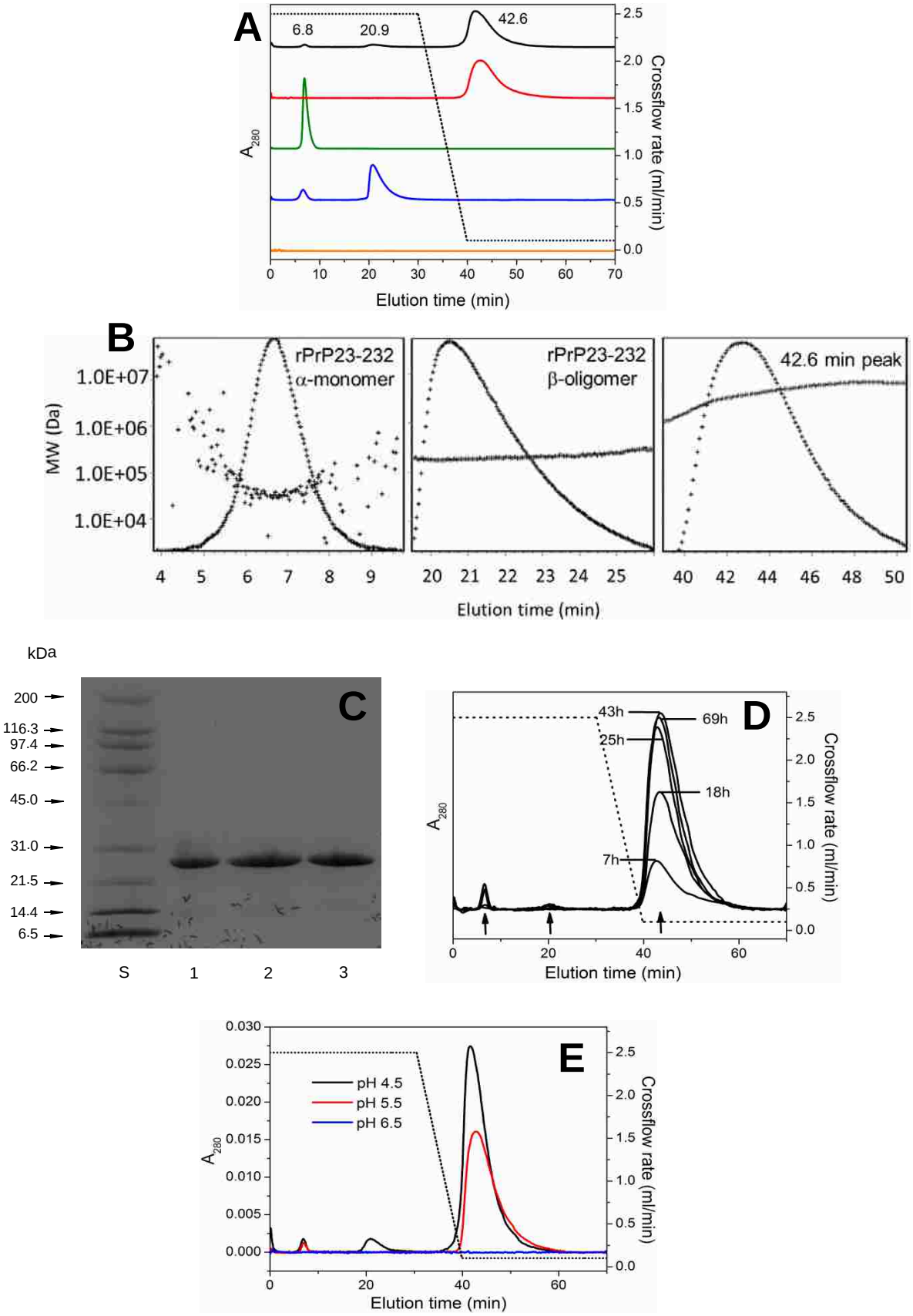

Figure 2-6. Purification and size determination of soluble protofilaments.

(A) AF4 analysis of rPrP23-232 conformers: black, the low-pH supernatant; red, re-injection of the 42.6 min protofilament peak 72 h after collection; green, pure α-monomer; and blue, β-oligomer. The elution profile of low-pH treated rPrP90-232 fibrils (orange) is included for comparison. The crossflow rate is denoted by dotted line. (B) Semi-log mass elugram plots for the rPrP23-232 conformers separated using AF4 (Figure 2-6A). Molar masses were calculated to be 25 kDa, α-monomer; 180 kDa, β-oligomer, and 5.5 MDa, protofilaments. (C) 8-25% SDS-PAGE analysis of rPrP23-232 conformers. Lane S, MW standard; lane 1, α-monomer at pH 6.5; lane 2, fibril at pH 6.5; lane 3, fibril incubated at pH 4.5 for 72 hours. (D)Time course of protofilament formation as monitored by AF4. (E) pH dependence of protofilament formation.

D. The effect of pH and salt on protofilament formation

To confirm the pH-dependent nature of this phenomenon, we assessed the stability of rPrP23-232 fibrils after incubation at pH 6.5, 5.5, and 4.5 for 3 days. AF4 analysis (**Figure 2-6E**) showed that soluble protofilaments are also formed at pH 5.5, although the centroid of the protofilament peak shifted to a higher apparent molecular weight (43.7 min, 8.5 MDa, ~370 monomers) compared with the results obtained at pH 4.5. No short protofilaments were formed at pH 6.5. These data confirm that fibril dissociation and the size distribution of the products are pH dependent, and that rPrP23-232 fibrils are stable under neutral conditions.

The effect of salt on protofilament formation has also been investigated. The data suggest that lateral dissociation of mature fibrils into protofilaments occurs within 24 hours, with or without 0.1 M NaCl. However, when salt is present, axial dissociation to produce measurable quantities of short, soluble protofilaments takes longer (~8 days, **Figure 2-7 E-J**) compared with the reaction in the absence of NaCl (2~3 days, **Figure 2-7 A-D**). The soluble protofilaments are qualitatively the same (compare **Figure 2-7 K** with **Figure 2-6A**) though the yield is somewhat lower in the presence

of 0.1 M NaCl.

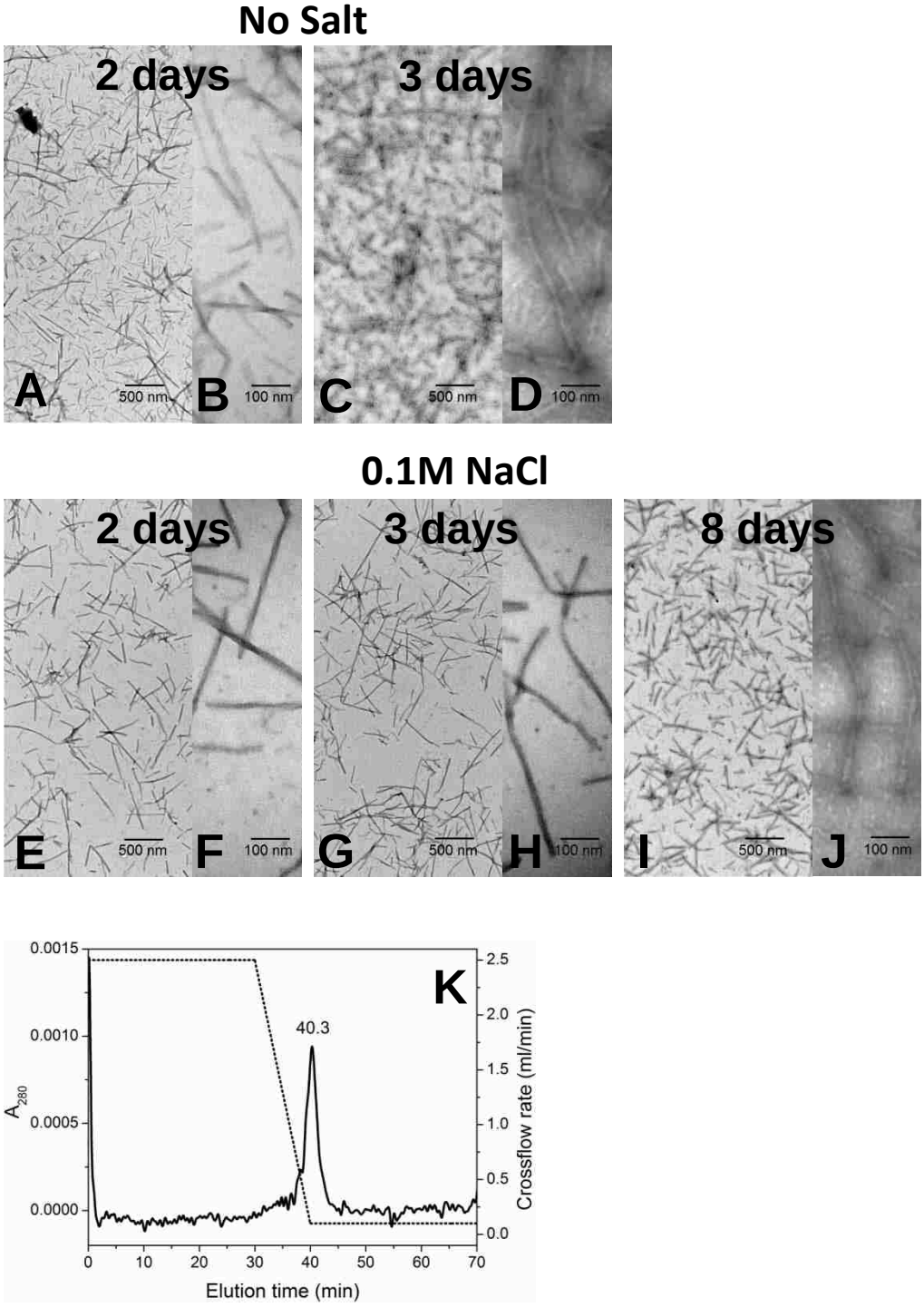

Figure 2-7. Effect of salt on the dissociation of rPrP23-232 fibrils into protofilaments.

TEM images of rPrP23-232 fibrils showing the time dependence of pH-triggered lateral and axial dissociation. Images taken at 20,000× (scale bar 500 nm) or 100,000× magnification (scale bar 100 nm). Top panel:

dissociation of rPrP23-232 fibrils after incubation for 2 days (A, B) or 3 days (C,D) at pH 4.5 in the absence of NaCl. Middle panel: dissociation of rPrP23-232 fibrils after incubation for 2 days (E, F), 3 days (G, H), or 8 days (I, J) at pH 4.5 in the presence of 0.1M NaCl. Bottom Panel: After 8 days, the sample containing salt was subjected to AF4 analysis (K), which showed an elution peak at 40.3 min.

E. Characterization of soluble protofilaments

The CD spectrum of the soluble protofilament fraction (42.6 min peak) is shown in Figure 2-8A. The protofilament signal is markedly different from both the α-monomer and the β-oligomer. A single negative peak centered at 216 nm was associated with a rather large MRE value (-12,000 $deg \cdot cm^2 \cdot dmol^{-1} \cdot residue^{-1}$). Secondary structure analyses indicate that the soluble protofilaments have considerably less α-helix and more β-sheet in comparison with the α-monomer (**Table 2-2**) [288, 289]. Although the overall shapes and MRE values of the protofilaments and the β-oligomer are quite different, the predicted secondary structure content is surprisingly similar. However, CD spectroscopy often misestimates β-sheet content due to the significant overlap of the β-sheet absorption band with that from α-helices. We could not obtain a solution CD spectrum of fibrils at neutral pH for direct comparison with the protofilaments, probably because they scatter too much light. The solution CD spectrum of similar fibrils has been previously published [189], but these fibrils were in an acidic buffer and thus the reported CD signal may actually be that of dissociated, soluble protofilaments. The amyloid nature of the soluble protofilaments was confirmed by their resistance to thermal denaturation and the ThT fluorescence assay (**Figure 2-8B & C**).

Table 2-2. Secondary-structure composition of rPrP23-232 conformers as estimated from CD Spectra

Secondary structure type	α-monomer	β-oligomer	protofilaments
α-helix	23%	4%	7%
β-sheet	26%	38%	30%
Turn	21%	25%	25%
Loop/Unordered	29%	32%	37%

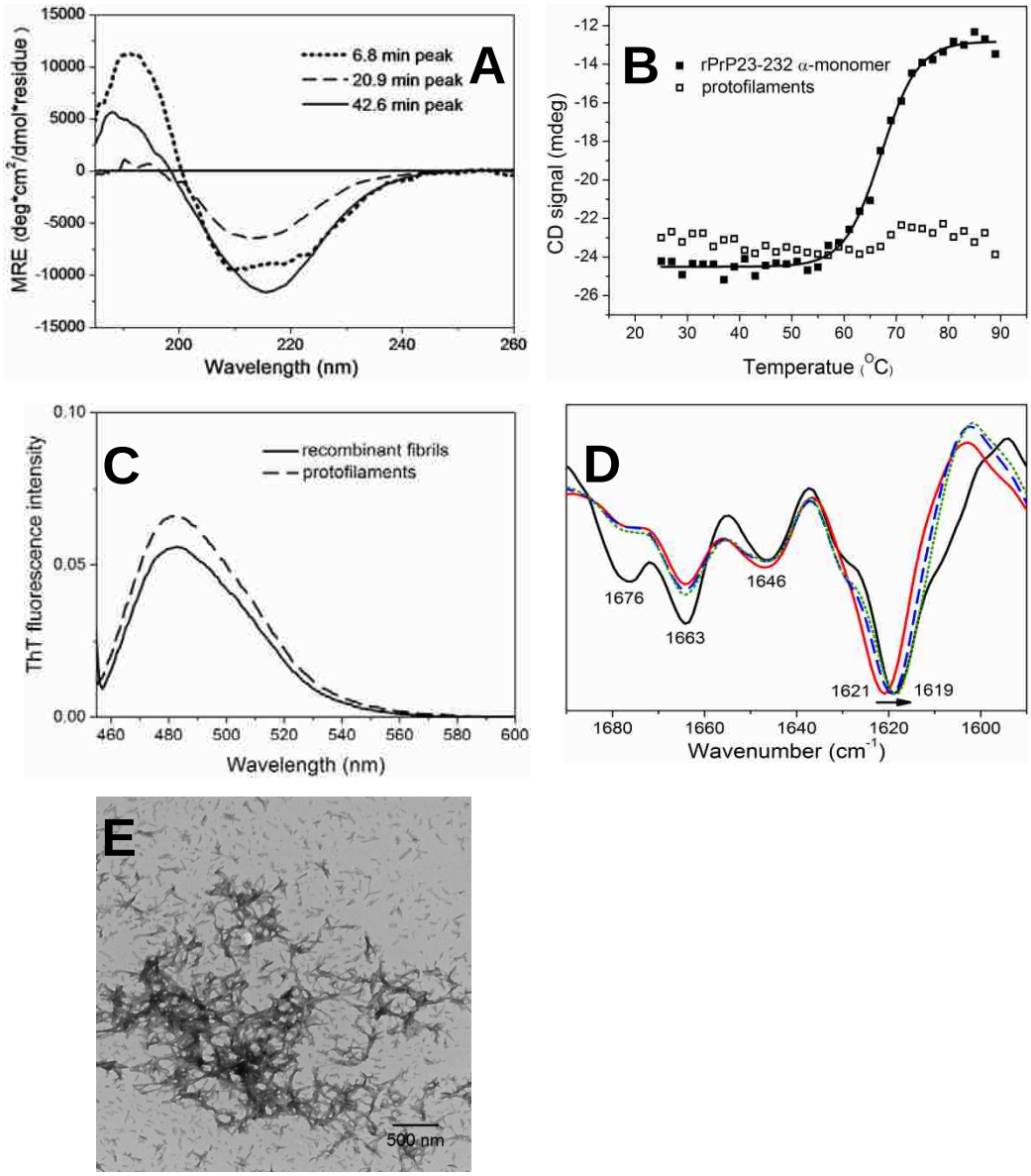

Figure 2-8. Biophysical characterization of rPrP23-232 protofilaments.

(A) CD spectra of the supernatant components after separation by AF4.

(B) Thermal denaturation profiles of soluble protofilaments recorded at 216nm. The data for rPrP23-232 α-monomer recorded at 222nm is included for comparison, which shows two-state behavior with a T_m of ~67 °C when fitting to the sigmoidal Boltzmann equation [273]. (C) ThT fluorescence emission spectra of soluble protofilaments. Spectra were recorded at a protein concentration of 5 μM and ThT concentration of 10 μM in 20 mM NaOAc, pH 4.5. The ThT fluorescence of fibrils at pH 6.5 is included for comparative purposes. (D) Second derivative FT-IR spectra of protofilaments at pH 4.5 (solid red); 10 min (dashed blue) and 72 h (dotted green) after raising the pH to 7.0. The spectrum of the parent fibrils at pH 7.0 is included for comparison (solid black). (E) TEM image of aggregates formed after 72 h at pH 7.0.

The identities of 2 minor components eluted at 6.8 and 20.9 min under high crossflow were confirmed by circular dichroism (CD) [232, 274], shown in **Figure 2-8A**. The CD spectrum of the 6.8 min peak was dominated by negative bands at 209 and 222 nm with a mean residue ellipticity (MRE) of -8,100 $deg \cdot cm^2 \cdot dmol^{-1} \cdot residue^{-1}$ at 222nm. This compares well with the α-monomer made by refolding rPrP23-232 (MRE = -8,800 $deg \cdot cm^2 \cdot dmol^{-1} \cdot residue^{-1}$). The high β-sheet content of the 20.9 min peak was evidenced by both the overall shape of the CD spectrum (a single minimum at 213 nm) and the smaller MRE value of -6,450 $deg \cdot cm^2 \cdot dmol^{-1} \cdot residue^{-1}$. The CD spectrum of purified β-oligomer made by refolding has a similar negative band at 213 nm (MRE = -6,300 $deg \cdot cm^2 \cdot dmol^{-1} \cdot residue^{-1}$). We then compared the secondary structure of the soluble protofilaments with that of their parent rPrP23-232 fibrils using FT-IR spectroscopy (**Figure 2-8D**). Unlike CD, FT-IR spectroscopy may be used for both solution and solid samples and is better suited for the characterization of β-sheet structure. Taking into account the limitations of both techniques, the FT-IR results are reasonably consistent with the results obtained from CD. The high cross-β sheet content of protofilaments is evident in the strong single amide I band centered at

1621 cm^{-1} (solid red line), which is shifted to slightly higher frequency as compared with the recombinant fibrils (1619 cm^{-1}, solid black line). A shoulder at 1628 cm^{-1} in the fibril spectrum is absent in the protofilament spectrum. The amide I bands previously assigned to turns and loops (1663 cm^{-1} and 1676 cm^{-1}) [168, 189, 277] were less substantial in protofilaments as compared with fibrils, possibly indicating some unfolding of these structures. Overall, the spectrum of protofilaments is quite similar to the parent fibrils.

Raising the pH of the protofilaments to 7.0 caused an immediate shift of the β-sheet amide I band from 1621 cm^{-1} to 1619 cm^{-1}, and the shoulder at 1628 cm^{-1} appeared, becoming more defined after 72 hours incubation at pH 7.0 (**Figure 2-8D**, dashed blue and dotted green lines). Overall the data suggest that the minor differences in the β-strand structure between protofilaments at acidic pH and fibrils are pH-dependent and largely reversible. However, we did not observe any re-assembly of protofilaments into twisted or parallel fibrils by TEM; instead, clumps of aggregates were formed when the pH was raised (**Figure 2-8E**). In regions of the TEM image where individual structures could be isolated and measured, the widths of the structures were ~14 nm, resembling protofilaments and not fibrils.

Overall, the biophysical and spectroscopic data suggest the main secondary structural characteristics of amyloid fibrils are preserved in the soluble protofilaments with slightly pH-dependent and eversible difference.

F. Ability of protofilaments to accelerate PrP conversion

Typical fibril formation shows a characteristic nucleation-dependent pattern with

three kinetic phases: the initial lag phase is followed by a steep log phase and then a final plateau. It has been well-established that in the presence of pre-formed fibril seeds, conversion under partially denaturing conditions is accelerated with a dramatically shortened lag phase [277]. We examined whether this also held true for pre-formed protofilament seeds under physiologically relevant conditions, i.e. in the absence of denaturants.

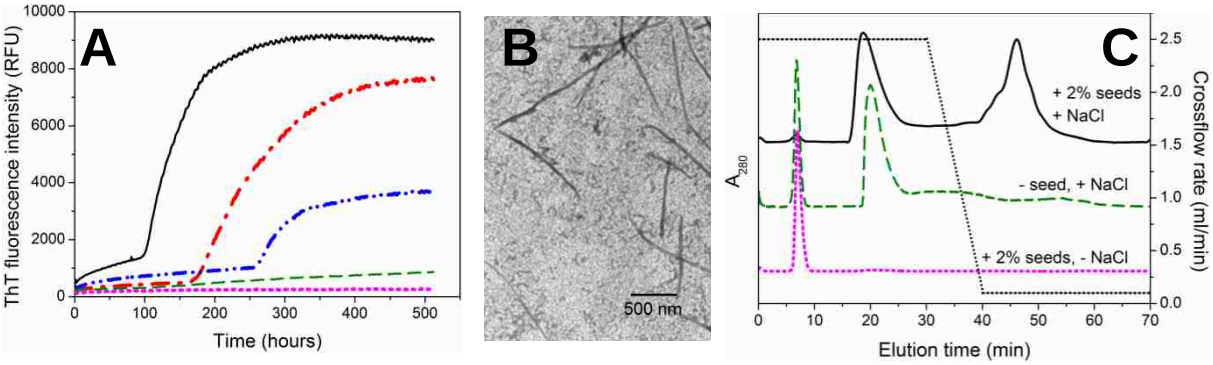

Figure 2-9. Protofilament-seeded conversion of rPrP23-232 α-monomer under mildly acidic, non-denaturing conditions.

(A) Kinetics as followed by the ThT fluorescence assay. Seed concentration: 2% (black); 1% (red); 0.5% (blue); and 0% (green); α-monomer + 2% seed in the absence of NaCl (magenta). (B) TEM image of products formed after 3 weeks in 2% seeded reaction with NaCl. (C) AF4 analysis of the conversion products of 2% seed + NaCl (black); 0% seed + NaCl (green); and 2% seed without NaCl (magenta).

Propagation experiments were performed using conformers of rPrP23-232, in 20 mM NaOAc, 0.1 M NaCl, pH 4.5 to approximate the environment of late endosomal vesicles. A direct comparison between fibrils and protofilaments is not possible since fibrils dissociate into protofilaments of varying lengths in less than 24 h at pH 4.5. Similarly, protofilaments form amorphous aggregates at neutral pH.

The ratio of soluble protofilaments (seeds) to α-monomer was varied from 0-2 %

(**Figure 2-9A**). The unseeded control samples showed little change even after 3 weeks, but all seeded experiments followed a typical nucleation-dependent polymerization mechanism. Adding more protofilament seeds proportionally shortened the incubation times and increased both the rate of the log phase kinetics and the final plateau levels of ThT fluorescence intensity. However, overall the lag phase was significantly elongated (days) as compared with reactions carried out in the presence of denaturants (hours) [277].

After 3 weeks the products from the 2% seeded reaction were examined by TEM imaging (**Figure 2-9B**). There were considerable amounts of small particles present in the sample. This was confirmed by AF4 (**Figure 2-9C**, top trace), which detected both β-oligomer (retention time 20.9 min) and ThT-binding high-molecular-weight aggregates that were larger than the seeds themselves (broad peak with retention time ~46 min). Control experiments showed that this peak results from conversion of the α-monomer, as the seeds themselves (retention time 42.6 min) are undetectable at the highest concentration used (**Figure 2-9C**, bottom trace).

The TEM image in Figure 2-9B also indicated that some highly elongated, unbranched structures had also formed in the reaction, with an approximate width of 34 ± 5 nm. This width matches that of the parent fibrils produced under partially denaturing conditions (**Figure 2-3E**) and not that of the protofilament seeds.

The presence of salt (0.1 M NaCl) facilitated the conversion process. No log phase was ever achieved in the seeding experiments carried out without salt, even when 2% seeds were added in the system (**Figure 2-9A**, dotted magenta trace). AF4

showed that the α-monomer is mostly unreactive and remains in the starting, monomeric state (**Figure 2-9C**, dotted magenta trace). The destabilizing effect of salt on α-monomer has been previously documented [298]. Thus, in the presence of 0.1 M NaCl, analysis of the unseeded control (**Figure 2-9C**, dashed green trace) shows that the peak at 6.8 min (the α-monomer) has decreased and larger products appear at longer retention times. The major product is the β-oligomer (peak at 20.9 min). Small amounts of non-ThT binding aggregates are also formed, which result in the elevated baseline at later elution times. This is consistent with the kinetic assay, which showed little change in fluorescence intensity even after 3 weeks when seeds were omitted from the system (**Figure 2-9A**, dashed green trace).

IV. Discussion

The current study demonstrates that full-length rPrP fibrils dissociate when they are exposed to mildly acidic conditions. As judged from microscopy imaging, dissociation occurs in two dimensions: lateral and axial. Lateral dissociation involves the disassembly of mature fibrils into constituent protofilaments, while axial dissociation further divides the protofilaments along the fibrillar axis into smaller entities of variable lengths. To our knowledge, the ability of mature amyloid fibrils to undergo dissociation into protofilaments under mildly acidic conditions has not been previously reported. The pH conditions used here are similar to those found in late endosomal and lysosomal vesicles. Kinetic analysis shows that the protofilaments preserve the ability to propagate *in vitro* and thus may be of physiologic relevance, as

our conditions mimic those of late endocytic and lysosomal vesicles.

A. Mechanism of fibril dissociation

Two possible mechanisms for fibril dissociation have been proposed in the literature: mechanical stress-induced dissociation and chaperone-mediated dissociation [268, 299]. The results from this study suggest another possible mechanism; fibril dissociation into protofilaments induced by low pH.

The pH dependence of protofilament formation suggests that protonation of Asp, Glu, and/or His residues are keys to dissociation. According to the parallel, in-register β-structure proposed by the Surewicz group, the amyloid core has only one charged residue, Glu211, buried within the dry interface. This residue forms a hydrogen bond with Gln186 to stabilize the otherwise unfavorable intermolecular electrostatic interactions [177]. Protonation of Glu211 could abolish this interaction and facilitate the disassembly the fibril, but if this were true we would have expected that both rPrP90-232 and rPrP23-232 fibrils would dissociate under acidic conditions. The rPrP90-232 fibrils remain intact at pH 4.5, which essentially rules out this explanation.

The lack of dissociation in N-terminally truncated fibrils (rPrP90-232) at low pH indicates that the N-terminal region of PrP is important to the dissociation process. In full-length hamster PrP, this region (residues 23-140) is quite basic, containing 0 Asp, 0 Glu, 4 Arg, 7 Lys, and 7 His; this pattern is highly conserved among mammalian PrPs. His residues have a pK_a of ~6.8 and thus are the only residues present that could account for the observed pH effect. We hypothesize that protonation of His residues in

a domain already enriched with positively charged residues leads to charge repulsion, which causes the dissociation of fibrillar superstructures into protofilaments. Conformational perturbations induced by charge repulsion in residues 90-140 (contains 3 of the conserved His) have been reported in studies of human truncated rPrP90-231, with an associated pK_a of 5.5 [178]. Given that we did not observe dissociation of N-terminally truncated fibrils (hamster rPrP90-232) into protofilaments, we postulate that the four additional His residues found in residues 23-89 play an important role in acid-induced fibril dissociation. Additional studies to test this hypothesis will be necessary. The slower dissociation of mature fibrils in the presence of salt may be associated with the shield effect of counterions on charged residues.

B. Protofilament structure and seeding capability

Some of the protofilaments are small enough to be considered soluble. These have an average length of about 65 nm and an apparent molecular weight of ~5.5 MDa (~250 monomeric subunits). The soluble protofilaments retain the hallmark characteristics of full-length amyloid fibrils and share the same amyloid core. Small but mostly reversible pH-dependent differences in the β-sheet core structure were noted by FT-IR. The protofilaments have a unique CD spectrum compared with other soluble forms of PrP.

At pH 4.5 in the presence of 0.1 M NaCl and α-monomer, protofilaments are efficient seeds. The propagated products are mostly elongated protofilaments, though a few fibrils are detectable after several weeks. This fits with our initial observations

that the yield of soluble protofilaments from parent fibrils was higher when salt was omitted from the acidic buffer. It is likely that the presence of counterions in the buffer shields the large positive charge on the N-terminal domains of individual protofilaments, permitting some fibrils to be formed when there is an excess of α-monomer present.

The effect of salt on fibril formation noted by others [254, 255] is confirmed in our research that shows no α-monomer was converted to high order aggregates in the absence of NaCl. Prion protein exhibits reduced thermodynamic stability over a wide range of NaCl concentrations (20-200 mM) at both neutral and acidic pH [298]. The destabilizing effect of NaCl on α-monomers may decrease the energy barrier that separates α-monomers from the amyloid fibrils [232] and thus will facilitate the conversion. Another possible mechanism may relate to the screening effect of counterions in the solution that attenuates the repulsion between biomolecules and promotes aggregation [74].

C. Pathological relevance of pH-induced protofilament formation

A number of studies have proposed that the endocytic pathway, including endosomes and lysosomes, is important for the PrP^{Sc} conversion *in vivo* [42, 67, 162, 268, 269]. Although most efforts have been devoted to illustrating the destabilizing effect of these acidic vesicles on the global structure and thermodynamic stability of PrP^{C} [163, 164, 240], less attention has been paid to its impact on mature amyloids. We show here that in addition to destabilizing α-monomers and thus facilitating

primary nucleation, low pH may also contribute to fibril dissociation, a secondary nucleation event that is necessary for efficient conversion and maintenance of the prion state [300]. Results from the present *in vitro* studies offer direct evidence that at low pH mature fibrils can dissociate both laterally and axially into protofilaments, which are then able to recruit and convert α-monomer. Assuming that a similar dissociation mechanism occurs *in vivo*, protofilaments of PrP^{Sc} formed in the lysosome might be excellent seeds for the propagation of PrP^{C} during its normal recycling from the cell surface via the endocytic pathway [67].

It has been observed in PMCA experiments that decreasing the particle size by longer sonication results in a reduction in infectious titer, which indicates a more efficient clearance by the cells [301]. In line with this assumption, it has been reported that stimulating autophagy with lithium [302] has a protective role on prion infected hosts. Thus, seeding effects of protofilaments *in vivo* might be counter-balanced by cellular clearance mechanisms. This suggests the net effect of low pH-induced fibril dissociation on PrP^{Sc} propagation may depend on the size of protofilaments generated *in vivo*. While ~5% of the protofilaments were soluble, the majority were ~ 50-400 nm in length (**Figure 2-3G**) and therefore less likely to be steered into the degradation pathway. These insoluble protofilaments are much shorter than the mature fibrils, and would be more efficient seeds for secondary nucleation events, per PrP subunit.

In summary, we provide experimental evidence that mildly acidic conditions resembling those of late endosomal and lysosomal vesicles are sufficient to dissociate rPrP23-232 fibrils laterally and axially. The dissociation is believed to involve charge

repulsion of protonated His residues in the N-terminal domain. The protofilaments thus formed retain amyloid characteristics and are competent seeds for propagating new prions. Thus, late endocytic and lysosomal vesicles are sites of efficient prion propagation not only because they destabilize the α-monomer, but because they accelerate the dissociation of fibrils into protofilament seeds.

CHAPTER III:

EFFECT OF pH AND FIBRILLATION ON COPPER BINDING TO PRION PROTEIN

I. Introduction

Although the precise physiological functions of PrP^C is still unknown, it is clear that PrP^C binds several divalent cations *in vivo*, with high affinity for Cu(II) [303, 304]. A large effort has been made to characterize the structural features of the copper centers in PrP and to understand the physiological and pathological relevance of copper binding to PrP. Several copper-related functions have been suggested for PrP^C, including superoxide dismutase (SOD)-like activity [305], anti-oxidation [306], copper sequestration [307] and copper-induced PrP^C internalization [115, 308]. In addition, a substantial and somewhat confusing body of literature describes the role of copper in the prion diseases, although no consensus has been achieved [295, 309]. Below, we first review the literature on the coordination structures and affinity of copper binding to PrP. The physiological and pathological implications of PrP-copper interactions will be discussed afterwards.

A. Copper binding in the octarepeat region

Two primary copper binding sites have been identified [310], the four octarepeat regions (OR) found in the N-terminal domain [307] and the fifth binding site located within residues 91-111 [307, 311]. It is well accepted that the octarepeat region is the major copper binding site [307]. There have been some rather controversial studies that indicate the existence of other binding sites, including some in the C-terminal domain [312, 313], and binding sites that are only observed under low pH conditions [312, 313]. Non-specific binding sites have also been detected at high copper

concentrations (> 10x protein) [312].

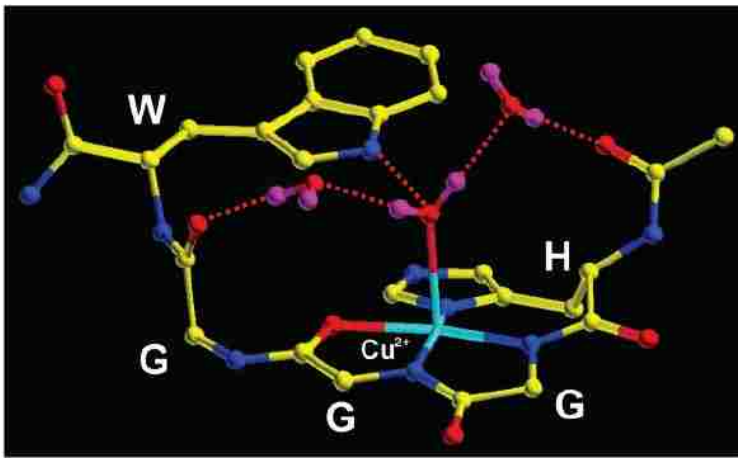

Figure 3-1. Structure of Cu(II) bound pentapeptide, HGGGW.

Structure of component 1, in which the copper ion is coordinated with an equatorial binding mode of 3N1O (reproduced from reference [314], reprinted with permission from American Chemical Society, Copyright 2002).

The octarepeat region, which is composed of 4 (occasionally 5) tandem sequences of PHGGGWGQ (four repeats encompassing residues 60–91 in human and hamster PrP), has been extensively investigated [72]. The X-band EPR spectrum and crystal structure of the Cu(II)-bound HGGGW segment (pH 7.4) reveals that Cu(II) is equatorially coordinated with a 3N1O binding mode (3 nitrogens and 1 oxygen serve as ligands to the metal ion), involving the imidazole N_{δ}, 2 deprotonated backbone amide nitrogens from adjacent glycine residues, and the oxygen atom of the carbonyl group from the second glycine [314, 315]. In the crystal structure, a water molecule is axially ligated at a longer distance via its oxygen atom. This water bridges the copper ion and the indole nitrogen of the tryptophan residue [314, 315] (**Figure 3-1**). However, molecular dynamics (MD) simulations and theoretical calculations suggest that this axially coordinated water is not incorporated into the coordination sphere and

can be easily removed at room temperature [316-318].

Further research showed that coordination is influenced by copper load [319, 320]. Component 3 is the main species observed only at low copper occupancy (< 1 equivalent). This component displays 3N1O or 4N modes that involve one Cu(II) binding to nitrogens that come from His residues of multiple ORs [321-323]. It is worthwhile to note that this coordination cannot rule out the possibility that His residues may come from more than one PrP monomer, especially in the fibrillar form when monomer subunits are in close proximity. The previously characterized 3N1O arrangement, which is termed component 1, dominates at high copper occupancy (≥ 2 equivalents of Cu(II). Component 2 is present at intermediate occupancy and has a 2N2O coordination mode, which involves the imidazole N_{δ} and one amide nitrogen of the histidine residue [319, 323] (**Figure 3-2A**). Switching from component 3 to component 1 requires structural rearrangements of the N-terminal region, which may serve specific biological functions [324].

The redox properties of these components have been investigated by several groups, whose work yields contradictory results. One working hypothesis is that component 3 is redox active, whereas component 1 is not, and its formation effectively quenches the redox cycling activity of Cu(II) [325]. Studies on a synthetic peptide containing four ORs demonstrate that component 3 has the ability to reduce Cu(II) to Cu(I) at both pH 7.4 and 6.4 [326, 327]. This hypothesis has been disputed on the grounds that the redox potential of the Cu(II)-component 3/Cu(I)-component 3 couple is higher than that of O_2/H_2O_2 couple, which makes redox cycling on

component 3 impossible [328]. Instead, these researchers propose that component 1 leads to the generation of H_2O_2 (sub-μM level) in the presence of O_2 and ascorbic acid [328]. However, voltammetric data show that copper might dissociate from the component 1 site as a consequence of Cu(II) reduction [329]. These findings suggest that additional studies on the redox behavior of copper bound PrP are needed, which would help elucidate the possible functions of PrP^C.

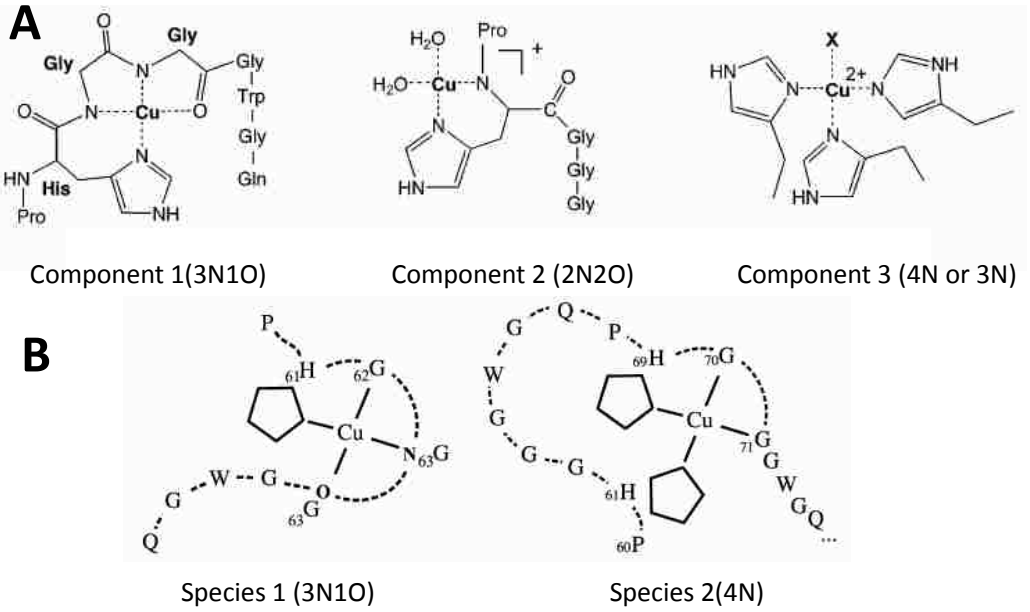

Figure 3-2. Models of the coordination modes of Cu(II) binding to the octarepeats region.

(A) Coordination modes of copper binding to octarepeats peptides proposed by Millhauser's group. Component 1, observed at ≥ 2 equivalents of Cu(II); component 2, between 1 and 2 equivalents of Cu(II); and component 3, at ≤ 1 equivalents of Cu(II) (reproduced from reference [319], reprinted with permission from American Chemical Society, Copyright 2005). (B) Coordination modes of copper binding to octarepeats in full-length protein proposed by Parak's group (reproduced from reference [330], reprinted with permission from Elsevier Limited, Copyright 2007).

Work on full-length rPrP23-232 α-monomer using a suite of EPR techniques along with EXAFS (extended X-ray absorption fine spectroscopy) only partially agrees with the coordination modes of copper complexes in OR peptides discussed

above. The coordination mode observed at low copper occupancy, called species 2, displays a 4N configuration involving two imidazole nitrogens and two glycine amide nitrogens (**Figure 3-2B**) [330, 331]. This structure is different from that of component 3, although the all-nitrogen atom ligation of copper is similar. At higher copper concentrations, the coordination of species 1 was detected, which is identical to that of component 1. This disparity may reflect the presence of the C-terminal domain on copper binding in the octarepeat region, or different experimental conditions, or both. Component 2 was not detected.

B. Copper binding at the fifth binding site

The fifth binding site that follows the OR region has been reported to include His96 and His111 residues. Unlike the ORs, the fifth binding site region is part of the proteinase K-resistant core of PrP^{Sc} [4]. The His111 residue is also located in the so-called HD domain, which has a high propensity to form β-sheets [81] and amyloid fibrils [82, 83] *in vitro.* PrP92-96 (GGGTH in hamster) and PrP106-113 (KTNMKHMA in hamster) have each been identified as the minimal sequence required for copper binding [332]. Although His96 is more favored as the key copper ligand in some studies [320, 333], other groups suggest His111 to be the most important residue involved in copper binding [334, 335]. This discrepancy might reflect differences in experimental conditions, as temperature-dependent differences have been observed between room temperature NMR and low-temperature EPR. Using peptides that encompass various parts of the fifth binding site region, Berti et al showed that at room temperature, Met112 stabilizes the Cu(II)-complex at

His111 through hydrophobic shielding, which makes His111 the preferred nitrogen ligand over His96 [332]. However, at liquid nitrogen temperature, binding at His96 was preferred. Others report that copper coordination to His96 or His111 depends on the sequence of the neighboring residues, and thus is different across species [311]. His111 has the highest affinity in human whereas His96 is the preferred ligand in chicken PrP. On the other hand, it has also been reported that both His residues bind to Cu(II) with similar affinity [310].

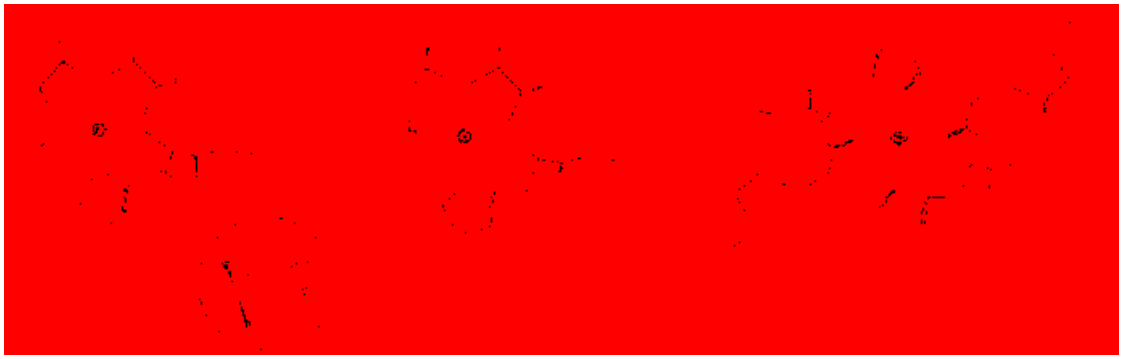

Figure 3-3. Models of the coordination modes of Cu(II) binding to the fifth binding site.

Coordination modes of Cu(II) binding to His96 and/or His111 proposed by Viles's group. Complex 1, observed at pH 9; complex 2, at pH 6.5; and complex 3, at pH 5.5 (reproduced from reference [335], reprinted with permission from the Biochemical Society, Copyright 2007).

Copper coordination modes of the fifth binding site have also been studied as a function of pH by the Viles group [335, 336]. At pH 6.5, copper is coordinated with a 3N1O equatorial coordination mode. Increasing the pH shifts the coordination to a 4N complex with a pK_a of 7.5 [337]. This implies that at cellular physiological pH, the coordination environment around these binding sites is a mixture of two species [336, 337]. The sulfur atom of Met109 may also serve a weak axial ligand, which favors

coordination of Cu(II) at His111, especially for the 3N1O coordination mode [337]. Lowering pH to 5.5 and/or substoichiometric amounts of Cu(II) could convert this site to a 2N2O coordination mode involving both histidine side chains [335, 336] (**Figure 3-3**). Recent studies indicated that at pH 5.5, histidine residues within and outside the octarepeats region have a preference to form inter-site macrochelate structures containing multiple His residues with the highest affinity among all copper coordination modes [338-340]. Copper binding to His96 and/or His111 is difficult to identify in peptide or protein samples that contain the OR region, since any signal from the fifth binding site is obscured by those from the ORs [330, 331, 341].

Redox studies on peptides of the fifth binding site demonstrate a quasi-reversible Cu(II)/Cu(I) redox reaction at the copper center with His111 as ligand. Copper-bound peptide containing His111 produces superoxide radical in the presence of ascorbate and oxygen [342]. The authors suggest this to be a possible neurotoxic mechanism. At His96, switching the coordination mode from 3N1O to 4N by raising the pH is accompanied by a structural rearrangement that brings Trp99 into the vicinity of the copper ion. This makes it easier to oxidize Trp99 to produce a highly reactive Trp radical species [336].

C. The affinity of PrP for Cu(II)

The precise affinity of PrP for Cu(II) has been hotly contested. There has been considerable variability in reported affinity of the octarepeat region for copper, ranging from micromolar to femtomolar [343-345]. Studies by Millhauser's group have placed the affinity of each coordination mode for copper into the more

biologically plausible nano- to micro- molar range, with evidence for negative cooperativity [319, 320, 346]. Positive cooperativity has also been claimed in earlier research using fluorescence and circular dichroism techniques [347]. It is important to consider differences in buffers, pH, and temperature when comparing the rather disparate results.

Using surface plasmon resonance (SPR) analysis, two groups demonstrated that the affinity of the fifth binding site for copper is in the mid-micromolar range [333, 334]. In contrast, Viles's group found that its affinity is in the nanomolar range and higher than that of octarepeats region [348]. Earlier results from Millhauser's group also pointed towards a sequential binding mechanism, in which the His96 residue is occupied prior to copper binding to the octarepeats [307]. The affinity of the fifth binding site for Cu(II) is dramatically influenced by the peptide fragment length [335]. Using isothermal titration calorimetry and cyclic voltammetry, Brown's group reported extensive cooperativity between different binding sites [349]. While they found that both octarepeats region and the fifth binding site have sub-nanomolar affinity for Cu(II), they suggest that the first binding event occurs within the octarepeat region [349]. A micromolar binding affinity has also been reported for the C-terminal domain [312, 313], but these data were not reproducible [310].

It is important to emphasize that copper binding to PrP is significantly influenced by the experimental conditions. The investigation techniques used and mathematical models chosen may also lead to deviation in the results. Thus, one has to be very cautious when comparing different experimental results. Furthermore, as mentioned

earlier, most data regarding copper binding to PrP come from peptide experiments, which may not wholly recapitulate the behavior of the real protein. Interactions between different domains or binding sites in the protein may also complicate the results [350].

D. Physiological significance and pathological implications of PrP-Cu(II) interaction

Initially it was thought that PrP^C itself is not a major component of the copper trafficking system [350] since PrP^C knockout ($PrP^{C\,-/-}$) mice are basically healthy as compared with wild type animals [125]. This is further supported by a study that showed only minimal difference in the brain copper content between wild type mice and $PrP^{C\,-/-}$ mice [351]. However, growing evidence suggests that PrP^C is involved in maintaining copper homeostasis [320, 352, 353]. One recent study found that the level of PrP^C *in vivo* is closely related with other proteins associated with copper uptake, storage and export from the cell [354]. Thus, it is plausible that other proteins of the copper trafficking system compensated for the loss of PrP in the earlier knockout experiments.

The role of copper in PrP^C internalization is supported by the observation that exposure to high Cu(II) concentrations (> 250 μM) stimulates endocytosis of PrP^C [355]. Surprisingly, studies at physiological concentrations of Cu(II) lead to the conclusion that PrP^C does not participate in the uptake of extracellular Cu(II) [356]. Conflicting results have been reported regarding copper-induced PrP^C internalization at physiological levels of Cu(II) (8 μM in blood plasma and 15 μM at the synapse)

[357], leaving the matter unsettled. It has recently been suggested that PrP^C may act as a copper transporter in the synaptic cleft, where peak copper concentrations reach 100-300 μM during neuronal depolarization [358]. Thus, PrP^C may thus be part of a mechanism to facilitate transferring Cu(II) back into the intracellular space after neuronal signaling, delivering copper to the intracellular copper transportation system [320].

The ability of PrP-bound Cu(II) to undergo redox cycling [359] has invoked the proposal that PrP^C may possess superoxide dismutase (SOD)-like activity [305]. The picture is further colored by the reduction of SOD activity by 10 - 50 % in PrP knockout mice as compared with wild type [360]. However, the original observation of SOD-like activity was measured in vitro using physiologically irrelevant copper concentrations (in the presence of 5 mM of $CuSO_4$) [305, 350]. The SOD hypothesis is further challenged by the failure to detect any SOD-like activity both *in vivo* and *in vitro* using more robust methods [361-363]. An alternative hypothesis is that PrP^C may protect cells from copper-induced oxidative stress by functioning as a sacrificial antioxidant of free radical superoxide generated by redox-active Cu(II) [364, 365].

The role of copper binding in the conversion of PrP^C to PrP^{Sc} and in the pathogenesis of prion diseases has also been controversial [366]. It has been shown that copper chelation delays the onset of prion disease in scrapie infected mice [367]. In contrast, a significant delay in prion disease onset was also observed in scrapie-infected hamsters treated with copper [368]. *In vitro,* copper seems to promote self-association of PrP^C and acquisition of protease K resistance [309, 369], but other

studies show that copper inhibits fibril formation [295]. These contradictory results suggest a complex relationship between copper and PrP conversion [370]. It has been suggested that the effect of copper on conversion may depend on PrP conformation [295]; while copper prevents conversion of rPrP 23-230 α-monomer to amyloid fibrils, it also stabilizes preformed amyloid fibrils.

E. Techniques to elucidate PrP-Cu(II) interactions

Different techniques have been used to elucidate the interactions between PrP and Cu(II) ions, including fluorescence spectroscopy, circular dichroism spectroscopy (CD), mass spectrometry, isothermal titration calorimeter (ITC), and electron paramagnetic resonance spectroscopy (EPR). Two major techniques employed in this dissertation, ITC and EPR, are described in detail below.

Modern ITC instruments operate on the heat compensation principle [371]. They measure the amount of power necessary to maintain the temperature equilibrium between a reference and sample cell as a function of time. The binding of copper to PrP is measured in a titration experiment, with copper being added to the protein solution in small aliquots. The results are displayed in the form of a titration isotherm (**Figure 3-4**).

Curve-fitting of the resultant isotherm to an appropriate binding model provides the stoichiometry (n), binding constant (K_a), and change in enthalpy (ΔH°). The dissociation constant (K_d) may be calculated as the reciprocal of K_a. The change in entropy (ΔS) is calculated using ΔG = -RT*ln K_a and ΔS = (ΔH - ΔG) /T. The curve fitting function of the ITC software (Origin 7.0, OriginLab) provides one set of

binding sites model to analyze any number (n) of identical sites; and two sets of binding sites model to analyze two independent sites (any number of each site) with distinct thermodynamic properties. A sequential binding mode is also provided to examine the interaction between multiple non-identical sites, assuming the binding of a ligand to one site will be affected by previous binding events, as long as the thermodynamic difference between bindings at individual sites is sufficiently large.

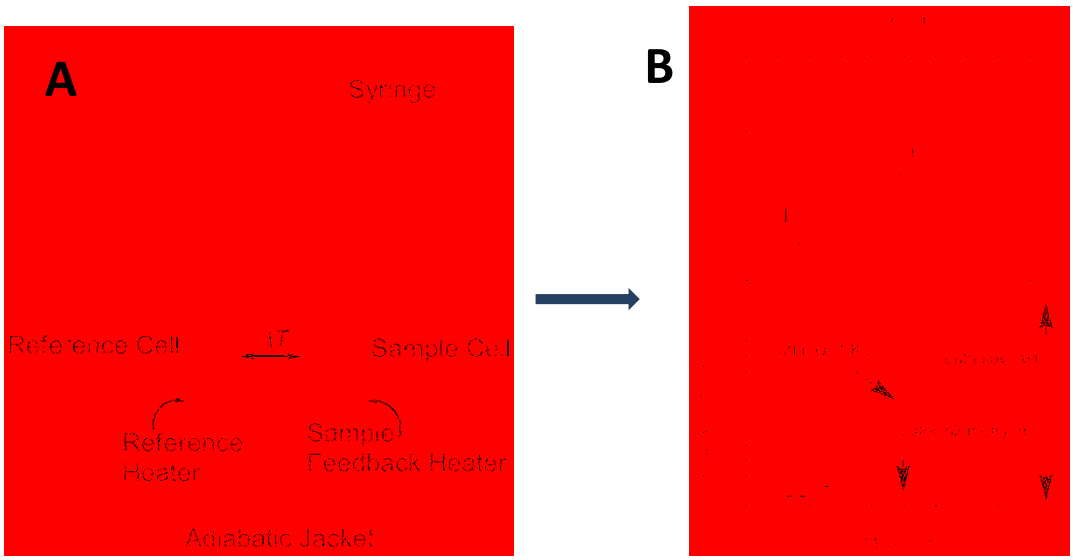

Figure 3-4. Schematic diagram of an ITC instrument.

(A) In a typical ITC instrument, the sample cell and the reference cell are kept at same temperature and housed in an adiabatic jacket. A small constant power (reference power) is applied to the reference cell throughout the ITC experiment, which sets the approximate value of the baseline when the system is fully equilibrated. During a titration, the heat change associated with binding between the ligand and macromolecules results in a temperature change in the sample cell. The temperature difference between the reference and sample cells (ΔT) is detected by a thermopile/thermocouple detector. Consequently, the feedback heater will change the power applied to the sample cell accordingly to reestablish temperature equilibrium between the reference and sample cells. (B) The time integral of differential power (DP, µcal/sec) between the reference and sample cell yields a measurement of thermal energy of the binding reaction, ΔH [372, 373].

EPR is a technique used to study atoms with unpaired electrons. Cu(II) has the

electronic configuration of $4s^0 3d^9$ and is a spin quantum number I = 3/2 system, and is thus EPR-active. Although the EPR signals of copper proteins do not provide detailed structural information at the resolution level provided by X-ray crystallography, much information can be gleaned regarding the nature of the metal ligands (N, O, or S are most common) and their coordination geometries [374].

When an unpaired electron is placed in an external magnetic field B_0, the interaction between the electron spin moment and the magnetic field splits the degeneracy of the electron spin states, creating two spin states ($M_s = \pm 1/2$) (**Figure 3-5A**). The energy difference between the two states is given by the equation

$$E = h\nu = g\beta_e H,$$

where *h* is Plank's constant, *v* is frequency of the spectrometer (for X-band EPR, this is about 9.5 GHz), *g* is a dimensionless g-factor that describes the intrinsic magnetic moment μ of the electron ($g = 2.0023$ for the free electron in space), β_e is the Bohr magneton, and *H* is the external magnetic field at which the resonance condition is satisfied [375]. Resonance absorption occurs when the frequency/radiation energy satisfies the equation. For reasons associated with instrument design, the EPR spectrum is conventionally presented as the first derivative of the absorption signal (**Figure 3-5B**).

Unlike a free electron, an atom possesses orbital angular momentum L in addition to the intrinsic spin angular momentum S. Thus, the g factor contains intrinsic structural information as it is affected by spin-orbit coupling. For some atoms like H, N, O, and C, the g-factor will be very close to that calculated for the free

electron in space, whereas for others, particularly metal ions, the g-factor may differ significantly. Additionally, since the orbitals of a molecule often exhibit directional dependence (anisotropic), the g-factor may also be anisotropic since it arises from spin-orbit coupling.

For every molecule with an unpaired electron, a unique axis system may be defined using the terms g_x, g_y, and g_z. The g-factor EPR signal will be "split" along these axes. For some atoms, the three principle g-factors are similar and thus the signal is isotropic ($g_x = g_y = g_z$). For others, each g-factor is discernible from the others (($g_x \neq g_y \neq g_z$, called rhombic). In others, only one g-factor will be different. This last situation is termed an axial signal ($g_x = g_y \neq g_z$) and by convention, the g-factor that is different is called $g_{\parallel}$ (g-parallel) and the two that are similar (g_x and g_y,) are collectively known as $g_{\perp}$ (g-perpendicular). Biologically relevant Cu(II) complexes are typically axial systems.

The magnetic field experienced by the unpaired electron is also affected by its nucleus, if the atom has a non-zero spin quantum number, I. In this case, the spin of the nucleus can cause the absorption band to be split into a specific number of hyperfine peaks, where the number of hyperfines = 2I +1. This is termed hyperfine coupling and is called A. In anisotropic systems, hyperfine splitting (A-value) may only be observed for one or two of the directional g-factors. The magnitude of the A-value is related to the environment and coordination geometry of the atom containing the unpaired electron. In the case of Cu(II), which has a d^9 electron configuration with a single unpaired electron, the interaction between the electron

spin and the nuclear spin gives rise to four features of nuclear hyperfine splitting since the spin quantum number (I) of Cu(II) is 3/2 (**Figure 3-5C**). The parallel region ($g_{\parallel}$ and $A_{\parallel}$) is particularly informative regarding the coordination number, geometry, and identity of the copper ligands.

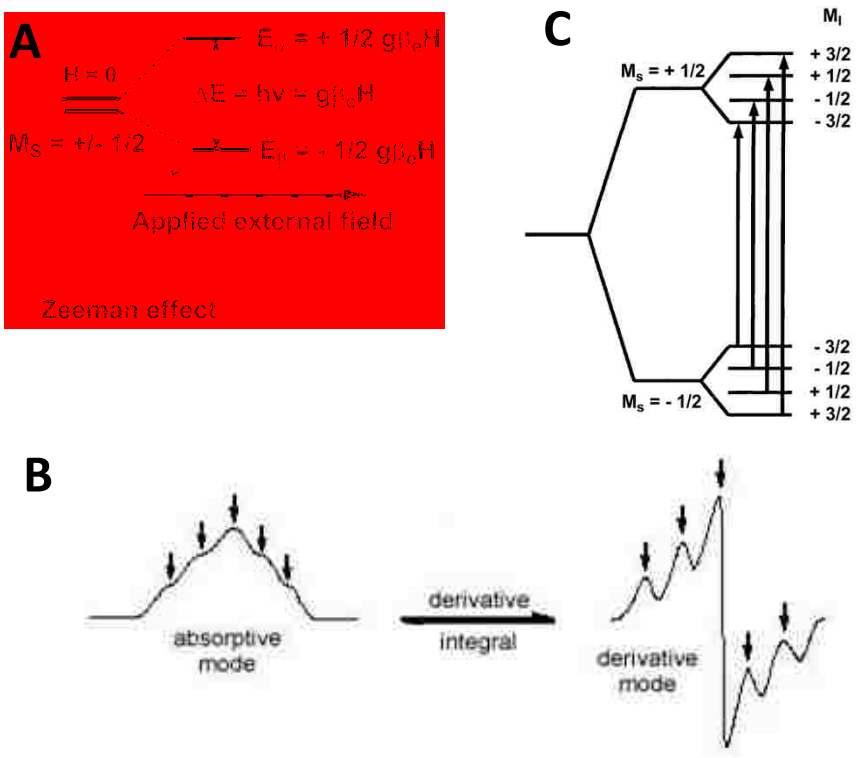

Figure 3-5. Schematic diagram of EPR theory.

(A) The schematic diagram of energy level for the simplest system (free electron) as a function of applied external magnetic field. The energy difference between two spin states is shown. (B) Examples of absorption and first derivative EPR spectra. (C) The schematic diagram of energy level of Cu(II) systems (S = 1/2 and I = 3/2). The arrows indicate allowed transitions with the selection rules of $\Delta M_S = \pm 1$ and $\Delta M_I = 0$.

Nearby nuclei with non-zero spin quantum numbers, which include nitrogen ligands to copper, may also further split the signal. Since these nuclei are further away from the unpaired electron, their effect, termed superhyperfine splitting, is normally smaller than hyperfine splitting. The number of superhyperfine peaks also follows the

2I+1 rule. Note that the true formula is actually 2(N)*I + 1, where N = the number of equivalent nuclei with non-zero spin.

The g-factors and A-values of structurally well-defined copper complexes and copper proteins have been measured and tabulated. Their distribution on what is known as the Peisach-Blumberg Plot provides assignments of ligands for unknown complexes [374](**Figure 3-6**). However, it is important to keep in mind that due to the dependence of $g_{\parallel}$ and $A_{\parallel}$ on the net charges of the overall complex, the Peisach-Blumberg plot alone only serves a rough guideline for coordination sphere assignment.

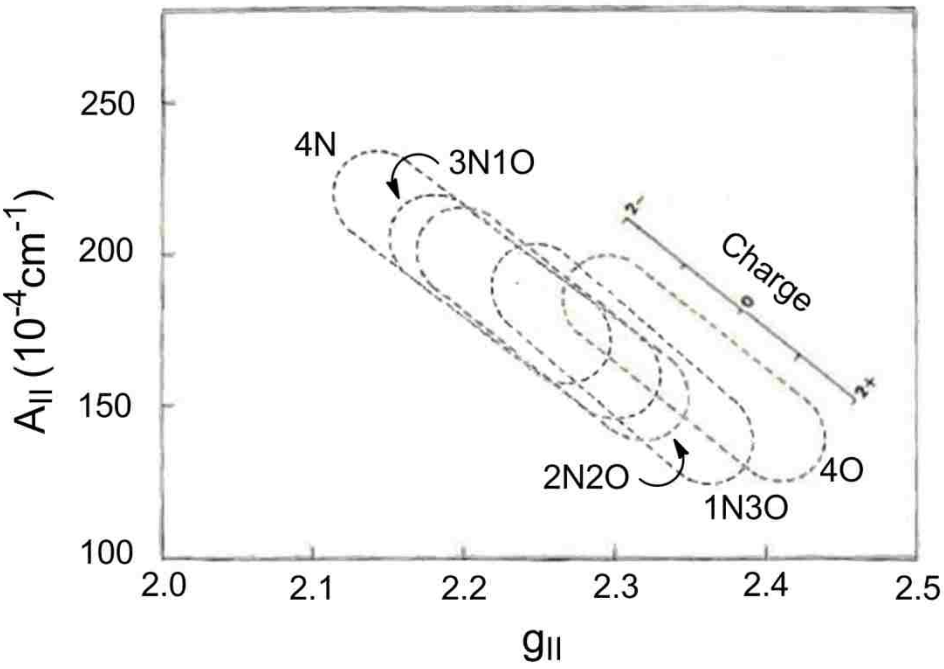

Figure 3-6. Original Peisach-Blumberg Plot of type II Cu(II) complexes [374].

Data obtained from copper complexes with sulfur ligands have been added and the data tabulated (see Table 5-1 in Chapter V).

F. Rationale and Aims

The ambiguities in copper coordination discussed above highlights the need for a

thorough analysis of copper-prion interactions, so a comprehensive understanding of the role of copper in prion diseases can be achieved. In contrast to PrP^{C}, much less attention has been devoted to understanding the interaction between PrP^{Sc} and copper, which may be more pathologically relevant. All important putative copper binding sites, including the fifth binding site, are located in the unstructured N-terminal domain of PrP^{C}. However, whether these binding sites adopt different coordination modes in PrP^{Sc} is still unknown; nor do we know whether the N-terminal domain remains unstructured after amyloidosis. Although the octarepeats region are not part of the β-sheet core of the most widely accepted theoretical and experimental models [170, 171, 177, 187] proposed for PrP^{Sc} to date, the region where the fifth binding site is located plays a pivotal role in misfolding [376] and appears to be highly protected in authentic PrP^{Sc} [187]. Given our results regarding the effects of charge in the N-terminal domain in influencing the fibril to protofilament dissociation, it is important to consider the effects of copper binding on this domain. Therefore, comparative analyses of copper-prion interactions in rPrP α-monomer and fibrils, serving as substitutes for PrP^{C} and PrP^{Sc}, respectively, will be useful to elucidating the role of copper in modulating the conversion of PrP^{C} to PrP^{Sc} and its contribution to prion diseases.

The first aim of this research is to determine the copper binding affinity for different PrP conformers. This goal is achieved using ITC, from which the reaction stoichiometry, association equilibrium constants, and change in enthalpies can be fully quantified. The second aim is to examine the coordination mode(s) of Cu(II) in PrP

conformers. This goal is approached using EPR. This methodology is complementary to ITC and provides insight into the Cu(II)-PrP coordination geometries and the identity of the coordinating ligands. Completion of these aims provides a deeper understanding of copper binding to rPrP fibrils. Additionally, by comparing thermodynamic and EPR parameters obtained for different conformers, uncertainty about whether conversion from PrP^{C} to PrP^{Sc} will alter copper binding properties can be addressed. Our results demonstrate that His96 is the most important copper ligand in the fifth binding site, and His111 is not required. As expected, we confirm that copper binding to both the octarepeat region and the fifth binding site is highly pH-dependent. The major finding of the present research is that the types of coordination structures of Cu(II)-PrP complexes are largely similar between α-monomer and fibrils. However, the ratios of the different coordination modes have changed in the fibril. This finding might help to elucidate the pathogenesis of prion diseases.

II. Experimental procedures

A. Protein expression and purification

A detailed description of the experimental procedures used to express and purify recombinant hamster PrP23-232 and PrP90-232 is provided in Chapter II.

B. Mutagenesis

Mutations of the histidine residues in the putative binding site of rPrP90-232,

H96A and H111A, were prepared from the template plasmid pET24PrP90 expressing wild-type rPrP90-232 via site-directed mutagenesis using a QuikChange kit (Stratagene). Small-scale plasmid purification was performed with a QIAprep miniprep kit (Qiagen) using standard protocols. The sequences of the mutations were verified and then the plasmids were transformed into BL21 (DE3)-Rosetta cells (Novagen) for large-scale expression. Mutagenesis was confirmed by DNA sequencing at the Murdock Sequencing Facility (University of Montana, Missoula, MT).

The following oligonucleotide primers were used: H96A, 5'-GGT CAA GGA GGT GGC ACC GCT AAT CAG TGG AAC AAG CCC-3' for the forward primer and 5'-GGG CTT GTT CCA CTG ATT AGC GGT GCC ACC TCC TTG ACC-3'for the reverse primer; H111A, 5'-CCA AAA ACC AAC ATG AAG GCC ATG GCC GGC GCT GCT GCG-3' for the forward primer and 5'-CGC AGC AGC GCC GGC CAT GGC CTT CAT GTT GGT TTT TGG-3' for the reverse primer.

C. Preparation of recombinant PrP conformers

A detailed description of the experimental procedures used to prepare the α-helical forms (α-monomer) and fibrillar forms is provided in Chapter II. The secondary structure of the α-monomer was confirmed using CD. Fibrils were confirmed using the ThT fluorescence assay and TEM imaging [251].

D. Asymmetric flow field-flow fractionation (AF4)

A detailed description of the experimental procedures employed to characterize

the size of PrP conformers using AF4 is provided in Chapter II.

E. Circular dichroism (CD)

The protocol of CD experiments is detailed in Chapter II.

F. Isothermal titration calorimeter (ITC)

In this study, all ITC measurements were carried out at 25 °C on a VP-ITC microcalorimeter (MicroCal). Both copper and protein solutions were prepared in the same buffer (from the same flask) and the pH of the metal solution was matched to within 0.05 pH units of the protein solution prior to the titration. These procedures minimized any heat changes from possible mismatches in salt or hydronium ion concentrations. All samples used in the experiments, except the fibrillar form, were passed through 0.22 μm regenerated cellulose membrane syringe filter (Corning) to remove small aggregates. All solutions were thoroughly degassed before the titrations were performed.

In a typical ITC experiment, ten microliters of 3 mM buffered copper sulfate solution were delivered over 10 s into the sample cell, which was filled with ~ 1.4 ml of buffered PrP solution at a concentration of 50 μM. The sample cell was stirred constantly at 300 rpm by the syringe to maintain homogeneous mixing and keep the mechanical noise to a minimum. A total of 25 injections were performed to ensure that all the binding sites had been saturated. To account for diffusion of the solutions during the insertion of the syringe a small (2 μL) aliquot was delivered at the beginning of the experiment and the first data point was then deleted from data

analysis. Each injection was followed by a 5 min period to allow the reference power baseline to be re-established before the next injection. Titration of the copper sulfate solution into a protein-free buffer was recorded as a baseline, and then subtracted from each experimental titration to correct for the effect of any heat of dilution or metal/buffer reaction. After subtraction of this blank, the binding isotherm was then fitted with ITC software (Origin 7.0 OriginLab) using an appropriate binding model to yield the reaction stoichiometry, association equilibrium constants, change in enthalpies, and change in entropies as described in the previous paragraph.

G. Electron paramagnetic resonance (EPR)

The continuous wave (cw) X-band EPR spectra were collected on a Bruker EMX, X-band spectrometer at Montana State University. The following conditions were used: microwave frequency, ~9.3 GHz; microwave power, 0.3-0.7 mW, modulation amplitude, 10 G; and modulation frequency, 100 kHz. EPR spectra were recorded at 77 K using a finger quartz Dewar with liquid nitrogen.

EPR experiments were carried out in either 20 mM 2-(N-morpholino) ethanesulfonic acid (MES), pH 5.5 or 20 mM piperazine-N,N'-bis(2-ethanesulfonic acid) (PIPES), pH 7.0 to evaluate the effect of pH on the coordination modes of copper in Cu(II)-PrP complexes. Buffer solutions mixed with free Cu(II) (up to 1 mM $CuCl_2$) did not show any significant copper signals; and copper ions bridged by chloride ions are EPR silent due to coupling between copper centers [315]. All samples for EPR experiments were prepared with $^{63}CuCl_2$ (98.9%, Cambridge Isotope Laboratories). The ^{63}Cu isotope was used to avoid inhomogeneous broadening of the

EPR lines caused by the mixture of naturally occurring isotopes ^{63}Cu and ^{65}Cu. The stock $^{63}CuCl_2$ solution was adjusted to pH ~ 4 with concentrated sodium hydroxide.

Double integrations of EPR spectra were calculated and normalized to a standard protein concentration to quantify the amount of spin-active Cu(II) incorporated into the PrP conformers. The EPR signals were calibrated by comparing their signal intensities to a standard solution of $Cu(EDTA)_2$ made by mixing 100 μM $CuCl_2$ with 10 mM ethylenediaminetetraacetic acid (EDTA) at pH 8.0. Unbound Cu(II) in the form of copper hydroxide gives a broad signal of very small amplitude near the $g_\perp$ region and makes negligible contributions to the integration. The coordination configurations were derived from Peisach and Blumberg analysis using $g_\parallel$ and $A_\parallel$ directly measured from EPR spectra [374]. The cw X-band EPR spectra of type II Cu(II)-protein complexes show distinctive features with $g_\parallel > g_\perp > 2.0023$ and a hyperfine splitting of $g_\parallel$ into the expected four features with $A_\parallel$ being in the range of ~ 450–750 MHz and $A_\perp < 100$ MHz [377]. The $M_I = +3/2$ line of the parallel region overlaps with the perpendicular region, which makes it difficult to directly determine $g_\perp$ and $A_\perp$ at this frequency.

EPR spectral simulations were carried out using the EasySpin program [378]. The spin Hamiltonian of the system can be written as:

$$\widehat{H} = \beta_e \hat{S} g B + A \hat{S} \hat{I}$$

where the terms describe the electronic Zeeman interaction and the interaction between the electron spin and nuclear spins that include ^{63}Cu (the hyperfine interaction) as well as ^{14}N (the superhyperfine interaction). β_e is the Bohr magneton,

B is the external magnetic field at which the resonance condition is satisfied, g is the dimensionless electron g-factor, and A is the hyperfine coupling/splitting constant. S and I are the operators for electron and nuclear spins, respectively.

III. Results

A. Copper binding to the fifth binding site at neutral pH

The characteristics of copper binding to the fifth binding site at pH 7.0 were investigated by ITC and EPR using rPrP90-232 conformers. The stoichiometry and affinity of the binding were determined by ITC at 25 °C in 0.1 M Tris-Cl, pH 7.5, to prevent the precipitation of cupric hydroxide (K_{sp} = 2.20 x 10^{-20} M^3) [379]. It is known that under these conditions a single Cu(II) ion is complexed by 4 Tris molecules in the form of Cu(II)$(Tris)_4$, which has a log stability constant ($log\beta_4$) of 14.1 [380].

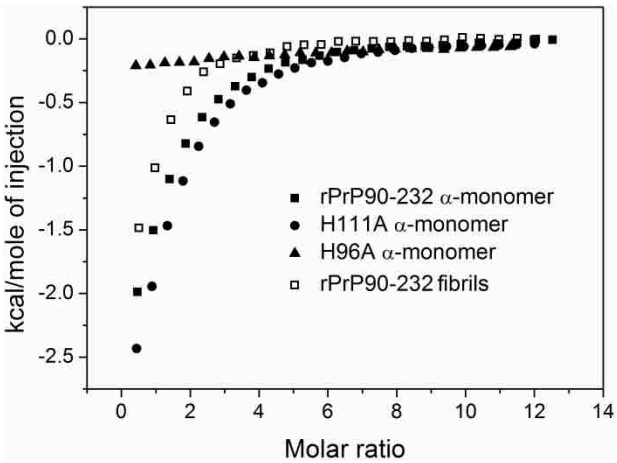

Figure 3-7. ITC isotherms for copper binding to rPrP90-232 conformers and mutants.

Recombinant PrP90-232 α-monomer (■), 46 μM; H111A α-monomer (●), 48 μM; H96A α-monomer (▲), 51 μM; and rPrP90-232 fibrils (□), 46 μM. Parameters for fitting the isotherms to the model of one set of binding sites are given in **Table 3-1**.

The titration isotherm of rPrP90-232 α-monomer by $Cu(Tris)_4^{2+}$ complex is shown in **Figure 3-7**. Fitting these data to a model with a single type (set) of binding site provided a stoichiometry (n) of 1.02. The pH-dependent apparent binding constant (K_a) was determined to be 2.18×10^4 M^{-1}, which translates to a K_d of 45 μM, and the change in enthalpy (ΔH) was -4.4 kcal/mol (**Table 3-1**). This is in line with SPR results [333, 334]. The reliability of the fitting was evident by the small standard deviation (3%) and χ^2 values. The fifth binding site includes 2 histidine residues, His96 and His111, thus the titration isotherm was also fitted with a model that contains two sets of binding sites, which assumes that the macromolecule has 2 groups of independent sites. The best fit to the isotherm revealed a stoichiometry of 2.8 and 0.8 respectively, but had such a large standard deviation (34%) that it was deemed an inappropriate model. Fitting the isotherm to the sequential binding sites model, which is most suitable for a system where the binding of a ligand to one site will be affected by previous binding events, was also attempted since intra-region cooperation between His96 and His111 was recently reported and resolved with sequential model [341, 381]. This fitting routine yielded a K_d of 47 μM and ΔH of -4.6 kcal/mol for one site and 2.2 mM and -0.89 kcal/mol for a second site. The parameters for the first site were very close to those obtained from the one site model, and those of the second site could be considered as non-specific binding with no biological significance due to the comparatively weak affinity. Overall, the results indicate that there is only one type of site in rPrP90-232 that is able to coordinate Cu(II), at room temperature in a Tris-buffered solution at pH 7.5.

To elucidate the contributions of His96 and His111 residues to the binding process and the resulting coordination site [311, 332-335], H96A and H11A mutants were constructed. The titration isotherm of Cu(II) binding to H111A was similar to that of wild-type (**Figure 3-7**), with a binding stoichiometry of 1.1 when fitted with the one set of binding sites model. The apparent dissociation constant and ΔH were 47 μM and -5.0 kcal/mol respectively, which are very close to wild-type protein. Unlike wild-type and H111A, the titration isotherm of H96A displayed no inflection points after subtraction of the buffer signal (**Figure 3-7)**. These data suggest that His96 is required to coordinate Cu(II), whereas His111 is not involved in binding or is insufficient. This conclusion is agreement with those observed using SPR [333].

Table 3-1. ITC parameters of Cu(II) binding to truncated rPrP90-232 conformers

	α-monomer			**H111A α-monomer**	**H96A α-monomer**	**Fibrils**
	1 set of sites	sequential model (N=2)		1 set of sites	1 set of sites	1 set of sites
N	1.02 ± 0.03			1.1 ± 0.02	n.d	0.84 ± 0.04
K_d (μM)	45 ± 1.5	47	2200	47 ± 0.9	n.d.	24 ± 1.6
ΔH(kcal/mol)	-4.4 ± 0.15	-4.6	-0.89	-5.0 ± 0.09	n.d.	-2.9 ± 0.16
ΔS(cal/mol-K)	4.96	4.42	15.1	2.94	n.d	11.4
χ^2	99	60.2		58	n.d.	171

n.d.: Not determined.

The effect of fibrillation on copper binding to the fifth binding site was examined using rPrP90-232 fibrils. The isotherm (**Figure 3-7)** was characterized by a steeper slope in the initial stage as compared with that of α-monomer, which suggests that the binding of Cu(II) is tighter in rPrP90-232 fibrils. This graphic interpretation was

supported by the regression analysis of the isotherm using the one set of sites model, which yielded a K_d of 24 μM. The stoichiometry (n) was 0.84. This value is lower than expected, and could be caused by an error in actual fibril concentration, as fibrils tend to adsorb to the glass surface of the loading syringe, which would reduce the actual fibril concentration in the sample cell. We also attempted to fit the data with the stoichiometry of reaction being fixed to 1, as rPrP90-232 α-monomer only possess one Cu(II) binding site at His96. This resulted in only minor changes, yielding a K_d of 19.3 ± 1. μM and ΔH of -2.4 ± 0.4 kcal/mol. However, the χ^2 value of this fit is much larger as compared with fitting when all parameters were free-floating (329 vs. 171). These data demonstrated that the fifth binding site binds only one Cu(II) in both α-monomer and fibril. However, fibrillation increased the affinity for Cu(II) 2-fold.

The copper coordination of the fifth binding site was then examined by EPR at 77K. There is a large temperature difference between the EPR and ITC experiments, but since ΔH is negative, we expect that the affinity for copper will increase as the temperature decreases. This will also be true for adventitious copper binding. Another condition worthy of note is the buffer system. The Tris system is not used for EPR, as the EPR signal from the $Cu(Tris)_4^{2+}$ complex will interfere with the analysis. Additionally, the pK_a of Tris is quite sensitive to temperature, increasing 0.03 pH units per °C decrease). Thus, non-coordinating Good's buffers were used for EPR. The EPR spectra of both rPrP90-232 conformers showed typical features for type II copper centers (**Figure 3-8**), indicative of a tetragonal Cu(II) center with a half-occupied d_{x2-y2} orbital [377]. Two distinct species were identified in the EPR

spectra for the rPrP90-232 α-monomer (**Figure 3-8A and C**) (**Table 3-2**). At 1 molar equivalent of Cu(II) and below, the spectra were dominated by the signal with $g_{\parallel}$ = 2.20, $g_{\perp}$ = 2.037, and $A_{\parallel}$ = 565 MHz (Spectrum 1). Continuously increasing the Cu(II) load to 1.5 molar equivalents and higher led to the emergence of another signal with $g_{\parallel}$ = 2.27, $g_{\perp}$ = 2.047, and $A_{\parallel}$ = 504 MHz (Spectrum 2). This is in agreement with previous studies [307]. The second signal continued to grow slowly, and both signals saturated when ~ 4-5 molar equivalents of Cu(II) had been added.

We also determined the amount of copper loaded into the protein as a function of the total copper added. This copper loading curve was determined from integration of the total EPR signal as compared with copper-EDTA standards, and indicated 2 molar equivalents of Cu(II) were bound per PrP (**Figure 3-8E**). The copper loading curve also showed that the spin intensity of the first signal increased almost linearly with added copper. These data suggests rPrP90-232 α-monomer has two copper binding sites at 77K. The first site takes up copper preferentially, which gives rise to the EPR signal observed at low copper loading. The second site binds copper much more weakly and only appears at high copper concentration, which corresponds to the EPR signal that appeared at high copper load. This conclusion is not in conflict with ITC data, which only identifies only one copper binding site at 298K (**Table 3-1**). As pointed out previously, the affinity of rPrP90-232 conformers for Cu(II) is expected to increase significantly at 77 K, which implies that weak binding events that cannot be detected by ITC at 25 °C will become discernible in low-temperature EPR experiments. Therefore, we tentatively assign the first EPR signal to the binding site

identified by ITC, i.e. His96, which binds Cu(II) in the micromolar range. The second EPR signal is assigned as adventitious binding, which has much lower affinity at room temperature.

The EPR spectra for rPrP90-232 fibrils also showed two signals that were basically the same as for the α-monomer (**Figure 3-8A and C, Table 3-2**). However, the two signals increased almost equally as a function of added Cu(II), which suggests they have similar affinities for copper. No saturation was observed for either of the signals as judged by EPR spectra and binding titration curve, indicating that the His96 5^{th} binding site has a decreased affinity for copper in fibrils than in the α-monomer. This is predicted from the smaller, less negative ΔH of copper binding to fibrils, assuming that the samples have at least partially equilibrated at the lower temperature used in EPR.

The magnetic parameters for the EPR spectra of both rPrP90-232 conformers are summarized in **Table 3-2**. According to the Peisach-Blumberg plot [374], the first binding site has at least 2 nitrogen ligands (2N2O) but could contain up to 4 nitrogen ligands (4N). The second binding site has at least 1 nitrogen ligand (1N3O) but could also contain up to 4 nitrogen ligands (4N). We note that a decrease in $A_{\parallel}$ is typically associated with the loss of a nitrogen ligand [320], indicating that the second binding site may have more oxygen ligands than the first site. The magnetic parameters for the first binding site are quite close to the reported His96 binding site in the α-monomer conformer of 3N1O configuration ($g_{\parallel}$ = 2.21, $A_{\parallel}$ = 588 MHz) [307]. For this site, Cu(II) was determined to be coordinated by the N_{δ} atom of the histidyl imidazole and

the remaining 2 nitrogens provided by deprotonated backbone amide groups. The oxygen is provided by a backbone carbonyl [307, 336]. This assignment is consistent with our previous conclusion based on ITC results that His96 is the major binding site. In hindsight, we should have measured the EPR spectrum of the H96A and H111A mutants in both α-monomeric and fibrillar conformers, to nail down the assignment of each signal. It would also be quite informative to measure the room temperature EPR spectra of the rPrP90-232 α-monomer and fibrils for a direct comparison with ITC data. However this approach might be impeded by the much lower affinities at room temperature (~40 μM).

Altogether, these data demonstrate that both rPrP90-232 conformers possess 2 copper binding sites. However, His96 is the only site with high affinity under physiologic conditions. Although adventitious binding of copper is not remarkable at room temperature, it might make a significant contribution to data collected at low temperature.

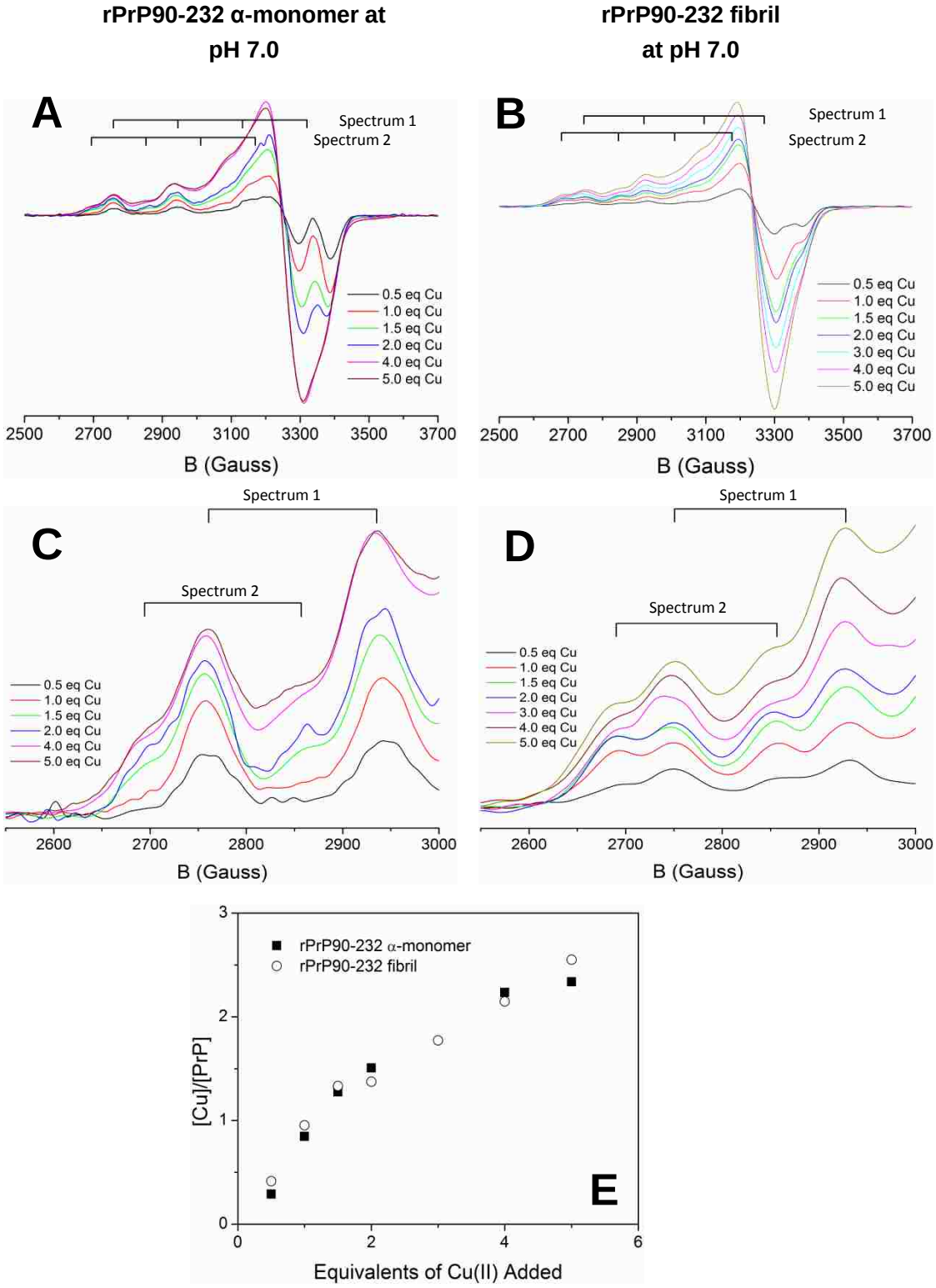

Figure 3-8. Titration of rPrP90-232 conformers with Cu(II) at pH 7.0.

Titration was performed with 145 μM of rPrP90-232 α-monomer and 107 μM of rPrP90-232 fibril in 20 mM PIPES, pH 7.0. (A) and (B) show the X-band of EPR spectra of the rPrP90-232 α-monomer and rPrP90-232 fibril

respectively. (C) and (D) The 2600-3000 Gauss region was enlarged to demonstrate the presence of two distinct Cu(II) complexes (E) Integrated EPR spin intensity vs. [$CuCl_2$] added.

B. Copper binding to the fifth binding site at pH 5.5

The fifth binding site contains protonatable histidine side chains (minimally His96), thus the Cu(II) coordination structure was further probed at pH 5.5 to examine the effect of pH on copper binding. The EPR data for copper binding to rPrP90-232 α-monomer indicates a single mode of binding at low copper concentrations. The EPR parameters of this binding mode are $g_{\parallel}$ = 2.29, $g_{\perp}$ = 2.067, and $A_{\parallel}$ = 479 MHz (spectrum 3). This signal continued to grow in as more copper was added. Additionally, another signal emerged with similar $g_{\perp}$ and $A_{\parallel}$ but a distinct $g_{\parallel}$ of 2.22 (Spectrum 4) (**Figure 3-9A and C**). These data suggest that rPrP90-232 α-monomer has two distinct copper binding sites of slightly different affinity at pH 5.5. The first site binds Cu(II) preferentially at low copper concentration, whereas the second site only binds Cu(II) at high copper concentration, which implies relatively low affinity for this site and might be a result of adventitious binding. The EPR spectra of rPrP90-232 fibril were dominated by a signal with $g_{\parallel}$ = 2.27, $g_{\perp}$ = 2.06, and $A_{\parallel}$ = 529 MHz (Spectrum 5) (**Figure 3-9B and D**). However, a close inspection of the signals showed asymmetry in the first three hyperfines, which indicates that there are really two signals/binding sites with only slightly different EPR magnetic parameters. Unlike that observed at pH 7.5, both rPrP90-232 conformers showed no sign of saturation at pH 5.5 even at 4 molar equivalents Cu(II) added (**Figure 3-9E**).

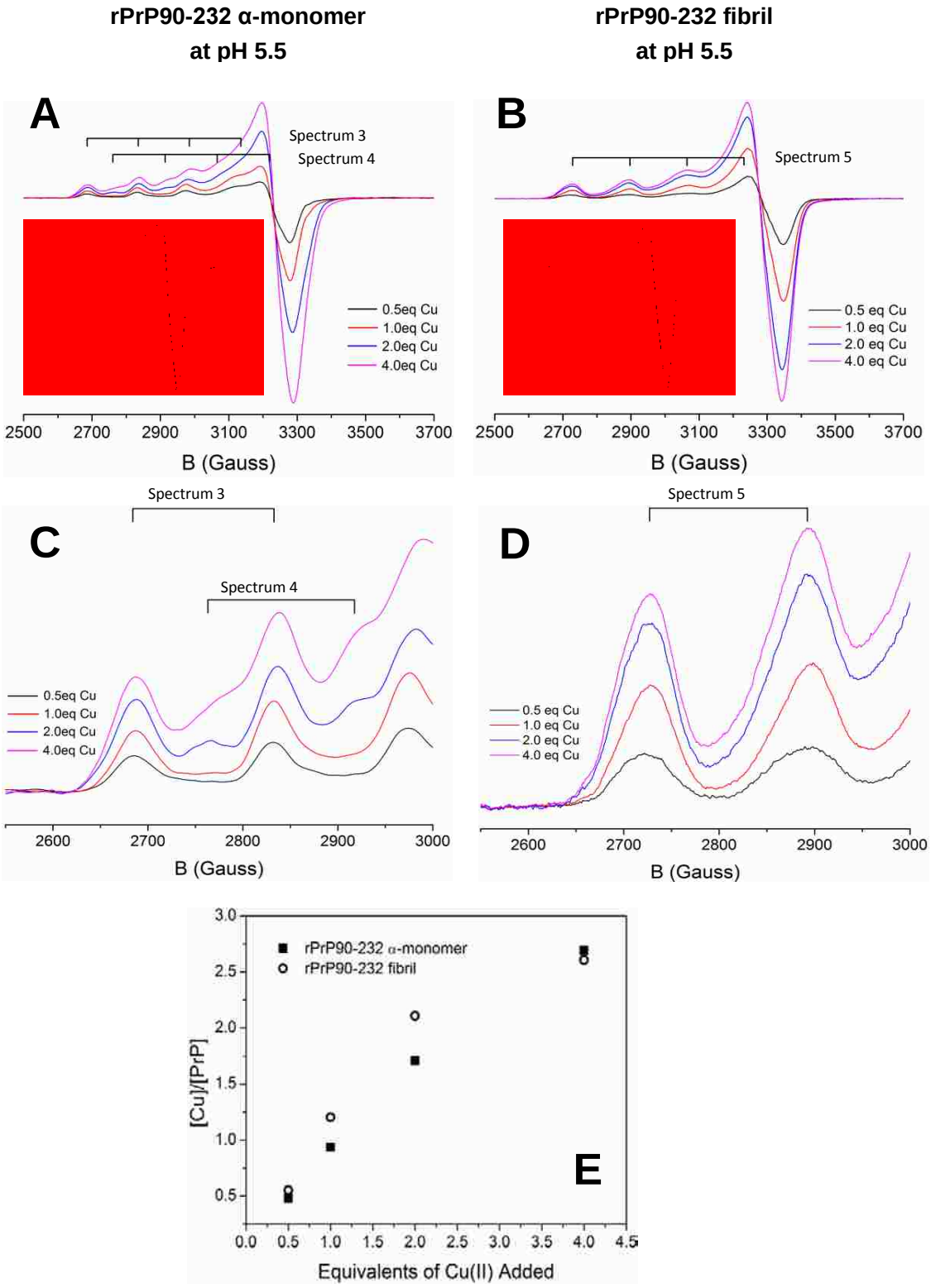

Figure 3-9. Titration of rPrP90-232 conformers with Cu(II) at pH 5.5.

Titration was performed with 190 μM of rPrP90-232 α-monomer and

377 μM of rPrP90-232 fibril in 20 mM MES, pH 5.5. (A) The X-band of EPR spectra of rPrP90-232 α-monomer collected at ~ 9.322 GHz. (B) The X-band of EPR spectra of rPrP90-232 fibril collected at ~ 9.465 GHz. The frequency difference accounts for the difference in the X-axis position of the spectra. Insets show the simulated spectra (dashed lines) of the EPR spectra at 1 molar equivalent of Cu(II) in **Figure 3-13**A and **Figure 3-13**B respectively. Magnetic parameters for these simulations are: $g_{\perp} = 2.061$, $g_{\parallel} = 2.294$, $A_{\perp} = 22.0$ MHz and $A_{\parallel} = 474.33$ MHz; $g_{\perp} = 2.056$, $g_{\parallel} = 2.276$, $A_{\perp} = 31.5$ MHz and $A_{\parallel} = 521.9$ MHz respectively. (C) and (D) The 2600-3000 Gauss region was enlarged in the inset to demonstrate the presence of multiple Cu(II) complexes at pH 5.5 as the Cu(II) concentration increases. (E) Integrated EPR spin intensity as a function of $CuCl_2$ added to the protein solution.

The magnetic parameters of these distinct species are summarized in **Table 3-2**. All copper centers in rPrP90-232 conformers observed at pH 5.5 satisfy 2-4 nitrogen coordination [374]. Since at pH 5.5, amide nitrogens will strongly prefer to be protonated and thus no longer able to coordinate Cu(II), the most plausible nitrogen donor is the imidazole nitrogen of His residues. One might expect a copper center with 2 histidine residues for all species observed in rPrP90-232 conformers at pH 5.5, which should be more stable than one with 1 amide nitrogen and 1 histidine nitrogen. On the other hand, the number of oxygen ligands will increase at pH 5.5 due to the loss of N-coordination and replacement by water or perhaps carbonyl oxygen. Lowering the pH changes the coordination modes of the fifth binding site as compared with those at pH 7.5, with a probable loss of a nitrogen ligand, which we presume to be an amide nitrogen. The results also suggest that both rPrP90-232 conformers contain 2 copper binding sites at pH 5.5.

C. Copper binding to the octarepeat region at neutral pH

After demonstrating the effect of pH and fibrillation on copper binding to the

fifth binding site, we then focused on understanding their effect on copper binding to the octarepeat region using rPrP23-232.

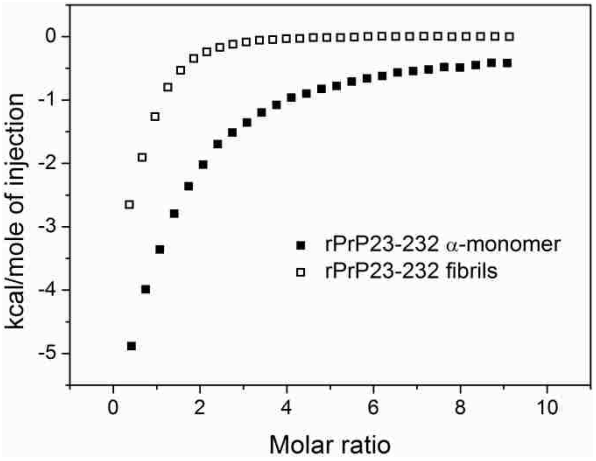

Figure 3-10. ITC isotherms for copper binding to rPrP23-232 conformers.

rPrP23-232 α-monomer (■), 46 μM; rPrP23-232 fibrils (□), 51 μM.

Copper binding to rPrP23-232 conformers at neutral pH was first investigated using ITC. Unlike rPrP90-232 α-monomer, the titration isotherm of Cu(II) binding to the rPrP23-232 α-monomer was complicated by the presence of exothermic reactions at the end stage of titration, even when the heat change resulting from dilution or metal/buffer reaction was subtracted (**Figure 3-10**). This indicates a secondary event that could not be accounted for by the blank titration. Samples after ITC experiments were therefore subjected to AF4 analysis to further investigate the interaction between Cu(II) and rPrP23-232 α-monomer. In contrast to Cu(II)-bound rPrP90-232 α-monomer, which was dominated by a single monomeric elution peak (**Figure 3-11D**), the AF4 trace of the rPrP23-232 α-monomer sample after Cu(II) titration showed a major elution peak at 12.2 min with two minor peaks at 6.3 and 40.9 min (**Figure 3-11A**). This implicates the formation of higher molecular weight species

during copper titration, which may well be responsible for the exothermic events at the end stage of the ITC experiment.

The 6.3 min and 40.9 min elution peaks can be respectively assigned to monomeric and a large multimeric rPrP23-232 species based on evidence presented in Chapter II. The major peak showed a much shorter elution time (12.2 min) than that of rPrP23-232 octameric β-oligomer (~20.9 min), indicating it is less than octameric. This species is assigned as an rPrP23-232 dimer based on calculated molecular weight (51 KDa) using monomer (~ 6.3 min) and octamer as standards, though this is just a rough approximation. Far-UV CD of the mixture showed two negative peaks at 209 and 222 nm and a MRE of -6,841 $deg \cdot cm^2 \cdot dmol^{-1} \cdot residue^{-1}$ at 222nm (**Figure 3-11B**). This MRE is smaller than the MRE of Cu(II)-free rPrP23-232 α-monomer (-8,376 $deg \cdot cm^2 \cdot dmol^{-1} \cdot residue^{-1}$), which suggests a loss of α-helicity and/or formation of new structure. The non-fibrillar characteristics of post-ITC samples were supported by the ThT fluorescence assays, which showed no emission at 485 nm (**Figure 3-11C**). Our results suggest that Cu(II) is able to promote oligomerization of the rPrP23-232 α-monomer, and indeed convert the monomer into a dimeric species. Although the resultant species failed to be characterized as having extended β-sheet characteristics, it does have reduced α-helical features.

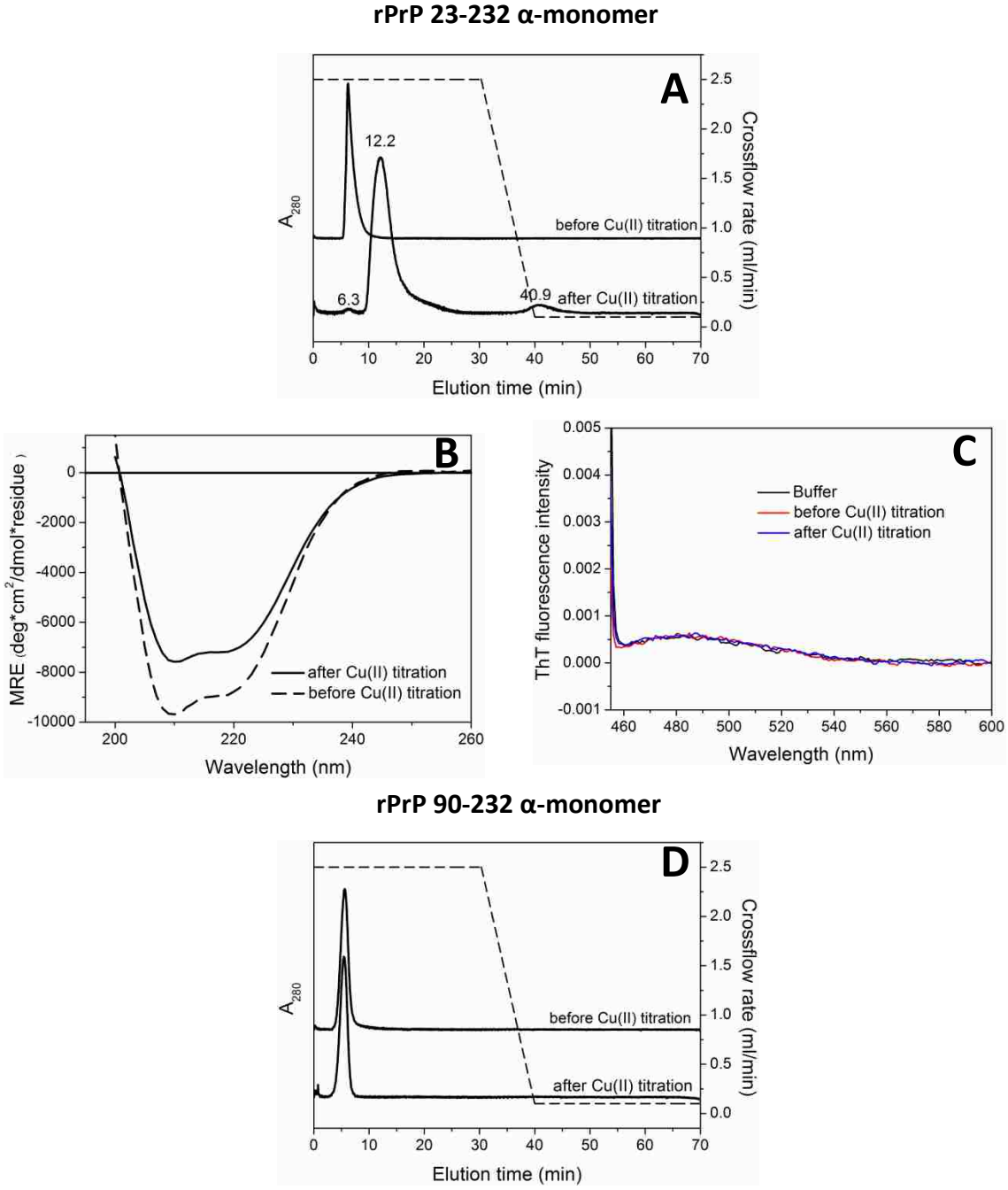

Figure 3-11. Characterization of post-ITC products of rPrP23-232 and rPrP90-232 α-monomer.

(A) AF4 elution profiles of rPrP23-232 α-monomer before and after ITC Cu(II) titration. (B) Far-UV CD spectra of rPrP23-232 α-monomer before and after ITC Cu(II) titration. (C) ThT fluorescence spectra of rPrP23-232 α-monomer before and after ITC Cu(II) titration. (D) AF4 elution profiles of rPrP90-232 α-monomer before and after ITC Cu(II) titration.

Similar to rPrP90-232 fibrils, copper binding to rPrP23-232 fibrils also showed a

steeper slope in the initial stage (**Figure 3-10**), which suggests a higher binding affinity than that of its α-helical conformer. Unfortunately, analysis of the ITC isotherm was hindered by the lack of an appropriate model to account for the presence of three different coordination modes with negative cooperativity as a function of copper occupancy [319]. In fact no regression model available in the Origin 7.0 package provided by the manufacturer could be fitted to the data with confidence. A simple graphic interpretation of the titration isotherm indicates the presence of only one binding site. Attempts to fit the data with one set of binding sites model yielded a binding stoichiometry of 0.89 ± 0.04 with K_d of 7.5 ± 1.5 μM, ΔH of -3.0 ± 0.15 kcal/mol, and ΔS of 13.4 cal/mol-K. This is quite close to that observed for rPrP90-232 fibril except for the higher affinity (lower K_d) (**Table 3-1**). However, the quality of this model is relatively poor as evident by the large χ^2 of 5657. ITC research on copper binding to rPrP23-232 α-monomer has been reported previously using glycine buffer and fitted with the sequential binding sites model [341, 381]. However, no goodness of fit parameters was given, and no comparison of fits to other models was reported. We believe that this model only accounts for interactions between different independent binding sites; it is not appropriate to apply it to a binding event involving a switch from one coordination mode to another. Further, a binding event with negative cooperativity would display an ITC isotherm with more than one phase and different slopes, indicative of the distinct binding affinities. This has never been observed in this study or in any published data [341, 381].

The EPR spectra of both rPrP23-232 conformers showed three sets of hyperfine

splitting patterns ($A_{\parallel}$) as a function of Cu(II) concentration, suggesting the formation of three distinct Cu(II)-prion complexes. The magnetic parameters, $g_{\parallel}$ and $A_{\parallel}$, of these complexes are summarized in Table 3-2. These values approximately match the parameters of species identified by Millhauser's group using synthetic peptides covering the whole octarepeat region [307, 319, 320]. Thus, these three complexes are assigned as component I, II, and III accordingly. The changes in the $g_{\parallel}$ and $A_{\parallel}$ have been ascribed to the changes in the ligand environment around the cupric ion, ranging from three nitrogen and one oxygen (3N1O) for component I, two nitrogens and two oxygens (2N2O) for component II to four nitrogens (4N) for component III.

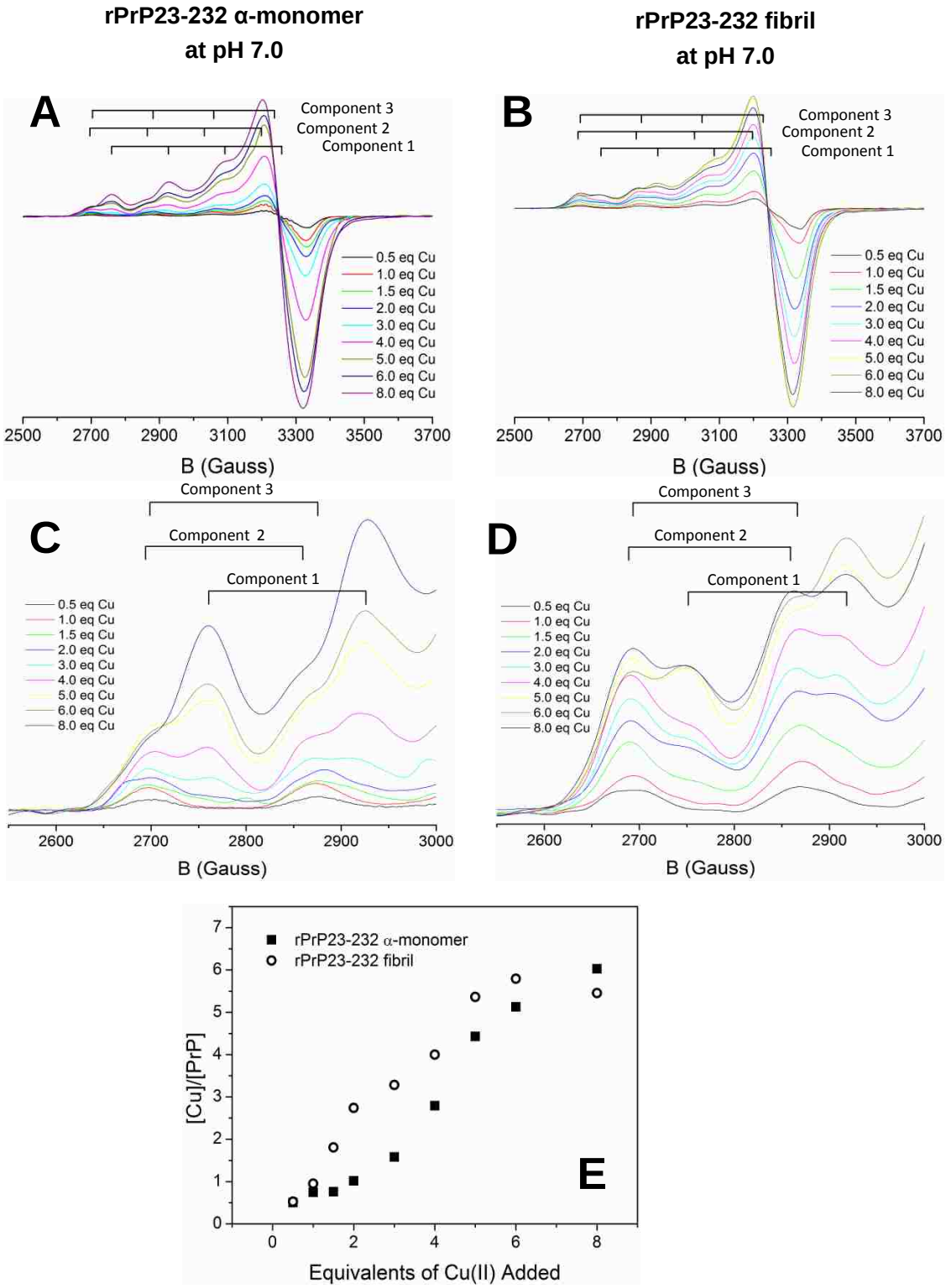

Figure 3-12. Titration of rPrP23-232 conformers with Cu(II) at pH 7.0.

Titration was performed with 125 μM of rPrP23-232 α-monomer and 107 μM of rPrP23-232 fibril in 20 mM PIPES, pH 7.0. (A) and (B) show the

X-band of EPR spectra of the rPrP23-232 α-monomer and rPrP23-232 fibril respectively. (C) and (D) The 2600-3000 Gauss region was enlarged in the inset to demonstrate the presence of three Cu(II) complexes at pH 7.0 as the Cu(II) concentration increases. (E) Integrated EPR spin intensity as the function of $CuCl_2$ added to the solution.

As anticipated from the Millhauser studies [319, 321], in rPrP23-232 α-monomer, component III dominated at < 1 molar equivalent of Cu(II). With continued addition of 1-2 molar equivalents of copper, the position of the EPR signals gradually shifted to lower field range; this is consistent with the formation of component II. At 3 molar equivalents, component III was completely replaced by component II and the signal of component I emerged at this point. Integration of the spectrum indicates that about half of the copper (1.5 molar equivalents) has been taken up by the protein. From 3 molar equivalents and onwards, EPR spectra revealed a coexistence of components I and II. The intensity of component I grew with increasing additions of Cu(II) although component II was still clearly present (**Figure 3-12A and C**) at the highest concentration of the experiment.

Three similar species were also characterized in the EPR spectra of rPrP23-232 fibril, confirming that rPrP23-232 fibril binds Cu(II) with the same coordination modes as the α-monomer (**Figure 3-12B and D**). However, component II is more dominant in the fibrillar form, as its signal grew in almost equally with component I even at high equivalents of copper added, suggesting approximately similar affinity for copper exists between these two species in the fibrillar conformer. The spin quantitation (**Figure 3-12E**) indicates that additional copper binds to the full length protein at 77K. Of note, the EPR spectrum of mouse PrP121-231 at pH 7.4 with less

one equivalent of copper added consists of a component I-type signal even no octarepeat or canonical 5th binding site (His96) is present in this peptide [312]. It is therefore worthwhile considering the possibility that the C-terminal region has at least one binding site with a very similar coordination mode as found in the N-terminal domain.

The differences in binding behavior between rPrP23-232 conformers are clearly demonstrated in their copper loading curves (**Figure 3-12**E). Both conformers were found to bind about 6 equivalents of Cu(II) per PrP at pH 7.0, with 5.8 ± 0.6 for α-monomer and 6.0 ± 0.2 for fibril. Considering the octarepeat region takes up 4 equivalents of Cu(II), His96 binds 1 equivalent of Cu(II), and at least 1 equivalent of adventitious copper may bind, the stoichiometry detected by EPR suggests that all binding sites in rPrP23-232 preserve their ability to bind Cu(II) in the fibril form. However, the sigmoidal titration curve of rPrP23-232 α-monomer is replaced by a hyperbolic curve in fibril. Similar sigmoidal binding curves have been reported for rPrP23-232 α-monomer or an octarepeat peptide using EPR [307] or CD [304, 315], although an alternative explanation has been offered) [346]. Since component III, which has a reported K_d ~ 0.1 nM, only forms at one molar equivalent of copper or below [319, 320, 346], the titrations done here mostly report on total copper uptake by component II (K_d ~ 13 μM) and / or component I (K_d ~ 7 μM) [346], as few points were taken below 1 equivalent of copper. For rPrP23-232 fibril, the relative affinities of these components are different, perhaps due to conformational changes as suggested in our studies of the truncated rPrP90-232 conformers. This hypothesis is

supported by the observation that the EPR spectra of rPrP23-232 fibril showing equal distribution between component II and component I.

Altogether, these data demonstrate that both rPrP23-232 α-monomer and rPrP23-232 fibril bind Cu(II) at neutral pH. They each form three identical complexes as a function of Cu(II) concentration. However, we propose that affinities of component I and component II for copper are different as a consequence of conformational change. Fibrils made from constructs containing only one component will be helpful to clarify these mysteries, as would visible CD experiments, which selectively monitor component I. Additionally, we note that inconsistencies between ITC and EPR data may largely be due to temperature differences.

D. Copper binding to octarepeat region at pH 5.5

Each of the four octarepeat regions contains one histidine residue, whose protonation status (and thus copper ligation status) will be affected by environmental pH. Therefore, the Cu(II) coordination structure was also explored at pH 5.5. EPR spectra for rPrP23-232 conformers are shown in **Figure 3-13**. Comparison of the conformers revealed very similar spectra with typical type II Cu(II) geometry. At 0.5 molar equivalent of Cu(II), the spectrum consisted of a set of signals with $g_{\parallel}$ = 2.25, $g_{\perp}$ = 2.055 and $A_{\parallel}$ = 569 MHz (spectrum 6) (**Table 3-2**). As the copper loading was raised, the $g_{\parallel}$ and hyperfine splittings shifted to a lower field. At 8 molar equivalents of copper, a signal with $g_{\parallel}$ = 2.28, $g_{\perp}$ = 2.064 and $A_{\parallel}$ = 530 MHz (spectrum 7) (**Table 3-2**) was observed. Simulation showed reasonable fits to the experiment data; with calculated magnetic parameters matching measured ones (**Figure 3-13D**). The

contribution of aqueous copper to the spectra could be ruled out as judged from the $A_{\parallel}$ value of the hyperfine splitting in the parallel region [307, 315]. The changes in magnetic parameters with copper loading suggests that changes in the coordinating ligands of the copper center(s) occur, similar to those observed between component 3 and component 2. The decrease of $A_{\parallel}$ indicates that there may be an increase in the number of oxygen ligands as the copper load is increased. A Peisach–Blumberg plot is rather uninformative regarding the coordination mode of spectrum 6 (4N, 3N1O, 2N2O, or 1N3O configuration). However, it does appear that a loss of one nitrogen has occurred for the species associated with spectrum 7 (1N3O, 2N2O, or 3N1O). In both rPrP23-232 conformers, the intensity of the EPR signals increases linearly with the equivalents of Cu(II) added to the solution, until maximal binding of about 4 Cu(II) ions per PrP molecule is achieved (**Figure 3-13E**).

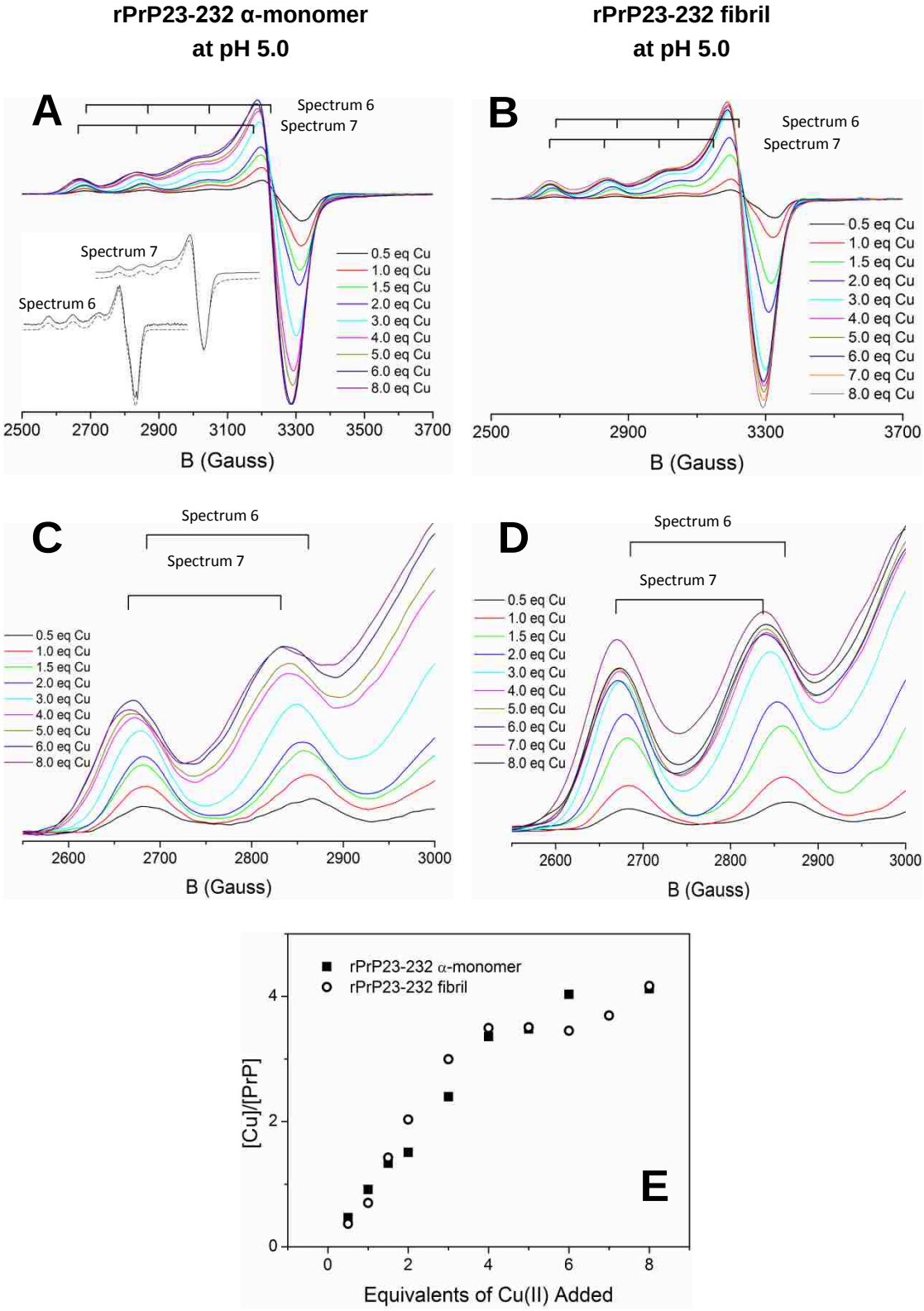

Figure 3-13. Titration of rPrP23-232 conformers with Cu(II) at pH 5.5.

Titration was performed with 197 μM of rPrP23-232 α-monomer and 136 μM of rPrP23-232 fibril in 20 mM MES, pH 5.5. (A) and (B) show the

X-band of EPR spectra of the rPrP23-232 α-monomer and rPrP23-232 fibril respectively. Insets show the simulated spectra (dashed lines) of spectrum 6 collected at 1 molar equivalent of Cu(II) and spectrum 7 collected at 6 molar equivalents of Cu(II). Magnetic parameters for these simulations are: $g_{\perp}$ =2.053, $g_{\parallel}$ = 2.256, $A_{\perp}$ = 45.98 MHz and $A_{\parallel}$ = 568.82 MHz for spectrum 6, and $g_{\perp}$=2.058, $g_{\parallel}$ = 2.282, $A_{\perp}$ = 20.77 MHz and $A_{\parallel}$ = 526.33 MHz for spectrum 7. (C) and (D) The 2600-3000 Gauss region was enlarged in the inset to demonstrate the shift of hyperfine splitting pattern at pH 5.5 as the Cu(II) concentration increases. (E) Integrated EPR signal intensity as the function of $CuCl_2$ added to the solution.

Table 3-2. Measured EPR parameters of Cu(II) complexes formed with rPrP90-232 and rPrP23-232 conformers.

Species	$g_{\parallel}$	$g_{\perp}$	$A_{\parallel}$		Possible coordinations
			$_{\parallel}$MH	$10^{-4}cm^{-1}$	
rPrP90-232 conformers at pH 7.5					
Spectrum 1	2.20	2.037	565	189	3N1O [307]
Spectrum 2	2.27	2.047	504	168	1N-4N, but likely less N than spectrum 1
rPrP90-232 α-monomer at pH 5.5					
Spectrum 3	2.29	2.069	479	160	2N-4N, containing O from water or carbonyl
Spectrum 4	2.22	2.069	475	158	
rPrP90-232 fibril at pH 5.5					
Spectrum 5	2.27	2.06	529	176	2N-4N, containing O from water or carbonyl
rPrP23-232 conformers at pH 7.5 [319]					
Component 1	2.22	n.d.	490	163	3N1O [319]
Component 2	2.26	n.d.	533	178	2N2O [319]
Component 3	2.25	n.d.	573	191	3N1O or 4N [319]
rPrP23-232 conformers at pH 5.5					
Spectrum 6	2.25	2.055	569	189	1N-4N (component 3?)
Spectrum 7	2.28	2.064	530	177	1N-3N, one less N than spectrum 6 (component 2?)

Taken together, these data suggest the interactions between Cu(II) and PrP are indeed pH dependent, which is in agreement with previous data [307, 335, 340].

IV. Discussion

In order to better clarify the effect of conversion of PrP^{C} to PrP^{Sc} on copper binding to PrP and the role played by copper in prion diseases pathogenesis, a comprehensive understanding on the interactions between copper and different PrP conformers is necessary. Although there has been a long list of publications on the relationship between PrP^{C} and copper [319, 321, 343, 346, 382-386], due to the inconsistency of methods used to evaluate their interaction, copper binding to PrP^{C} is still a matter that generates much controversy. Copper binding in PrP^{Sc} is a field that is relatively unexplored.

Here, we present a preliminary comparative study on copper binding to rPrP conformers, α-monomer and fibril, at physiologically relevant pH values. Using ITC, we show that His96 is the major copper binding site in the fifth binding site while His111 itself is not sufficient or required. Furthermore, we demonstrate that rPrP23-232 α-monomer forms a higher molecular weight species, most likely a dimer, after copper binding. From this point of view, ITC alone is not an appropriate approach to study copper binding in full-length PrP α-monomer, unless every single event can be independently isolated. However, data need to be collected under uniform conditions of pH, buffer salts, and temperature for a clear picture to emerge.

As validated by both ITC and EPR, conversion of α-monomer to rPrP fibril does not abolish the ability of rPrP to bind copper. The coordination structures of Cu(II) complexes are largely similar between α-monomer and fibril. However, the relative affinities of the different coordination modes have changed somewhat in the fibril.

Our results confirm that copper binding to both the octarepeats and the fifth binding site are affected by pH.

E. The role of copper binding in PrP aggregation

It has been reported that copper binding induces small-size aggregates of PrP with amyloid characteristics [309, 369]. However, our results reveal that rPrP23-232 α-monomer mainly forms a dimer, along with a small amount of high molecular weight aggregates (**Figure 3-11B**). The post-ITC sample only shows decreased α-helicity and/or increased random coil as judged from CD results; no increase in β-sheet is detected (**Figure 3-11B & C**). ThT fluorescence assay rules out the presence of amyloid features in the sample (**Figure 3-11D**). These data are supported by recent research on the effect of copper binding on the secondary structure and folding stability of α-monomeric PrP23-232, which did not show any generation of β-sheet structures [387]. Interestingly, in previous research, amyloid features were determined by the PK-resistance assay in the presence of Cu(II) [309, 369]. But it has been pointed out that Cu(II) also binds to PK and destroys its activity, thereby causing PK-resistance [388]. Thus, prior results that reported amyloid formation in the presence of copper need to be viewed with caution. Birkmann's group has reported a pre-amyloid state in the presence of SDS, in which the partially α-helical and partially denatured PrP is in a monomer-dimer equilibrium [389, 390]. They believe this state is an essential step during fibrillation. Our results implicate the presence of a similar quaternary state after copper binding. We postulate that the dimeric species might represent an intermediate of fibril formation. Furthermore, although copper-induced

dimerization is a separate event from fibrillation by shaking in the presence of denaturants, the dimer could be a more favored yet transient substrate for fibrillation. This hypothesis can be tested by isolating the copper-induced dimer via AF4 and monitoring the evolution of monomer, dimer, and fibrils under optimal fibrillation conditions.

Results from the present research shows that octarepeat region is required for copper-dependent dimerization/aggregation since the PrP90-232 α-monomer remains in a monomeric state even in the excess of Cu(II). One possible explanation is that copper induced dimerization/aggregation is mediated by the formation of component III, in which the multiple histidine ligands come from more than one prion subunit. However, in the α-monomer, this type of self-association always occurs at sub-stoichiometric quantities of Cu(II) and disappears as Cu(II) load increases due to the formation of component 1 (Cu(II) coordinated by one octarepeat with only one imidazole N_{δ} donor) [340]. The persistence of dimer and high molecular weight aggregates that do not retain the features of component 3 at 9 molar equivalents of Cu(II) argues against this. Another probable mechanism involves the noncovalent cross-linking between PrP molecules mediated by the glutamine residues in the octarepeat region. It proposes that the octarepeat region forms ordered structures only when it is fully copper-loaded [319], bringing the glutamine residues close to each other and facilitating the aggregation process [314]. This may explain the existence of aggregates at high copper concentrations. Additional experiments are warranted in which copper loading is both monitored by EPR and correlated with the appearance of

higher MW species by AF4.

F. Location of the fifth copper binding site

Wide disparity exists in the literature regarding copper binding to His96 and/or His111 residues. Some of these have been addressed from the point of sequence context. It has been recently reported that the presence of a tyrosine residue in chicken PrP makes the His110 (equivalent to hamster His96) the stronger Cu(II) binding site [311]. As illustrated in **Table 3-3**, however, no such a sequence difference is identifiable between hamster and mouse PrP, although the His residues show opposite affinity for copper. The inconsistency in the literature might also result from variation in experimental conditions. As an example, using glycine as the chelator in the ITC buffer, one group found that His111 has a greater affinity for copper than His96 in mouse PrP [349, 381]. However, a careful examination of the methods shows that the Cu(II) donating species are heterogeneous due to the presence of multiple Cu(II)-glycine species under the experimental conditions used [380]. Furthermore, glycine allows for the formation of ternary complexes with PrP bound copper [346]. This makes the data less straightforward to interpret.

In the present study, we used a large excess of Tris-Cl to ensure Cu(II)$Tris_4$ was the sole copper-donating species in the titrant. ITC data from PrP90-232 wild-type and histidine mutants strongly argue that His96 residue is sufficient for Cu(II) binding in the fifth binding site with an apparent dissociation constant in the micromolar range. Deletion of His111 has little to no effect on the ITC titration isotherm. This hints that His111 is not required in the coordination as postulated by other researchers [333].

Table 3-3. Alignment of prion sequence 91-120 of hamster, mouse human and chicken.

Species [311]	Aligned sequence
PrP_Ha	QGGGTHNQWNKPSKP-KTNMKHMAGAAAAGA 30
PrP_Mu	QGGGTHNQWNKPNKP-KTSMKHMAGAAAAGA 30
PrP_Hu	QGGGTHSQWNKPSKP-KTNMKHMAGAAAAGA 30
PrP_Ch	SGGSYHNQ—-KPWKPPKTNFKHVAGAAAAGA 29

G. pH dependence of copper binding in PrP

The effect of pH on Cu(II) binding in PrP has been attributed to its effect on the protonation status of ligands in the first coordination shell, including the carbonyl oxygen, the imidazole nitrogen, and the amide nitrogen. These ligands become more available for coordination as the pH increases. The amide nitrogen usually deprotonates from pH 13 to 15 [391, 392]. However, copper binding to the nearby histidine residue, which serves as the primary ligating site for the metal ion, markedly promotes deprotonation of the amide nitrogen. In acetylglycylglycylhistidine, the pK_a is 6.5 and 7.4 for first and second deprotonation, respectively [391, 392]. The amide nitrogen becomes a nitrogen donor to coordinate Cu(II) after deprotonation. This Cu(II)-amide bond is sensitive to pH and the copper will dissociate when the environmental pH drops. The pK_a of free histidyl side chain is ~ 6.5. However, its pK_a changes significantly in different environments. The pK_a of the His nitrogen bound to copper is much lower; it does not protonate until very low pH is reached. Thus, at low pH, the histidyl side chain provides the major Cu(II) coordination site. When the pH decreases to very low values (<4.5), only oxygen is available for metal coordination.

The data presented herein confirm the pH dependence of Cu(II) binding in both

the octarepeat region and the fifth binding site, as revealed by the significant differences in the magnetic parameters of EPR spectra recorded at pH 7.0 and pH 5.5 (**Table 3-2**). This finding agrees well with the results of other researchers on PrP-copper interactions [307, 315, 320, 393].

Magnetic parameters obtained from the present EPR studies suggest that the fifth binding site may adopt a 3N1O configuration at pH 7.0 (spectrum 1) (**Figure 3-8**), which is in line with published results (**Figure 3-3**) [335, 336]. Three different copper complexes as a function of Cu(II) concentration have also been resolved from the EPR spectra of rPrP23-232 α-monomer (**Figure 3-8Figure 3-12**), whose magnetic parameters measured by us match well to the three components reported by Millhouser's group [319, 323]. These results confirm that the material used in this study bear typical characteristics of Cu(II)-PrP interactions. An additional signal (spectrum 2) arising from adventitious binding is resolvable in the EPR spectra of rPrP90-232 conformers as well. Its larger $A_{\parallel}$ indicates fewer coordinating nitrogen ligands in this species, most likely with a 2N2O or 1N3O coordination mode. Spin integration of EPR signals reveals ~ 6 molar equivalents of Cu(II) have been incorporated into rPrP23-232 α-monomer, including the octarepeats and the fifth binding site. Signals arising from the fifth binding site (spectrum 1) are not discernible from those from the octarepeats region, which is expected given the similarities between the EPR spectrum of PrP90-232 and that of the full-length protein.

The coordination of Cu(II)-PrP complexes formed at pH 5.5 is still difficult to

pinpoint. Backbone amide nitrogens are much less likely to deprotonate and serve as ligands to copper at this pH. Thus the imidazole nitrogens of histidine residues become the primary nitrogen donors. For rPrP90-232 α-monomer, its EPR spectrum is dominated by a single species (spectrum 3) at < 1 equivalent of bound Cu(II), yet the EPR parameters suggest there is more than one nitrogen ligated to the copper. Thus, spectrum 3 may be a multiple histidine species, with a probable 2N configuration. Previous CD and EPR data proposed a 2N2O configuration for the PrP90-126 peptide at pH 5.5, in which the Cu(II) is shared between His96 and His111 [335]. Oxygen ligands are also present in this species, whose origin can be differentiated by other spectroscopic techniques, such as electron–nuclear double resonance (ENDOR) and hyperfine sublevel correlation (HYSCORE) [336]. The coordination structure for spectrum 4 might be similar to spectrum 3. Meanwhile, participation of histidine residues from the C-terminal domain at pH 5.5 cannot be ruled out. This can be clarified using structures without the C-terminal region or by the systematic mutation of other His residues.

For the rPrP23-232 α-monomer, the magnetic parameters for spectra 6 and 7 recorded at pH 5.5 bear strong resemblance to those of components 3 and 2 respectively, suggesting a probable 4N configuration for spectrum 6 and a 2N2O configuration for spectrum 7. We proposed that spectrum 6, which is the binding mode occurring at low Cu(II) occupancy, coordinates Cu(II) through 4 imidazole nitrogens from the unstructured region. Increased Cu(II) occupancy favors the formation of a new species with EPR spectrum 7, in which Cu(II) is coordinated by 2

imidazole nitrogens. It has been reported that this 2N2O coordination mode of component 2 is the intermediate state during component 3 to component 1 transition at pH 7.4 [320]. At pH 5.5, if the amide nitrogen is no longer available to coordinate Cu(II), the copper center might be trapped in this intermediate state and be unable to convert to component 1. This implies that the octarepeat region can bind only up to 2 molar equivalents of copper at pH 5.5. The EPR titration curve showed that 4 molar equivalents of Cu(II) could be incorporated into the α-monomer, we believe the additional 2 equivalents of Cu(II) are bound at the fifth binding site and another adventitious binding site of much lower affinity, as demonstrated for the rPrP90-232 protein. Similar to rPrP23-232 α-monomer at pH7.0, signals arising from these two sites might not be discernible in the full-length protein. NMR studies on copper binding to full-length human rPrP at pH 5.5 advocates the coexistence of copper binding to both the octarepeat region and the fifth binding site [340]. Switching from N_{δ} to N_{ε} coordination in the imidazole ring to facilitate the 2N2O configuration might also be necessary [393]. Even the involvement of the N-terminal amine group in the coordination has been implicated [340]!

The pH dependence of Cu(II) binding in PrP is physiologically relevant to its functions *in vivo*. As Cu(II)-loaded PrP is trafficked from the plasma membrane to the endosomal compartments, it will experience a similar pH change used in the present research. We have shown here that the Cu(II)-PrP complexes adopt distinct coordination modes as a function of pH. Clearly, this in turn will affect its affinity for copper along with modulating redox properties. Furthermore, the propagation of

multiple histidine Cu(II) complexes under low pH conditions may favor the aggregation of PrP within the endosomal pathways. In lysosomes or copper storage vesicles, where the pH is about 4.5, the Cu(II) might be released from the protein altogether.

H. Effect of fibrillation on copper binding

Results from the present study show that the fibrillar forms of PrP bind copper with coordination structures that are quite similar to their α-helical counterparts (**Table 3-2**). However, the relative ratios of the different copper binding modes are affected by fibrillation, especially at pH 7.0. While spectrum 1 is the major species in rPrP90-232 α-monomer at low copper equivalents, the spin intensity splits almost equally between spectra 1 and 2 in the fibrillar form at the same copper concentration (**Figure 3-8**). Similar results were found in rPrP23-232, where component 1 is the major species at high copper equivalents in the α-monomer. In the fibril state, component 2 and component 1 grow in simultaneously as Cu(II) loading increases (**Figure 3-12**). These effects may be the consequences of conformational changes in fibril. There may also be differences in coordination modes associated with changes in affinities for copper as a function of temperature, which we have demonstrated based on ITC results. Room temperature EPR experiments on the fibrillar form will rule out or support the possible role of temperature on binding affinity, illuminating the contribution of each coordination mode under more physiologically relevant conditions. The redistribution of spin intensity between different coordination modes in the fibrillar form could have some effects on PrP physiological functions. It has

been suggested that component 1 may regulate the generation of H_2O_2 [328], which is believed to be a signaling messenger and involved a variety of cellular event [394]. If this holds true, a decrease in the amount of component 1 in fibrils might lead to less production of H_2O_2, which can further influence other physiological processes. From this point of view, conversion of PrP^{C} to PrP^{Sc} can still be treated as a loss-of-function.

In summary, we confirmed here that copper binding in both rPrP90-232 and rPrP23-232 conformers is sensitive to pH changes, which we believe is mainly due to the protonation status of amide nitrogen ligands under different pH conditions. We demonstrated that both the octarepeats and the fifth binding site preserve their ability to bind Cu(II) in the fibrillar state. Similar coordination modes are characterized in both α-monomer and fibril. However, the relative ratios of the different binding modes have changed in the fibril. This change might have potential effects on redox properties of the fibril.

CHAPTER IV:

GENERAL DISCUSSION

The overall goal of this study was to investigate the effect of mildly acidic pH on the stability of rPrP fibrils and evaluate the impact of fibrillation on the copper binding characteristics of rPrP. Results from this study reveal some new properties of PrP fibrils. As these aspects have not been addressed previously, the information from this study allows for the opportunity to explore the pathogenesis of prion disease from new perspectives.

I. Low-pH induced fibril dissociation

Contrary to the prevailing thought that prion amyloid fibrils are inert, stable final products of amyloidogenesis, the present study demonstrates that incubation of rPrP23-232 fibril at pH 4.5 – 5.5 results in lateral and axial dissociation of fibrils into protofilaments. Dissociation occurs even in the presence of high (0.1 M) concentration of NaCl, albeit at slower rate. Morphological evidence suggests that the protofilaments are single- or possibly double-stranded, and are about 50% of the width of the original fibrils. They are heterogeneous in length. The amyloid nature of protofilaments was confirmed by amyloid-specific ThT fluorescence and other spectroscopies. Based on their behavior in ultracentrifugation, protofilaments can be further separated into two categories: about 5% of the original rPrP23-232 fibrils form protofilaments that are small enough to be considered as soluble, with a molecular weight around 5.8 MDa and radius of gyration around 27.4 nm. A very small amount of monomeric and octameric PrP is also found in the soluble fraction. The rest of the protofilaments are still relatively long and form a pellet after ultracentrifugation. In

sharp contrast, the rPrP90-232 fibrils are unaffected at pH 4.5 and keep the typical unbranched, twisted structures. This difference is of interest as PrP90-232, which contains the protease-resistant core of PrP^{Sc} [4] and is sufficient to propagate the prion diseases, has been widely used as a substitute for PrP^{Sc} in prion research [175].

Results from this study conclude that low pH dissociation of rPrP23-232 fibrils into protofilaments does not involve changes in the amyloid core or its secondary structure. Investigation of the amyloid core region of protofilaments using partial PK digestion and mass spectrometry showed that the amyloid core comprises residues 157-220, which is consistent with those detected for fibrils [176, 177]. Further efforts to compare the secondary structure of rPrP23-232 protofilaments with their fibrillar counterparts using FT-IR revealed quite similar spectra, with only subtle, pH-related differences in the β-sheet structure. The PK digestion results, combined with the spectroscopic data, suggest that protofilaments possess the main structural characteristics of their parent fibrils. Thus, fibril dissociation is not triggered by the folding of the N-terminal domain of rPrP23-232 into a PK-resistant β-sheet structure, nor the unfolding of the PK-resistant amyloid core. The minor spectral differences observed between protofilaments and fibrils were largely reversible as the pH of protofilaments was increased to 7.0, and morphological changes of protofilaments at pH 7.0 were observed by TEM as well. The pH dependence indicates the contribution of protonatable residues to the dissociation process.

While the dissociation of fibrils into protofilaments or smaller particles is an essential step of the secondary nucleation process, its mechanism has been poorly

understood. One possible mechanism proposed by this study is that the accumulation of positive charges in the N-terminal region of rPrP23-232, specifically due to the protonation of His residues within the octarepeats region, results in charge repulsion among individual rPrP23-232 molecules, leading to the dissociation of fibrils into protofilaments. This hypothesis is supported by the fact that fibril dissociation is pH dependent and no protofilaments form at neutral pH. Increasing the pH from 4.5 to 5.5 led to the formation of longer protofilaments as compared with the size of protofilaments formed at pH 4.5. Additional evidence for the charge repulsion mechanism is the observation that N-terminally truncated fibrils do not dissociate at low pH, even though the amyloid core is nearly identical to that of rPrP23-232 fibrils. An informative experiment to test this mechanism would be the use of a single rPrP23-232 mutant, in which all the four octarepeat histidine residues are mutated to alanine to abolish charge repulsion.

It is noteworthy that the stability of rPrP90-232 fibrils under mildly acidic conditions might be one reason for the failure to induce prion disease using recombinant mouse PrP89-231 in wild-type animals [52, 53, 67]. Thus, examination of the complex interactions between low pH-induced fibril dissociation and prion propagation would be a fruitful avenue for future studies in prion diseases.

Although tentative, this proposed mechanism is intriguing and of pathological relevance. As demonstrated by the kinetic results of this study, protofilaments are efficient seeds for fibrillation *in vitro* under mildly acidic conditions in the absence of denaturants. PrP^{Sc} may be subject to a similar dissociation mechanism after it is

autophagized and transported into the lysosome [67, 271], where the pH is similar to that used in this study [272]. The protofilaments of PrP^{Sc} formed in the lysosome may serve as excellent seeds for conversion of PrP^{C} into PrP^{Sc} as PrP^{C} recycles from the plasma membrane into the endocytic pathway [67], thus maintaining the prion state. This mechanism may exert significant effects on the onset of prion diseases.

Expansion of the octarepeats is associated with the early onset of human prion diseases [395]. The average onset age for patients with five to nine octarepeat insertions is 38 years, which is about three decades earlier than the age of onset for those with a normal number of octarepeats [395]. A few mechanisms have been proposed for this association, including altered copper binding activity [396] and a more rapid binding between PrP molecules [397]. Alternatively, data from this work implicate that the early onset may be the result of accelerated fibril dissociation in the lysosome. Additional positive charges will accumulate in the N-terminal region due to the octarepeat insertions that add additional histidine residues. This hypothesis can be tested *in vitro* using octarepeat variants with different numbers of octarepeats and monitoring their relative rates of dissociation.

Data from this study suggest that protofilaments, particularly the shortened, soluble forms, could be candidates for the neurotoxic species of prion diseases. Current views on the identity of neurotoxic species hold that they are transient, soluble intermediates generated on the path to, or as a side product of, making insoluble fibrils from misfolded protein [194, 200, 201]. The biochemical nature of these intermediates is not well understood, but it is generally accepted that the

intermediates have to be generated intra-neuronally to exert toxicity [194, 196]. A large and somewhat confusing body of literature describes many types of PrP intermediates [251, 252, 389, 398] and their roles in prion diseases neurotoxicity are still intensely debated. Although still preliminary, we note that the soluble protofilaments identified in our studies might be good candidates for toxicity for the following reasons: they may be generated intra-neuronally in the late endocytic pathway, they have a secondary structure characteristic of amyloid fibrils, and they exert enhanced seeding activity under physiologically relevant conditions. The role of protofilaments in prion neurotoxicity represents a fascinating aspect of prion pathogenesis that clearly warrants future study.

An important future experiment arising from this study is to determine whether authentic PrP^{Sc} behaves similarly under lysosomal condition. The ion composition of lysosome lumen is quite different from the buffer we used in the present research. As an initial step, the stability of rPrP23-232 fibril has also been tested in a buffer that mimics lysosomal conditions (20 mM NaOAc, 60 mM KCl, 5 mM $CaCl_2$, pH 4.5) [399]. In this preliminary experiment, we found that recombinant fibrils dissociated into short protofilaments within 72 hours (**Figure 4-1**), which is comparable to those in the absence of NaCl. This demonstrated that dissociation of fibrils occurs relatively rapidly under more physiologic-like conditions. Molecular crowding in the lysosome has also been reported to contribute to fibrillation [400]. Investigating pH-induced fibril dissociation in the presence of crowding agents would be worthwhile. *In vivo* experiments to isolate lysosomes from scrapie-infected cells or animals will extend

our knowledge on fibril dissociation even further.

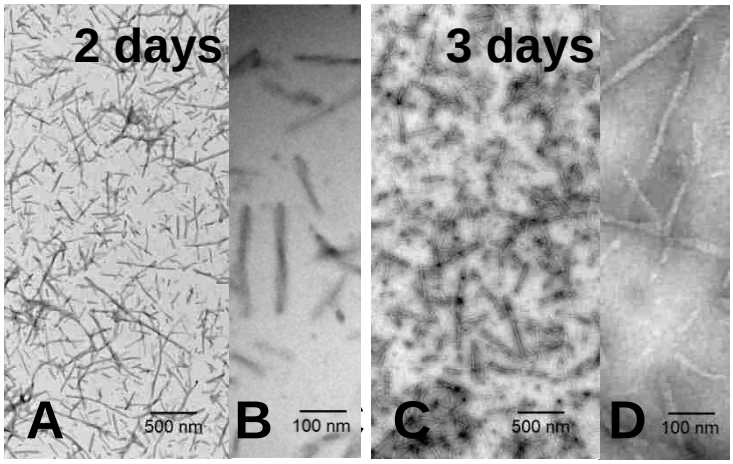

Figure 4-1. Dissociation of rPrP23-232 fibrils into protofilaments in lysosome-like buffer.

TEM images of rPrP23-232 fibrils showing the time dependence of pH-triggered lateral and axial dissociation after incubation for 2 days (A, B) and 3 days (C, D) in 20 mM NaOAc, 60 mM KCl, 5 mM $CaCl_2$, pH 4.5. Images taken at 20,000× (scale bar 500 nm) or 100,000× magnification (scale bar 100 nm).

This work also revealed the co-existence of rPrP23-232 α-monomer, albeit at low concentrations, with protofilaments at low pH. The source of the monomeric rPrP is not clear. One possibility is that unconverted monomers adsorb to the surface of amyloid fibrils. We believe this to be implausible, because the fibrils were extensively washed prior to the dissociation experiments. Furthermore, the monomeric peak is absent in the AF4 elution profile of fibrils at pH 7.0. For other amyloid fibrils like PI(3)K-SH3 and Aβ, recycling molecules by dissociation and re-association of monomers at the ends of fibrils has been reported [401, 402]. This leads us to hypothesize that prion fibrils may employ a similar, pH-dependent mechanism in which the monomers within the fibrils dissociate from the fibril edges and refold back to the α-monomer. This is an area that will need to be investigated further. This goal

can be achieved by a time course study using H/D exchange mass spectrometry, in which changes in the population of fully H/D exchanged molecules and partially H/D exchanged molecules over time indicates the rate of recycling [401]. These data may highlight the dynamic nature of prion amyloid fibrils and help develop new therapeutic strategies.

In conclusion, the study described here was carried out with the aim of probing the behavior of rPrP fibrils under mildly acidic conditions. Data obtained from this work have paved the way for further characterization of the mechanism of low pH induced fibril dissociation, which might be associated with charge repulsion in the N-terminal region of rPrP23-232 molecules. This work has also addressed the seeding activity of protofilaments in the absence of denaturants. Such considerations are of particular importance in understanding of prion propagation *in vivo*, as the endocytic pathway is a major site for conversion of PrP^{C} to PrP^{Sc} [42, 67, 162, 268, 269]. Numerous questions regarding the role played by fibril dissociation in prion diseases remains, including the neurotoxicity of protofilaments and recycling between monomers within fibrils and a monomer pool in solution. The answers to these questions will enlighten our understanding of the mysterious mechanisms of prion infectivity and toxicity.

II. Copper binding to prion conformers

Our initial exploration of copper-prion interaction focused on the so-called fifth binding site that is located within residues 91-111. The characteristics of binding

events at this site are the subject of controversy. Fitting the titration isotherm of rPrP90-232 α-monomer to single set of binding sites model suggested the presence of only one primary copper binding site in this region. ITC experiments with histidine mutants, H96A and H111A, revealed the His96 residue to be required for copper binding. The thermodynamic parameters of the H111A mutant are similar to that of the wild type, which suggests that His111 is not part of the complex under the conditions tested. The affinity of His96 for Cu(II) is in the low micromolar range, which is close to the affinity reported by surface plasmon resonance [333]. The fifth binding site has been reported to have a femtomolar affinity for copper using tryptophan fluorescence quenching [383]. However, as argued by many other groups, quenching mechanisms that do not represent direct Cu(II) binding, such as collisional quenching between aqueous, unbound copper and tryptophan, also contribute to the quenching of the fluorescence [90, 403]. This may overestimate the binding affinity. ITC studies on recombinant mouse PrP23-232 has found a nanomolar affinity for the fifth binding site [343]. We were not able to reproduce this result under the current experiment settings. As noted in chapter III, we believe this disparity might be due to specific buffer conditions.

Upon successfully identifying His96 is the major residue in the fifth binding site, efforts were devoted to characterizing the thermodynamic parameters of copper binding in full-length α-monomeric protein using ITC. This was complicated by the persistence of unusual exothermic reactions at the end stage of titration, which led to an investigation of the final products of ITC titration. Using AF4, we found the

formation of a rPrP23-232 dimeric species (although trimer cannot be ruled out) occurred during the ITC experiment, which is the most likely reason for the observed exothermic anomalies. Although the product shows decreased α-helical features by CD spectrometry, it does not possess amyloid characteristics. In sharp contrast, the rPrP90-232 α-monomer remains monomeric even in a large excess of Cu(II). These results are interesting for several reasons. First, it implies that the octarepeat region is required for dimer or trimer formation. Second, the observation of quaternary structure at high copper load could rule out the possibility that the dimerization (or trimerization) is mediated by the formation of a multi-histidine complex (component 3) [340] since component 3 dissociates at high copper occupancy and is replaced by component 1. A time course study on dimerization as a function of copper loading will provide more insight into the underlying mechanism. Third, it raises the concern regarding the previously reported ITC data on copper binding to recombinant full-length prion protein [341, 343, 349]. Although ITC is sensitive in determining the thermodynamic parameters of association and dissociation reactions, it cannot differentiate the contribution of more than one reaction to the overall thermodynamic evolution of the system. In our hands, for the case of copper binding to rPrP23-232, both copper binding and rPrP23-232 oligomerization contribute to the final isotherm, and both must then be used to fit the existing mathematical models. Thus, it is inappropriate to interpret ITC data based on the assumption that the isotherm solely reports on copper binding [341, 343, 349]. The identity of the copper-induced dimer can be further characterized by AF4 (size), CD (secondary structure, especially

α-helical component) and FTIR (secondary structure, especially β-sheet component). The contact sites in this dimeric species can be further identified using chemical cross-linking and mass spectrometry. Its potential capability to convert to a fibrillar form can be tested using the ThT fluorescence assay and monitoring the amount of monomer, dimer, and fibril over time under optimal fibrillation conditions. These proposed studies will help elucidate the role of copper-induced dimer in fibrillation.

The present studies also confirmed the pH-dependence of copper binding to PrP as evident by distinct electron paramagnetic resonance parameters collected at pH 7.0 and 5.5 respectively. This is not surprising because one would expect all amides to be protonated at pH 5.5 even in the presence Cu(II); histidyl side chains and water would become the major Cu(II) ligands at low pH. The EPR spectra suggested multi-histidine complexes in both octarepeats and the fifth binding site at low pH. This is consistent with previous studies [320, 335, 340].

A major part of this work was to assess the effect of conversion of rPrP α-monomer to fibril on copper binding. We found that fibrils retain the ability to bind copper at both neutral and mildly acidic pH. The coordination structures of the copper centers in fibrils are quite similar to those observed in α-monomer based on EPR parameters. However, the detailed characterization of the ligands in the first coordination shell of these binding modes identified in the fibril form is hindered by the limitations of X-band cw-EPR. Despite this, our EPR results still provide clues to design future studies. For example, we noticed that the multi-histidine species, component 3, in the fibrillar form might be formed between histidines located on

different monomers rather than different octarepeats of the same monomer. This question can be addressed by producing protein where His residues are globally replaced by thio-histidine, and then fibrils are formed using a mixture of all-His and all-thioHis monomers. It is possible to dissect the coordination shells using extended X-ray absorption fine structure spectroscopy (EXAFS) (**Figure 4-2**). EXAFS is an element-specific technique that investigates the scatter of electrons that are emitted from the core of a nucleus upon bombardment of the sample by powerful X-rays. EXAFS gives statistical information about the neighboring atoms around the emitting atom due to interference between the outgoing photo-electron wave and the backscattered electron waves caused by the neighboring atoms in the first coordination shell. It is sensitive to the metal redox species, coordination numbers, and the bond angles and bond lengths of the neighboring atoms [404]. Thus, if the copper ion is coordinated by a histidine residue from one monomer and a thio-histidine from another monomer, it will produce a distinct EXAFS spectrum compared with a mixture of all-His and all-thioHis proteins. Furthermore, in combination with multi-frequency EPR, other techniques, such as electron spin echo envelope modulation (ESEEM), pulsed electron nuclear double resonance (ENDOR), and hyperfine sublevel correlation (HYSCORE) can reveal the coordination structures of the copper centers.

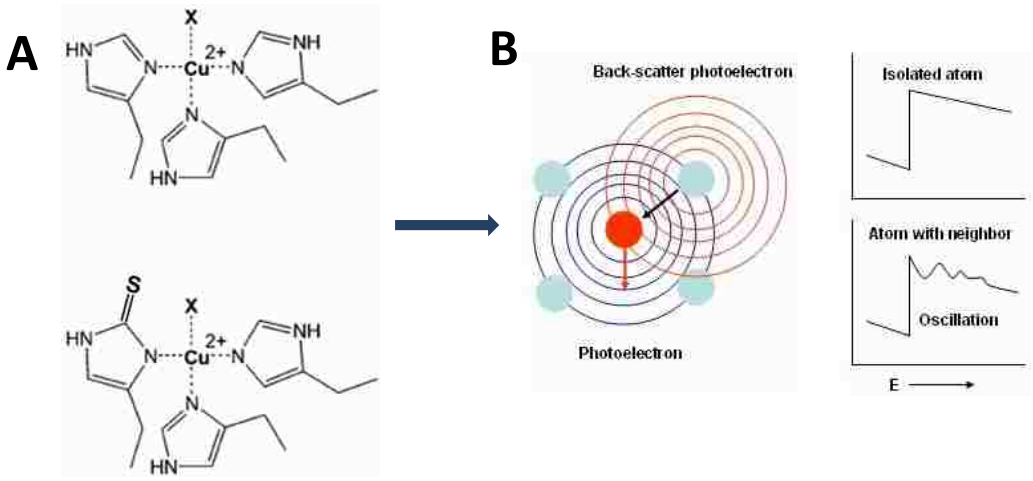

Figure 4-2. Schematic diagram of the proposed thio-histidine and EXAFS experiments.

(A) The structure of thio-histidine, in which the hydrogen is replaced by sulfur. Adapted from [319]. (B) Hydrogen and sulfur backscatters the outgoing photo-electron wave differently, thus they can be differentiated in the EXAFS spectrum. Adapted from [404].

Although the fibrillar form shows similar copper coordination modes to α-monomer, the relative affinities of the different complexes are somewhat different. The underlying mechanism of this observation is still unclear. Conformational change in the N-terminal region after fibrillation may contribute to the disparity. But it may also simply reflect temperature-dependent changes in the affinities for copper, as predicted from ITC results. Room temperature EPR experiments on both conformers will rule out or support this possibility, illuminating the contribution of each coordination mode in the fibril from under more physiologically relevant conditions. These aspects highlight the importance of examining room temperature copper binding to rPrP fibrils in the future.

Of note, we have reported that rPrP23-232 fibrils dissociate into protofilaments under acidic conditions. Results from this part of study show that rPrP23-232

protofilaments still possess the ability to bind Cu(II) at pH 5.5. Furthermore, the coordination modes are identical to that of α-monomers. This suggests that dissociation of rPrP23-232 fibrils has no effect on copper binding properties. Recombinant PrP23-232 fibrils dissociate into much smaller protofilaments at pH 4.5. However, imidazole nitrogen is typically protonated at ~pH 4.5 and thus is less likely to coordinate Cu(II). Consequently, the relationship between fibril dissociation and copper binding was only pursued at pH 5.5. One key future experiment is to determine the effect, if any, of copper bound to fibrils at pH 7 on the rate of dissociation into protofilaments, as a function of pH.

While the ability of PrP to bind Cu(II) has been well established and beyond doubt, there is still no consensus regarding the affinity of each binding site and the way that the cupric ion is coordinated by the PrP. This study supports the models where His96 is the imidazole ligand in the fifth binding site, which binds copper with low micromolar affinity. This study has also confirmed many previous reports concerning Cu(II) binding to PrP. More importantly, this study provides preliminary data on copper binding in rPrP fibrils, which may lead to further advances in our knowledge of the role of copper in neurodegeneration.

CHAPTER V:

APPENDIX

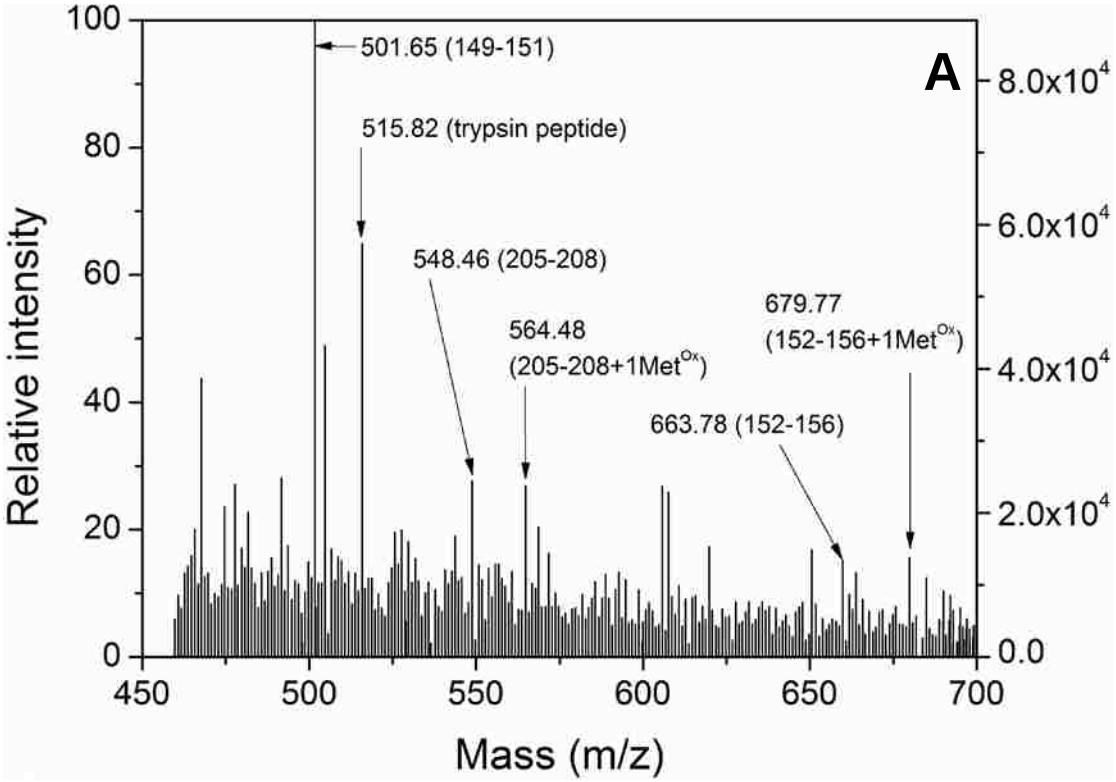
A
501.65 (149-151)
515.82 (trypsin peptide)
548.46 (205-208)
564.48
(205-208+1Met^Ox)
663.78 (152-156)
679.77
(152-156+1Met^Ox)
Relative intensity
Mass (m/z)
100
80
60
40
20
0
450
500
550
600
650
700
8.0x10^4
6.0x10^4
4.0x10^4
2.0x10^4
0.0

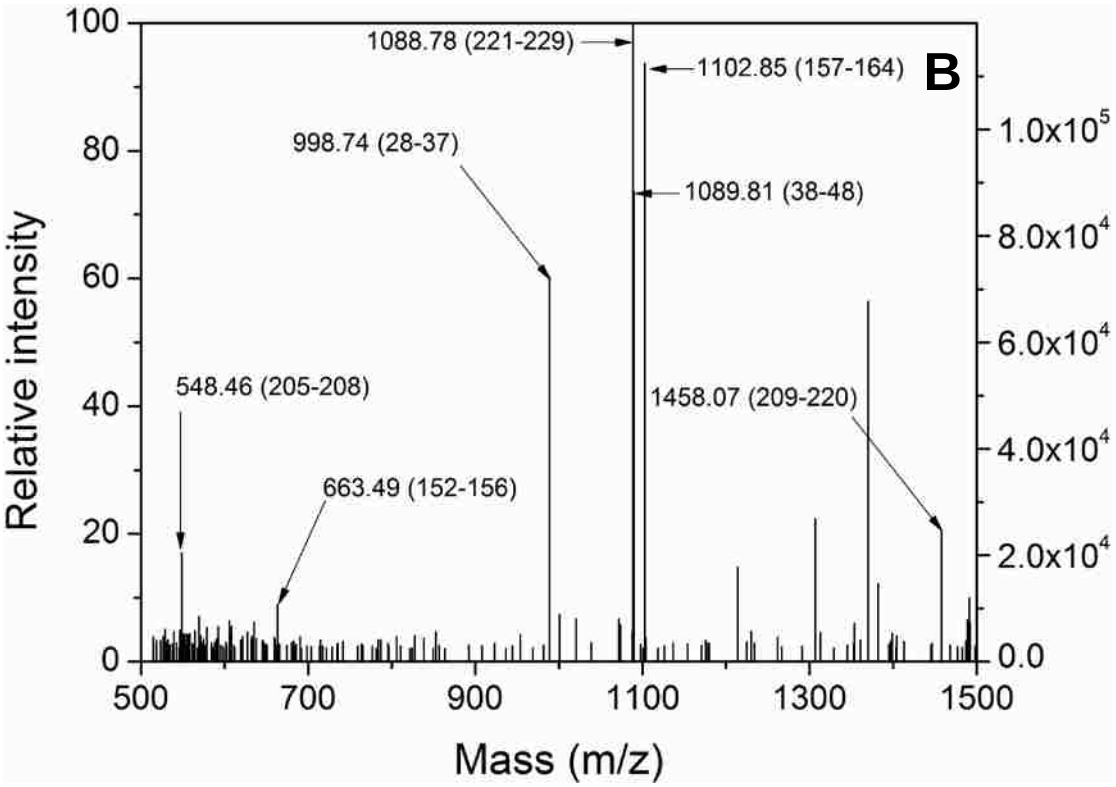
B
1088.78 (221-229)
1102.85 (157-164)
998.74 (28-37)
1089.81 (38-48)
548.46 (205-208)
1458.07 (209-220)
663.49 (152-156)
Relative intensity
Mass (m/z)
100
80
60
40
20
0
500
700
900
1100
1300
1500
1.0x10^5
8.0x10^4
6.0x10^4
4.0x10^4
2.0x10^4
0.0

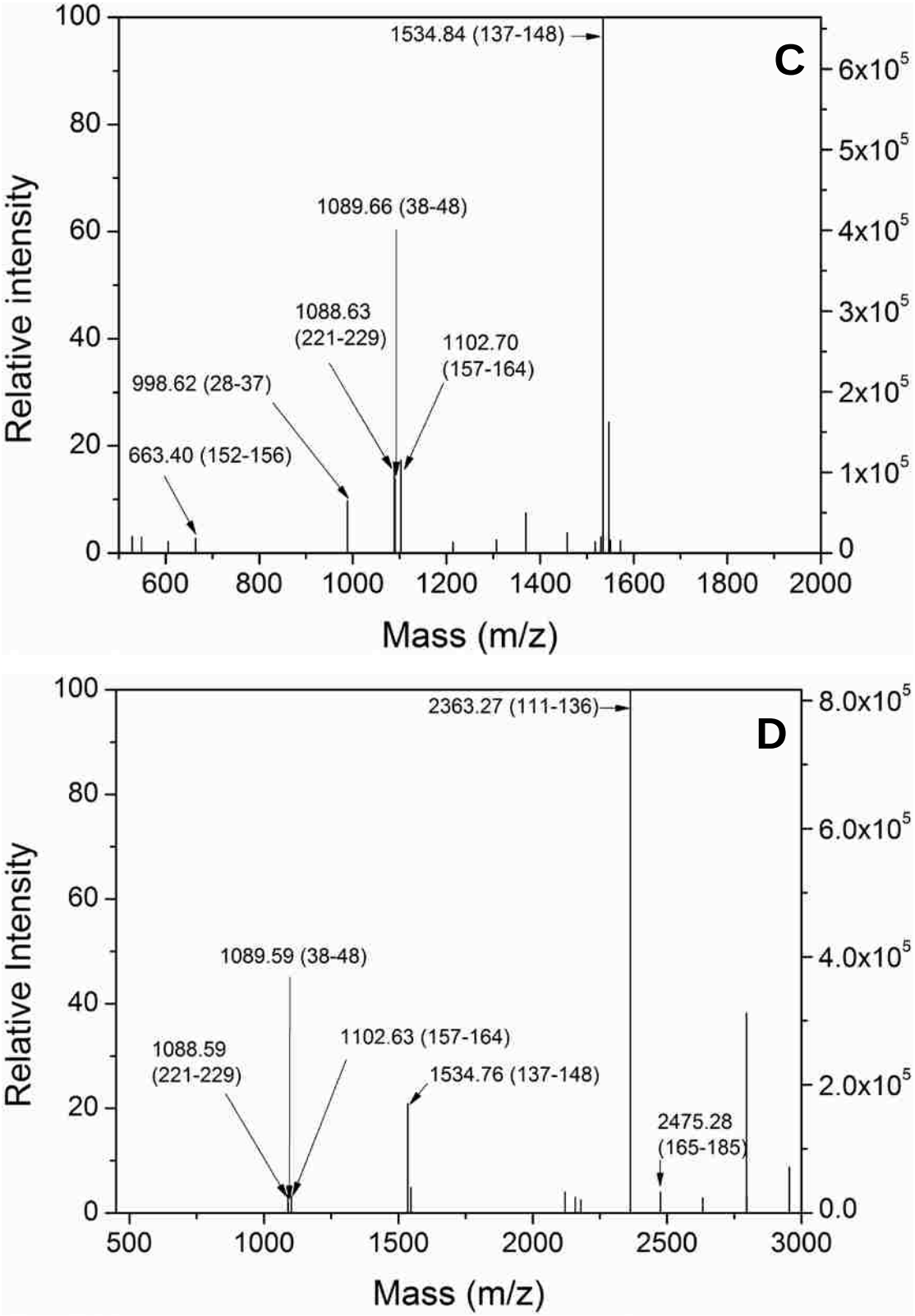

Figure 5-1. MALDI-TOF spectra of tryptic digest peptides of rPrP23-232 α-monomer.

Samples were tryptic digested at a 1:10 (w/w) trypsin to rPrP23-232 ration and reduced with 10 mM DTT. All data were collect in reflectron

mode. (A) 450-700 Da mass range; (B) 500-1500 Da mass range; (C) 500-2000 Da mass range; and (D) 450-3000 Da mass range. The masses are reported and the corresponding tryptic peptides are identified by residue numbers in parentheses.

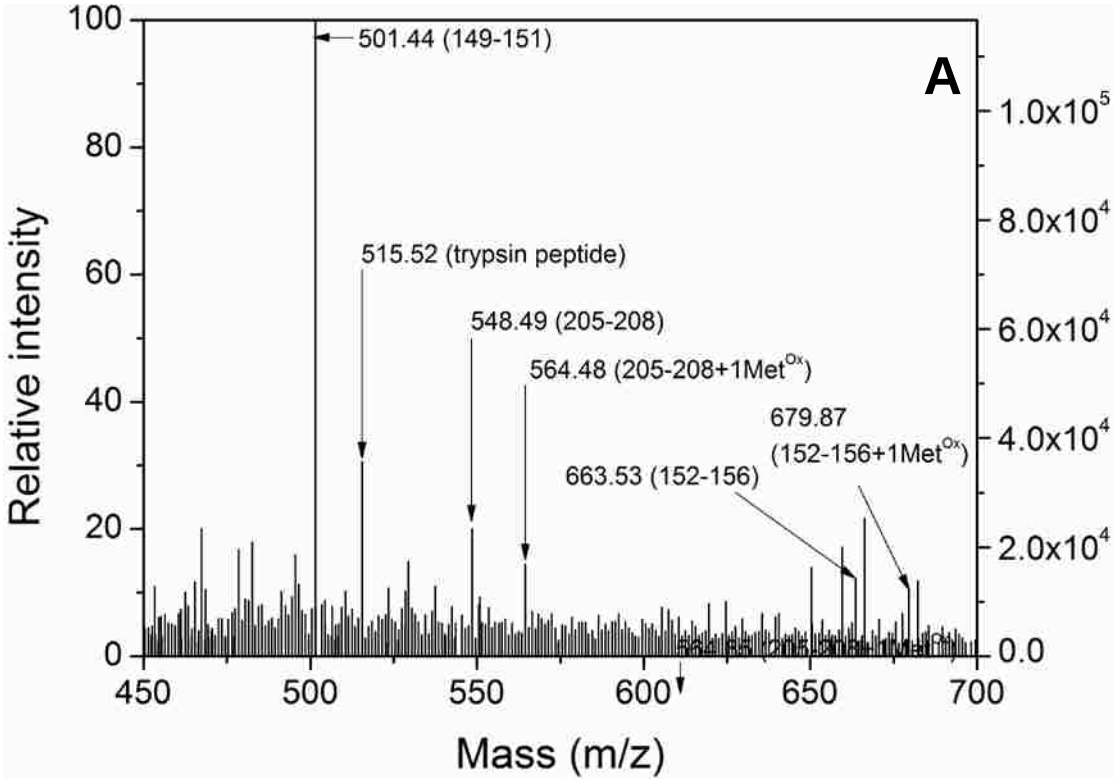
A
501.44 (149-151)
515.52 (trypsin peptide)
548.49 (205-208)
564.48 (205-208+1Met^Ox)
679.87
(152-156+1Met^Ox)
663.53 (152-156)
Relative intensity
Mass (m/z)
100
80
60
40
20
0
450
500
550
600
650
700
1.0x10^5
8.0x10^4
6.0x10^4
4.0x10^4
2.0x10^4
0.0

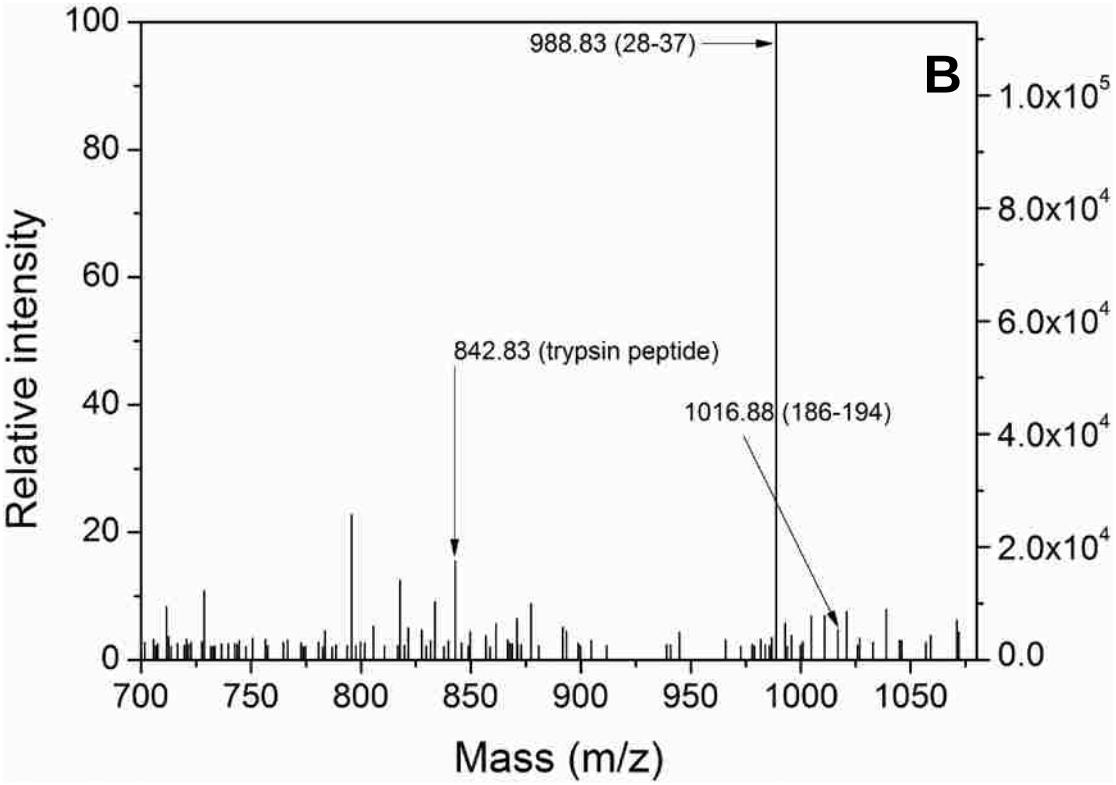
B
988.83 (28-37)
842.83 (trypsin peptide)
1016.88 (186-194)
Relative intensity
Mass (m/z)
100
80
60
40
20
0
700
750
800
850
900
950
1000
1050
1.0x10^5
8.0x10^4
6.0x10^4
4.0x10^4
2.0x10^4
0.0

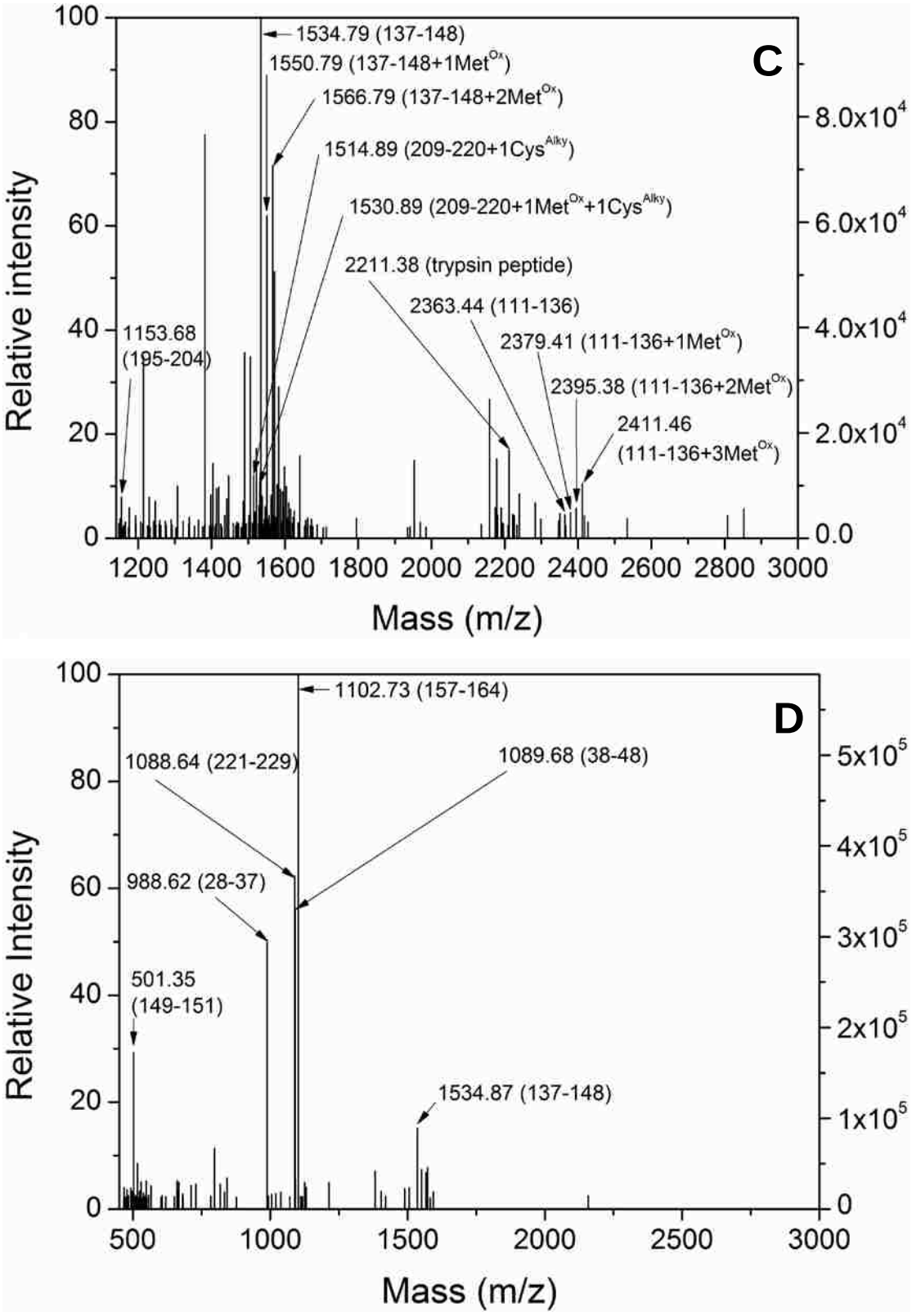

Figure 5-2. MALDI-TOF spectra of in-gel tryptic digest peptides of rPrP23-232 fibril.

After SDS-PAGE, excised bands were in-gel tryptic digested at about 1:10 (w/w) trypsin to rPrP23-232 ration, reduced with 10 mM DTT, and

alkylated with 100 mM iodoacetamide. All data were collect in reflectron mode. (A) 450-700 Da mass range; (B) 700-1080 Da mass range; (C) 1100-3000 Da mass range; and (D) 450-3000 Da mass range.

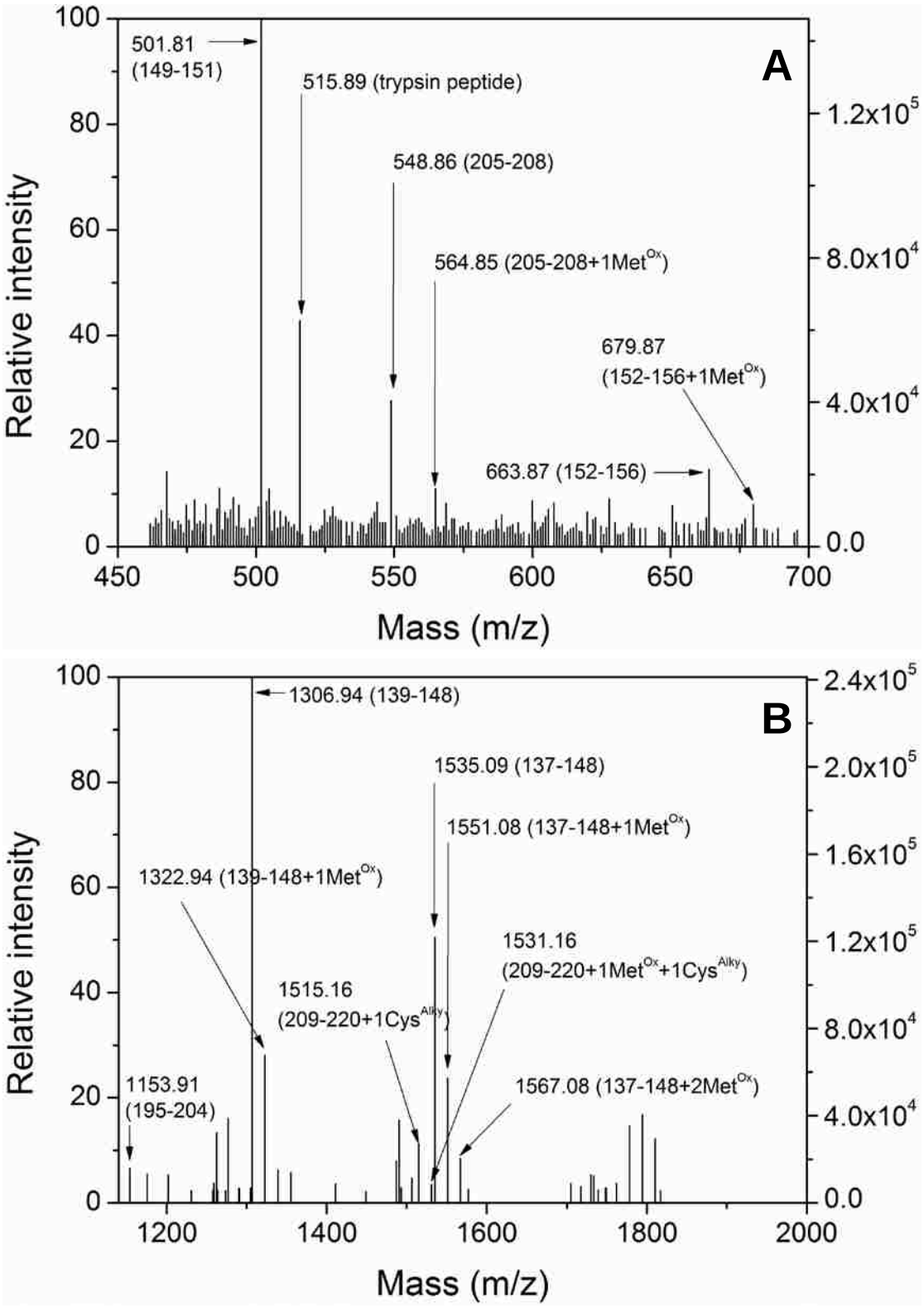
A
501.81
(149-151)
515.89 (trypsin peptide)
548.86 (205-208)
564.85 (205-208+1Met^Ox)
679.87
(152-156+1Met^Ox)
663.87 (152-156)
Relative intensity
Mass (m/z)
B
1306.94 (139-148)
1535.09 (137-148)
1551.08 (137-148+1Met^Ox)
1322.94 (139-148+1Met^Ox)
1531.16
(209-220+1Met^Ox+1Cys^Alky)
1515.16
(209-220+1Cys^Alky)
1153.91
(195-204)
1567.08 (137-148+2Met^Ox)
Relative intensity
Mass (m/z)

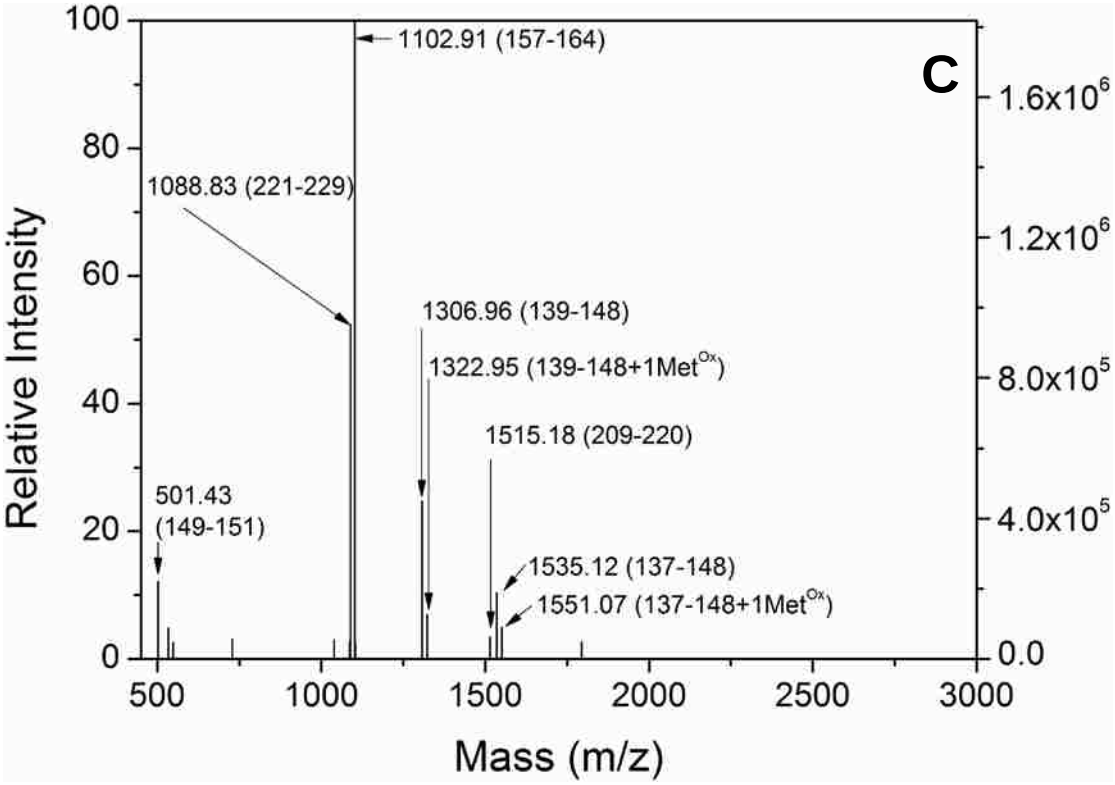

Figure 5-3. MALDI-TOF spectra of in-gel tryptic digest peptides of the 12 KDa PK-resistant fragment of rPrP23-232 fibrils.

After SDS-PAGE, excised bands were in-gel tryptic digested at about 1:10 (w/w) trypsin to protein ration, reduced with 10 mM DTT, and alkylated with 100 mM iodoacetamide. All data were collect in reflectron mode. (A) 450-700 Da mass range; (B) 1140-2000 Da mass range; and (C) 450-3000 Da mass range.

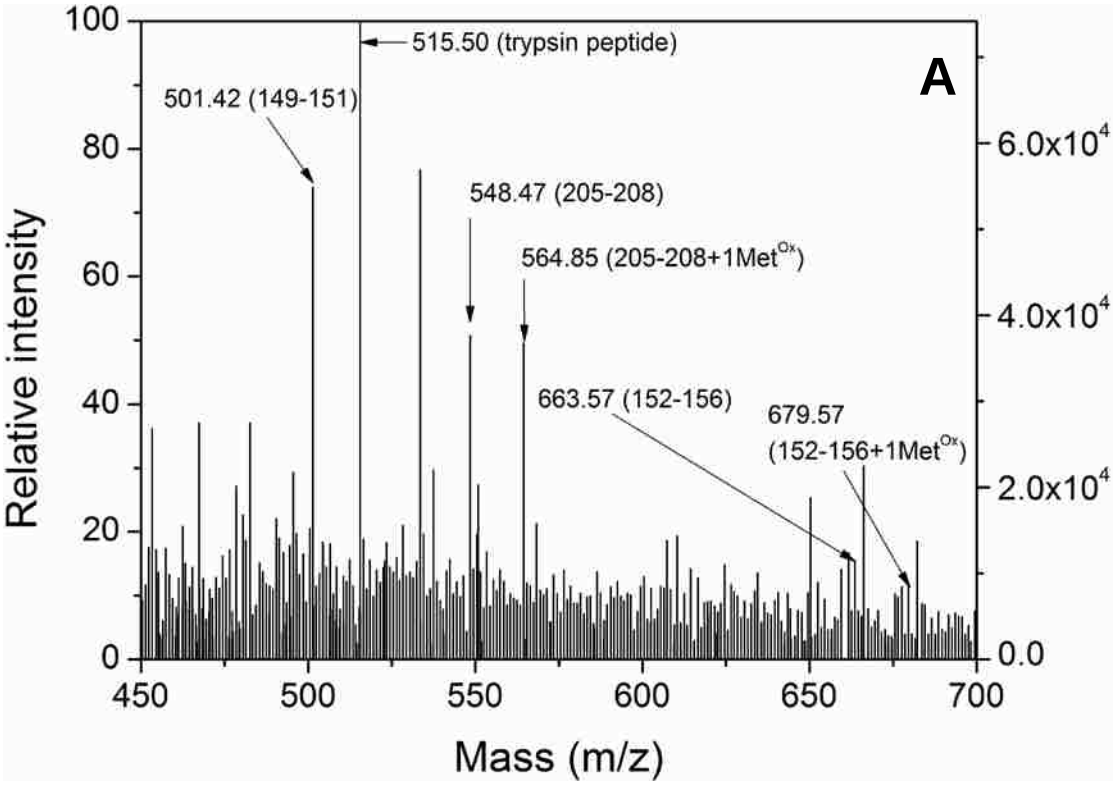
A
515.50 (trypsin peptide)
501.42 (149-151)
548.47 (205-208)
564.85 (205-208+1Met^Ox)
663.57 (152-156)
679.57
(152-156+1Met^Ox)
Relative intensity
Mass (m/z)
100
80
60
40
20
0
450
500
550
600
650
700
6.0x10^4
4.0x10^4
2.0x10^4
0.0

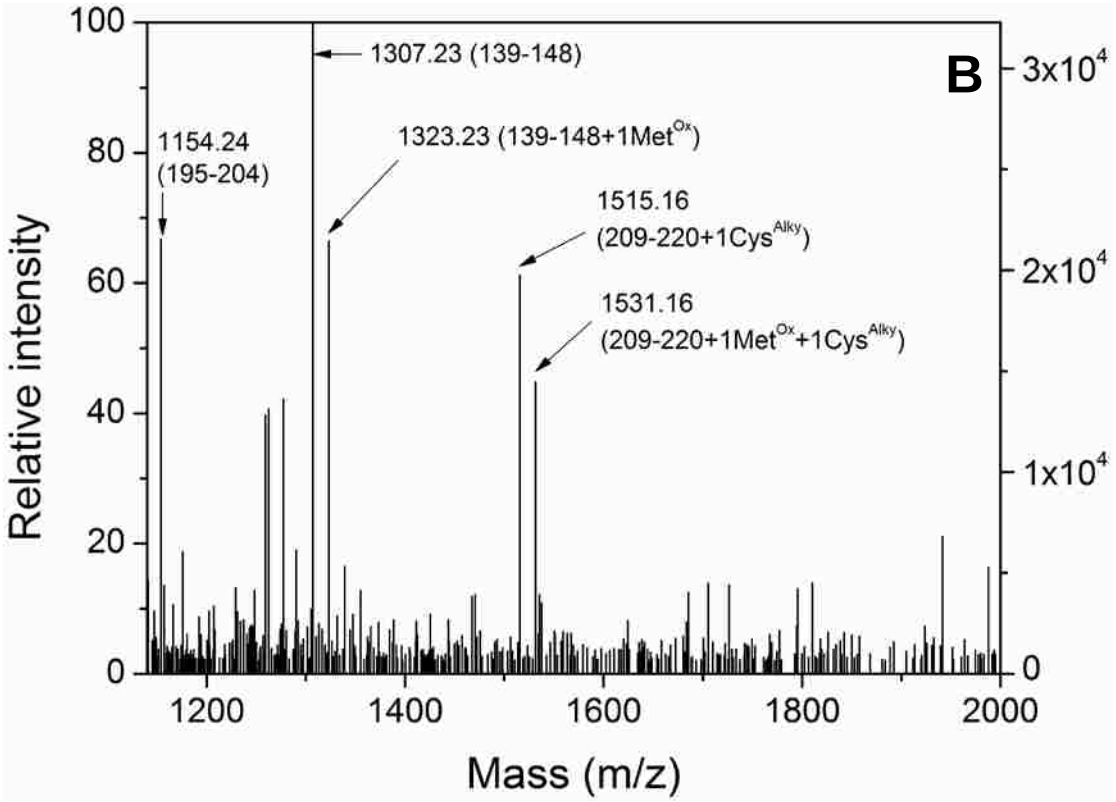
B
1307.23 (139-148)
1154.24
(195-204)
1323.23 (139-148+1Met^Ox)
1515.16
(209-220+1Cys^Alky)
1531.16
(209-220+1Met^Ox+1Cys^Alky)
Relative intensity
Mass (m/z)
100
80
60
40
20
0
1200
1400
1600
1800
2000
3x10^4
2x10^4
1x10^4
0

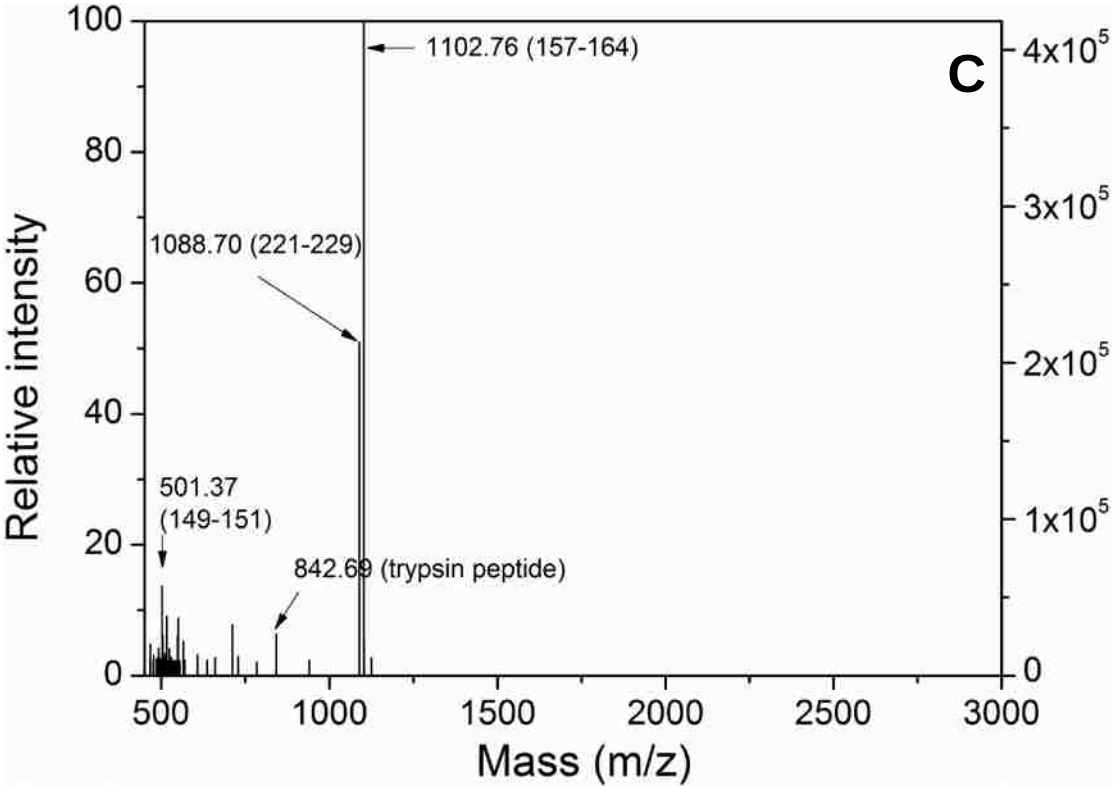

Figure 5-4. MALDI-TOF spectra of in-gel tryptic digest peptides of the 9 KDa PK-resistant fragment of rPrP23-232 fibrils.

After SDS-PAGE, excised bands were in-gel tryptic digested at about 1:10 (w/w) trypsin to protein ration, reduced with 10 mM DTT, and alkylated with 100 mM iodoacetamide. All data were collect in reflectron mode. (A) 450-700 Da mass range; (B) 1140-2000 Da mass range; and (C) 450-3000 Da mass range.

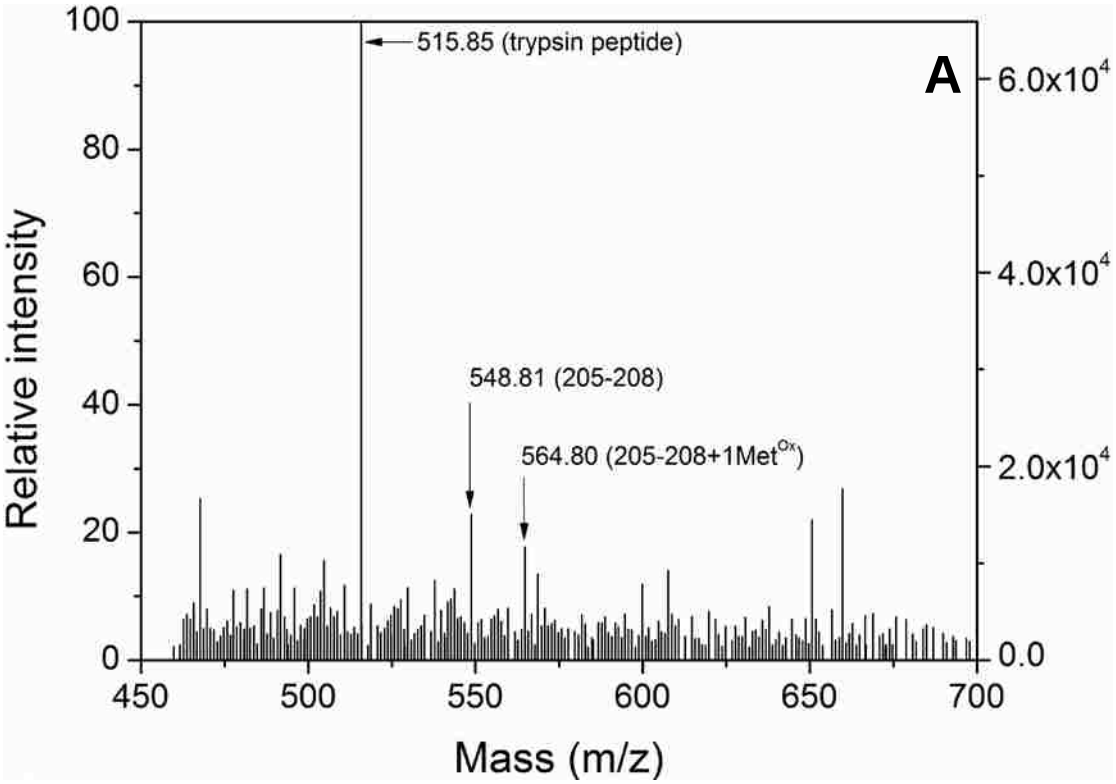
A
515.85 (trypsin peptide)
548.81 (205-208)
564.80 (205-208+1Met^Ox)
Relative intensity
Mass (m/z)
100
80
60
40
20
0
450
500
550
600
650
700
6.0x10^4
4.0x10^4
2.0x10^4
0.0

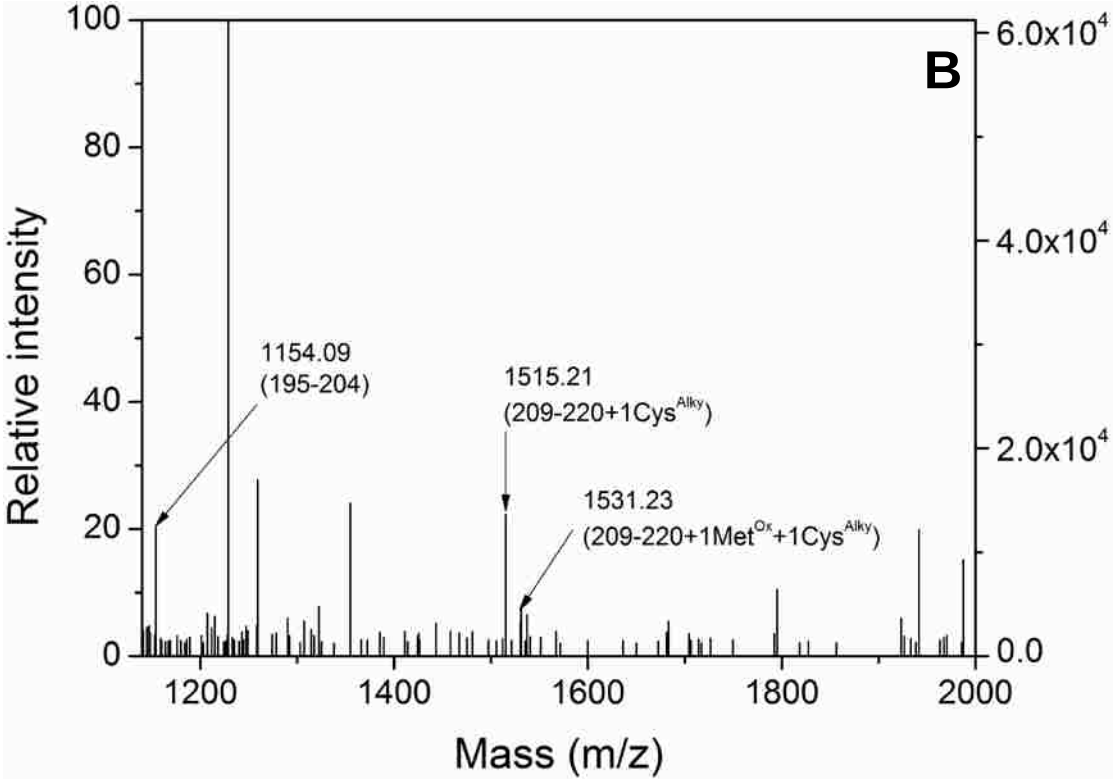
B
1154.09
(195-204)
1515.21
(209-220+1Cys^Alky)
1531.23
(209-220+1Met^Ox+1Cys^Alky)
Relative intensity
Mass (m/z)
100
80
60
40
20
0
1200
1400
1600
1800
2000
6.0x10^4
4.0x10^4
2.0x10^4
0.0

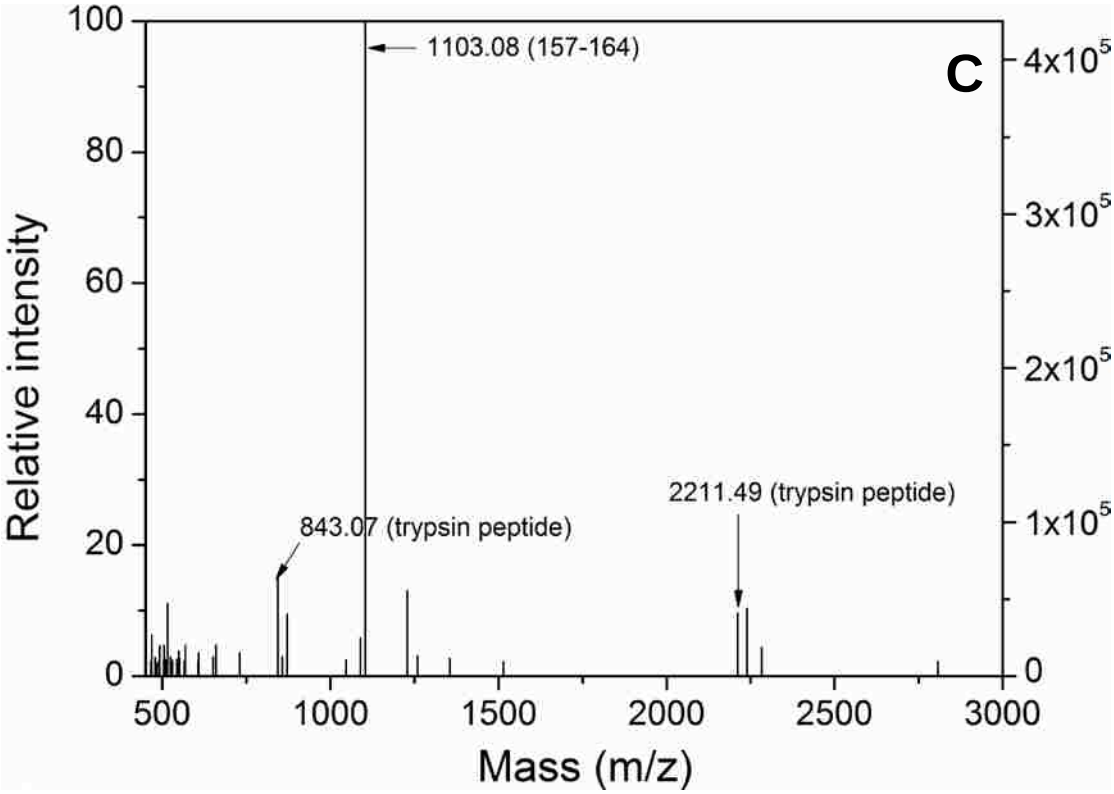

Figure 5-5. MALDI-TOF spectra of in-gel tryptic digest peptides of the 7 KDa PK-resistant fragment of rPrP23-232 fibrils.

After SDS-PAGE, excised bands were in-gel tryptic digested at about 1:10 (w/w) trypsin to protein ration, reduced with 10 mM DTT, and alkylated with 100 mM iodoacetamide. All data were collect in reflectron mode. (A) 450-700 Da mass range; (B) 1140-2000 Da mass range; and (C) 450-3000 Da mass range.

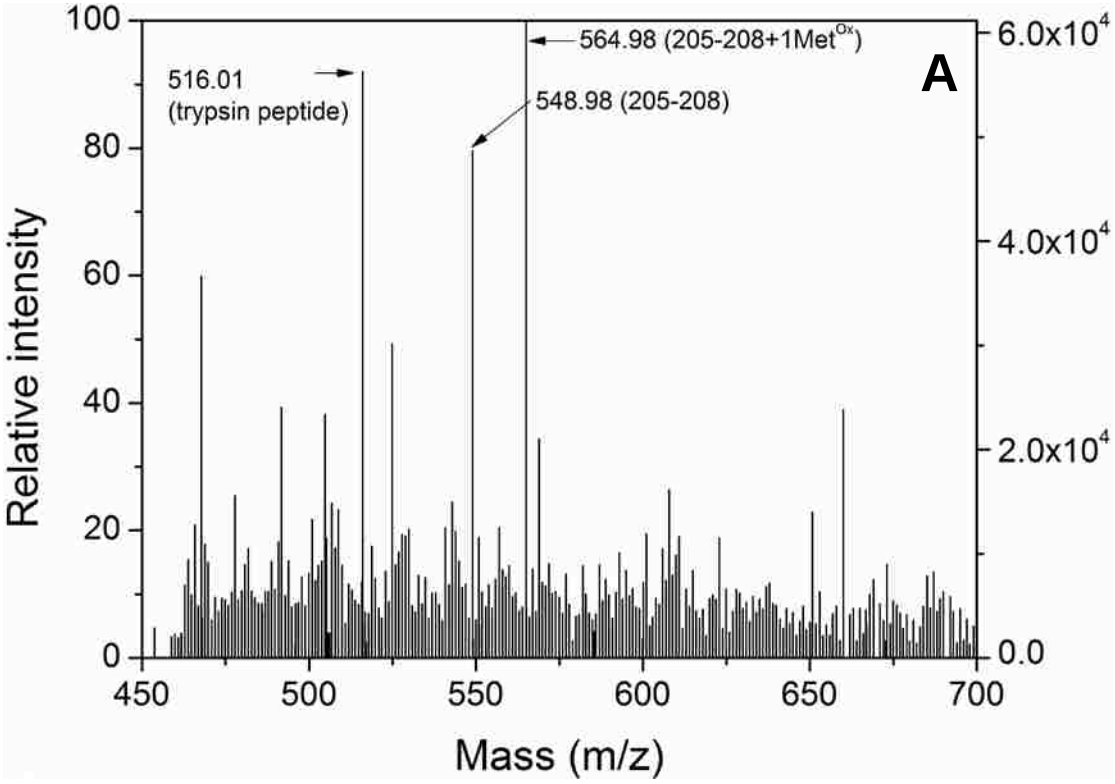
A
564.98 (205-208+1Met^Ox)
516.01
(trypsin peptide)
548.98 (205-208)
Relative intensity
Mass (m/z)
100
80
60
40
20
0
450
500
550
600
650
700
6.0x10^4
4.0x10^4
2.0x10^4
0.0

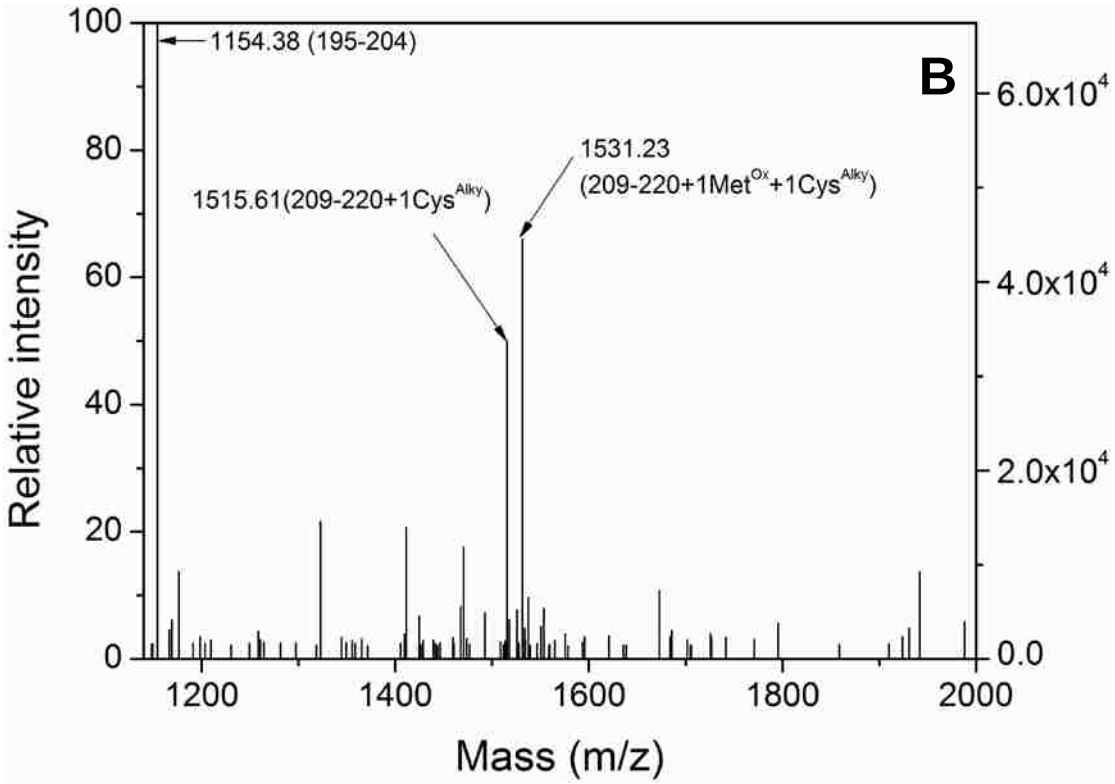
B
1154.38 (195-204)
1531.23
(209-220+1Met^Ox+1Cys^Alky)
1515.61(209-220+1Cys^Alky)
Relative intensity
Mass (m/z)
100
80
60
40
20
0
1200
1400
1600
1800
2000
6.0x10^4
4.0x10^4
2.0x10^4
0.0

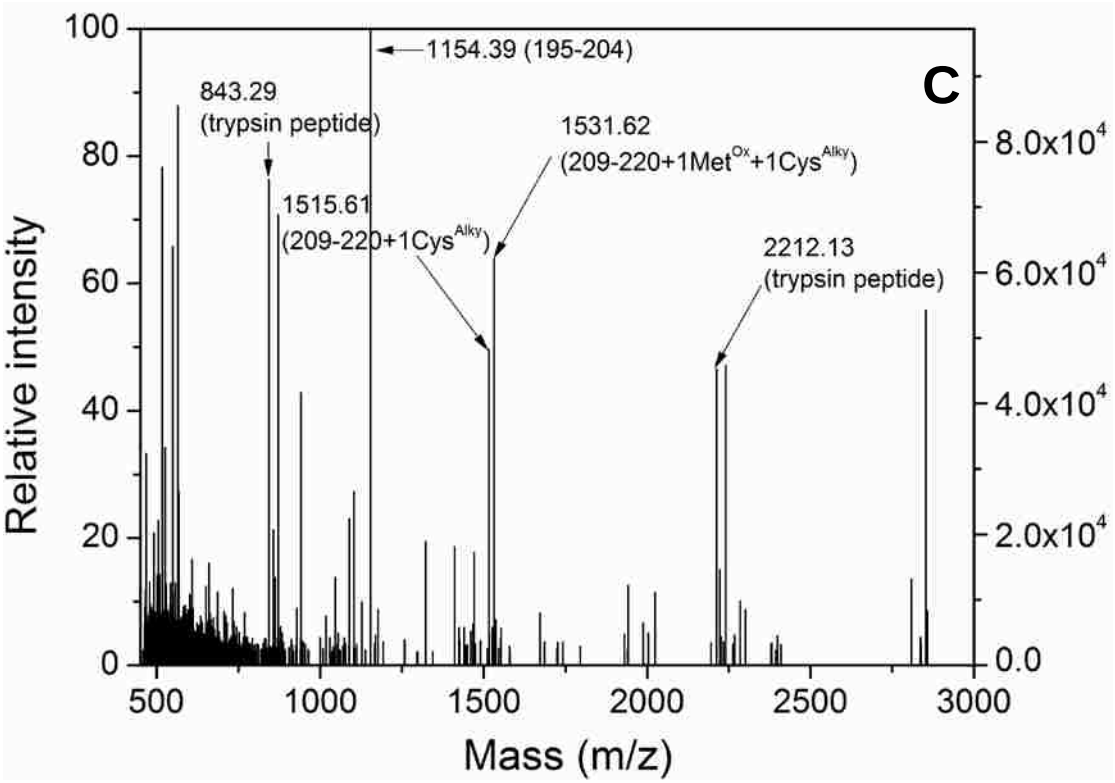

Figure 5-6. MALDI-TOF spectra of in-gel tryptic digest peptides of the 5.5 KDa PK-resistant fragment of rPrP23-232 fibrils.

After SDS-PAGE, excised bands were in-gel tryptic digested at about 1:10 (w/w) trypsin to protein ration, reduced with 10 mM DTT, and alkylated with 100 mM iodoacetamide. All data were collect in reflectron mode. (A) 450-700 Da mass range; (B) 1140-2000 Da mass range; and (C) 450-3000 Da mass range.

Table 1. Parameters for Copper Complexes*

	$g_{\parallel}$	$A_{\parallel}$ (G)	Donor atoms
Type 2 Complexes (light blue)			
$Cu(dtc)_2$	2.09	130	S-S-S-S
CuKTS	2.14	187	S-S-N-N
CuPTS+GSH	2.14	180	S-S-N-N
CuPTS+ascites cells	2.13	178	S-S-N-N
Cu(PTS)(His)	2.19	169	S-N-N-N
CuPTS+en	2.19	169	S-N-N-N
CuPTS	2.20	186	S-N-N-O
$Cu(PTS)(OH_2)$	2.21	185	S-N-N-O
CuBLM	2.21	175	N-N-N-N
CuTPP	2.18	176	N-N-N-N
Cu-serum albumin	2.18	213	N-N-N-N
Cu-carnosine	2.20	190	N-N-N-N
Cu+excess histidine	2.22	183	N-N-N-N
Cu-pMMO	2.24	185	N-N-N-N
Cu^{2+}+ascites cells	2.25	180	N-N-N-N (possibly)
Cu-prion protein	2.23	158	N-N-N-O
CuEDTA(pH 6)	2.29	155	N-N-O-O
Cu^{2+} in excess acetylacetonate	2.28	167	O-O-O-O
$Cu(OH)_4$	2.40	113	O-O-O-O
$CuSO_4$ in DMF	2.40	128	O-O-O-O
Type 1 Complexes (dark blue)			
type 2-depleted fungal laccase	2.19	90	N-N-S
Laccase	2.30	40	N-N-S
Azurin	2.25	57	N-N-S
Mixed Valence Cu-Cu (purple)			
Cu_A-N_2OR	2.18	38	N-Cu-S_2-Cu-N
Cu_A-*CcO* (bovine)	2.18	38	N-Cu-S_2-Cu-N
Cu_A-*CcO* (*R. sphaeroides*)	2.19	30	N-Cu-S_2-Cu-N
Cu_A(engineered in *P. aeruginosa* azurin)	2.18	56	N-Cu-S_2-Cu-N
Cu_2L^{3+}	2.02($g_{\parallel}$<$g_{\perp}$)	~20	N_4-Cu-Cu-N_4

* Abbreviations: dtc, dithiocarbamate; KTS, oxobutyraldehyde bis(thiosemicarbazones); PTS, 2-formylpyridine monothiosemicarbazone; en, ethylenediamine; His, histidine; BLM, bleomycin; TPP, tetraphenylporphyrin; pMMO, particulate methanemonooxygenase; EDTA, ethylenedeaminetetraacetic acid; DMF, dimethylformamide; N_2OR, nitrous oxide reductase; *CcO*, cytochrome *c* oxidase, L, $N[CH_2CH_2N(H)CH_2CH_2N(H)CH_2CH_2]_3N$.
NOTE: net charges of the cupric complexes are not indicated.

Table 5-1. Parameters for copper complexes (expansion of the original Peisach-Blumberg plot).

This table includes a list of copper model compounds, their EPR parameters, and coordination configuration (reproduced from reference [405], reprinted with permission from Springer, Copyright 2005).

CHAPTER VI:

REFERENCES

1. Alper, T., D.A. Haig, and M.C. Clarke, *The exceptionally small size of the scrapie agent.* Biochemical and biophysical research communications, 1966. **22**(3): p. 278-84.
2. Griffith, J.S., *Self-replication and scrapie.* Nature, 1967. **215**(5105): p. 1043-4.
3. Prusiner, S.B., *Novel proteinaceous infectious particles cause scrapie.* Science, 1982. **216**(4542): p. 136-44.
4. Prusiner, S.B., D.F. Groth, D.C. Bolton, S.B. Kent, and L.E. Hood, *Purification and structural studies of a major scrapie prion protein.* Cell, 1984. **38**(1): p. 127-34.
5. Maji, S.K., M.H. Perrin, M.R. Sawaya, S. Jessberger, K. Vadodaria, R.A. Rissman, P.S. Singru, K.P. Nilsson, R. Simon, D. Schubert, D. Eisenberg, J. Rivier, P. Sawchenko, W. Vale, and R. Riek, *Functional amyloids as natural storage of peptide hormones in pituitary secretory granules.* Science, 2009. **325**(5938): p. 328-32.
6. Miller, G., *Neurodegeneration. Could they all be prion diseases?* Science, 2009. **326**(5958): p. 1337-9.
7. Wickner, R.B., H.K. Edskes, F. Shewmaker, T. Nakayashiki, A. Engel, L. McCann, and D. Kryndushkin, *Yeast prions: evolution of the prion concept.* Prion, 2007. **1**(2): p. 94-100.
8. Wickner, R.B., F. Shewmaker, D. Kryndushkin, and H.K. Edskes, *Protein inheritance (prions) based on parallel in-register beta-sheet amyloid structures.* BioEssays : news and reviews in molecular, cellular and developmental biology, 2008. **30**(10): p. 955-64.
9. Sipe, J.D. and A.S. Cohen, *Review: history of the amyloid fibril.* J Struct Biol, 2000. **130**(2-3): p. 88-98.
10. Olanow, C.W. and S.B. Prusiner, *Is Parkinson's disease a prion disorder?* Proc Natl Acad Sci U S A, 2009. **106**(31): p. 12571-2.
11. Prusiner, S.B., *Prion diseases and the BSE crisis.* Science, 1997. **278**(5336): p. 245-51.
12. Aguzzi, A., *Cell biology: Beyond the prion principle.* Nature, 2009. **459**(7249): p. 924-5.
13. Prusiner, S.B., *Prions.* Proc Natl Acad Sci U S A, 1998. **95**(23): p. 13363-83.
14. Schneider, K., H. Fangerau, B. Michaelsen, and W.H. Raab, *The early history of the transmissible spongiform encephalopathies exemplified by scrapie.* Brain Res Bull, 2008. **77**(6): p. 343-55.
15. Hinnell, C., M.B. Coulthart, G.H. Jansen, N.R. Cashman, J. Lauzon, A. Clark, F. Costello, C. White, R. Midha, S. Wiebe, and S. Furtado, *Gerstmann-Straussler-Scheinker disease due to a novel prion protein gene mutation.* Neurology, 2011. **76**(5): p. 485-7.
16. Castilla, J., C. Hetz, and C. Soto, *Molecular mechanisms of neurotoxicity of pathological prion protein.* Curr Mol Med, 2004. **4**(4): p. 397-403.
17. Mallucci, G.R., *Prion neurodegeneration: Starts and stops at the synapse.* Prion, 2009. **3**(4).
18. Kovacs, G.G. and H. Budka, *Molecular pathology of human prion diseases.* International journal of molecular sciences, 2009. **10**(3): p. 976-99.
19. Soto, C., *Unfolding the role of protein misfolding in neurodegenerative diseases.* Nat Rev Neurosci, 2003. **4**(1): p. 49-60.
20. Hainfellner, J.A., P.P. Liberski, D.C. Guiroy, L. Cervenakova, P. Brown, D.C. Gajdusek, and H. Budka, *Pathology and immunocytochemistry of a kuru brain.* Brain Pathol, 1997. **7**(1): p. 547-53.
21. Abrahantes, J.C., M. Aerts, B. van Everbroeck, C. Saegerman, D. Berkvens, H. Geys, K. Mintiens, S. Roels, and P. Cras, *Classification of sporadic Creutzfeldt-Jakob disease based on clinical and neuropathological characteristics.* Eur J Epidemiol, 2007. **22**(7): p. 457-65.

22. Ironside, J.W. and M.W. Head, *Neuropathology and molecular biology of variant Creutzfeldt-Jakob disease.* Current topics in microbiology and immunology, 2004. **284**: p. 133-59.
23. Gambetti, P., Q. Kong, W. Zou, P. Parchi, and S.G. Chen, *Sporadic and familial CJD: classification and characterisation.* British medical bulletin, 2003. **66**: p. 213-39.
24. Gambetti, P., Z. Dong, J. Yuan, X. Xiao, M. Zheng, A. Alshekhlee, R. Castellani, M. Cohen, M.A. Barria, D. Gonzalez-Romero, E.D. Belay, L.B. Schonberger, K. Marder, C. Harris, J.R. Burke, T. Montine, T. Wisniewski, D.W. Dickson, C. Soto, C.M. Hulette, J.A. Mastrianni, Q. Kong, and W.Q. Zou, *A novel human disease with abnormal prion protein sensitive to protease.* Ann Neurol, 2008. **63**(6): p. 697-708.
25. Collinge, J., J. Whitfield, E. McKintosh, J. Beck, S. Mead, D.J. Thomas, and M.P. Alpers, *Kuru in the 21st century--an acquired human prion disease with very long incubation periods.* Lancet, 2006. **367**(9528): p. 2068-74.
26. Collinge, J., *Prion diseases of humans and animals: their causes and molecular basis.* Annu Rev Neurosci, 2001. **24**: p. 519-50.
27. DeArmond, S.J. and S.B. Prusiner, *Etiology and pathogenesis of prion diseases.* Am J Pathol, 1995. **146**(4): p. 785-811.
28. Unit, T.N.C.-J.D.R.S. *Variant Creutzfeldt-Jakob Disease Current Data*. 2012 [cited 2012 04/20]; Available from: http://www.cjd.ed.ac.uk/vcjdworld.htm.
29. Aguzzi, A., C. Sigurdson, and M. Heikenwaelder, *Molecular mechanisms of prion pathogenesis.* Annu Rev Pathol, 2008. **3**: p. 11-40.
30. Da Costa Dias, B. and S.F. Weiss, *A kiss of a prion: new implications for oral transmissibility.* J Infect Dis, 2010. **201**(11): p. 1615-6.
31. Corona, C., C. Porcario, F. Martucci, B. Iulini, B. Manea, M. Gallo, C. Palmitessa, C. Maurella, M. Mazza, M. Pezzolato, P. Acutis, and C. Casalone, *Olfactory system involvement in natural scrapie disease.* J Virol, 2009. **83**(8): p. 3657-67.
32. Haley, N.J., C.K. Mathiason, S. Carver, M. Zabel, G.C. Telling, and E.A. Hoover, *Detection of CWD prions in salivary, urinary, and intestinal tissues of deer: potential mechanisms of prion shedding and transmission.* J Virol, 2011.
33. Castilla, J., A. Brun, F. Diaz-San Segundo, F.J. Salguero, A. Gutierrez-Adan, B. Pintado, M.A. Ramirez, L. del Riego, and J.M. Torres, *Vertical transmission of bovine spongiform encephalopathy prions evaluated in a transgenic mouse model.* J Virol, 2005. **79**(13): p. 8665-8.
34. Murray, K., J. Peters, L. Stellitano, A.M. Winstone, C. Verity, and R.G. Will, *Is there evidence of vertical transmission of variant Creutzfeldt-Jakob disease?* J Neurol Neurosurg Psychiatry, 2010.
35. Palmer, M.S., A.J. Dryden, J.T. Hughes, and J. Collinge, *Homozygous prion protein genotype predisposes to sporadic Creutzfeldt-Jakob disease.* Nature, 1991. **352**(6333): p. 340-2.
36. Collinge, J., M.S. Palmer, and A.J. Dryden, *Genetic predisposition to iatrogenic Creutzfeldt-Jakob disease.* Lancet, 1991. **337**(8755): p. 1441-2.
37. Hizume, M., A. Kobayashi, K. Teruya, H. Ohashi, J.W. Ironside, S. Mohri, and T. Kitamoto, *Human prion protein (PrP) 219K is converted to PrPSc but shows heterozygous inhibition in variant Creutzfeldt-Jakob disease infection.* J Biol Chem, 2009. **284**(6): p. 3603-9.
38. Brandel, J.P., C.A. Heath, M.W. Head, E. Levavasseur, R. Knight, J.L. Laplanche, J.P. Langeveld,

J.W. Ironside, J.J. Hauw, J. Mackenzie, A. Alperovitch, R.G. Will, and S. Haik, *Variant Creutzfeldt-Jakob disease in France and the United Kingdom: Evidence for the same agent strain.* Ann Neurol, 2009. **65**(3): p. 249-56.

39. Armstrong, R.A., P.L. Lantos, and N.J. Cairns, *What determines the molecular composition of abnormal protein aggregates in neurodegenerative disease?* Neuropathology, 2008. **28**(4): p. 351-65.
40. Goldfarb, L.G., R.B. Petersen, M. Tabaton, P. Brown, A.C. LeBlanc, P. Montagna, P. Cortelli, J. Julien, C. Vital, W.W. Pendelbury, and et al., *Fatal familial insomnia and familial Creutzfeldt-Jakob disease: disease phenotype determined by a DNA polymorphism.* Science, 1992. **258**(5083): p. 806-8.
41. Lee, S., L. Antony, R. Hartmann, K.J. Knaus, K. Surewicz, W.K. Surewicz, and V.C. Yee, *Conformational diversity in prion protein variants influences intermolecular beta-sheet formation.* EMBO J, 2010. **29**(1): p. 251-62.
42. Caughey, B. and G.S. Baron, *Prions and their partners in crime.* Nature, 2006. **443**(7113): p. 803-10.
43. Bueler, H., A. Aguzzi, A. Sailer, R.A. Greiner, P. Autenried, M. Aguet, and C. Weissmann, *Mice devoid of PrP are resistant to scrapie.* Cell, 1993. **73**(7): p. 1339-47.
44. Kocisko, D.A., J.H. Come, S.A. Priola, B. Chesebro, G.J. Raymond, P.T. Lansbury, and B. Caughey, *Cell-free formation of protease-resistant prion protein.* Nature, 1994. **370**(6489): p. 471-4.
45. Saborio, G.P., B. Permanne, and C. Soto, *Sensitive detection of pathological prion protein by cyclic amplification of protein misfolding.* Nature, 2001. **411**(6839): p. 810-3.
46. Castilla, J., P. Saa, C. Hetz, and C. Soto, *In vitro generation of infectious scrapie prions.* Cell, 2005. **121**(2): p. 195-206.
47. Barria, M.A., A. Mukherjee, D. Gonzalez-Romero, R. Morales, and C. Soto, *De novo generation of infectious prions in vitro produces a new disease phenotype.* PLoS Pathog, 2009. **5**(5): p. e1000421.
48. Deleault, N.R., B.T. Harris, J.R. Rees, and S. Supattapone, *Formation of native prions from minimal components in vitro.* Proc Natl Acad Sci U S A, 2007. **104**(23): p. 9741-6.
49. Legname, G., I.V. Baskakov, H.O. Nguyen, D. Riesner, F.E. Cohen, S.J. DeArmond, and S.B. Prusiner, *Synthetic mammalian prions.* Science, 2004. **305**(5684): p. 673-6.
50. Colby, D.W., K. Giles, G. Legname, H. Wille, I.V. Baskakov, S.J. DeArmond, and S.B. Prusiner, *Design and construction of diverse mammalian prion strains.* Proceedings of the National Academy of Sciences of the United States of America, 2009. **106**(48): p. 20417-22.
51. Baskakov, I.V. and L. Breydo, *Converting the prion protein: what makes the protein infectious.* Biochim Biophys Acta, 2007. **1772**(6): p. 692-703.
52. Makarava, N., G.G. Kovacs, O. Bocharova, R. Savtchenko, I. Alexeeva, H. Budka, R.G. Rohwer, and I.V. Baskakov, *Recombinant prion protein induces a new transmissible prion disease in wild-type animals.* Acta Neuropathol, 2010. **119**(2): p. 177-87.
53. Wang, F., X. Wang, C.G. Yuan, and J. Ma, *Generating a prion with bacterially expressed recombinant prion protein.* Science, 2010. **327**(5969): p. 1132-5.
54. Manuelidis, L., Y. Liu, and B. Mullins, *Strain-specific viral properties of variant Creutzfeldt-Jakob disease (vCJD) are encoded by the agent and not by host prion protein.* J Cell Biochem, 2009. **106**(2): p. 220-31.

55. Radulescu, R.T. and C. Korth, *Prion function and dysfunction: a structure-based scenario.* Med Hypotheses, 1996. **46**(3): p. 225-8.
56. Caughey, B., G.J. Raymond, and R.A. Bessen, *Strain-dependent differences in beta-sheet conformations of abnormal prion protein.* J Biol Chem, 1998. **273**(48): p. 32230-5.
57. Makarava, N. and I.V. Baskakov, *The same primary structure of the prion protein yields two distinct self-propagating states.* J Biol Chem, 2008. **283**(23): p. 15988-96.
58. Baskakov, I.V., *Switching in amyloid structure within individual fibrils: implication for strain adaptation, species barrier and strain classification.* FEBS Lett, 2009. **583**(16): p. 2618-22.
59. Wiltzius, J.J., M. Landau, R. Nelson, M.R. Sawaya, M.I. Apostol, L. Goldschmidt, A.B. Soriaga, D. Cascio, K. Rajashankar, and D. Eisenberg, *Molecular mechanisms for protein-encoded inheritance.* Nat Struct Mol Biol, 2009. **16**(9): p. 973-8.
60. Soto, C., *Protein misfolding and disease; protein refolding and therapy.* FEBS letters, 2001. **498**(2-3): p. 204-7.
61. Kane, M.D., W.J. Lipinski, M.J. Callahan, F. Bian, R.A. Durham, R.D. Schwarz, A.E. Roher, and L.C. Walker, *Evidence for seeding of beta -amyloid by intracerebral infusion of Alzheimer brain extracts in beta -amyloid precursor protein-transgenic mice.* J Neurosci, 2000. **20**(10): p. 3606-11.
62. Meyer-Luehmann, M., J. Coomaraswamy, T. Bolmont, S. Kaeser, C. Schaefer, E. Kilger, A. Neuenschwander, D. Abramowski, P. Frey, A.L. Jaton, J.M. Vigouret, P. Paganetti, D.M. Walsh, P.M. Mathews, J. Ghiso, M. Staufenbiel, L.C. Walker, and M. Jucker, *Exogenous induction of cerebral beta-amyloidogenesis is governed by agent and host.* Science, 2006. **313**(5794): p. 1781-4.
63. Desplats, P., H.J. Lee, E.J. Bae, C. Patrick, E. Rockenstein, L. Crews, B. Spencer, E. Masliah, and S.J. Lee, *Inclusion formation and neuronal cell death through neuron-to-neuron transmission of alpha-synuclein.* Proc Natl Acad Sci U S A, 2009. **106**(31): p. 13010-5.
64. Danzer, K.M., S.K. Krebs, M. Wolff, G. Birk, and B. Hengerer, *Seeding induced by alpha-synuclein oligomers provides evidence for spreading of alpha-synuclein pathology.* J Neurochem, 2009. **111**(1): p. 192-203.
65. Morales, R., L.D. Estrada, R. Diaz-Espinoza, D. Morales-Scheihing, M.C. Jara, J. Castilla, and C. Soto, *Molecular cross talk between misfolded proteins in animal models of Alzheimer's and prion diseases.* J Neurosci, 2010. **30**(13): p. 4528-35.
66. Cobb, N.J. and W.K. Surewicz, *Prion diseases and their biochemical mechanisms.* Biochemistry, 2009. **48**(12): p. 2574-85.
67. Caughey, B., G.S. Baron, B. Chesebro, and M. Jeffrey, *Getting a grip on prions: oligomers, amyloids, and pathological membrane interactions.* Annu Rev Biochem, 2009. **78**: p. 177-204.
68. Lundmark, K., G.T. Westermark, S. Nystrom, C.L. Murphy, A. Solomon, and P. Westermark, *Transmissibility of systemic amyloidosis by a prion-like mechanism.* Proc Natl Acad Sci U S A, 2002. **99**(10): p. 6979-84.
69. Zhang, B., Y. Une, X. Fu, J. Yan, F. Ge, J. Yao, J. Sawashita, M. Mori, H. Tomozawa, F. Kametani, and K. Higuchi, *Fecal transmission of AA amyloidosis in the cheetah contributes to high incidence of disease.* Proc Natl Acad Sci U S A, 2008. **105**(20): p. 7263-8.
70. Solomon, A., T. Richey, C.L. Murphy, D.T. Weiss, J.S. Wall, G.T. Westermark, and P. Westermark, *Amyloidogenic potential of foie gras.* Proc Natl Acad Sci U S A, 2007. **104**(26): p.

10998-1001.

71. Stahl, N., D.R. Borchelt, K. Hsiao, and S.B. Prusiner, *Scrapie prion protein contains a phosphatidylinositol glycolipid.* Cell, 1987. **51**(2): p. 229-40.
72. Kim, Y., J. Lee, and C. Lee, *In silico comparative analysis of DNA and amino acid sequences for prion protein gene.* Transbound Emerg Dis, 2008. **55**(2): p. 105-14.
73. Moser, M., R.J. Colello, U. Pott, and B. Oesch, *Developmental expression of the prion protein gene in glial cells.* Neuron, 1995. **14**(3): p. 509-17.
74. Guest, W.C., S.S. Plotkin, and N.R. Cashman, *Toward a mechanism of prion misfolding and structural models of PrP(Sc): current knowledge and future directions.* J Toxicol Environ Health A, 2011. **74**(2-4): p. 154-60.
75. Riek, R., S. Hornemann, G. Wider, M. Billeter, R. Glockshuber, and K. Wuthrich, *NMR structure of the mouse prion protein domain PrP(121-321).* Nature, 1996. **382**(6587): p. 180-2.
76. Knaus, K.J., M. Morillas, W. Swietnicki, M. Malone, W.K. Surewicz, and V.C. Yee, *Crystal structure of the human prion protein reveals a mechanism for oligomerization.* Nat Struct Biol, 2001. **8**(9): p. 770-4.
77. Wuthrich, K. and R. Riek, *Three-dimensional structures of prion proteins.* Adv Protein Chem, 2001. **57**: p. 55-82.
78. Forloni, G., N. Angeretti, R. Chiesa, E. Monzani, M. Salmona, O. Bugiani, and F. Tagliavini, *Neurotoxicity of a prion protein fragment.* Nature, 1993. **362**(6420): p. 543-6.
79. Henriques, S.T. and M.A. Castanho, *Is PrP(106-126) Fragment Involved in the Membrane Activity of the Prion Protein?* Curr Protein Pept Sci, 2010. **11**(5): p. 326-33.
80. Alier, K., Z. Li, D. Mactavish, D. Westaway, and J.H. Jhamandas, *Ionic mechanisms of action of prion protein fragment PrP(106-126) in rat basal forebrain neurons.* J Neurosci Res, 2010. **88**(10): p. 2217-27.
81. Walsh, P., J. Yau, K. Simonetti, and S. Sharpe, *Morphology and secondary structure of stable beta-oligomers formed by amyloid peptide PrP(106-126).* Biochemistry, 2009. **48**(25): p. 5779-81.
82. Dorosz, J., R. Volinsky, E. Bazar, S. Kolusheva, and R. Jelinek, *Phospholipid-induced fibrillation of a prion amyloidogenic determinant at the air/water interface.* Langmuir, 2009. **25**(21): p. 12501-6.
83. Walsh, P., K. Simonetti, and S. Sharpe, *Core structure of amyloid fibrils formed by residues 106-126 of the human prion protein.* Structure, 2009. **17**(3): p. 417-26.
84. Solomon, I.H., J.E. Huettner, and D.A. Harris, *Neurotoxic mutants of the prion protein induce spontaneous ionic currents in cultured cells.* The Journal of biological chemistry, 2010. **285**(34): p. 26719-26.
85. Solomon, I.H., N. Khatri, E. Biasini, T. Massignan, J.E. Huettner, and D.A. Harris, *An N-terminal Polybasic Domain and Cell Surface Localization Are Required for Mutant Prion Protein Toxicity.* J Biol Chem, 2011. **286**(16): p. 14724-36.
86. Solomon, I.H., J.A. Schepker, and D.A. Harris, *Prion neurotoxicity: insights from prion protein mutants.* Curr Issues Mol Biol, 2010. **12**(2): p. 51-61.
87. James, T.L., H. Liu, N.B. Ulyanov, S. Farr-Jones, H. Zhang, D.G. Donne, K. Kaneko, D. Groth, I. Mehlhorn, S.B. Prusiner, and F.E. Cohen, *Solution structure of a 142-residue recombinant prion protein corresponding to the infectious fragment of the scrapie isoform.* Proc Natl

Acad Sci U S A, 1997. **94**(19): p. 10086-91.

88. Haigh, C.L., S.Y. Marom, and S.J. Collins, *Copper, endoproteolytic processing of the prion protein and cell signalling.* Front Biosci, 2010. **15**: p. 1086-104.
89. Zahn, R., *The octapeptide repeats in mammalian prion protein constitute a pH-dependent folding and aggregation site.* Journal of molecular biology, 2003. **334**(3): p. 477-88.
90. Dong, S.L., S.A. Cadamuro, F. Fiorino, U. Bertsch, L. Moroder, and C. Renner, *Copper binding and conformation of the N-terminal octarepeats of the prion protein in the presence of DPC micelles as membrane mimetic.* Biopolymers, 2007. **88**(6): p. 840-7.
91. Millhauser, G.L., *Copper binding in the prion protein.* Acc Chem Res, 2004. **37**(2): p. 79-85.
92. Taubner, L.M., E.A. Bienkiewicz, V. Copie, and B. Caughey, *Structure of the Flexible Amino-Terminal Domain of Prion Protein Bound to a Sulfated Glycan.* J Mol Biol, 2010. **395**(3): p. 475-490.
93. Riek, R., G. Wider, M. Billeter, S. Hornemann, R. Glockshuber, and K. Wuthrich, *Prion protein NMR structure and familial human spongiform encephalopathies.* Proceedings of the National Academy of Sciences of the United States of America, 1998. **95**(20): p. 11667-72.
94. Hosszu, L.L., N.J. Baxter, G.S. Jackson, A. Power, A.R. Clarke, J.P. Waltho, C.J. Craven, and J. Collinge, *Structural mobility of the human prion protein probed by backbone hydrogen exchange.* Nature structural biology, 1999. **6**(8): p. 740-3.
95. Swietnicki, W., R.B. Petersen, P. Gambetti, and W.K. Surewicz, *Familial mutations and the thermodynamic stability of the recombinant human prion protein.* The Journal of biological chemistry, 1998. **273**(47): p. 31048-52.
96. van der Kamp, M.W. and V. Daggett, *The consequences of pathogenic mutations to the human prion protein.* Protein Eng Des Sel, 2009. **22**(8): p. 461-8.
97. Apetri, A.C., K. Surewicz, and W.K. Surewicz, *The effect of disease-associated mutations on the folding pathway of human prion protein.* The Journal of biological chemistry, 2004. **279**(17): p. 18008-14.
98. Hart, T., L.L. Hosszu, C.R. Trevitt, G.S. Jackson, J.P. Waltho, J. Collinge, and A.R. Clarke, *Folding kinetics of the human prion protein probed by temperature jump.* Proc Natl Acad Sci U S A, 2009. **106**(14): p. 5651-6.
99. Calzolai, L. and R. Zahn, *Influence of pH on NMR structure and stability of the human prion protein globular domain.* The Journal of biological chemistry, 2003. **278**(37): p. 35592-6.
100. Tseng, C.Y., C.P. Yu, and H.C. Lee, *Integrity of H1 helix in prion protein revealed by molecular dynamic simulations to be especially vulnerable to changes in the relative orientation of H1 and its S1 flank.* Eur Biophys J, 2009. **38**(5): p. 601-11.
101. Welker, E., L.D. Raymond, H.A. Scheraga, and B. Caughey, *Intramolecular versus intermolecular disulfide bonds in prion proteins.* The Journal of biological chemistry, 2002. **277**(36): p. 33477-81.
102. Zahn, R., A. Liu, T. Luhrs, R. Riek, C. von Schroetter, F. Lopez Garcia, M. Billeter, L. Calzolai, G. Wider, and K. Wuthrich, *NMR solution structure of the human prion protein.* Proceedings of the National Academy of Sciences of the United States of America, 2000. **97**(1): p. 145-50.
103. Gossert, A.D., S. Bonjour, D.A. Lysek, F. Fiorito, and K. Wuthrich, *Prion protein NMR structures of elk and of mouse/elk hybrids.* Proceedings of the National Academy of Sciences of the United States of America, 2005. **102**(3): p. 646-50.
104. Soto, C., *Constraining the loop, releasing prion infectivity.* Proceedings of the National

Academy of Sciences of the United States of America, 2009. **106**(1): p. 10-1.

105. Christen, B., S. Hornemann, F.F. Damberger, and K. Wuthrich, *Prion protein NMR structure from tammar wallaby (Macropus eugenii) shows that the beta2-alpha2 loop is modulated by long-range sequence effects.* Journal of molecular biology, 2009. **389**(5): p. 833-45.
106. Sigurdson, C.J., K.P. Nilsson, S. Hornemann, M. Heikenwalder, G. Manco, P. Schwarz, D. Ott, T. Rulicke, P.P. Liberski, C. Julius, J. Falsig, L. Stitz, K. Wuthrich, and A. Aguzzi, *De novo generation of a transmissible spongiform encephalopathy by mouse transgenesis.* Proc Natl Acad Sci U S A, 2009. **106**(1): p. 304-9.
107. DeMarco, M.L. and V. Daggett, *Characterization of cell-surface prion protein relative to its recombinant analogue: insights from molecular dynamics simulations of diglycosylated, membrane-bound human prion protein.* J Neurochem, 2009. **109**(1): p. 60-73.
108. Chakrabarti, O., A. Ashok, and R.S. Hegde, *Prion protein biosynthesis and its emerging role in neurodegeneration.* Trends Biochem Sci, 2009. **34**(6): p. 287-95.
109. Tatzelt, J. and K.F. Winklhofer, *Folding and misfolding of the prion protein in the secretory pathway.* Amyloid, 2004. **11**(3): p. 162-72.
110. Walter, P., R. Gilmore, and G. Blobel, *Protein translocation across the endoplasmic reticulum.* Cell, 1984. **38**(1): p. 5-8.
111. Chen, L., Y. Yang, J. Han, B.Y. Zhang, L. Zhao, K. Nie, X.F. Wang, F. Li, C. Gao, X.P. Dong, and C.M. Xu, *Removal of the glycosylation of prion protein provokes apoptosis in SF126.* J Biochem Mol Biol, 2007. **40**(5): p. 662-9.
112. Ermonval, M., D. Petit, A. Le Duc, O. Kellermann, and P.F. Gallet, *Glycosylation-related genes are variably expressed depending on the differentiation state of a bioaminergic neuronal cell line: implication for the cellular prion protein.* Glycoconj J, 2009. **26**(4): p. 477-93.
113. Taylor, D.R., I.J. Whitehouse, and N.M. Hooper, *Glypican-1 mediates both prion protein lipid raft association and disease isoform formation.* PLoS Pathog, 2009. **5**(11): p. e1000666.
114. Martins, V.R., F.H. Beraldo, G.N. Hajj, M.H. Lopes, K.S. Lee, M.M. Prado, and R. Linden, *Prion protein: orchestrating neurotrophic activities.* Curr Issues Mol Biol, 2010. **12**(2): p. 63-86.
115. Kang, Y.S., X. Zhao, J. Lovaas, E. Eisenberg, and L.E. Greene, *Clathrin-independent internalization of normal cellular prion protein in neuroblastoma cells is associated with the Arf6 pathway.* J Cell Sci, 2009. **122**(Pt 22): p. 4062-9.
116. Deriziotis, P. and S.J. Tabrizi, *Prions and the proteasome.* Biochim Biophys Acta, 2008. **1782**(12): p. 713-22.
117. Ma, J., R. Wollmann, and S. Lindquist, *Neurotoxicity and neurodegeneration when PrP accumulates in the cytosol.* Science, 2002. **298**(5599): p. 1781-5.
118. Lin, D.T., J. Jodoin, M. Baril, C.G. Goodyer, and A.C. Leblanc, *Cytosolic prion protein is the predominant anti-Bax prion protein form: exclusion of transmembrane and secreted prion protein forms in the anti-Bax function.* Biochim Biophys Acta, 2008. **1783**(10): p. 2001-12.
119. Solomon, I.H., J.A. Schepker, and D.A. Harris, *Prion Neurotoxicity: Insights from Prion Protein Mutants.* Curr Issues Mol Biol, 2009. **12**(2): p. 51-62.
120. Borchelt, D.R., M. Rogers, N. Stahl, G. Telling, and S.B. Prusiner, *Release of the cellular prion protein from cultured cells after loss of its glycoinositol phospholipid anchor.* Glycobiology, 1993. **3**(4): p. 319-29.
121. Parkin, E.T., N.T. Watt, A.J. Turner, and N.M. Hooper, *Dual mechanisms for shedding of the cellular prion protein.* J Biol Chem, 2004. **279**(12): p. 11170-8.

122. Fevrier, B., D. Vilette, F. Archer, D. Loew, W. Faigle, M. Vidal, H. Laude, and G. Raposo, *Cells release prions in association with exosomes.* Proc Natl Acad Sci U S A, 2004. **101**(26): p. 9683-8.

123. Cisse, M.A., C. Sunyach, S. Lefranc-Jullien, R. Postina, B. Vincent, and F. Checler, *The disintegrin ADAM9 indirectly contributes to the physiological processing of cellular prion by modulating ADAM10 activity.* J Biol Chem, 2005. **280**(49): p. 40624-31.

124. Aguzzi, A. and M. Polymenidou, *Mammalian prion biology: one century of evolving concepts.* Cell, 2004. **116**(2): p. 313-27.

125. Bueler, H., M. Fischer, Y. Lang, H. Bluethmann, H.P. Lipp, S.J. DeArmond, S.B. Prusiner, M. Aguet, and C. Weissmann, *Normal development and behaviour of mice lacking the neuronal cell-surface PrP protein.* Nature, 1992. **356**(6370): p. 577-82.

126. Nicolas, O., R. Gavin, and J.A. del Rio, *New insights into cellular prion protein (PrPc) functions: the "ying and yang" of a relevant protein.* Brain Res Rev, 2009. **61**(2): p. 170-84.

127. Mehrpour, M. and P. Codogno, *Prion protein: From physiology to cancer biology.* Cancer Lett, 2010. **290**(1): p. 1-23.

128. Martins, V.R., F.H. Beraldo, G.N. Hajj, M.H. Lopes, K.S. Lee, M.M. Prado, and R. Linden, *Prion Protein: Orchestrating Neurotrophic Activities.* Curr Issues Mol Biol, 2009. **12**(2): p. 63-86.

129. Hwang, D., I.Y. Lee, H. Yoo, N. Gehlenborg, J.H. Cho, B. Petritis, D. Baxter, R. Pitstick, R. Young, D. Spicer, N.D. Price, J.G. Hohmann, S.J. Dearmond, G.A. Carlson, and L.E. Hood, *A systems approach to prion disease.* Mol Syst Biol, 2009. **5**: p. 252.

130. Linden, R., V.R. Martins, M.A. Prado, M. Cammarota, I. Izquierdo, and R.R. Brentani, *Physiology of the prion protein.* Physiol Rev, 2008. **88**(2): p. 673-728.

131. Mouillet-Richard, S., M. Ermonval, C. Chebassier, J.L. Laplanche, S. Lehmann, J.M. Launay, and O. Kellermann, *Signal transduction through prion protein.* Science, 2000. **289**(5486): p. 1925-8.

132. Spielhaupter, C. and H.M. Schatzl, *PrPC directly interacts with proteins involved in signaling pathways.* J Biol Chem, 2001. **276**(48): p. 44604-12.

133. Rossi, D., A. Cozzio, E. Flechsig, M.A. Klein, T. Rulicke, A. Aguzzi, and C. Weissmann, *Onset of ataxia and Purkinje cell loss in PrP null mice inversely correlated with Dpl level in brain.* EMBO J, 2001. **20**(4): p. 694-702.

134. Zanata, S.M., M.H. Lopes, A.F. Mercadante, G.N. Hajj, L.B. Chiarini, R. Nomizo, A.R. Freitas, A.L. Cabral, K.S. Lee, M.A. Juliano, E. de Oliveira, S.G. Jachieri, A. Burlingame, L. Huang, R. Linden, R.R. Brentani, and V.R. Martins, *Stress-inducible protein 1 is a cell surface ligand for cellular prion that triggers neuroprotection.* EMBO J, 2002. **21**(13): p. 3307-16.

135. Anantharam, V., A. Kanthasamy, C.J. Choi, D.P. Martin, C. Latchoumycandane, J.A. Richt, and A.G. Kanthasamy, *Opposing roles of prion protein in oxidative stress- and ER stress-induced apoptotic signaling.* Free Radic Biol Med, 2008. **45**(11): p. 1530-41.

136. Collinge, J., M.A. Whittington, K.C. Sidle, C.J. Smith, M.S. Palmer, A.R. Clarke, and J.G. Jefferys, *Prion protein is necessary for normal synaptic function.* Nature, 1994. **370**(6487): p. 295-7.

137. Tobler, I., T. Deboer, and M. Fischer, *Sleep and sleep regulation in normal and prion protein-deficient mice.* J Neurosci, 1997. **17**(5): p. 1869-79.

138. Tobler, I., S.E. Gaus, T. Deboer, P. Achermann, M. Fischer, T. Rulicke, M. Moser, B. Oesch, P.A. McBride, and J.C. Manson, *Altered circadian activity rhythms and sleep in mice devoid of*

prion protein. Nature, 1996. **380**(6575): p. 639-42.

139. Criado, J.R., M. Sanchez-Alavez, B. Conti, J.L. Giacchino, D.N. Wills, S.J. Henriksen, R. Race, J.C. Manson, B. Chesebro, and M.B. Oldstone, *Mice devoid of prion protein have cognitive deficits that are rescued by reconstitution of PrP in neurons.* Neurobiol Dis, 2005. **19**(1-2): p. 255-65.
140. Le Pichon, C.E., M.T. Valley, M. Polymenidou, A.T. Chesler, B.T. Sagdullaev, A. Aguzzi, and S. Firestein, *Olfactory behavior and physiology are disrupted in prion protein knockout mice.* Nat Neurosci, 2009. **12**(1): p. 60-9.
141. Gadotti, V.M., S.P. Bonfield, and G.W. Zamponi, *Depressive-like behaviour of mice lacking cellular prion protein.* Behav Brain Res, 2011.
142. Chiarini, L.B., A.R. Freitas, S.M. Zanata, R.R. Brentani, V.R. Martins, and R. Linden, *Cellular prion protein transduces neuroprotective signals.* EMBO J, 2002. **21**(13): p. 3317-26.
143. Lopes, M.H., G.N. Hajj, A.G. Muras, G.L. Mancini, R.M. Castro, K.C. Ribeiro, R.R. Brentani, R. Linden, and V.R. Martins, *Interaction of cellular prion and stress-inducible protein 1 promotes neuritogenesis and neuroprotection by distinct signaling pathways.* J Neurosci, 2005. **25**(49): p. 11330-9.
144. Nisbet, R.M., C.F. Harrison, V.A. Lawson, C.L. Masters, R. Cappai, and A.F. Hill, *Residues surrounding the glycosylphosphatidylinositol anchor attachment site of PrP modulate prion infection: insight from the resistance of rabbits to prion disease.* J Virol, 2010. **84**(13): p. 6678-86.
145. Bounhar, Y., Y. Zhang, C.G. Goodyer, and A. LeBlanc, *Prion protein protects human neurons against Bax-mediated apoptosis.* J Biol Chem, 2001. **276**(42): p. 39145-9.
146. Xu, K., X. Wang, Q. Shi, C. Chen, C. Tian, X.L. Li, R.M. Zhou, Y.L. Chu, and X.P. Dong, *Human prion protein mutants with deleted and inserted octarepeats undergo different pathways to trigger cell apoptosis.* J Mol Neurosci, 2011. **43**(3): p. 225-34.
147. Yap, Y.H. and Y.H. Say, *Resistance against apoptosis by the cellular prion protein is dependent on its glycosylation status in oral HSC-2 and colon LS 174T cancer cells.* Cancer Lett, 2011. **306**(1): p. 111-9.
148. Ramljak, S., A.R. Asif, V.W. Armstrong, A. Wrede, M.H. Groschup, A. Buschmann, W. Schulz-Schaeffer, W. Bodemer, and I. Zerr, *Physiological role of the cellular prion protein (PrPc): protein profiling study in two cell culture systems.* J Proteome Res, 2008. **7**(7): p. 2681-95.
149. Roucou, X., P.N. Giannopoulos, Y. Zhang, J. Jodoin, C.G. Goodyer, and A. LeBlanc, *Cellular prion protein inhibits proapoptotic Bax conformational change in human neurons and in breast carcinoma MCF-7 cells.* Cell Death Differ, 2005. **12**(7): p. 783-95.
150. Graner, E., A.F. Mercadante, S.M. Zanata, O.V. Forlenza, A.L. Cabral, S.S. Veiga, M.A. Juliano, R. Roesler, R. Walz, A. Minetti, I. Izquierdo, V.R. Martins, and R.R. Brentani, *Cellular prion protein binds laminin and mediates neuritogenesis.* Brain Res Mol Brain Res, 2000. **76**(1): p. 85-92.
151. Rieger, R., F. Edenhofer, C.I. Lasmezas, and S. Weiss, *The human 37-kDa laminin receptor precursor interacts with the prion protein in eukaryotic cells.* Nat Med, 1997. **3**(12): p. 1383-8.
152. Santuccione, A., V. Sytnyk, I. Leshchyns'ka, and M. Schachner, *Prion protein recruits its neuronal receptor NCAM to lipid rafts to activate p59fyn and to enhance neurite outgrowth.*

J Cell Biol, 2005. **169**(2): p. 341-54.

153. Malaga-Trillo, E., G.P. Solis, Y. Schrock, C. Geiss, L. Luncz, V. Thomanetz, and C.A. Stuermer, *Regulation of embryonic cell adhesion by the prion protein.* PLoS Biol, 2009. **7**(3): p. e55.
154. Miranda, A., E. Pericuesta, M.A. Ramirez, and A. Gutierrez-Adan, *Prion protein expression regulates embryonic stem cell pluripotency and differentiation.* PLoS One, 2011. **6**(4): p. e18422.
155. Peralta, O.A., W.R. Huckle, and W.H. Eyestone, *Expression and knockdown of cellular prion protein (PrPC) in differentiating mouse embryonic stem cells.* Differentiation, 2011. **81**(1): p. 68-77.
156. Richt, J.A., P. Kasinathan, A.N. Hamir, J. Castilla, T. Sathiyaseelan, F. Vargas, J. Sathiyaseelan, H. Wu, H. Matsushita, J. Koster, S. Kato, I. Ishida, C. Soto, J.M. Robl, and Y. Kuroiwa, *Production of cattle lacking prion protein.* Nat Biotechnol, 2007. **25**(1): p. 132-8.
157. Isaacs, J.D., G.S. Jackson, and D.M. Altmann, *The role of the cellular prion protein in the immune system.* Clin Exp Immunol, 2006. **146**(1): p. 1-8.
158. Parkin, E.T., N.T. Watt, I. Hussain, E.A. Eckman, C.B. Eckman, J.C. Manson, H.N. Baybutt, A.J. Turner, and N.M. Hooper, *Cellular prion protein regulates beta-secretase cleavage of the Alzheimer's amyloid precursor protein.* Proc Natl Acad Sci U S A, 2007. **104**(26): p. 11062-7.
159. Resenberger, U.K., A. Harmeier, A.C. Woerner, J.L. Goodman, V. Muller, R. Krishnan, R.M. Vabulas, H.A. Kretzschmar, S. Lindquist, F.U. Hartl, G. Multhaup, K.F. Winklhofer, and J. Tatzelt, *The cellular prion protein mediates neurotoxic signalling of beta-sheet-rich conformers independent of prion replication.* EMBO J, 2011.
160. Merz, P.A., R.J. Kascsak, R. Rubenstein, R.I. Carp, and H.M. Wisniewski, *Antisera to scrapie-associated fibril protein and prion protein decorate scrapie-associated fibrils.* J Virol, 1987. **61**(1): p. 42-9.
161. Prusiner, S.B., M.P. McKinley, K.A. Bowman, D.C. Bolton, P.E. Bendheim, D.F. Groth, and G.G. Glenner, *Scrapie prions aggregate to form amyloid-like birefringent rods.* Cell, 1983. **35**(2 Pt 1): p. 349-58.
162. Marijanovic, Z., A. Caputo, V. Campana, and C. Zurzolo, *Identification of an intracellular site of prion conversion.* PLoS Pathog, 2009. **5**(5): p. e1000426.
163. Kelly, J.W., *The alternative conformations of amyloidogenic proteins and their multi-step assembly pathways.* Curr Opin Struct Biol, 1998. **8**(1): p. 101-6.
164. van der Kamp, M.W. and V. Daggett, *Influence of pH on the human prion protein: insights into the early steps of misfolding.* Biophys J, 2010. **99**(7): p. 2289-98.
165. Sim, V.L. and B. Caughey, *Ultrastructures and strain comparison of under-glycosylated scrapie prion fibrils.* Neurobiol Aging, 2009. **30**(12): p. 2031-42.
166. Sunde, M., L.C. Serpell, M. Bartlam, P.E. Fraser, M.B. Pepys, and C.C. Blake, *Common core structure of amyloid fibrils by synchrotron X-ray diffraction.* J Mol Biol, 1997. **273**(3): p. 729-39.
167. Caughey, B.W., A. Dong, K.S. Bhat, D. Ernst, S.F. Hayes, and W.S. Caughey, *Secondary structure analysis of the scrapie-associated protein PrP 27-30 in water by infrared spectroscopy.* Biochemistry, 1991. **30**(31): p. 7672-80.
168. Ollesch, J., E. Kunnemann, R. Glockshuber, and K. Gerwert, *Prion protein alpha-to-beta transition monitored by time-resolved Fourier transform infrared spectroscopy.* Appl Spectrosc, 2007. **61**(10): p. 1025-31.

169. Surewicz, W.K. and M.I. Apostol, *Prion Protein and Its Conformational Conversion: A Structural Perspective.* Topics in current chemistry, 2011.
170. DeMarco, M.L. and V. Daggett, *From conversion to aggregation: protofibril formation of the prion protein.* Proc Natl Acad Sci U S A, 2004. **101**(8): p. 2293-8.
171. Govaerts, C., H. Wille, S.B. Prusiner, and F.E. Cohen, *Evidence for assembly of prions with left-handed beta-helices into trimers.* Proc Natl Acad Sci U S A, 2004. **101**(22): p. 8342-7.
172. Yang, S., H. Levine, J.N. Onuchic, and D.L. Cox, *Structure of infectious prions: stabilization by domain swapping.* FASEB journal : official publication of the Federation of American Societies for Experimental Biology, 2005. **19**(13): p. 1778-82.
173. Malolepsza, E., M. Boniecki, A. Kolinski, and L. Piela, *Theoretical model of prion propagation: a misfolded protein induces misfolding.* Proceedings of the National Academy of Sciences of the United States of America, 2005. **102**(22): p. 7835-40.
174. Langedijk, J.P., G. Fuentes, R. Boshuizen, and A.M. Bonvin, *Two-rung model of a left-handed beta-helix for prions explains species barrier and strain variation in transmissible spongiform encephalopathies.* Journal of molecular biology, 2006. **360**(4): p. 907-20.
175. DeMarco, M.L., J. Silveira, B. Caughey, and V. Daggett, *Structural properties of prion protein protofibrils and fibrils: an experimental assessment of atomic models.* Biochemistry, 2006. **45**(51): p. 15573-82.
176. Lu, X., P.L. Wintrode, and W.K. Surewicz, *Beta-sheet core of human prion protein amyloid fibrils as determined by hydrogen/deuterium exchange.* Proceedings of the National Academy of Sciences of the United States of America, 2007. **104**(5): p. 1510-5.
177. Cobb, N.J., F.D. Sonnichsen, H. McHaourab, and W.K. Surewicz, *Molecular architecture of human prion protein amyloid: a parallel, in-register beta-structure.* Proceedings of the National Academy of Sciences of the United States of America, 2007. **104**(48): p. 18946-51.
178. Cobb, N.J., A.C. Apetri, and W.K. Surewicz, *Prion protein amyloid formation under native-like conditions involves refolding of the C-terminal alpha-helical domain.* J Biol Chem, 2008. **283**(50): p. 34704-11.
179. Ganchev, D.N., N.J. Cobb, K. Surewicz, and W.K. Surewicz, *Nanomechanical properties of human prion protein amyloid as probed by force spectroscopy.* Biophys J, 2008. **95**(6): p. 2909-15.
180. Wasmer, C., A. Lange, H. Van Melckebeke, A.B. Siemer, R. Riek, and B.H. Meier, *Amyloid fibrils of the HET-s(218-289) prion form a beta solenoid with a triangular hydrophobic core.* Science, 2008. **319**(5869): p. 1523-6.
181. Shewmaker, F., R.B. Wickner, and R. Tycko, *Amyloid of the prion domain of Sup35p has an in-register parallel beta-sheet structure.* Proceedings of the National Academy of Sciences of the United States of America, 2006. **103**(52): p. 19754-9.
182. Wickner, R.B., F. Shewmaker, D. Kryndushkin, and H.K. Edskes, *Protein inheritance (prions) based on parallel in-register beta-sheet amyloid structures.* Bioessays, 2008. **30**(10): p. 955-64.
183. Baxa, U., R.B. Wickner, A.C. Steven, D.E. Anderson, L.N. Marekov, W.M. Yau, and R. Tycko, *Characterization of beta-sheet structure in Ure2p1-89 yeast prion fibrils by solid-state nuclear magnetic resonance.* Biochemistry, 2007. **46**(45): p. 13149-62.
184. Wickner, R.B., F. Dyda, and R. Tycko, *Amyloid of Rnq1p, the basis of the [PIN+] prion, has a parallel in-register beta-sheet structure.* Proceedings of the National Academy of Sciences of

the United States of America, 2008. **105**(7): p. 2403-8.

185. Nelson, R., M.R. Sawaya, M. Balbirnie, A.O. Madsen, C. Riekel, R. Grothe, and D. Eisenberg, *Structure of the cross-beta spine of amyloid-like fibrils.* Nature, 2005. **435**(7043): p. 773-8.
186. Smirnovas, V., J.I. Kim, X. Lu, R. Atarashi, B. Caughey, and W.K. Surewicz, *Distinct structures of scrapie prion protein (PrPSc)-seeded versus spontaneous recombinant prion protein fibrils revealed by hydrogen/deuterium exchange.* J Biol Chem, 2009. **284**(36): p. 24233-41.
187. Smirnovas, V., G.S. Baron, D.K. Offerdahl, G.J. Raymond, B. Caughey, and W.K. Surewicz, *Structural organization of brain-derived mammalian prions examined by hydrogen-deuterium exchange.* Nature structural & molecular biology, 2011. **18**(4): p. 504-6.
188. Nazabal, A., S. Hornemann, A. Aguzzi, and R. Zenobi, *Hydrogen/deuterium exchange mass spectrometry identifies two highly protected regions in recombinant full-length prion protein amyloid fibrils.* J Mass Spectrom, 2009. **44**(6): p. 965-77.
189. Ostapchenko, V.G., M.R. Sawaya, N. Makarava, R. Savtchenko, K.P. Nilsson, D. Eisenberg, and I.V. Baskakov, *Two amyloid States of the prion protein display significantly different folding patterns.* J Mol Biol, 2010. **400**(4): p. 908-21.
190. Kryndushkin, D.S., R.B. Wickner, and R. Tycko, *The Core of Ure2p Prion Fibrils Is Formed by the N-Terminal Segment in a Parallel Cross-beta Structure: Evidence from Solid-State NMR.* J Mol Biol, 2011. **409**(2): p. 263-77.
191. Sawaya, M.R., S. Sambashivan, R. Nelson, M.I. Ivanova, S.A. Sievers, M.I. Apostol, M.J. Thompson, M. Balbirnie, J.J. Wiltzius, H.T. McFarlane, A.O. Madsen, C. Riekel, and D. Eisenberg, *Atomic structures of amyloid cross-beta spines reveal varied steric zippers.* Nature, 2007. **447**(7143): p. 453-7.
192. Vitagliano, L., F. Stanzione, A. De Simone, and L. Esposito, *Dynamics and stability of amyloid-like steric zipper assemblies with hydrophobic dry interfaces.* Biopolymers, 2009. **91**(12): p. 1161-71.
193. Mallucci, G.R., S. Ratte, E.A. Asante, J. Linehan, I. Gowland, J.G. Jefferys, and J. Collinge, *Post-natal knockout of prion protein alters hippocampal CA1 properties, but does not result in neurodegeneration.* EMBO J, 2002. **21**(3): p. 202-10.
194. Radford, H.E. and G.R. Mallucci, *The Role of GPI-anchored PrP(C) in Mediating the Neurotoxic Effect of Scrapie Prions in Neurons.* Curr Issues Mol Biol, 2009. **12**(2): p. 119-128.
195. Mallucci, G.R., M.D. White, M. Farmer, A. Dickinson, H. Khatun, A.D. Powell, S. Brandner, J.G. Jefferys, and J. Collinge, *Targeting cellular prion protein reverses early cognitive deficits and neurophysiological dysfunction in prion-infected mice.* Neuron, 2007. **53**(3): p. 325-35.
196. Soto, C., *Reversibility of prion-induced neurodegeneration.* Lancet Neurol, 2007. **6**(4): p. 294-5.
197. Abrahantes, J.C., M. Aerts, B. van Everbroeck, C. Saegerman, D. Berkvens, H. Geys, K. Mintiens, S. Roels, and P. Cras, *Classification of sporadic Creutzfeldt-Jakob disease based on clinical and neuropathological characteristics.* European journal of epidemiology, 2007. **22**(7): p. 457-65.
198. Race, R., A. Raines, G.J. Raymond, B. Caughey, and B. Chesebro, *Long-term subclinical carrier state precedes scrapie replication and adaptation in a resistant species: analogies to bovine spongiform encephalopathy and variant Creutzfeldt-Jakob disease in humans.* J Virol, 2001. **75**(21): p. 10106-12.
199. Chesebro, B., M. Trifilo, R. Race, K. Meade-White, C. Teng, R. LaCasse, L. Raymond, C. Favara,

G. Baron, S. Priola, B. Caughey, E. Masliah, and M. Oldstone, *Anchorless prion protein results in infectious amyloid disease without clinical scrapie.* Science, 2005. **308**(5727): p. 1435-9.

200. Collinge, J. and A.R. Clarke, *A general model of prion strains and their pathogenicity.* Science, 2007. **318**(5852): p. 930-6.

201. Sandberg, M.K., H. Al-Doujaily, B. Sharps, A.R. Clarke, and J. Collinge, *Prion propagation and toxicity in vivo occur in two distinct mechanistic phases.* Nature, 2011. **470**(7335): p. 540-2.

202. Aksenov, M.Y., M.V. Aksenova, D.A. Butterfield, K. Hensley, C. Vigo-Pelfrey, and J.M. Carney, *Glutamine synthetase-induced enhancement of beta-amyloid peptide A beta (1-40) neurotoxicity accompanied by abrogation of fibril formation and A beta fragmentation.* J Neurochem, 1996. **66**(5): p. 2050-6.

203. Race, R.E., S.A. Priola, R.A. Bessen, D. Ernst, J. Dockter, G.F. Rall, L. Mucke, B. Chesebro, and M.B. Oldstone, *Neuron-specific expression of a hamster prion protein minigene in transgenic mice induces susceptibility to hamster scrapie agent.* Neuron, 1995. **15**(5): p. 1183-91.

204. Castilla, J., C. Hetz, and C. Soto, *Molecular mechanisms of neurotoxicity of pathological prion protein.* Current molecular medicine, 2004. **4**(4): p. 397-403.

205. Hetz, C.A. and C. Soto, *Stressing out the ER: a role of the unfolded protein response in prion-related disorders.* Current molecular medicine, 2006. **6**(1): p. 37-43.

206. Rane, N.S., S.W. Kang, O. Chakrabarti, L. Feigenbaum, and R.S. Hegde, *Reduced translocation of nascent prion protein during ER stress contributes to neurodegeneration.* Developmental cell, 2008. **15**(3): p. 359-70.

207. Nunziante, M., K. Ackermann, K. Dietrich, H. Wolf, L. Gadtke, S. Gilch, I. Vorberg, M. Groschup, and H.M. Schatzl, *Proteasomal dysfunction and ER stress enhance trafficking of prion protein aggregates through the secretory pathway and increase accumulation of PrPSc.* The Journal of biological chemistry, 2011.

208. Whatley, B.R., L. Li, and L.S. Chin, *The ubiquitin-proteasome system in spongiform degenerative disorders.* Biochim Biophys Acta, 2008. **1782**(12): p. 700-12.

209. Torres, M., K. Castillo, R. Armisen, A. Stutzin, C. Soto, and C. Hetz, *Prion protein misfolding affects calcium homeostasis and sensitizes cells to endoplasmic reticulum stress.* PLoS One, 2010. **5**(12): p. e15658.

210. Rana, A., D. Gnaneswari, S. Bansal, and B. Kundu, *Prion metal interaction: is prion pathogenesis a cause or a consequence of metal imbalance?* Chem Biol Interact, 2009. **181**(3): p. 282-91.

211. Yokoyama, T., K. Masujin, Y. Iwamaru, M. Imamura, and S. Mohri, *Alteration of the biological and biochemical characteristics of bovine spongiform encephalopathy prions during interspecies transmission in transgenic mice models.* J Gen Virol, 2009. **90**(Pt 1): p. 261-8.

212. Xanthopoulos, K., M. Polymenidou, S.J. Bellworthy, S.L. Benestad, and T. Sklaviadis, *Species and strain glycosylation patterns of PrPSc.* PLoS One, 2009. **4**(5): p. e5633.

213. Wadsworth, J.D. and J. Collinge, *Molecular pathology of human prion disease.* Acta Neuropathol, 2011. **121**(1): p. 69-77.

214. Zampieri, M., G. Legname, and C. Altafini, *Investigating the conformational stability of prion strains through a kinetic replication model.* PLoS Comput Biol, 2009. **5**(7): p. e1000420.

215. Spassov, S., M. Beekes, and D. Naumann, *Structural differences between TSEs strains investigated by FT-IR spectroscopy.* Biochim Biophys Acta, 2006. **1760**(7): p. 1138-49.

216. Li, J., S. Browning, S.P. Mahal, A.M. Oelschlegel, and C. Weissmann, *Darwinian evolution of*

prions in cell culture. Science, 2010. **327**(5967): p. 869-72.

217. Thackray, A.M., L. Hopkins, R. Lockey, J. Spiropoulos, and R. Bujdoso, *Emergence of multiple prion strains from single isolates of ovine scrapie.* J Gen Virol, 2011. **92**(Pt 6): p. 1482-91.
218. Mahal, S.P., S. Browning, J. Li, I. Suponitsky-Kroyter, and C. Weissmann, *Transfer of a prion strain to different hosts leads to emergence of strain variants.* Proc Natl Acad Sci U S A, 2010. **107**(52): p. 22653-8.
219. Wadsworth, J.D., S. Joiner, A.F. Hill, T.A. Campbell, M. Desbruslais, P.J. Luthert, and J. Collinge, *Tissue distribution of protease resistant prion protein in variant Creutzfeldt-Jakob disease using a highly sensitive immunoblotting assay.* Lancet, 2001. **358**(9277): p. 171-80.
220. Nilsson, K.P., S. Joshi-Barr, O. Winson, and C.J. Sigurdson, *Prion strain interactions are highly selective.* J Neurosci, 2010. **30**(36): p. 12094-102.
221. Kimberlin, R.H. and C.A. Walker, *Pathogenesis of scrapie: agent multiplication in brain at the first and second passage of hamster scrapie in mice.* J Gen Virol, 1979. **42**(1): p. 107-17.
222. Scott, M., D. Foster, C. Mirenda, D. Serban, F. Coufal, M. Walchli, M. Torchia, D. Groth, G. Carlson, S.J. DeArmond, D. Westaway, and S.B. Prusiner, *Transgenic mice expressing hamster prion protein produce species-specific scrapie infectivity and amyloid plaques.* Cell, 1989. **59**(5): p. 847-57.
223. Priola, S.A. and B. Chesebro, *A single hamster PrP amino acid blocks conversion to protease-resistant PrP in scrapie-infected mouse neuroblastoma cells.* J Virol, 1995. **69**(12): p. 7754-8.
224. Apostol, M.I., J.J. Wiltzius, M.R. Sawaya, D. Cascio, and D. Eisenberg, *Atomic structures suggest determinants of transmission barriers in mammalian prion disease.* Biochemistry, 2011. **50**(13): p. 2456-63.
225. Patino, M.M., J.J. Liu, J.R. Glover, and S. Lindquist, *Support for the prion hypothesis for inheritance of a phenotypic trait in yeast.* Science, 1996. **273**(5275): p. 622-6.
226. Paushkin, S.V., V.V. Kushnirov, V.N. Smirnov, and M.D. Ter-Avanesyan, *Propagation of the yeast prion-like [psi+] determinant is mediated by oligomerization of the SUP35-encoded polypeptide chain release factor.* EMBO J, 1996. **15**(12): p. 3127-34.
227. Brown, J.C. and S. Lindquist, *A heritable switch in carbon source utilization driven by an unusual yeast prion.* Genes Dev, 2009. **23**(19): p. 2320-32.
228. Alberti, S., R. Halfmann, O. King, A. Kapila, and S. Lindquist, *A systematic survey identifies prions and illuminates sequence features of prionogenic proteins.* Cell, 2009. **137**(1): p. 146-58.
229. Nakayashiki, T., C.P. Kurtzman, H.K. Edskes, and R.B. Wickner, *Yeast prions [URE3] and [PSI+] are diseases.* Proceedings of the National Academy of Sciences of the United States of America, 2005. **102**(30): p. 10575-80.
230. Sindi, S.S. and T.R. Serio, *Prion dynamics and the quest for the genetic determinant in protein-only inheritance.* Curr Opin Microbiol, 2009. **12**(6): p. 623-30.
231. Watt, B., G. van Niel, D.M. Fowler, I. Hurbain, K.C. Luk, S.E. Stayrook, M.A. Lemmon, G. Raposo, J. Shorter, J.W. Kelly, and M.S. Marks, *N-terminal domains elicit formation of functional Pmel17 amyloid fibrils.* J Biol Chem, 2009. **284**(51): p. 35543-55.
232. Baskakov, I.V., G. Legname, S.B. Prusiner, and F.E. Cohen, *Folding of prion protein to its native alpha-helical conformation is under kinetic control.* J Biol Chem, 2001. **276**(23): p. 19687-90.

233. Kuwata, K., Y.O. Kamatari, K. Akasaka, and T.L. James, *Slow conformational dynamics in the hamster prion protein.* Biochemistry, 2004. **43**(15): p. 4439-46.

234. Hosszu, L.L., C.R. Trevitt, S. Jones, M. Batchelor, D.J. Scott, G.S. Jackson, J. Collinge, J.P. Waltho, and A.R. Clarke, *Conformational properties of beta-PrP.* J Biol Chem, 2009. **284**(33): p. 21981-90.

235. Dima, R.I. and D. Thirumalai, *Probing the instabilities in the dynamics of helical fragments from mouse PrPC.* Proc Natl Acad Sci U S A, 2004. **101**(43): p. 15335-40.

236. Langella, E., R. Improta, and V. Barone, *Checking the pH-induced conformational transition of prion protein by molecular dynamics simulations: effect of protonation of histidine residues.* Biophys J, 2004. **87**(6): p. 3623-32.

237. Blinov, N., M. Berjanskii, D.S. Wishart, and M. Stepanova, *Structural domains and main-chain flexibility in prion proteins.* Biochemistry, 2009. **48**(7): p. 1488-97.

238. Chebaro, Y. and P. Derreumaux, *The conversion of helix H2 to beta-sheet is accelerated in the monomer and dimer of the prion protein upon T183A mutation.* J Phys Chem B, 2009. **113**(19): p. 6942-8.

239. van der Kamp, M.W. and V. Daggett, *Molecular Dynamics as an Approach to Study Prion Protein Misfolding and the Effect of Pathogenic Mutations.* Top Curr Chem, 2011.

240. Campos, S.R., M. Machuqueiro, and A.M. Baptista, *Constant-pH molecular dynamics simulations reveal a beta-rich form of the human prion protein.* J Phys Chem B, 2010. **114**(39): p. 12692-700.

241. Apetri, A.C., K. Maki, H. Roder, and W.K. Surewicz, *Early intermediate in human prion protein folding as evidenced by ultrarapid mixing experiments.* J Am Chem Soc, 2006. **128**(35): p. 11673-8.

242. Kuwata, K., H. Li, H. Yamada, G. Legname, S.B. Prusiner, K. Akasaka, and T.L. James, *Locally disordered conformer of the hamster prion protein: a crucial intermediate to PrPSc?* Biochemistry, 2002. **41**(41): p. 12277-83.

243. Swietnicki, W., R. Petersen, P. Gambetti, and W.K. Surewicz, *pH-dependent stability and conformation of the recombinant human prion protein PrP(90-231).* The Journal of biological chemistry, 1997. **272**(44): p. 27517-20.

244. Peretz, D., R.A. Williamson, Y. Matsunaga, H. Serban, C. Pinilla, R.B. Bastidas, R. Rozenshteyn, T.L. James, R.A. Houghten, F.E. Cohen, S.B. Prusiner, and D.R. Burton, *A conformational transition at the N terminus of the prion protein features in formation of the scrapie isoform.* Journal of molecular biology, 1997. **273**(3): p. 614-22.

245. Novitskaya, V., N. Makarava, A. Bellon, O.V. Bocharova, I.B. Bronstein, R.A. Williamson, and I.V. Baskakov, *Probing the conformation of the prion protein within a single amyloid fibril using a novel immunoconformational assay.* The Journal of biological chemistry, 2006. **281**(22): p. 15536-45.

246. DeMarco, M.L. and V. Daggett, *Molecular mechanism for low pH triggered misfolding of the human prion protein.* Biochemistry, 2007. **46**(11): p. 3045-54.

247. Muramoto, T., S.J. DeArmond, M. Scott, G.C. Telling, F.E. Cohen, and S.B. Prusiner, *Heritable disorder resembling neuronal storage disease in mice expressing prion protein with deletion of an alpha-helix.* Nature medicine, 1997. **3**(7): p. 750-5.

248. Apetri, A.C. and W.K. Surewicz, *Kinetic intermediate in the folding of human prion protein.* J Biol Chem, 2002. **277**(47): p. 44589-92.

249. Hosszu, L.L., M.A. Wells, G.S. Jackson, S. Jones, M. Batchelor, A.R. Clarke, C.J. Craven, J.P. Waltho, and J. Collinge, *Definable equilibrium states in the folding of human prion protein.* Biochemistry, 2005. **44**(50): p. 16649-57.
250. Orte, A., N.R. Birkett, R.W. Clarke, G.L. Devlin, C.M. Dobson, and D. Klenerman, *Direct characterization of amyloidogenic oligomers by single-molecule fluorescence.* Proc Natl Acad Sci U S A, 2008. **105**(38): p. 14424-9.
251. Baskakov, I.V., G. Legname, M.A. Baldwin, S.B. Prusiner, and F.E. Cohen, *Pathway complexity of prion protein assembly into amyloid.* J Biol Chem, 2002. **277**(24): p. 21140-8.
252. Tahiri-Alaoui, A., V.L. Sim, B. Caughey, and W. James, *Molecular heterosis of prion protein beta-oligomers. A potential mechanism of human resistance to disease.* J Biol Chem, 2006. **281**(45): p. 34171-8.
253. Wang, J., C. Tan, H.F. Chen, and R. Luo, *All-atom computer simulations of amyloid fibrils disaggregation.* Biophys J, 2008. **95**(11): p. 5037-47.
254. Jain, S. and J.B. Udgaonkar, *Salt-induced modulation of the pathway of amyloid fibril formation by the mouse prion protein.* Biochemistry, 2010. **49**(35): p. 7615-24.
255. Jain, S. and J.B. Udgaonkar, *Evidence for stepwise formation of amyloid fibrils by the mouse prion protein.* J Mol Biol, 2008. **382**(5): p. 1228-41.
256. Massi, F. and J.E. Straub, *Energy landscape theory for Alzheimer's amyloid beta-peptide fibril elongation.* Proteins, 2001. **42**(2): p. 217-29.
257. Nguyen, P.H., M.S. Li, G. Stock, J.E. Straub, and D. Thirumalai, *Monomer adds to preformed structured oligomers of Abeta-peptides by a two-stage dock-lock mechanism.* Proc Natl Acad Sci U S A, 2007. **104**(1): p. 111-6.
258. Reddy, G., J.E. Straub, and D. Thirumalai, *Dynamics of locking of peptides onto growing amyloid fibrils.* Proc Natl Acad Sci U S A, 2009. **106**(29): p. 11948-53.
259. Morris, A.M., M.A. Watzky, and R.G. Finke, *Protein aggregation kinetics, mechanism, and curve-fitting: a review of the literature.* Biochim Biophys Acta, 2009. **1794**(3): p. 375-97.
260. Serio, T.R., A.G. Cashikar, A.S. Kowal, G.J. Sawicki, J.J. Moslehi, L. Serpell, M.F. Arnsdorf, and S.L. Lindquist, *Nucleated conformational conversion and the replication of conformational information by a prion determinant.* Science, 2000. **289**(5483): p. 1317-21.
261. Gajdusek, D.C., *Transmissible and non-transmissible amyloidoses: autocatalytic post-translational conversion of host precursor proteins to beta-pleated sheet configurations.* J Neuroimmunol, 1988. **20**(2-3): p. 95-110.
262. Prusiner, S.B., *Molecular biology of prion diseases.* Science, 1991. **252**(5012): p. 1515-22.
263. Come, J.H., P.E. Fraser, and P.T. Lansbury, Jr., *A kinetic model for amyloid formation in the prion diseases: importance of seeding.* Proc Natl Acad Sci U S A, 1993. **90**(13): p. 5959-63.
264. Scheibel, T., J. Bloom, and S.L. Lindquist, *The elongation of yeast prion fibers involves separable steps of association and conversion.* Proc Natl Acad Sci U S A, 2004. **101**(8): p. 2287-92.
265. Padrick, S.B. and A.D. Miranker, *Islet amyloid: phase partitioning and secondary nucleation are central to the mechanism of fibrillogenesis.* Biochemistry, 2002. **41**(14): p. 4694-703.
266. Wall, J., M. Schell, C. Murphy, R. Hrncic, F.J. Stevens, and A. Solomon, *Thermodynamic instability of human lambda 6 light chains: correlation with fibrillogenicity.* Biochemistry, 1999. **38**(42): p. 14101-8.
267. Knowles, T.P., C.A. Waudby, G.L. Devlin, S.I. Cohen, A. Aguzzi, M. Vendruscolo, E.M. Terentjev,

M.E. Welland, and C.M. Dobson, *An analytical solution to the kinetics of breakable filament assembly.* Science, 2009. **326**(5959): p. 1533-7.

268. Lee, K.S. and B. Caughey, *A simplified recipe for prions.* Proceedings of the National Academy of Sciences of the United States of America, 2007. **104**(23): p. 9551-2.
269. Borchelt, D.R., A. Taraboulos, and S.B. Prusiner, *Evidence for synthesis of scrapie prion proteins in the endocytic pathway.* The Journal of biological chemistry, 1992. **267**(23): p. 16188-99.
270. Taraboulos, A., D. Serban, and S.B. Prusiner, *Scrapie prion proteins accumulate in the cytoplasm of persistently infected cultured cells.* The Journal of cell biology, 1990. **110**(6): p. 2117-32.
271. Heiseke, A., Y. Aguib, and H.M. Schatzl, *Autophagy, prion infection and their mutual interactions.* Current issues in molecular biology, 2010. **12**(2): p. 87-97.
272. Lee, R.J., S. Wang, and P.S. Low, *Measurement of endosome pH following folate receptor-mediated endocytosis.* Biochim Biophys Acta, 1996. **1312**(3): p. 237-42.
273. Speare, J.O., T.S. Rush, 3rd, M.E. Bloom, and B. Caughey, *The role of helix 1 aspartates and salt bridges in the stability and conversion of prion protein.* J Biol Chem, 2003. **278**(14): p. 12522-9.
274. Lennon, C.W., H.D. Cox, S.P. Hennelly, S.J. Chelmo, and M.A. McGuirl, *Probing structural differences in prion protein isoforms by tyrosine nitration.* Biochemistry, 2007. **46**(16): p. 4850-60.
275. Nozaki, Y., *The preparation of guanidine hydrochloride.* Methods in enzymology, 1972. **26 PtC**: p. 43-50.
276. Gasteiger, E., C. Hoogland, A. Gattiker, S. Duvaud, M.R. Wilkins, R.D. Appel, and A. Bairoch, *Protein Identification and Analysis Tools on the ExPASy Server*, in *The Proteomics Protocols Handbook*, J.M. Walker, Editor 2005, Humana Press. p. 571-607.
277. Bocharova, O.V., L. Breydo, A.S. Parfenov, V.V. Salnikov, and I.V. Baskakov, *In vitro conversion of full-length mammalian prion protein produces amyloid form with physical properties of PrP(Sc).* J Mol Biol, 2005. **346**(2): p. 645-59.
278. Tahiri-Alaoui, A. and W. James, *Rapid formation of amyloid from alpha-monomeric recombinant human PrP in vitro.* Protein Sci, 2005. **14**(4): p. 942-7.
279. Atarashi, R., R.A. Moore, V.L. Sim, A.G. Hughson, D.W. Dorward, H.A. Onwubiko, S.A. Priola, and B. Caughey, *Ultrasensitive detection of scrapie prion protein using seeded conversion of recombinant prion protein.* Nat Methods, 2007. **4**(8): p. 645-50.
280. Walsh, D.M., A. Lomakin, G.B. Benedek, M.M. Condron, and D.B. Teplow, *Amyloid beta-protein fibrillogenesis. Detection of a protofibrillar intermediate.* J Biol Chem, 1997. **272**(35): p. 22364-72.
281. Silveira, J.R., A.G. Hughson, and B. Caughey, *Fractionation of prion protein aggregates by asymmetrical flow field-flow fractionation.* Methods Enzymol, 2006. **412**: p. 21-33.
282. Moon, M.H., P.S. Williams, D. Kang, and I. Hwang, *Field and flow programming in frit-inlet asymmetrical flow field-flow fractionation.* J Chromatogr A, 2002. **955**(2): p. 263-72.
283. Giddings, J.C. and K.D. Caldwell, *Field-flow fractionation: choices in programmed and nonprogrammed operation.* Anal Chem, 1984. **56**(12): p. 2093-9.
284. Wyatt, P.J., *Light scattering and the absolute characterization of macromolecules.* Anal Chim Acta, 1993. **272**(1): p. 1-40.

285. Andersson, M., B. Wittgren, and K.G. Wahlund, *Accuracy in multiangle light scattering measurements for molar mass and radius estimations. Model calculations and experiments.* Anal Chem, 2003. **75**(16): p. 4279-91.
286. Lee, S., P.O. Nilsson, G.S. Nilsson, and K.G. Wahlund, *Development of asymmetrical flow field-flow fractionation-multi angle laser light scattering analysis for molecular mass characterization of cationic potato amylopectin.* J Chromatogr A, 2003. **1011**(1-2): p. 111-23.
287. Pelton, J.T. and L.R. McLean, *Spectroscopic methods for analysis of protein secondary structure.* Anal Biochem, 2000. **277**(2): p. 167-76.
288. Lobley, A., L. Whitmore, and B.A. Wallace, *DICHROWEB: an interactive website for the analysis of protein secondary structure from circular dichroism spectra.* Bioinformatics, 2002. **18**(1): p. 211-2.
289. Whitmore, L. and B.A. Wallace, *DICHROWEB, an online server for protein secondary structure analyses from circular dichroism spectroscopic data.* Nucleic Acids Res, 2004. **32**(Web Server issue): p. W668-73.
290. Surewicz, W.K., H.H. Mantsch, and D. Chapman, *Determination of protein secondary structure by Fourier transform infrared spectroscopy: a critical assessment.* Biochemistry, 1993. **32**(2): p. 389-94.
291. Dong, A., P. Huang, and W.S. Caughey, *Protein secondary structures in water from second-derivative amide I infrared spectra.* Biochemistry, 1990. **29**(13): p. 3303-8.
292. Shevchenko, A., M. Wilm, O. Vorm, and M. Mann, *Mass spectrometric sequencing of proteins silver-stained polyacrylamide gels.* Analytical chemistry, 1996. **68**(5): p. 850-8.
293. Strohalm, M., D. Kavan, P. Novak, M. Volny, and V. Havlicek, *mMass 3: a cross-platform software environment for precise analysis of mass spectrometric data.* Analytical chemistry, 2010. **82**(11): p. 4648-51.
294. Halliday, D. and R. Resnick, in *Physics for Students of Science and Engineering, Combined Ed.* 1960, John Wiley & Sons Inc. : New York. p. 216-244.
295. Bocharova, O.V., L. Breydo, V.V. Salnikov, and I.V. Baskakov, *Copper(II) inhibits in vitro conversion of prion protein into amyloid fibrils.* Biochemistry, 2005. **44**(18): p. 6776-87.
296. Hjelmeland, L.M. and A. Chrambach, *Solubilization of functional membrane proteins.* Methods Enzymol, 1984. **104**: p. 305-18.
297. Notari, S., S. Capellari, A. Giese, I. Westner, A. Baruzzi, B. Ghetti, P. Gambetti, H.A. Kretzschmar, and P. Parchi, *Effects of different experimental conditions on the PrPSc core generated by protease digestion: implications for strain typing and molecular classification of CJD.* The Journal of biological chemistry, 2004. **279**(16): p. 16797-804.
298. Apetri, A.C. and W.K. Surewicz, *Atypical effect of salts on the thermodynamic stability of human prion protein.* J Biol Chem, 2003. **278**(25): p. 22187-92.
299. Sun, Y., N. Makarava, C.I. Lee, P. Laksanalamai, F.T. Robb, and I.V. Baskakov, *Conformational stability of PrP amyloid fibrils controls their smallest possible fragment size.* J Mol Biol, 2008. **376**(4): p. 1155-67.
300. Wang, Y.Q., A.K. Buell, X.Y. Wang, M.E. Welland, C.M. Dobson, T.P. Knowles, and S. Perrett, *Relationship between Prion Propensity and the Rates of Individual Molecular Steps of Fibril Assembly.* J Biol Chem, 2011. **286**(14): p. 12101-7.
301. Weber, P., L. Reznicek, G. Mitteregger, H. Kretzschmar, and A. Giese, *Differential effects of prion particle size on infectivity in vivo and in vitro.* Biochem Biophys Res Commun, 2008.

369(3): p. 924-8.

302. Heiseke, A., Y. Aguib, C. Riemer, M. Baier, and H.M. Schatzl, *Lithium induces clearance of protease resistant prion protein in prion-infected cells by induction of autophagy.* Journal of neurochemistry, 2009. **109**(1): p. 25-34.
303. Singh, N., D. Das, A. Singh, and M.L. Mohan, *Prion protein and metal interaction: physiological and pathological implications.* Curr Issues Mol Biol, 2010. **12**(2): p. 99-107.
304. Brown, D.R., K. Qin, J.W. Herms, A. Madlung, J. Manson, R. Strome, P.E. Fraser, T. Kruck, A. von Bohlen, W. Schulz-Schaeffer, A. Giese, D. Westaway, and H. Kretzschmar, *The cellular prion protein binds copper in vivo.* Nature, 1997. **390**(6661): p. 684-7.
305. Brown, D.R., B.S. Wong, F. Hafiz, C. Clive, S.J. Haswell, and I.M. Jones, *Normal prion protein has an activity like that of superoxide dismutase.* Biochem J, 1999. **344 Pt 1**: p. 1-5.
306. Kuwahara, C., A.M. Takeuchi, T. Nishimura, K. Haraguchi, A. Kubosaki, Y. Matsumoto, K. Saeki, T. Yokoyama, S. Itohara, and T. Onodera, *Prions prevent neuronal cell-line death.* Nature, 1999. **400**(6741): p. 225-6.
307. Burns, C.S., E. Aronoff-Spencer, G. Legname, S.B. Prusiner, W.E. Antholine, G.J. Gerfen, J. Peisach, and G.L. Millhauser, *Copper coordination in the full-length, recombinant prion protein.* Biochemistry, 2003. **42**(22): p. 6794-803.
308. Perera, W.S. and N.M. Hooper, *Ablation of the metal ion-induced endocytosis of the prion protein by disease-associated mutation of the octarepeat region.* Current biology : CB, 2001. **11**(7): p. 519-23.
309. Qin, K., D.S. Yang, Y. Yang, M.A. Chishti, L.J. Meng, H.A. Kretzschmar, C.M. Yip, P.E. Fraser, and D. Westaway, *Copper(II)-induced conformational changes and protease resistance in recombinant and cellular PrP. Effect of protein age and deamidation.* J Biol Chem, 2000. **275**(25): p. 19121-31.
310. Walter, E.D., D.J. Stevens, A.R. Spevacek, M.P. Visconte, A. Dei Rossi, and G.L. Millhauser, *Copper binding extrinsic to the octarepeat region in the prion protein.* Current protein & peptide science, 2009. **10**(5): p. 529-35.
311. Valensin, D., K. Gajda, E. Gralka, G. Valensin, W. Kamysz, and H. Kozlowski, *Copper binding to chicken and human prion protein amylodogenic regions: differences and similarities revealed by Ni2+ as a diamagnetic probe.* J Inorg Biochem, 2010. **104**(1): p. 71-8.
312. Cereghetti, G.M., A. Schweiger, R. Glockshuber, and S. Van Doorslaer, *Electron paramagnetic resonance evidence for binding of Cu(2+) to the C-terminal domain of the murine prion protein.* Biophys J, 2001. **81**(1): p. 516-25.
313. Van Doorslaer, S., G.M. Cereghetti, R. Glockshuber, and A. Schweiger, *Unraveling the Cu2+ Binding Sites in the C-Terminal Domain of the Murine Prion Protein: A Pulse EPR and ENDOR Study.* J. Phys. Chem. B, 2001. **105**(8): p. 1631-1639.
314. Burns, C.S., E. Aronoff-Spencer, C.M. Dunham, P. Lario, N.I. Avdievich, W.E. Antholine, M.M. Olmstead, A. Vrielink, G.J. Gerfen, J. Peisach, W.G. Scott, and G.L. Millhauser, *Molecular features of the copper binding sites in the octarepeat domain of the prion protein.* Biochemistry, 2002. **41**(12): p. 3991-4001.
315. Aronoff-Spencer, E., C.S. Burns, N.I. Avdievich, G.J. Gerfen, J. Peisach, W.E. Antholine, H.L. Ball, F.E. Cohen, S.B. Prusiner, and G.L. Millhauser, *Identification of the Cu2+ binding sites in the N-terminal domain of the prion protein by EPR and CD spectroscopy.* Biochemistry, 2000. **39**(45): p. 13760-71.

316. Guerrieri, F., V. Minicozzi, S. Morante, G. Rossi, S. Furlan, and G. La Penna, *Modeling the interplay of glycine protonation and multiple histidine binding of copper in the prion protein octarepeat subdomains.* J Biol Inorg Chem, 2009. **14**(3): p. 361-74.
317. Marino, T., N. Russo, and M. Toscano, *On the copper(II) ion coordination by prion protein HGGGW pentapeptide model.* J Phys Chem B, 2007. **111**(3): p. 635-40.
318. Ling, Y., R.L. Khade, and Y. Zhang, *Structural, EPR superhyperfine, and NMR hyperfine properties of the Cu-octarepeat binding site in the prion protein.* J Phys Chem B, 2011. **115**(11): p. 2663-70.
319. Chattopadhyay, M., E.D. Walter, D.J. Newell, P.J. Jackson, E. Aronoff-Spencer, J. Peisach, G.J. Gerfen, B. Bennett, W.E. Antholine, and G.L. Millhauser, *The octarepeat domain of the prion protein binds Cu(II) with three distinct coordination modes at pH 7.4.* J Am Chem Soc, 2005. **127**(36): p. 12647-56.
320. Millhauser, G.L., *Copper and the prion protein: methods, structures, function, and disease.* Annu Rev Phys Chem, 2007. **58**: p. 299-320.
321. Wells, M.A., C. Jelinska, L.L. Hosszu, C.J. Craven, A.R. Clarke, J. Collinge, J.P. Waltho, and G.S. Jackson, *Multiple forms of copper (II) co-ordination occur throughout the disordered N-terminal region of the prion protein at pH 7.4.* Biochem J, 2006. **400**(3): p. 501-10.
322. Hodak, M., R. Chisnell, W. Lu, and J. Bernholc, *Functional implications of multistage copper binding to the prion protein.* Proc Natl Acad Sci U S A, 2009. **106**(28): p. 11576-81.
323. Kowalski, J.M. and B. Bennett, *Spin Hamiltonian Parameters for Cu(II)-Prion Peptide Complexes from L-Band Electron Paramagnetic Resonance Spectroscopy.* J Am Chem Soc, 2011.
324. Valensin, G., E. Molteni, D. Valensin, M. Taraszkiewicz, and H. Kozlowski, *Molecular dynamics study of the Cu2+ binding-induced "structuring" of the N-terminal domain of human prion protein.* J Phys Chem B, 2009. **113**(11): p. 3277-9.
325. Shearer, J., K.E. Rosenkoetter, P.E. Callan, and C. Pham, *One octarepeate expansion to the human prion protein alters both the Zn2+ and Cu2+ coordination environments within the octarepeate domain.* Inorg Chem, 2011. **50**(4): p. 1173-5.
326. Ruiz, F.H., E. Silva, and N.C. Inestrosa, *The N-terminal tandem repeat region of human prion protein reduces copper: role of tryptophan residues.* Biochemical and biophysical research communications, 2000. **269**(2): p. 491-5.
327. Miura, T., S. Sasaki, A. Toyama, and H. Takeuchi, *Copper reduction by the octapeptide repeat region of prion protein: pH dependence and implications in cellular copper uptake.* Biochemistry, 2005. **44**(24): p. 8712-20.
328. Liu, L., D. Jiang, A. McDonald, Y. Hao, G.L. Millhauser, and F. Zhou, *Copper redox cycling in the prion protein depends critically on binding mode.* Journal of the American Chemical Society, 2011. **133**(31): p. 12229-37.
329. Bonomo, R.P., G. Imperllizzeri, G. Pappalardo, E. Rizzarelli, and G. Tabbi, *Copper(II) binding modes in the prion octapeptide PHGGGWGQ: a spectroscopic and voltammetric study.* Chemistry, 2000. **6**(22): p. 4195-202.
330. Weiss, A., P. Del Pino, U. Bertsch, C. Renner, M. Mentler, K. Grantner, L. Moroder, H.A. Kretzschmar, and F.G. Parak, *The configuration of the Cu(2+) binding region in full-length human prion protein compared with the isolated octapeptide.* Vet Microbiol, 2007. **123**(4): p. 358-66.

331. del Pino, P., A. Weiss, U. Bertsch, C. Renner, M. Mentler, K. Grantner, F. Fiorino, W. Meyer-Klaucke, L. Moroder, H.A. Kretzschmar, and F.G. Parak, *The configuration of the Cu2+ binding region in full-length human prion protein.* Eur Biophys J, 2007. **36**(3): p. 239-52.

332. Berti, F., E. Gaggelli, R. Guerrini, A. Janicka, H. Kozlowski, A. Legowska, H. Miecznikowska, C. Migliorini, R. Pogni, M. Remelli, K. Rolka, D. Valensin, and G. Valensin, *Structural and dynamic characterization of copper(II) binding of the human prion protein outside the octarepeat region.* Chemistry, 2007. **13**(7): p. 1991-2001.

333. Treiber, C., A.R. Thompsett, R. Pipkorn, D.R. Brown, and G. Multhaup, *Real-time kinetics of discontinuous and highly conformational metal-ion binding sites of prion protein.* J Biol Inorg Chem, 2007. **12**(5): p. 711-20.

334. Shearer, J. and P. Soh, *The copper(II) adduct of the unstructured region of the amyloidogenic fragment derived from the human prion protein is redox-active at physiological pH.* Inorg Chem, 2007. **46**(3): p. 710-9.

335. Klewpatinond, M. and J.H. Viles, *Fragment length influences affinity for Cu2+ and Ni2+ binding to His96 or His111 of the prion protein and spectroscopic evidence for a multiple histidine binding only at low pH.* The Biochemical journal, 2007. **404**(3): p. 393-402.

336. Hureau, C., C. Mathe, P. Faller, T.A. Mattioli, and P. Dorlet, *Folding of the prion peptide GGGTHSQW around the copper(II) ion: identifying the oxygen donor ligand at neutral pH and probing the proximity of the tryptophan residue to the copper ion.* J Biol Inorg Chem, 2008. **13**(7): p. 1055-64.

337. Rivillas-Acevedo, L., R. Grande-Aztatzi, I. Lomeli, J.E. Garcia, E. Barrios, S. Teloxa, A. Vela, and L. Quintanar, *Spectroscopic and electronic structure studies of copper(II) binding to His111 in the human prion protein fragment 106-115: evaluating the role of protons and methionine residues.* Inorg Chem, 2011. **50**(5): p. 1956-72.

338. Osz, K., Z. Nagy, G. Pappalardo, G. Di Natale, D. Sanna, G. Micera, E. Rizzarelli, and I. Sovago, *Copper(II) interaction with prion peptide fragments encompassing histidine residues within and outside the octarepeat domain: speciation, stability constants and binding details.* Chemistry, 2007. **13**(25): p. 7129-43.

339. Di Natale, G., K. Osz, Z. Nagy, D. Sanna, G. Micera, G. Pappalardo, I. Sovago, and E. Rizzarell, *Interaction of copper(II) with the prion peptide fragment HuPrP(76-114) encompassing four histidyl residues within and outside the octarepeat domain.* Inorg Chem, 2009. **48**(9): p. 4239-50.

340. Wells, M.A., G.S. Jackson, S. Jones, L.L. Hosszu, C.J. Craven, A.R. Clarke, J. Collinge, and J.P. Waltho, *A reassessment of copper(II) binding in the full-length prion protein.* The Biochemical journal, 2006. **399**(3): p. 435-44.

341. Davies, P., F. Marken, S. Salter, and D.R. Brown, *Thermodynamic and voltammetric characterization of the metal binding to the prion protein: insights into pH dependence and redox chemistry.* Biochemistry, 2009. **48**(12): p. 2610-9.

342. Shearer, J. and P. Soh, *The copper(II) adduct of the unstructured region of the amyloidogenic fragment derived from the human prion protein is redox-active at physiological pH.* Inorganic chemistry, 2007. **46**(3): p. 710-9.

343. Thompsett, A.R., S.R. Abdelraheim, M. Daniels, and D.R. Brown, *High affinity binding between copper and full-length prion protein identified by two different techniques.* J Biol Chem, 2005. **280**(52): p. 42750-8.

344. Viles, J.H., F.E. Cohen, S.B. Prusiner, D.B. Goodin, P.E. Wright, and H.J. Dyson, *Copper binding to the prion protein: structural implications of four identical cooperative binding sites.* Proc Natl Acad Sci U S A, 1999. **96**(5): p. 2042-7.
345. Stockel, J., J. Safar, A.C. Wallace, F.E. Cohen, and S.B. Prusiner, *Prion protein selectively binds copper(II) ions.* Biochemistry, 1998. **37**(20): p. 7185-93.
346. Walter, E.D., M. Chattopadhyay, and G.L. Millhauser, *The affinity of copper binding to the prion protein octarepeat domain: evidence for negative cooperativity.* Biochemistry, 2006. **45**(43): p. 13083-92.
347. Kramer, M.L., H.D. Kratzin, B. Schmidt, A. Romer, O. Windl, S. Liemann, S. Hornemann, and H. Kretzschmar, *Prion protein binds copper within the physiological concentration range.* The Journal of biological chemistry, 2001. **276**(20): p. 16711-9.
348. Nadal, R.C., P. Davies, D.R. Brown, and J.H. Viles, *Evaluation of copper2+ affinities for the prion protein.* Biochemistry, 2009. **48**(38): p. 8929-31.
349. Davies, P., P.C. McHugh, V.J. Hammond, F. Marken, and D.R. Brown, *Contribution of individual histidines to prion protein copper binding.* Biochemistry, 2011. **50**(50): p. 10781-91.
350. Kozlowski, H., M. Luczkowski, and M. Remelli, *Prion proteins and copper ions. Biological and chemical controversies.* Dalton Trans, 2010. **39**(28): p. 6371-85.
351. Giese, A., M. Buchholz, J. Herms, and H.A. Kretzschmar, *Mouse brain synaptosomes accumulate copper-67 efficiently by two distinct processes independent of cellular prion protein.* Journal of molecular neuroscience : MN, 2005. **27**(3): p. 347-54.
352. Viles, J.H., M. Klewpatinond, and R.C. Nadal, *Copper and the structural biology of the prion protein.* Biochem Soc Trans, 2008. **36**(Pt 6): p. 1288-92.
353. Davies, P. and D.R. Brown, *The chemistry of copper binding to PrP: is there sufficient evidence to elucidate a role for copper in protein function?* Biochem J, 2008. **410**(2): p. 237-44.
354. Kralovicova, S., S.N. Fontaine, A. Alderton, J. Alderman, K.V. Ragnarsdottir, S.J. Collins, and D.R. Brown, *The effects of prion protein expression on metal metabolism.* Mol Cell Neurosci, 2009. **41**(2): p. 135-47.
355. Westergard, L., H.M. Christensen, and D.A. Harris, *The cellular prion protein (PrP(C)): its physiological function and role in disease.* Biochim Biophys Acta, 2007. **1772**(6): p. 629-44.
356. Rachidi, W., D. Vilette, P. Guiraud, M. Arlotto, J. Riondel, H. Laude, S. Lehmann, and A. Favier, *Expression of prion protein increases cellular copper binding and antioxidant enzyme activities but not copper delivery.* J Biol Chem, 2003. **278**(11): p. 9064-72.
357. Haigh, C.L., K. Edwards, and D.R. Brown, *Copper binding is the governing determinant of prion protein turnover.* Mol Cell Neurosci, 2005. **30**(2): p. 186-96.
358. Vassallo, N. and J. Herms, *Cellular prion protein function in copper homeostasis and redox signalling at the synapse.* J Neurochem, 2003. **86**(3): p. 538-44.
359. Pushie, M.J., A. Rauk, F.R. Jirik, and H.J. Vogel, *Can copper binding to the prion protein generate a misfolded form of the protein?* Biometals, 2009. **22**(1): p. 159-75.
360. Klamt, F., F. Dal-Pizzol, M.L. Conte da Frota, Jr., R. Walz, M.E. Andrades, E.G. da Silva, R.R. Brentani, I. Izquierdo, and J.C. Fonseca Moreira, *Imbalance of antioxidant defense in mice lacking cellular prion protein.* Free radical biology & medicine, 2001. **30**(10): p. 1137-44.
361. Hutter, G., F.L. Heppner, and A. Aguzzi, *No superoxide dismutase activity of cellular prion*

protein in vivo. Biol Chem, 2003. **384**(9): p. 1279-85.

362. Jones, S., M. Batchelor, D. Bhelt, A.R. Clarke, J. Collinge, and G.S. Jackson, *Recombinant prion protein does not possess SOD-1 activity.* Biochem J, 2005. **392**(Pt 2): p. 309-12.
363. La Mendola, D., R.P. Bonomo, S. Caminati, G. Di Natale, S.S. Emmi, O. Hansson, G. Maccarrone, G. Pappalardo, A. Pietropaolo, and E. Rizzarelli, *Copper(II) complexes with an avian prion N-terminal region and their potential SOD-like activity.* J Inorg Biochem, 2009. **103**(2): p. 195-204.
364. Nadal, R.C., S.R. Abdelraheim, M.W. Brazier, S.E. Rigby, D.R. Brown, and J.H. Viles, *Prion protein does not redox-silence Cu2+, but is a sacrificial quencher of hydroxyl radicals.* Free Radic Biol Med, 2007. **42**(1): p. 79-89.
365. Kawano, T., *Prion-derived copper-binding peptide fragments catalyze the generation of superoxide anion in the presence of aromatic monoamines.* International journal of biological sciences, 2007. **3**(1): p. 57-63.
366. Singh, N., D. Das, A. Singh, and M.L. Mohan, *Prion Protein and Metal Interaction: Physiological and Pathological Implications.* Curr Issues Mol Biol, 2009. **12**(2): p. 99-108.
367. Sigurdsson, E.M., D.R. Brown, M.A. Alim, H. Scholtzova, R. Carp, H.C. Meeker, F. Prelli, B. Frangione, and T. Wisniewski, *Copper chelation delays the onset of prion disease.* The Journal of biological chemistry, 2003. **278**(47): p. 46199-202.
368. Hijazi, N., Y. Shaked, H. Rosenmann, T. Ben-Hur, and R. Gabizon, *Copper binding to PrPC may inhibit prion disease propagation.* Brain research, 2003. **993**(1-2): p. 192-200.
369. Tsiroulnikov, K., H. Rezaei, M. Dalgalarrondo, J.M. Chobert, J. Grosclaude, and T. Haertle, *Cu(II) induces small-size aggregates with amyloid characteristics in two alleles of recombinant ovine prion proteins.* Biochim Biophys Acta, 2006. **1764**(7): p. 1218-26.
370. Thakur, A.K., A.K. Srivastava, V. Srinivas, K.V. Chary, and C.M. Rao, *Copper alters aggregation behavior of prion protein and induces novel interactions between its N- and C-terminal regions.* The Journal of biological chemistry, 2011. **286**(44): p. 38533-45.
371. Leavitt, S. and E. Freire, *Direct measurement of protein binding energetics by isothermal titration calorimetry.* Current opinion in structural biology, 2001. **11**(5): p. 560-6.
372. Ladbury, J.E., *Application of isothermal titration calorimetry in the biological sciences: things are heating up!* BioTechniques, 2004. **37**(6): p. 885-7.
373. Pierce, M.M., C.S. Raman, and B.T. Nall, *Isothermal titration calorimetry of protein-protein interactions.* Methods, 1999. **19**(2): p. 213-21.
374. Peisach, J. and W.E. Blumberg, *Structural implications derived from the analysis of electron paramagnetic resonance spectra of natural and artificial copper proteins.* Archives of biochemistry and biophysics, 1974. **165**(2): p. 691-708.
375. WEIL, J.A. and J.R. BOLTON, *Electron Paramagnetic Resonance: Elementary Theory and Practical Applications*. 2nd ed2007, Hoboken, New Jersey: John Wiley & Sons, Inc.
376. Jones, C.E., S.R. Abdelraheim, D.R. Brown, and J.H. Viles, *Preferential Cu2+ coordination by His96 and His111 induces beta-sheet formation in the unstructured amyloidogenic region of the prion protein.* J Biol Chem, 2004. **279**(31): p. 32018-27.
377. Gaffney, B.J., *Unique Spectroscopic Features and Electronic Structures of Copper Proteins: Relation to Reactivity.* Biological magnetic resonance, 2009. **28**: p. 471-506.
378. Stoll, S. and A. Schweiger, *EasySpin, a comprehensive software package for spectral simulation and analysis in EPR.* J Magn Reson, 2006. **178**(1): p. 42-55.

379. Patnaik, P., *Handbook of inorganic chemicals*2002: McGraw-Hill.
380. Smith, R.M. and A.E. Martell, *Critical Stability Constants*. Vol. 6. 1989, New York: Plenum.
381. Davies, P., *The Metallochemistry of the Prion Protein*, in *Department of Biology and Biochemistry*2009, University of Bath: Bath. p. 190.
382. Wong, B.S., S.G. Chen, M. Colucci, Z. Xie, T. Pan, T. Liu, R. Li, P. Gambetti, M.S. Sy, and D.R. Brown, *Aberrant metal binding by prion protein in human prion disease.* Journal of neurochemistry, 2001. **78**(6): p. 1400-8.
383. Jackson, G.S., I. Murray, L.L. Hosszu, N. Gibbs, J.P. Waltho, A.R. Clarke, and J. Collinge, *Location and properties of metal-binding sites on the human prion protein.* Proceedings of the National Academy of Sciences of the United States of America, 2001. **98**(15): p. 8531-5.
384. Garnett, A.P. and J.H. Viles, *Copper binding to the octarepeats of the prion protein. Affinity, specificity, folding, and cooperativity: insights from circular dichroism.* The Journal of biological chemistry, 2003. **278**(9): p. 6795-802.
385. Morante, S., R. Gonzalez-Iglesias, C. Potrich, C. Meneghini, W. Meyer-Klaucke, G. Menestrina, and M. Gasset, *Inter- and intra-octarepeat Cu(II) site geometries in the prion protein: implications in Cu(II) binding cooperativity and Cu(II)-mediated assemblies.* The Journal of biological chemistry, 2004. **279**(12): p. 11753-9.
386. Tsenkova, R.N., I.K. Iordanova, K. Toyoda, and D.R. Brown, *Prion protein fate governed by metal binding.* Biochemical and biophysical research communications, 2004. **325**(3): p. 1005-12.
387. Younan, N.D., M. Klewpatinond, P. Davies, A.V. Ruban, D.R. Brown, and J.H. Viles, *Copper(II)-induced secondary structure changes and reduced folding stability of the prion protein.* Journal of molecular biology, 2011. **410**(3): p. 369-82.
388. Stone, L.A., G.S. Jackson, J. Collinge, J.D. Wadsworth, and A.R. Clarke, *Inhibition of proteinase K activity by copper(II) ions.* Biochemistry, 2007. **46**(1): p. 245-52.
389. Stohr, J., N. Weinmann, H. Wille, T. Kaimann, L. Nagel-Steger, E. Birkmann, G. Panza, S.B. Prusiner, M. Eigen, and D. Riesner, *Mechanisms of prion protein assembly into amyloid.* Proc Natl Acad Sci U S A, 2008. **105**(7): p. 2409-14.
390. Panza, G., J. Stohr, C. Dumpitak, D. Papathanassiou, J. Weiss, D. Riesner, D. Willbold, and E. Birkmann, *Spontaneous and BSE-prion-seeded amyloid formation of full length recombinant bovine prion protein.* Biochem Biophys Res Commun, 2008. **373**(4): p. 493-7.
391. Martin, R.B. and R.J. Sundberg, *Interactions of Histidine and Other Imidazole Derivatives with Transition Metal Ions in Chemical and Biological Systems.* Chemical Reviews, 1974. **74**(4): p. 471-517.
392. Sigel, H. and R.B. Martin, *Coordinating Properties of the Amide Bond. Stability and Structure of Metal Ion Complexes of Peptides and Related Ligands.* Chemical Reviews, 1982. **82**(4): p. 385-426.
393. Miura, T., A. Hori-i, H. Mototani, and H. Takeuchi, *Raman spectroscopic study on the copper(II) binding mode of prion octapeptide and its pH dependence.* Biochemistry, 1999. **38**(35): p. 11560-9.
394. Forman, H.J., M. Maiorino, and F. Ursini, *Signaling functions of reactive oxygen species.* Biochemistry, 2010. **49**(5): p. 835-42.
395. Prusiner, S.B., *Prion biology and diseases*. 2nd ed. Cold Spring Harbor monograph series2004, Cold Spring Harbor, N.Y.: Cold Spring Harbor Laboratory Press. xiii, 1050 p.

396. Stevens, D.J., E.D. Walter, A. Rodriguez, D. Draper, P. Davies, D.R. Brown, and G.L. Millhauser, *Early onset prion disease from octarepeat expansion correlates with copper binding properties.* PLoS pathogens, 2009. **5**(4): p. e1000390.

397. Moore, R.A., C. Herzog, J. Errett, D.A. Kocisko, K.M. Arnold, S.F. Hayes, and S.A. Priola, *Octapeptide repeat insertions increase the rate of protease-resistant prion protein formation.* Protein Sci, 2006. **15**(3): p. 609-19.

398. Jenkins, D.C., I.D. Sylvester, and T.J. Pinheiro, *The elusive intermediate on the folding pathway of the prion protein.* FEBS J, 2008. **275**(6): p. 1323-35.

399. Scott, C.C. and J. Gruenberg, *Ion flux and the function of endosomes and lysosomes: pH is just the start: the flux of ions across endosomal membranes influences endosome function not only through regulation of the luminal pH.* BioEssays : news and reviews in molecular, cellular and developmental biology, 2011. **33**(2): p. 103-10.

400. Zhou, Z., J.B. Fan, H.L. Zhu, F. Shewmaker, X. Yan, X. Chen, J. Chen, G.F. Xiao, L. Guo, and Y. Liang, *Crowded cell-like environment accelerates the nucleation step of amyloidogenic protein misfolding.* J Biol Chem, 2009. **284**(44): p. 30148-58.

401. Carulla, N., G.L. Caddy, D.R. Hall, J. Zurdo, M. Gairi, M. Feliz, E. Giralt, C.V. Robinson, and C.M. Dobson, *Molecular recycling within amyloid fibrils.* Nature, 2005. **436**(7050): p. 554-8.

402. Takeda, T. and D.K. Klimov, *Dissociation of Abeta(16-22) amyloid fibrils probed by molecular dynamics.* Journal of molecular biology, 2007. **368**(4): p. 1202-13.

403. Lakowicz, J.R., *Principles of fluorescence spectroscopy*. 3rd ed2006, New York: Springer. xxvi, 954 p.

404. Que, L., *Physical methods in bioinorganic chemistry : spectroscopy and magnetism*2000, Sausalito, Calif.: University Science Books. vii, 556 p.

405. Antholine, W.E., *Low Frequency EPR of Cu2+ in Proteins*, in *Biomedical EPR, Part A: Free Radicals, Metals, Medicine, and Physiology*, S.S. Eaton, G.R. Eaton, and L.J. Berliner, Editors. 2005, Kluwer Academic/Plenum Publishers: New York. p. 417-454.